Development of a Prototype Frequency Scanning Interferometric Absolute Distance Measurement System for the Survey & Alignment of the International Linear Collider.

John R Green
Keble College, Oxford

Thesis submitted in partial fulfilment of the requirements for the degree of Doctor of Philosophy at the University of Oxford

Trinity Term, 2007

Abstract

Development of a Prototype Frequency Scanning Interferometric Absolute Distance Measurement System for the Survey & Alignment of the International Linear Collider.

John R Green
Keble College, Oxford

Trinity Term, 2007

The LiCAS Rapid Tunnel Reference Surveyor (RTRS) is a robotic survey and alignment instrument designed to meet the requirements of the ILC to position the accelerator components to $200\mu m$ over $600m$. This investigation provides the proof-of-concept of the absolute distance measurement systems within the LiCAS RTRS.

The Frequency Scanning Interferometer (FSI) absolute distance measurement system utilised a telecoms tuneable laser source operating in the C-band (1535 to $1565nm$) and an Erbium Doped Fibre Amplifier. The measurement interferometers used a single fibre for delivery and return. Bespoke software systems for data acquisition, component control and data analysis were created. The data analysis consisted of a phase extraction algorithm and a spectral analysis technique developed to deal with unevenly sampled data.

Investigations using simulated interferometric data were undertaken to evaluate the *precision* (the standard deviation of a set of determined OPDs produced with identical inputs), the *accuracy* (the difference between the mean determined OPD and the input) and the *resolution* (the size of the smallest identifiable OPD variation) of the analysis procedure for both high and low quality data. The analysis precision was:

- $90nm$ over $4.5m$ for high quality signals (SNR=20);
- $402nm$ over $0.45m$ for low quality signals (SNR=1).

The analysis accuracy was:

- $35nm$ over $4.5m$ for high quality signals (SNR=20);
- $135nm$ over $0.45m$ for low quality signals (SNR=1).

The measurement precision of the open-air laboratory FSI system was $250nm$ over $4.5m$. The measurement resolution within the laboratory was approximately $1\mu m$ over $4.5m$, for combinations of around 20 measurements, indicating that $1\mu m$ length variations will be fully resolvable by combing sets of 3 measurements made by the 6 internal FSI lines within the RTRS. The performance of the RTRS FSI system is expected to exceed that of the laboratory system due to the introduction of evacuated reference and measurement interferometers.

The dominant source of systematic error with this investigation was due to measurements being undertaken in open air. However preliminary simulations of the RTRS system suggest that the measurement performance produced by the laboratory FSI systems is capable of exceeding the global alignment requirements at the ILC.

Preface

Particle physics is currently in a period of radical change. The demand for experimental evidence of extremely rare event at increasingly high energies places exceedingly tough requirements upon the investigating machines. The next generation of high-energy experiments provide some of the most challenging engineering problems ever faced. However the results will potentially offer solutions to some of the most fundamental questions in physics, including the origins of mass and the make up of dark matter.

Future high energy experiments must be able to produce collisions with both energy and luminosity orders of magnitude greater than anything achieved previously. The LHC construction is almost complete with significant results expected before the end of the decade. The ILC is taking shape on the drawing board with the linear collider community currently undertaking a global design effort.

One of the greatest challenges at the ILC will be alignment. Producing collisions between nanometer-sized beams that have travelled over $30km$ is equivalent to having two people, one at the Sun and the other at Jupiter, successfully colliding peas fired from pea-shooters. These extreme requirements mean that a rigourous alignment strategy must be employed beginning with the construction of the tunnel and the installation of the accelerator.

The focus of this thesis is the development of an absolute distance measurement system based upon Frequency Scanning Interferometry which forms part of a tunnel reference survey system. This system will provide a reference coordinate system within the tunnel during accelerator installation. This forms a critical part of the global alignment strategy which eventually culminates with beam-based systems producing the required collision luminosity to study physics at the TeV energy scale.

Chapter 1 deals with the nature of the physics expected above the current experimental energy threshold and discusses the advantages and drawbacks of circular and linear colliders as well as the choice of collision particle. An overview of the current design of the ILC is provided along with a review of the proposed alignment strategy and a detailed description of the proposed Rapid Tunnel Reference Surveyor solution.

Chapter 2 provides an introduction to the principles of the employed interferometric length measurement technique before detailing the equipment and procedures used within the laboratory. The data acquisition and storage systems are also outlined.

Chapter 3 discusses the data analysis and length calculation techniques developed for the interferometric length measurement system. The choice of analysis method is justified and the specifics of the implementations are detailed.

Chapter 4 covers investigations into the performance of the analysis procedure. The results of simulations evaluating the precision, accuracy and resolution of the length determination process in both nominal and exceptional scenarios are presented.

Chapter 5 presents the results of the laboratory investigations. These include the assessment of the stability of reference interferometers and the measurement precision over the short and long time scales. Investigations into the ability of the measurement system to resolve changes in length due to thermal variations and induced via a motion stage are also presented.

Finally conclusions are drawn in Chapter 6.

To my family.

Acknowledgements

Thank you all.

The author gratefully acknowledges financial support for this work from PPARC under the auspices of studentship PPA/S/S/2002/03526.

This thesis was written using the LaTeX 2_ε typesetting package. All graphs were produced using the GNUPlot 4 visualisation package, histograms with JAS3 and all other illustrations were produced by the author using NeoOffice unless explicitly stated. This thesis and the research it describes are original work carried out solely by the named author.

© John R. Green, 2007.
All rights reserved, no part of this publication may be reproduced, stored in a retrieval system, or transmitted in any form or by any means, electronic, mechanical, photocopying, recording or otherwise without the express permission of the author.
Published at the University of Oxford, United Kingdom.

Contents

Preface **i**

Acknowledgements **iv**

Contents **v**

List of Figures **viii**

List of Tables **xii**

1 Introduction **1**
1.1 Physics at the TeV Energy Scale . . . 1
1.1.1 The Standard Model . . . 1
1.1.2 Electroweak Symmetry Breaking . . . 2
1.1.3 Supersymmetry . . . 4
1.2 TeV Energy Colliders . . . 7
1.2.1 Lepton and Hadron Colliders . . . 9
1.2.2 Linear and Circular Accelerators . . . 10
1.2.3 Beam Collisions . . . 11
1.3 The International Linear Collider . . . 14
1.3.1 The Injector System . . . 14
1.3.2 Ring-to-Main-Linac . . . 18
1.3.3 The Main Accelerators . . . 19
1.3.4 The Beam Delivery System . . . 20
1.4 Alignment of the ILC . . . 22
1.4.1 Tunnel Construction and Reference Survey . . . 22
1.4.2 Module Construction and Installation . . . 25
1.4.3 Stabilisation . . . 27
1.5 The Rapid Tunnel Reference Surveyor . . . 27
1.5.1 System Overview . . . 28
1.5.2 The Measurement Systems . . . 29
1.5.3 Preliminary System Simulations . . . 32
1.6 Summary . . . 35

2 FSI System Description **36**
2.1 Introduction . . . 36
2.2 FSI and LiCAS . . . 36

2.2.1 FSI Basic Principles . . . 36
2.2.2 The FSI Implementations . . . 40
2.3 Laboratory Equipment . . . 44
2.3.1 The Tuneable Laser . . . 46
2.3.2 The Erbium Doped Fibre Amplifier . . . 51
2.3.3 Optical Fibres . . . 55
2.3.4 Reference Interferometers . . . 57
2.3.5 Measurement Interferometers . . . 59
2.3.6 Thermometry . . . 63
2.3.7 Motion Stages . . . 67
2.4 Data Acquisition . . . 67
2.4.1 Interferometric Signal Data Acquisition . . . 67
2.4.2 Triggering and Timing . . . 69
2.4.3 File Naming and Directory Structure . . . 70

3 Data Processing and Analysis 72
3.1 Introduction . . . 72
3.2 Data Preparation . . . 72
3.3 Phase Analysis . . . 74
3.3.1 The Carré Phase Extraction Implementation . . . 75
3.3.2 Phase Unwrapping . . . 76
3.3.3 Extraction and Unwrapping Error Removal . . . 79
3.4 Spectral Analysis . . . 82
3.4.1 Advantages of Spectral Analysis . . . 82
3.4.2 Spectral Analysis of Unevenly Sampled Data . . . 82
3.4.3 The Spectral Analysis Implementation . . . 84
3.4.4 Spectral Peak Identification . . . 87
3.5 Length Determination . . . 88
3.5.1 Length Calculation . . . 89
3.5.2 Length Corrections . . . 89
3.6 Summary . . . 93

4 Evaluation of Analysis and OPD Determination Techniques 94
4.1 Introduction . . . 94
4.2 Data Simulation . . . 94
4.2.1 Laser Tuning Curve Model . . . 95
4.2.2 Noise Model . . . 96
4.3 Nominal Performance Characterisation . . . 99
4.3.1 Precision . . . 99
4.3.2 Accuracy . . . 103
4.3.3 Resolution . . . 108
4.4 OPD Determination from Low Quality Data . . . 115
4.4.1 Affect of Noise within Measurement Interferometer Signals . . . 115
4.4.2 Affect of Noise within Reference Interferometer Signals . . . 117
4.5 Summary . . . 118

5 Laboratory Interferometer OPD Determination **119**
5.1 Introduction . . . 119
5.2 Reference Interferometer Stability . . . 119
5.2.1 Stability Over 24 Hours . . . 120
5.2.2 Stability Over 20 Minutes . . . 128
5.2.3 Stability Conclusions . . . 133
5.3 External Measurement Interferometer Performance . . . 134
5.3.1 Collimated Measurement Interferometers . . . 134
5.3.2 Bare Fibre Measurement Interferometers . . . 138
5.4 Internal Measurement Interferometer Precision . . . 141
5.4.1 1.6m OPD Measurement Interferometers . . . 142
5.4.2 Extension to Full Size Measurement Interferometers . . . 145
5.4.3 9m OPD Measurement Interferometers . . . 146
5.5 Internal Measurement Interferometer Resolution . . . 154
5.6 Summary . . . 162

6 Conclusions **164**

Bibliography **167**

A Abbreviations **172**

B List of Algebraic Symbols **174**

C Derivation of The Lomb Periodogram **176**

List of Figures

1.1 Higgs Production Mechanisms at the ILC . . . 3
1.2 Higgs Production Cross Sections at the ILC . . . 3
1.3 SUSY Production Mechanisms at the ILC . . . 5
1.4 SUSY Production Cross-sections at the ILC . . . 6
1.5 Examples of Predicted SUSY Mass Spectra . . . 6
1.6 Particle Beam Emittance Representation . . . 8
1.7 Schematic Representation of Beamstrahlung . . . 12
1.8 Schematic View of the ILC . . . 15
1.9 Overview of the Electron Source at the ILC . . . 16
1.10 Overview of the Undualtor Based Positron Source at the ILC . . . 17
1.11 Overview of the RTML at the ILC . . . 19
1.12 Prototype of an ILC RF Cavity . . . 20
1.13 Overview of the Proposed ILC Beam Delivery System . . . 21
1.14 Ground Motion Spectra for Various Proposed ILC Sites . . . 24
1.15 Cross Section of an ILC Accelerator Module . . . 26
1.16 Illustration of the ILC Tunnel Coordinate System . . . 28
1.17 Illustration of the RTRS Survey Technique . . . 29
1.18 Design Model of the 3-Car Prototype RTRS . . . 30
1.19 The RTRS Measurement Systems . . . 30
1.20 RTRS 20 Stop Wall Marker Position Determination Results . . . 32
1.21 Random Walk Model Explanations of Terms . . . 33
1.22 Extrapolation of SIMULGEO Results Using Random Walk Model . . . 34
1.23 RMS of Simulated Random Walk Trajectories . . . 34

2.1 Interferometric Signal Generation Schematic . . . 37
2.2 LiCAS Interferometer Geometry . . . 38
2.3 External FSI Patrol Region . . . 41
2.4 Returned Power for Bare Fibre Launches as a function of OPD . . . 42
2.5 Returned Power for Bare Fibre Launches as a function of Transverse Retroreflector Displacement . . . 42
2.6 Diagram of PLX 1.5 inch Sphere Mounted Retroreflector . . . 43
2.7 Overview of the Laboratory FSI System . . . 45
2.8 Laser Frequency as a Function Time . . . 48
2.9 Rate of Change of Laser Frequency . . . 49
2.10 Laser Tuning Curve Fit Residuals . . . 50
2.11 Tuneable Laser Output Spectrum . . . 51

2.12 Erbium 3+ Ion Energy Levels 52
2.13 Typical Erbium Doped Fibre Gain Curve 53
2.14 EDFA Output Spectrum 56
2.15 APC and SPC Fibre Launch Schematic 57
2.16 Michelson Reference Interferometer Schematic 58
2.17 Short Reference Interferometer Schematic 59
2.18 Single Fibre Interferometer Launch and Return 60
2.19 Schematic of the Internal FSI Collimation Solutions 61
2.20 Diagram of the Relative Internal MI Launch Positions. 63
2.21 Pt100 Resistance Response with respect to Temperature 65
2.22 Temperature Signal Shaping Board Schematic 65
2.23 Data Acquisition and Control Software Front Panel 68
2.24 Directory Structure of an Acquired Data Run 71

3.1 Flow Chart of the Analysis Procedure 73
3.2 Applied Cuts to Acquired Reference Interferometer Signal 74
3.3 Acquired Intensity Input and Extracted Phase Output of the 4-Point Carré Algorithm 77
3.4 Calculated Reference Interferometer Phase Advance 78
3.5 Instances of Phase Extraction Errors 79
3.6 Instance of a Phase Unwrapping Error 80
3.7 Reference Interferometer Phase Advance Per Point Histogram 81
3.8 Extracted SRI Spectral Peak 87
3.9 Calculated Air Refractivity as a function of Temperature 91
3.10 Calculated Air Refractivity as a function of Atmospheric Pressure 92
3.11 Calculated Air Refractivity as a function of Relative Humidity 93

4.1 Simulated Interferometer Signals with Laser Tuning Curve Variations 97
4.2 Simulated Interferometer Signals with Differing Noise Levels 98
4.3 OPD Precision for Simulated $9m$ OPD Interferometer 101
4.4 Histogram of Determined OPDs for Simulated $9m$ OPD Interferometer . . . 101
4.5 OPD Precision for Simulated $0.9m$ OPD Interferometer 102
4.6 Histogram of Determined OPDs for Simulated $0.9m$ OPD Interferometer . . 103
4.7 Determined OPD Accuracy for Simulated $9m$ OPD Interferometer 104
4.8 Difference Between Determined and Input OPD for Simulated $9m$ OPD Interferometer 104
4.9 Determined OPD Accuracy for Simulated $0.9m$ OPD Interferometer 106
4.10 Difference Between Determined and Input OPD for Simulated $0.9m$ OPD Interferometer 106
4.11 Determined and Simulated OPD Difference For a Range of Input OPDs . . . 107
4.12 Determined OPDs from the Internal MI Resolution Investigation 110
4.13 Internal Resolution OPD Variation Gradient Error for Small OPD Variations 111
4.14 Internal Resolution OPD Variation Gradient and Error Difference for Small OPD Variations 111
4.15 Determined OPDs from the External MI Resolution Investigation 113

4.16 Simulated External Resolution Error for Small Input OPD Variations 114
4.17 External Resolution OPD Variation Gradient and Error Difference for Small Input OPD Variations 114
4.18 Determined OPD Shift from Simulation Input as a function of Input SNR . . 115
4.19 Spectral SNR for Simulated Interferometer with Varied Input SNR 116
4.20 OPD Determination Precision as a Function of Spectral SNR 117

5.1 Temperature Variations within the Michelson Reference Interferometer over 24 hours 121
5.2 Michelson Reference Interferometer OPD Stability over 24 Hours 121
5.3 Michelson Reference Interferometer OPD Projection over 24 Hours 122
5.4 Temperature Variations of the Short Reference Interferometer over 24 hours 123
5.5 Temperature Difference Between the Short Reference Interferometer Body and the Retroreflector Mount over 24 hours 124
5.6 Uncorrected Short Reference Interferometer OPD over 24 Hours 125
5.7 Short Reference Interferometer OPD Stability over 24 Hours 125
5.8 Short Reference Interferometer OPD Projection over 24 Hours 126
5.9 Reference Interferometer OPD Ratio over 24 Hours 127
5.10 Michelson Reference Interferometer OPD Stability over 20 Minutes 128
5.11 Michelson Reference Interferometer OPD Projections over 20 Minutes 129
5.12 Short Reference Interferometer OPD Stability over 20 Minutes 130
5.13 Short Reference Interferometer OPD Projections over 20 Minutes 131
5.14 Reference Interferometer OPD Ratio over 20 Minutes 132
5.15 Diagram of the Collimated External MI Investigation 134
5.16 OPD of a Collimated External MI as a function of Transverse Retroreflector Displacement 135
5.17 Linear Fit Residuals of Collimated External MI OPD as a function of Transverse Retroreflector Displacement 136
5.18 Signal Peak Height of a Collimated External MI as a function of Transverse Retroreflector Displacement 136
5.19 Schematic of Long Arm Return Path as a function of Retroreflector Displacement 137
5.20 Diagram of the Bare Fibre External MI Investigation 139
5.21 OPD of a Bare Fibre External MI as a function of Transverse Retroreflector Displacement 139
5.22 Spectral SNR of a Bare Fibre External MI as a function of Transverse Retroreflector Displacement 140
5.23 Diagram of the Internal MI Investigation 141
5.24 Temperature Variations of the Aluminium and Air that formed the $1.6m$ OPD Interferometers 142
5.25 OPD of the $1.6m$ APC-MI as a function of Time 143
5.26 OPD of the $1.6m$ SPC-MI as a function of Time 143
5.27 $1.6m$ MI OPD Correlation 144
5.28 $1.6m$ MI OPD Correlation Linear Fit Residuals 144
5.29 OPD Determination Precision as a function of MI Length 145

5.30 OPD Ratio Stability as a function of MI Length 146
5.31 OPD of the $9m$ APC-MI as a function of Time over 6 minutes 147
5.32 OPD of the $9m$ SPC-MI as a function of Time over 6 minutes 147
5.33 $9m$ MI OPD Correlation over 6 minutes 148
5.34 $9m$ MI OPD Correlation Linear Fit Residuals 148
5.35 Temperature Variations of the Aluminium and Air that formed the $9m$ MIs . 150
5.36 OPD of the $9m$ APC-MI as a function of Time over 24 hours 150
5.37 OPD of the $9m$ SPC-MI as a function of Time over 24 hours 151
5.38 $9m$ MI OPD Correlation over 24 hours 152
5.39 $9m$ MI OPD Correlation Linear Fit Residuals 152
5.40 $9m$ MI OPDs as a function of Temperature 153
5.41 APC-MI OPD as a function of Stage Displacement for $2.5\mu m$ Increments . . 156
5.42 SPC-MI OPD as a function of Stage Displacement for $2.5\mu m$ Increments . . 156
5.43 $9m$ MI OPD Correlation During $2.5\mu m$ Increments Stage Displacement . . . 157
5.44 $9m$ MI OPD Correlation Linear Fit Residuals During $2.5\mu m$ Increments Stage Displacement 157
5.45 APC-MI OPD as a function of Stage Displacement for $50nm$ Increments . . 158
5.46 SPC-MI OPD as a function of Stage Displacement for $50nm$ Increments . . . 158
5.47 $9m$ MI OPD Gradient Determination Error for Induced Length Increments . 159
5.48 $9m$ MI OPD Difference between Gradient and Error on Gradient for Induced Length Increments 160
5.49 $9m$ MI OPDs Length Resolutions with Respect to Number of Measurements and Length Increment 161

List of Tables

1.1 Expected Higgs Boson Branching Ratio Measurement Precisions 4
1.2 ILC Baseline Design Beam Parameters 14
1.3 Electron Beam Parameters at the ILC 16
1.4 Positron Beam Parameters at the ILC 17
1.5 Overview of ILC Site Proposals 23
1.6 Accelerator Alignment Tolerances 25
1.7 Accelerator Emittance Growth Budget 26

2.1 Drift Error due to Wavelength Change During Nominal Laser Scan 46
2.2 Agilent 81642A Tuneable Laser Specifications 47
2.3 Keopsys KPS-BT-C-21-Bo-FA Specifications 55
2.4 Corning SMF-28 Specifications 56
2.5 Estimated Drift Error due to Dispersion within the Collimation Lens 62
2.6 Temperature Sensor Positions 64
2.7 Calibration Resistance and Corresponding Pt100 Temperature Values 66
2.8 MICOS UPM-160 Ultra Precision Linear Stage Specifications 67
2.9 NI PCI-6115 ADC Card Specifications 69
2.10 Definition of the Acquired Raw Data Files 71

3.1 Air Refractivity as a function of Temperature Linear Fit Results 90
3.2 Air Refractivity as a function of Atmospheric Pressure Linear Fit Results . . 91
3.3 Air Refractivity as a function of Relative Humidity Linear Fit Results 92

4.1 Laser Tuning Curve Simulation Parameters 96
4.2 Nominal Performance Characterisation Scan Parameters 100
4.3 Nominal Performance Characterisation Interferometer Parameters 100
4.4 Simulated Internal MI Precision Results 100
4.5 Simulated External MI Precision Results 102
4.6 Simulated Internal MI Accuracy Results 105
4.7 Simulated External MI Accuracy Results 105
4.8 Linear Fit Results for Difference between Determined and Input OPD . . . 107
4.9 Predicted Resolutions for the FSI Measurement Systems 109
4.10 Internal Resolution OPD Variation Gradient for Small OPD Variations . . . 109
4.11 External Resolution OPD Variation Gradient for Small OPD Variations . . . 112
4.12 Summary of Nominal Performance Characterisation 118

5.1 Michelson Reference Interferometer Stability Results over 24 Hours 122

5.2 Short Reference Interferometer Stability Results over 24 Hours 126
5.3 Reference Interferometer Stability OPD Ratio Results over 24 Hours 127
5.4 Michelson Reference Interferometer Stability Results over 20 Minutes 128
5.5 Short Reference Interferometer Stability Results over 20 Minutes 130
5.6 Reference Interferometer Stability OPD Ratio Results over 20 Minutes . . . 132
5.7 $1.6m$ MI OPD Correlation Results 143
5.8 MI OPD Correlation Linear Fit Results 146
5.9 $9m$ MI OPD Correlation Results on Short Time Scales 149
5.10 $9m$ MI OPD Correlation Results on Long Time Scales 151
5.11 Extracted Optical Table Thermal Expansion Results 154
5.12 MI OPD Fit Results for Stage Displacement with $2.5\mu m$ Increments 155
5.13 MI OPD Correlation Results During $2.5\mu m$ Increment Stage Displacement . 155
5.14 MI OPD Fit Results for Stage Displacement with $50nm$ Increments 155
5.15 Summary of Reference Interferometer Short and Long Term Stability 162
5.16 Summary of Relative Reference Interferometer Stability 162
5.17 Scale of Expansive and Refractive Effects within the Reference Interferometers 162
5.18 Mean Difference in OPD for $1.6m$ and $9m$ MIs 163
5.19 Summary of $9m$ MI Precision Results 163

6.1 Summary of Nominal Performance Characterisation Results 164
6.2 Summary of Drift Errors for Laboratory Interferometers 165
6.3 Summary of Error Scales for Laboratory Interferometers 166

Chapter 1

Introduction

The study of particle physics and the accelerator physics required to produce high energy particle collisions are now both considered to be mature fields. A modern experiment consisting of a high energy collider and particle detectors will take upwards of two decades to design and build and cost several billion dollars. International collaboration is the only viable method of undertaking such projects and it is important that every possible piece of information is gleaned from the acquired data. The accelerators themselves are some of the most complex machines ever constructed and understanding them in detail can be a lifetimes work. The very high luminosity requirements mean that the precise alignment of these very large and complex machines has become extremely critical.

1.1 Physics at the TeV Energy Scale

Current particle physics theories are the product of almost a century of refinement and incorporate virtually every observation made within the field. These theories account for a vast number of particle and resonance masses, decay paths and interaction cross-sections. The current model produces coupling and decay rate predictions which are among the most accurate in science. Several extensions to the current tested theory have been proposed which complete the picture and provide explanations for phenomenon beyond the current high energy frontier. A new generation of experiments is now required to test these proposals.

1.1.1 The Standard Model

The Standard Model states that all matter is composed of just two types of fundamental particles: quarks and leptons. Interactions between these fundamental particles are propagated by a third group of force carrying particles, the mediators. Each mediator corresponds to a different force: the *photon* (γ) propagates the electromagnetic force; the W^+, W^- and Z^0 for the weak force; and eight gluons (g) for the strong force[1].

[1]The most notable exception of the Standard Model is the absence of a description of the gravitational force. Current studies aim to produce a "Quantum Gravity" theory that unifies the Standard Model forces

The Standard Model contains the underlying symmetry group $SU(3)_c \times SU(2)_L \times U(1)_Y$. The $SU(3)$ group describes the strong force while the electromagnetic and weak force are unified to form a signal force under the $SU(2) \times U(1)$ group [1]. The Unification of the electroweak sector (the GWS model) provided an explanation for charged weak interactions via $W^{\pm}$ exchange and predicted the existence of neutral weak currents propagated by the Z^0 along with predictions for the masses of the mediators. However upon unification of the electromagnetic and weak forces it became impossible to maintain the exact symmetry of $SU(2) \times U(1)$. A spontaneous breaking of the symmetry occurs with the $W^{\pm}$ and Z^0 each gaining mass whilst the photon remains massless. The Standard Model must include a mechanism capable of explaining this spontaneous symmetry breaking.

It is very likely that most, if not all, of the particles in the TeV energy range will be discovered at the Large Hadron Collider (LHC) however precision measurements will require a second machine, the International Linear Collider (ILC). Making precision measurements at the ILC will improve the current constraints on the Standard Model. Both $\sin^2\theta_W$ and the mass of the W boson can be measured very precisely by lowering the collision energy into the range between 90 and $200GeV$. At these energies the ILC could deliver a hundred times more data than the Large Electron Positron (LEP) collider and so produce a corresponding increase in accuracy. The increased predictive power of a more precisely understood Standard Model provides direct information about physics scenarios at higher energies.

Even without the discovery of any new physics at the LHC a $500GeV$ e^+e^- machine will provide the ability to study top physics at a new level of precision. Several years of running the ILC at design luminosity could improve the precision of the measurement of the mass of the top quark from the present value of a few GeV to around $200MeV$ [2]. Moreover due to the extremely large top mass detailed determination of the decay properties of the top quark are likely to be key in understanding the mechanisms involved in electroweak symmetry breaking.

1.1.2 Electroweak Symmetry Breaking

The spontaneous symmetry breaking within the electroweak sector of the Standard Model can be accounted for by the existence of the Higgs field [3]. The simplest implementation of the Higgs theory introduces a single scalar boson, the *Higgs boson*. The introduction of the Higgs field provides the mechanism for all fundamental particles to become massive by coupling to the Higgs boson. There is no direct evidence for Higgs boson production currently available but data from the final run at LEP provides a lower limit on mass of around $119GeV$. However, currently running experiments can provide an indication as to the most likely mass of this illusive particle.

Comparing predictions with precision measurements made at the ILC will establish whether the Higgs mechanism is responsible for electroweak symmetry breaking and test the self consistency of the Standard Model. There are two main production mechanisms

with General Relativity to provide a consistent description of all known forces of nature. It is suggested that gravity may be propagated by a spin-2 boson called the *graviton*.

of the Standard Model Higgs boson at an e^+e^- linear collider. These are Higgs-strahlung, $e^+e^- \rightarrow HZ$, which dominates at low energies and WW-fusion, $e^+e^- \rightarrow H\nu_e\bar{\nu}_e$, which becomes more important at high energies. Feynman diagrams of these production processes are shown in figure 1.1. The production cross sections for both processes for a range of Higgs boson masses is shown in figure 1.2.

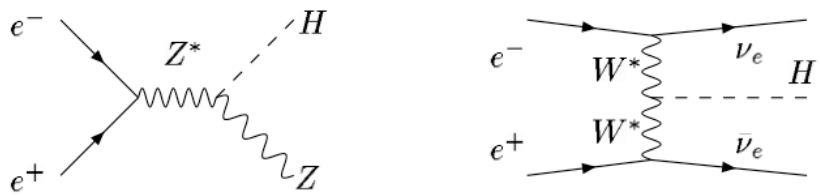

Figure 1.1: Feynman diagrams of the dominant Higgs boson production mechanisms in e^+e^- collisions at the ILC.

The cross-sections of Standard Model Higgs boson production via Higgs-strahlung and WW-fusion are approximately equal at around $\mathcal{O}(50fb)$ with $\sqrt{s} = 500GeV$ for $100GeV \leq M_H \leq 200GeV$, see figure 1.2. The ILC could produce a sample of around 80,000 Higgs bosons via the sum of these two production methods, although predominately through Higgs-strahlung, at $\sqrt{s} = 350GeV$ for $M_H = 120GeV$ with an integrated luminosity of $500fb^{-1}$ which corresponds to approximately two years of running [4].

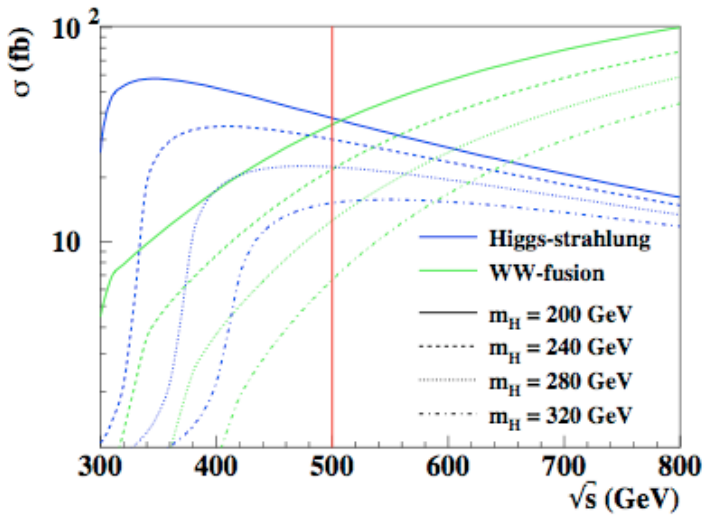

Figure 1.2: Production cross sections as predicted by the Standard Model of the Higgs boson as a function of ILC centre-of-mass energy for various Higgs boson masses [5].

Many of the properties of the Higgs boson can be determined in a model independent way by using the recoil mass technique in the Higgs-strahlung process. This will allow the Higgs boson mass to be determined with a precision of around $70MeV$ for $M_H \approx 120GeV$ at $\sqrt{s} = 350GeV$ with an integrated luminosity of $500fb^{-1}$ [6]. This precision can be increased to around $\Delta M_H \sim 40MeV$ by including the hadronic decays of the Z boson. For Higgs boson masses in the range of 150 to $180GeV$ a precision of the same order can be achieved.

The measurement of the Higgs boson branching ratio is extremely important. The prediction that the Higgs couplings to fermions are proportional to mass can be confirmed by measurements of the $b\bar{b}$, $c\bar{c}$ and $\tau\bar{\tau}$ fractions. There are numerous studies into the sensitivities of the Higgs boson branching ratios. Although slightly different assumptions of detector performance, centre-of-mass energy and analysis method were used consistent results were obtained. The expected precision of branching ratio measurements for $M_H = 120GeV$ are given in table 1.1. Accurate knowledge of these parameters will be vital for determining the processes involved in electroweak symmetry breaking and establishing a full understanding of the origin of mass.

Decay Mode	**Relative Precision (%)**	**References**
$b\bar{b}$	1.0 - 2.4	[7] [8] [9] [10]
$c\bar{c}$	8.1 - 12	[7] [8] [9] [10]
$\tau^+\tau^-$	4.6 - 7.1	[7] [8] [9]
gg	4.8 - 10	[7] [8] [9] [10]
WW	3.6 - 5.3	[7] [8] [9] [11]
$\gamma\gamma$	23 - 35	[9] [12]

Table 1.1: Expected precisions of the Higgs boson branching ratio measurements for $M_H = 120GeV$ and integrated luminosity of $500fb^{-1}$.

1.1.3 Supersymmetry

There are no shortages of theories predicting what physics exists at energies beyond those currently observed within the Standard Model. The concept of *Supersymmetry* (SUSY) is one such extension that is particularly appealing. Supersymmetry introduces the idea that every Standard Model particle has a "superpartner", collectively known as *sparticles*. The sparticles differ from their partners only in spin hence fermions have boson superpartners and vice versa. One of the main arguments for introducing SUSY is as a solution to the fine-tuning problem. By assigning fermions and bosons to common multiplets, quadratically divergent radiative corrections to the Higgs boson mass can be cancelled in a natural way by adding up bosonic and opposite sign fermionic loops [13][14].

It is clear, however, that this can not be an exact symmetry since no SUSY particles have yet been identified and as they have identical couplings they must be heavier. There exists a similar situation to the spontaneous symmetry breaking in the electroweak sector and so there must also exist a mechanism within SUSY for the breaking of this symmetry. The result is that the sparticles have much larger masses than their partners - a necessary condition since none have been found. Different SUSY theories vary in their description of how the symmetry is broken and this has wide ranging consequences for the predicted phenomenology. All SUSY theories make a number of explicit and testable predictions about the existence of particles outside of the Standard Model. In addition to the large number of sparticles SUSY theories also proposes the existence of additional Higgs bosons (both charged and neutral) [15].

A minimal inclusion of SUSY into the Standard Model results in the Minimally Supersymmetric Standard Model (MSSM) however further extension provides other significant benefits over the Standard Model as it currently stands. The eventual aim of these extensions is to produce a consistent theory which would unify gravity with the forces already covered by the Standard Model to produce a Grand Unified Theory (GUT). Within such a theory all four forces would be unified into a single force at a very high energy scale, known as the GUT scale [16].

The production mechanisms for neutral and charged SUSY particles in leptonic collisions are summarised in figure 1.3. The corresponding production cross-sections, assuming MSSM, at the ILC are given in figure 1.4. The total production cross-sections for the lightest neutralinos is around $\mathcal{O}(50fb)$, approximately equal to the total Higgs boson production cross-section at $\sqrt{s} = 500GeV$. The total production of the lightest charginos is several times greater, at around $\mathcal{O}(200fb)$, at the initial ILC design energy.

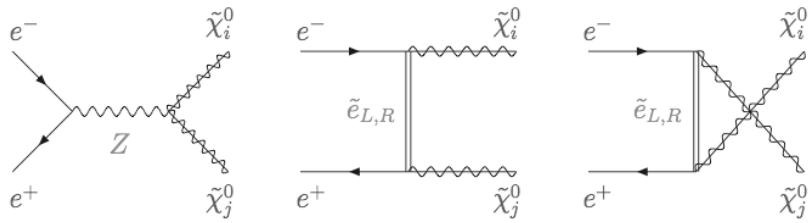

(a) Feynman diagram of neutralino production.

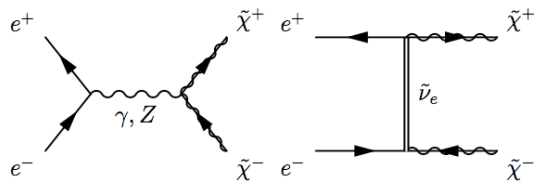

(b) Feynman diagram of chargino production.

Figure 1.3: Feynman diagrams of the dominant neutralino and chargino production mechanisms in e^+e^- collisions at the ILC.

If supersymmetry is realised in nature the absence of low energy observations of sparticles must be accounted for. Several explanations have been developed which lead to supersymmetric spectra within the energy range of the ILC, examples of predicted spectra are shown in figure 1.5. It is clear that these spectra vary dramatically and so the identification of only a few resonances will allow the correct SUSY model to be determined.

At the LHC many of the final states are overlapping which complicates the reconstruction of some of the SUSY particles. Only the combination of results from the LHC and the ILC can provide a complete picture. Most SUSY schemes predict light gauginos (superpartners of the Standard Model gauge bosons) and light sleptons. Neutralinos can be directly produced via $e_L^- e_R^+ \rightarrow \tilde{\chi}_2^0 \tilde{\chi}_2^0 \rightarrow 2(l^+l^-)\not{E}$ with the lightest observable neutralino detected via a 3-body decay: $\tilde{\chi}_2^0 \rightarrow l^+l^-\tilde{\chi}_1^0$, see figure 1.3a. Exploiting all the di-lepton modes should make it possible to measure the mass difference, $\Delta m(\tilde{\chi}_2^0 - \tilde{\chi}_1^0)$, to a precision of around $50MeV$ [18].

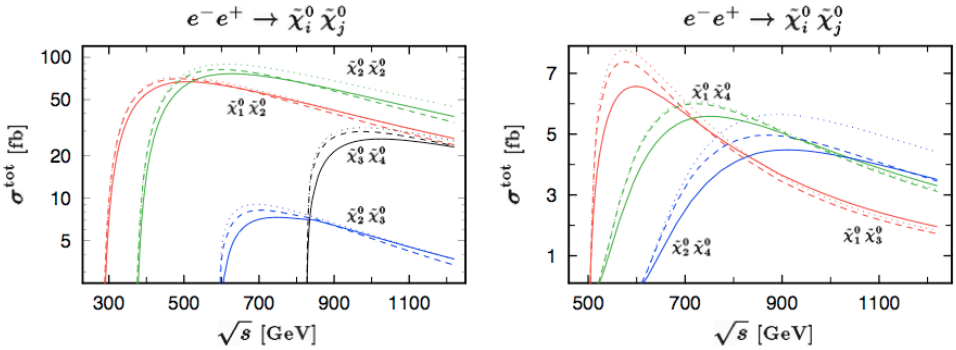

(a) Predicted production cross-sections for neutralinos at the ILC.

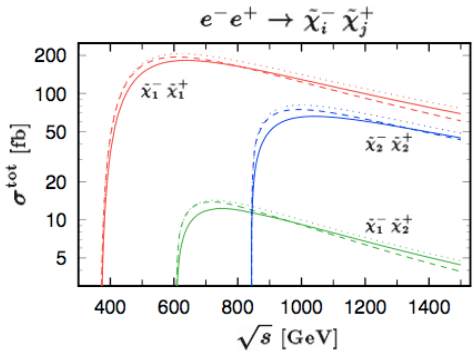

(b) Predicted production cross-sections for charginos at the ILC.

Figure 1.4: Predicted total production cross-sections for MSSM neutralinos and charginos at tree-level (dotted), with weak (dashed), and with complete corrections (solid) in e^+e^- collisions at the ILC [17].

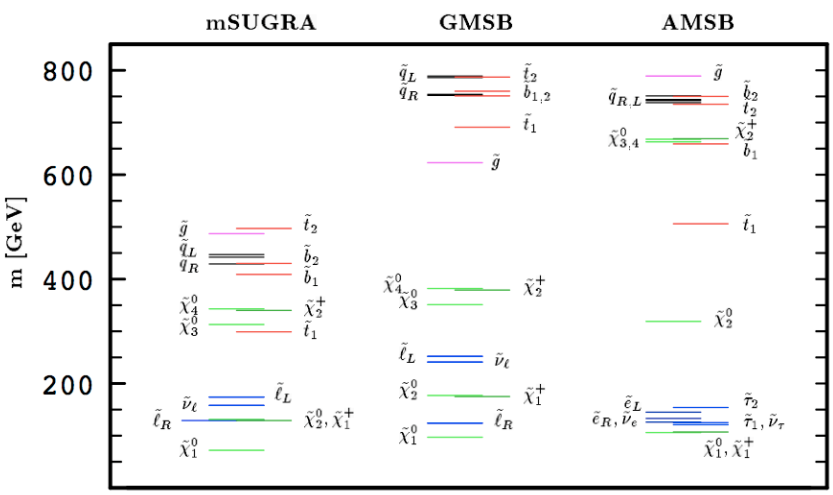

Figure 1.5: Examples of the SUSY particle mass spectra in three different models: mSUGRA (minimal supergravity); GMSB (gauge mediated supersymmetry breaking); AMSB (anomaly mediated supersymmetry breaking) [16].

Charginos will also be produced in large numbers at the ILC and using similar di-jet techniques as for neutralinos should allow the mass of the lightest charginos, $\tilde{\chi}_1^{\pm}$, to be determined with a precision of around $200MeV$. The rise in neutralino and chargino pair production cross-sections around the threshold, see figure 1.4b, should lead to mass resolution of around $\mathcal{O}(50MeV)$ with an integrated luminosity of $100fb^{-1}$ [19].

Scalar sleptons are the superpartners of the right-handed and left-handed leptons and are produced in pairs. One of the most straightforward cases is the production of right smuons: $e_R^- e_L^+ \rightarrow \tilde{\mu}_R^+ \tilde{\mu}_R^- \rightarrow \mu^- \tilde{\chi}_1^0 \mu^+ \tilde{\chi}_1^0$. Using a neutralino mass fixed from other measurements the mass of the $\tilde{\mu}_R$ should be resolvable to around $200MeV$ for an integrated luminosity of $50fb^{-1}$, corresponding to a few months of running at design luminosity, by measuring around the pair production threshold [18].

1.2 TeV Energy Colliders

The investigation of physics outside that currently described by the Standard Model can be approached in many ways. More precise measurements can be made at existing accelerator facilities which in turn allow more precise determinations of parameters within the Higgs and non-Standard Model sectors. However direct access to new physics requires new experiments capable of producing large numbers of collisions at TeV energies.

The quantity of particle interactions produced is as critical to accessing new physics as the energy of the colliding particles. A measure of the number of interactions that occur between the particles within two colliding beams is the *Luminosity*, $\mathcal{L}$, and is related to the beam properties of a linear collider, assuming symmetrical beams, by equation 1.1.

$$\mathcal{L} = \frac{nN^2 \mathcal{H}_{\mathcal{D}} f}{4\pi\sigma_x\sigma_y} \tag{1.1}$$

where n is the number of bunch pairs per train, N is the number of particles per bunch, f is the machine repetition rate, $\mathcal{H}_{\mathcal{D}}$ is the beam pinch enhancement (described in section 1.2.3), and σ_x and σ_y are the (r.m.s.) horizontal and vertical beam dimensions at the IP [20].

While producing many bunches each containing a large number of particles will increase the luminosity it is the bunch cross-section which is the dominating factor at the current technology frontier. The production of very small beam spot sizes requires the minimisation of the vertical and horizontal *emittance* of the beam, ε. The emittance is a measure of both the physical transverse size of the beam, x, and its divergence, i.e. the angle[2] of each particle trajectory within the beam, x'. Plotting position versus angle of each particle within a beam ideally forms an ellipse in transverse phase space (x,x'), as shown in figure 1.6. Hence the emittance represents the area of phase space occupied by the beam, equation 1.2.

$$\varepsilon_i \equiv \sigma_i \sigma_{i'} \tag{1.2}$$

where σ denotes the root mean square of the property, $i = x, y, z$.

[2]Since the angle of a particle trajectory in a particular plane (i.e. x) also defines the rate of change of position within that plane, the angle can be expressed using the symbol for velocity, x'.

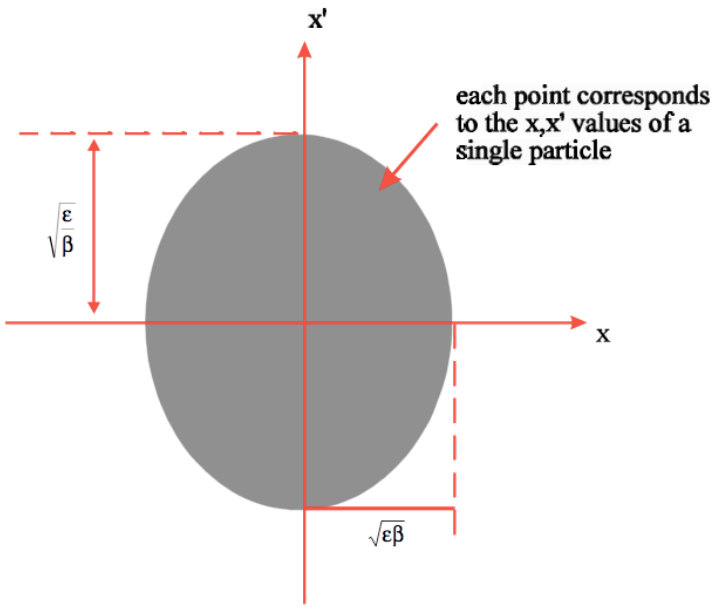

Figure 1.6: An idealised transverse phase space plot for a large number of particles in a beam [21]. The area of this phase space plot is defined as the (horizontal) emittance of the beam, ε_x. The amplitude function, β, is defined in [22].

To account for the natural reduction that occurs during beam acceleration, the emittance is often referred to in terms of the *normalised emittance*, ε_n, which is invariant under acceleration. The six dimensional normalised emittance is given by

$$\varepsilon_{6,n} \equiv detV \tag{1.3}$$

where V is the covariance matrix of x, x', y, y', z, and z'. Assuming no correlation between the space coordinates and velocities this reduces to

$$\varepsilon_{6,n} = \varepsilon_{x,n}\varepsilon_{y,n}\varepsilon_{z,n}. \tag{1.4}$$

The relationship between the normalised and unnormalised emittance is thus

$$\varepsilon_n \equiv \gamma\varepsilon \tag{1.5}$$

where γ is the Lorentz factor. Hence ε_n is often labelled $\gamma\varepsilon$.

The transverse beam sizes are then definable in terms of the emittance, equation 1.6.

$$\pi\sigma_x^2 = \beta_x\varepsilon_x \qquad \pi\sigma_y^2 = \beta_y\varepsilon_y \tag{1.6}$$

where β_x and β_y are the transverse amplitude functions of the focussing lattice in the x and y direction and are defined in [22]. A low value of β_i corresponds to strong focussing in that direction. By reducing the horizontal and vertical beam emittance the transverse size and divergence of the beam are also reduced therefore producing a beam that is smaller and more tightly constrained to the desired trajectory.

1.2.1 Lepton and Hadron Colliders

Historically hadron colliders have been viewed as 'discovery' machines whilst lepton machines have been used for 'precision' measurements. In fact both have their strengths and weaknesses and therefore both are required for a complete investigation. It is the choice of collision particle which is the most fundamental decision when designing a new machine.

The first evidence for physics beyond the Standard Model will most likely come from a hadron collider, if not the Tevatron then almost certainly the LHC at CERN which is expected to begin operation in 2008 [23]. However neither of these machines is capable of producing the precision measurements required to fully test the many postulated extensions to the Standard Model [15]. The Tevatron collides protons and anti-protons at a centre-of-mass energy of $2TeV$ whilst the LHC will produce $14TeV$ proton-proton collisions [24]. These high energies are more easily achieved in hadronic collision and hence so too are the production of new, more massive particles.

The production mechanisms for the Higgs and many predicted SUSY particles are similar in hadronic and leptonic collisions [16]. Although the latter lends itself much more to the extraction of precision results due to two main factors: leptonic interactions do not suffer from the fragmentation processes seen in hadronic collisions and therefore the final states are easier to measure completely and accurately; and the initial state energy of a lepton collision can be measured and controlled in a way not possible with hadronic collision since complete annihilation of incident leptons can be achieved.

The ease of reconstruction of leptonic collisions is due to the simplicity of the interactions. When a fundamental point-like particle (such as a lepton) collides with it's anti-particle complete annihilation results thus producing a final state that is exactly equal in energy to the initial state whilst containing no remnants from it. However in a high energy collision between composite particles (such as hadrons) the interactions occur between the constituents within the composite structure (quarks and gluons). This means that not only are the details of the collision impossible to define prior to the event but also that the final state is complicated due to the presence quark and gluon jets resulting from the confinement of the strongly interacting initial state remnants.

The composite nature of hadrons means that the collision energy is unknown since each component will carry a fraction of the total energy provided to the hadron by the accelerator. This is not the case for leptonic collisions since all the energy provided to the particles prior to the collision is transferred to the final state. It is therefore possible to use a lepton machine to scan the collision energy across a production threshold and determine the energy dependancies of a production cross-section. This technique is limited by the energy spread of the beam, typically a few percent, which is present from production and often increased during acceleration and collision, see section 1.2.3. Determination of the energy spectra of the beams is necessary to undertake such threshold measurements.

A further benefit is the ability to control the polarisation of one or both of the leptons beams. This allows the spin dependance of various final states to be measured, something that is not possible at a hadron collider, as well as significantly reducing unwanted final

states[3]. For these reasons the precision measurement of the properties, such as mass, width, production cross-section, branching ratios and self-coupling, of the Higgs boson and many of the predicted supersymmetric particles can be undertaken more completely with a lepton collider [25].

1.2.2 Linear and Circular Accelerators

The method of charged particle acceleration is essentially identical in linear and circular accelerators. A high E-field gradient is produced within cavities through which the particles are accelerated. However there are a number of fundamental differences between a linear accelerator, or *linac*, and a circular accelerator, or *synchrotron*.

Circular accelerators incorporate bending magnets between the accelerating cavities to produce a circular trajectory. The final beam energy can be achieved during multiple orbits and several interaction points can be positioned around the circumference of the machine. This means that the beams can continue to be accelerated and collided many times until the cumulative effects of multiple beam-beam interactions reduces the luminosity resulting in low quality beams that have to be dumped.

The linear accelerator is essentially a more simple concept: a single beam is accelerated along a straight trajectory. The energy of the beam is therefore proportional, for a given accelerating gradient, to the length of the accelerator since the beam passes through each accelerating cavity only once. Two acceleration paths are required, one for each beam, which are placed end-on-end to produce a linear collider which may also have multiple IPs. After passing through the IP the beams are discarded into a beam dump as they cannot be reused and new beams must be produced for each subsequent collision. Hence at a linear collider it is particularly important to maximise the number of particle collision per bunch crossing.

Energy Loss Through Synchrotron Radiation

There are other effects that must be taken into account when choosing a design concept for a collider. Not the least important of these is the process of synchrotron radiation emission by the particles within the beam. Synchrotron radiation is the emission of electromagnetic radiation by any charged particle undergoing an acceleration [26]. In the case of an acceleration in the direction of travel of the particle, such as within the accelerating cavities, the effect is unobservable. However when the direction of acceleration is perpendicular to the particle trajectory, as is the case within a bending magnet, the energy loss, per complete revolution of a high energy particle, due to synchrotron radiation can become a significant fraction of the total particle energy. The radiation is emitted in a cone approximately collinear with the direction of particle motion and the amount of energy lost by a particle deflected through a particular angle scales as E_{beam}^4. The radiated power due to synchrotron radiation also de-

[3]Theoretically it is possible to fully control the initial spin states of both leptons in an e^+e^- collision however there are practical difficulties to overcome, such as the production of spin-polarised positrons. Experimentally these difficulties reduce the spin polarisation of the beams to less than 100%.

pends on the rest mass of the particle, scaling like $1/m^4$ [27]. Thus the size of a synchrotron is strongly dependant upon the required collision energy and the choice of collision particle.

Consideration of this effect was one of the primary drivers for replacing the LEP electron-positron collider with the proton-proton colliding LHC since the energy loss due to this phenomenon is a factor of 10^{13} smaller for protons than for electrons in the same ring. In fact the LEP machine, producing beam energies of around $100GeV$ within a $27km$ ring, represents somewhat of an upper limit of what is reasonably achievable for an e^+e^- synchrotron. As the beam energy is increased it becomes more difficult to replace the enormous power dissipation. To produce a TeV scale collider, using current technology, would require a ring of several thousand kilometres in circumference hence a linear collider, where these shortcoming are not present, becomes a much more attractive option.

1.2.3 Beam Collisions

As well as producing collisions at the required energy the design of any collider must also maximise the luminosity. From equation 1.1 it is clear that the luminosity increases for more densely packed bunches (smaller beam spot size) and higher interaction rates (greater bunch crossing frequency). While both types of accelerators can make use of more frequent bunch crossing the number of collisions that each bunch has to undergo introduces associated problems. Although only a small fraction of the particles within the two colliding bunches actually annihilate to produce new particles the rest of the bunch does not pass through unaffected. The large numbers of charged particles moving at close to the speed of light induce very large electromagnetic fields which produce large forces on the opposite bunch.

In a synchrotron the bunch integrity must be maintained as much as possible so they can be recycled and used to produce further collisions. Since at a linear collider the bunches are disposed of after each collision the remnant of each bunch must only be contained and dumped. This means that squeezing the bunches to produce an almost flat geometry with virtually zero cross-sectional area, whilst increasing the destructive effects of the beam-beam interactions, can be used as a method of increasing the luminosity of a linear collider.

Beamstrahlung

The phenomenon of beamstrahlung is closely related to two other well-known phenomena: bremsstrahlung and synchrotron radiation. These processes involve the emission of a photon by an accelerated charged particle. Bremsstrahlung, or *braking radiation*, is the emission of a single photon by a charged particle as it traverses a bulk material and passes through the electromagnetic field of an atom or nucleus.

The emission of beamstrahlung occurs not in an absorbing medium but in the electromagnetic field of a charged bunch. As the two oppositely charged bunches pass through one another the electromagnetic fields surrounding each bunch cause the trajectories of the particles within the opposing bunch to bend, stimulating the emission of energetic photons. This process is illustrated schematically in figure 1.7.

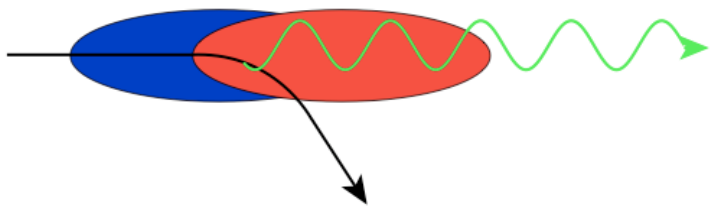

Figure 1.7: An illustration of beamstrahlung emission during a beam-beam collision. The modified trajectory of a single particle within the electron bunch (blue) is shown in black. The field associated with the positron bunch (red) causes the electron path to bend and emit a beamstrahlung photon (green).

For the bunch dimensions required at a TeV linear collider the average electromagnetic field in each bunch during collision will be $\mathcal{O}(1000T)$ [28]. Such large fields produce significant energy and luminosity degradation at the IP. Not only can beamstrahlung increase the energy spread within the beam but the beamstrahlung photons can also pair produce and cause scattering collisions within the bunch [29]. In addition, the beamstrahlung photons produced within the beam pipe can not be steered as is the case of the remnant of the beams and can produce background signal within the detectors.

The beamstrahlung process is characterised by the *beamstrahlung parameter*, Υ, which is a measure of the electromagnetic field seen by a beam particle in it's rest frame and is defined for an electron beam in equation 1.7.

$$\Upsilon \equiv \frac{q\hbar}{m_e^3 c^4}\left(p_\mu F^{\mu\lambda} p^\nu F_{\lambda\nu}\right)^{1/2} = \gamma \frac{\langle E + B \rangle}{B_c} \tag{1.7}$$

where m_e is the rest mass of the electron, q is the electric charge of the particle, p_μ is the electron four-momentum and $F_{\mu\nu}$ is the mean energy-momentum tensor of the bunch field. The critical bunch field, B_c, is defined as

$$B_c \equiv \frac{m_e^2 c^3}{q\hbar} \approx 5 \times 10^9 T \tag{1.8}$$

Since, during a single collision, the field strength will vary along the length of the bunch it is useful to estimate a range for the beamstrahlung parameter. The approximate average and maximum beamstrahlung parameter values, for a beam with a Gaussian particle density, can be estimated from

$$\Upsilon_{av} \approx \frac{5Nr_e^2\gamma}{6\alpha\sigma_z(\sigma_x + \sigma_y)} \qquad \Upsilon_{max} \approx \frac{2Nr_e^2\gamma}{\alpha\sigma_z(\sigma_x + 1.85\sigma_y)} \tag{1.9}$$

where N is the number of particles per bunch, r_e is the classical radius of the electron, α is the fine structure constant and σ_z is the (r.m.s.) bunch length at the IP.

Disruption

The effects of the classical electromagnetic fields surrounding each bunch during a collision are referred to as *Disruption*. These effects result in changes in the beam trajectories. Several

assumptions can be made to simplify the study of the extremely complex interactions between two charged bunches. The electric and magnetic fields can be considered as purely transverse since the bunches are highly relativistic and therefore Lorentz contracted. The absence of a longitudinal field results in bunch interactions only when they coincide and there is no longitudinal acceleration. The interaction between the two bunches dominates over the space charge interactions within each bunch and the electric field dominates, producing a purely transverse electrostatic potential [28].

The *disruption parameter*, $\mathcal{D}$, is defined in equation 1.10.

$$\mathcal{D}_{x,y} \equiv \frac{2Nr_e}{\gamma}\frac{\sigma_z}{\sigma_{x,y}(\sigma_x+\sigma_y)} \tag{1.10}$$

This parameter can be considered as the ratio of the (r.m.s.) bunch length to the effective focal length of the bunch[4]. Since the transverse beam dimensions may differ significantly it is usual to state a disruption parameter for each dimension. At a linear collider the vertical beam spread is much smaller than the horizontal and hence dominants. The equation of motion of a particle has solutions of the form $\sin At$ and $\cos At$, hence as the bunches pass through one-another sinusoidal oscillations occur. The number of oscillations is dependant upon the bunch length.

There are two primary outcomes of disruption. The mutual attraction of the two bunches causes the particle trajectories to curve. This, together with the induced oscillations, results in a large increase in the angular divergence of the beams as they exit the interaction region. Therefore care must be taken in transporting the bunches from the IP to the beam dumps. The second effect can produce an increase in luminosity, resulting from the mutual attraction of the bunches. This effect is particularly efficient at relatively small beam-beam offsets.

The Pinch Effect

The mutual attraction between the two bunches causes transverse bunch compression which results in a luminosity enhancement. This process of beam spot size reduction at the IP is known as the *pinch effect*. It is characterised by the pinch enhancement factor, $\mathcal{H}_\mathcal{D}$, which is the ratio of measured luminosity, $\mathcal{L}$, to the nominal luminosity in the absence of the enhancement, $\mathcal{L}_0$.

$$\mathcal{H}_\mathcal{D} \equiv \frac{\mathcal{L}}{\mathcal{L}_0} \tag{1.11}$$

Due to the complexities of the beam-beam interactions there is no precise method for the calculation of the pinch enhancement factor, however it can be approximated for a head-on collision by equation 1.12 [30].

$$\mathcal{H}_\mathcal{D} \approx \left(1+\mathcal{D}_y^{1/4}\left(\frac{\mathcal{D}_y^3}{1+\mathcal{D}_y^3}\right)\left[\ln\left(\sqrt{\mathcal{D}_y}+1\right)+2\ln\left(\frac{0.8}{A_y}\right)\right]\right)^{1/3} \tag{1.12}$$

where A_y is the divergence parameter and is given by

$$A_y \equiv \frac{\sigma_z}{\beta_y} \tag{1.13}$$

[4]Each bunch acts upon the opposing bunch like a lens.

The vertical disruption and divergence parameters are used since the beams at a linear collider will be smaller in the vertical and so the vertical disruption is greatest. The dependance of $\mathcal{H}_{\mathcal{D}}$ on $\mathcal{D}_y$ is dictated by the beam condition upon collision. A small disruption results in a luminosity enhancement due to the focussing of the beam-beam interaction. A larger disruption results in bunch disintegration which produces a luminosity degradation.

1.3 The International Linear Collider

The proposed International Linear Collider will be a linear e^+e^- collider based on superconducting RF acceleration technology. The initial centre-of-mass energy will be $500GeV$, 2.5 times the energy of the collisions produced at LEP. Additional accelerator component upgrades could increase this to $1TeV$. The design luminosity is $2 \times 10^{34} cm^{-2}s^{-1}$, 3 orders of magnitude greater than that of LEP at $200GeV$ [31]. The proposed layout of the ILC, as of early 2007, is shown in figure 1.8 with the baseline machine and beam parameters, including the ranges in which the final configuration will operate, are given in table 1.2. Multiple design parameter sets are currently being investigated including low bunch charge; large vertical beam size; low power; and high luminosity configurations [32]. These parameter sets define operating planes rather than points and as such are not independently selectable. This section deals with the nominal parameter set unless otherwise stated.

Parameter	**Symbol**	**min**	**nominal**	**max**
Bunch Charge	N	1×10^{10}	2×10^{10}	2×10^{10}
Number of Bunches	n_b	1320	2625	5120
Linac Bunch Interval / ns	t_b	189.2	369.2	480.0
Bunch Length (r.m.s.) / μm	σ_z	200	300	500
Beam Size (r.m.s.) at IP / nm	σ_x	474	639	640
	σ_y	3.5	5.7	9.9
Horizontal Emittance at IP / $mm.mrad$	$\gamma\varepsilon_x$	10	10	10
Vertical Emittance at IP / $mm.mrad$	$\gamma\varepsilon_y$	0.03	0.04	0.08
Beta Function at IP / mm	β_x	11	20	20
	β_y	0.2	0.4	0.6
Beamstrahlung Parameter	Υ_{av}	0.038	0.048	0.097
Disruption Parameter	$\mathcal{D}_x$	0.11	0.17	0.52
	$\mathcal{D}_y$	14	19.4	26.1
Pinch Enhancement Factor	$\mathcal{H}_{\mathcal{D}}$	1.48	1.71	2.18

Table 1.2: The baseline design beam parameters of the ILC [33].

1.3.1 The Injector System

The primary stages of the ILC are dedicated to the production and conditioning of electrons and positrons bunches prior to acceleration. The process of beam preparation and injection

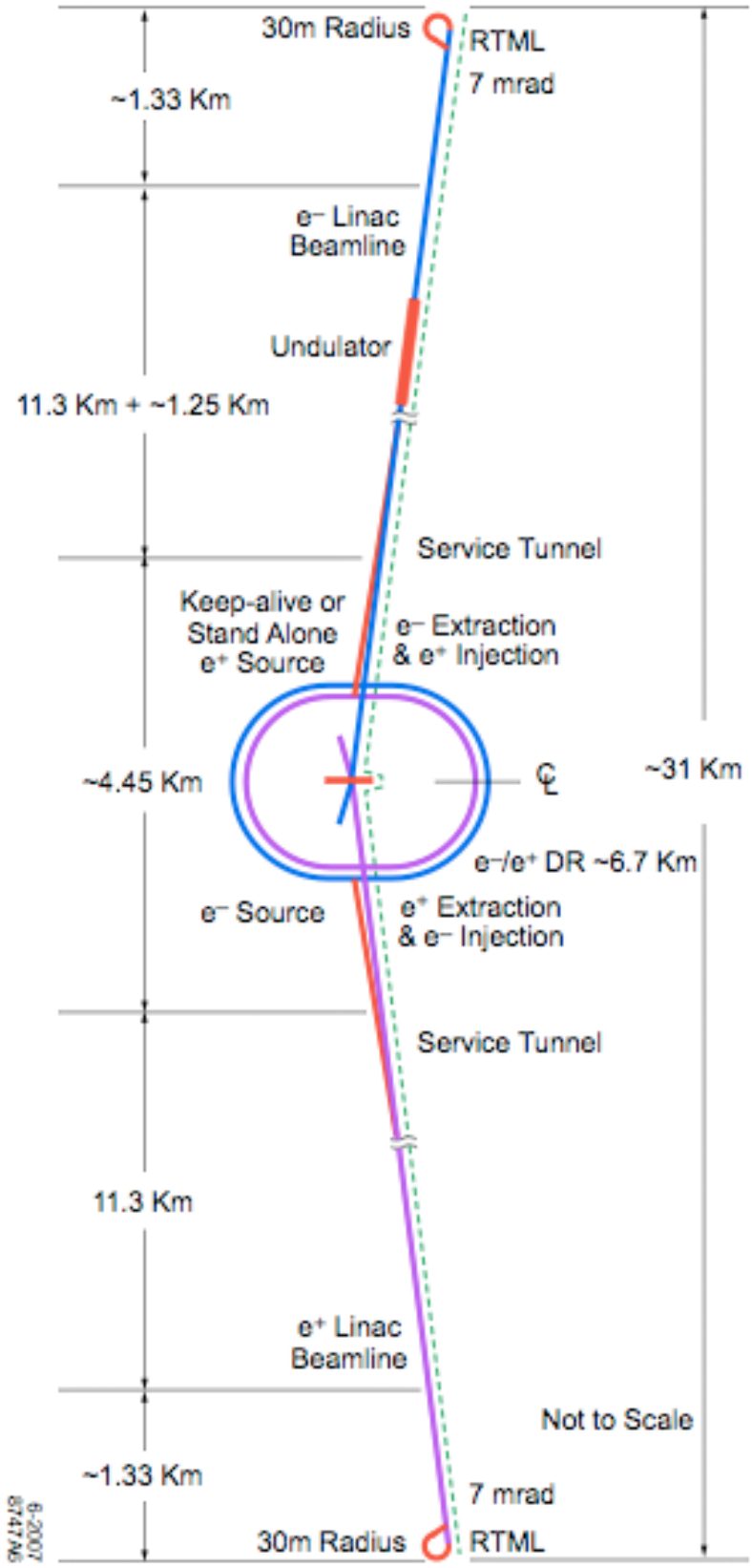

Figure 1.8: An overview of the proposed design of the approximately $31km$ ILC [31]

into the main accelerator at the ILC is described in this section. The injector system can be broken down into three distinct subsections.

The Electron Source

The current ILC design concept employes the photoelectric effect to liberate electrons from a photocathode. The very front end of the ILC consists of a Ti:Saphire drive laser which illuminates a photocathode producing approximately $2ns$ long electron bunches. These are compressed after production by bunchers and solenoids before being accelerated to around $100MeV$ via a room temperature linear accelerating cavity. Further acceleration is applied using superconducting cavities to produce $5GeV$ electrons prior to passing them into the damping rings. An overview of the electron source injector concept is shown in figure 1.9 with the electron beam parameters given in table 1.3

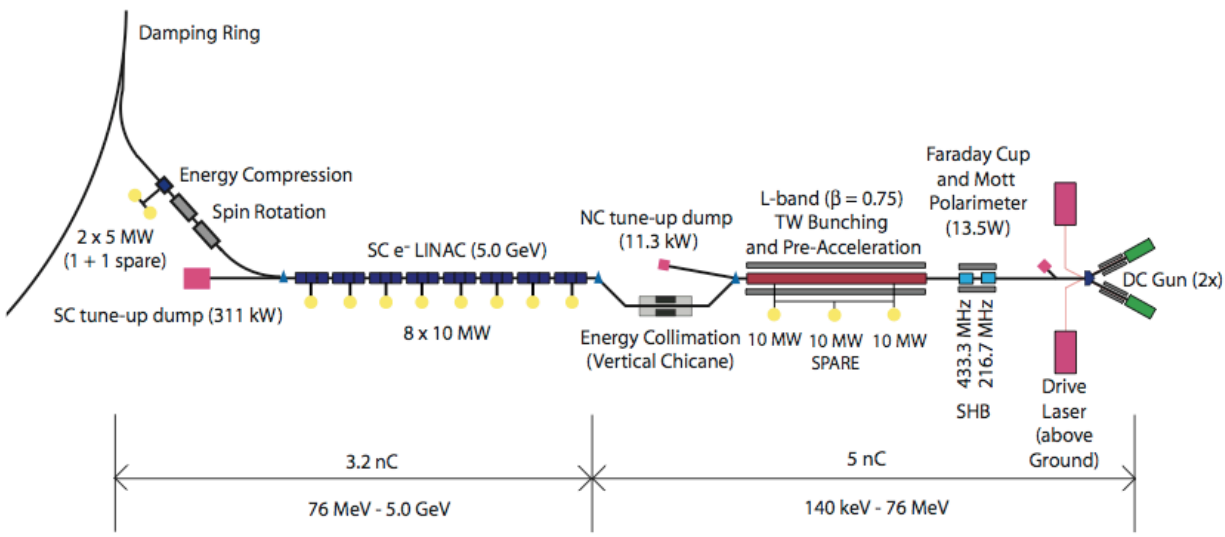

Figure 1.9: An overview of the proposed Electron Source injector concept at the ILC [31].

Parameter	Value
Electrons per Bunch	2×10^{10}
Bunches per Pulse	2625
Bunch Repetition Rate / MHz	3
Train Repetition Rate / Hz	5
Electron Energy / GeV	5
Electron Polarisation / %	> 80

Table 1.3: Electron beam parameters produced by the proposed Electron Source injector system at the ILC [33].

The Positron Source

The production of the large quantities of positrons required can only be achieved by instigating pair production of high energy photons. There are two positron production concepts present in the current ILC design, primarily to enhance system availability. The first uses a $100m$ long helical undulator placed at the $150GeV$ energy point in the electron line to produce circularly polarised photons. These photons undergo pair production in a high strength Ti:alloy target and the resulting positrons are collected. The positrons are captured and accelerated to $250MeV$. Accidentally captured electrons are discarded in a magnetic chicane before a further superconducting acceleration stage, operating at $30MeV/m$, is used to increase the positron beam energy to $5GeV$. The positrons are subsequently inserted into the damping rings. An overview of the proposed undulator based system is shown in figure 1.10 with the resultant positron beam parameters stated in table 1.4.

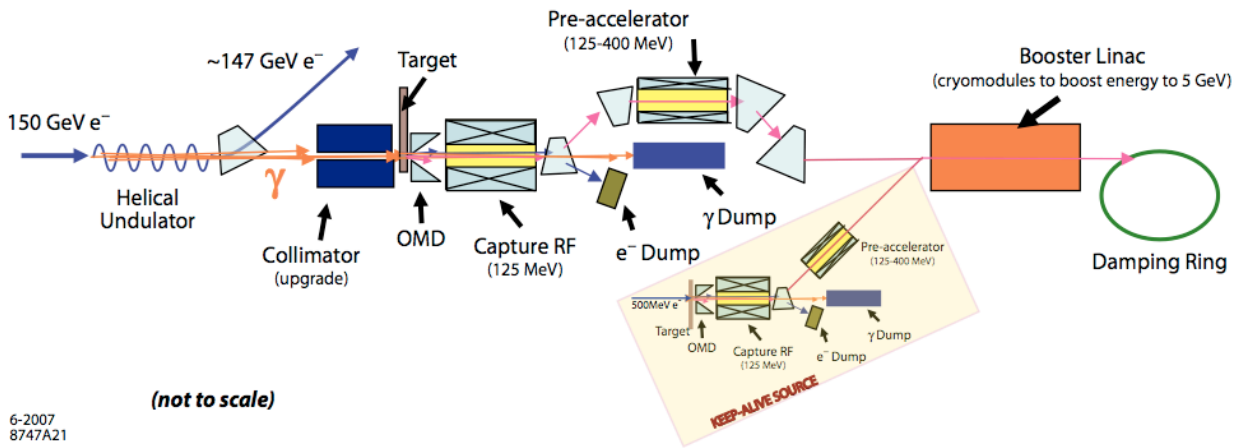

Figure 1.10: An overview of the proposed Undulator Based Positron Source at the ILC. The undulator is located at the $150GeV$ point in a chicane off the electron main linac [31].

Parameter	Value
Positrons per Bunch	2×10^{10}
Bunches per Pulse	2625
Train Repetition Rate / Hz	5
Positron Energy / GeV	5
Electron Drive Beam Energy / GeV	150
Electron Drive Beam Energy Loss / GeV	3.23
Positron Polarisation (upgrade) / %	60

Table 1.4: Positron beam parameters for the Undulator Based Positron Source [33].

A second positron source is also proposed which operates independent of the electron line. As well as potentially reducing downtime of the baseline configuration this source can also be used to produce polarised electrons providing e^-e^- and $\gamma\gamma$ options at the ILC. The scheme uses a high powered laser to produce Compton photons via interactions with electron circulating in an independent 'Compton Ring'. These high energy photons produce positrons

via pair production within a thin target. As with the undulator system the positrons are then captured and accelerated up to $5GeV$ before being inserted into the damping rings.

The Damping Rings

The requirement for extremely high luminosity at the ILC necessitates extremely small transverse beam sizes at the IP, as described in section 1.2. Rewriting equation 1.1 in a form that expresses the luminosity as a function of beam energy, equation 1.14, illustrates the need to compensate the reduction in luminosity caused by increasing the collision energy with a reduction in beam cross section at the IP.

$$\mathcal{L} = \frac{\mathcal{H}_{\mathcal{D}}}{4\pi E}\frac{NP}{\sigma_x \sigma_y} \tag{1.14}$$

where E is the beam energy and P is the beam power, all other symbols are as defined in equation 1.1.

To achieve the luminosity requirements at the IP the horizontal and vertical beam emittance must be minimised. The ILC design employes damping rings as the primary method of beam emittance reduction. The damping process involves circulating the particles many times around a dedicated storage ring. Each time the particles orbit the ring energy is lost in the direction of travel via synchrotron radiation, as discussed in section 1.2.2. The particles are then re-accelerated in the longitudinal direction thus reducing the beam emittance. Additional energy loss is produced by the presence of series of dipole magnets with alternating fields, known as *wigglers*. The wigglers induce undulations which create additional synchrotron radiation losses hence increasing the emittance reduction per revolution of the damping ring.

The current baseline design of the ILC contains one positron and one electron ring, each approximately $6km$ in circumference, placed within the same tunnel in the centre of the facility. The operating energy will be around $5GeV$ providing an optimum level for tuning the particles beams for low emittance whilst maintaining achievable beam acceptance requirements. Timing constraints resulting from the undulator based positron production mechanism may mean that the exact location of the damping rings with respect to the main accelerator my be site dependant. Electromagnets will be used as bending magnets throughout the rings, providing the ability to reverse the polarity allowing electrons to be stored in the positron rings, whilst the wigglers will employ superconducting magnets. The accelerating cavities will consist of superconducting RF units operating at $500MHz$.

1.3.2 Ring-to-Main-Linac

The Ring-to-Main-Linac (RTML) beam lines transport each the damped beam through the main accelerator tunnel. Once at the low energy end of the linac the beams are turned through 180° before the bunches are compressed and accelerated to around $15GeV$ prior to injection into the main accelerator. The low emittance of the $5GeV$ damped beams must be

maintained throughout the approximately $10km$ transport from the central damping rings to the beginning of the RTML bunch compressors. Therefore complex beam diagnostic and correction instrumentation is required. The alignment of this transport line is critical because the beam emittance degradation caused by component misalignment will be exacerbated since the $5GeV$ beams are not longitudinally compressed.

As well as transporting the beams the RTML beamlines perform several other functions. These include: collimating the beam halo generated in the damping rings; transforming the beam polarisation into the direction required at the IP; compensating for beam jitter; and bunch compression to the shorter length required in the main linac and at the IP. The approximate topology of the RTML is shown in figure 1.11.

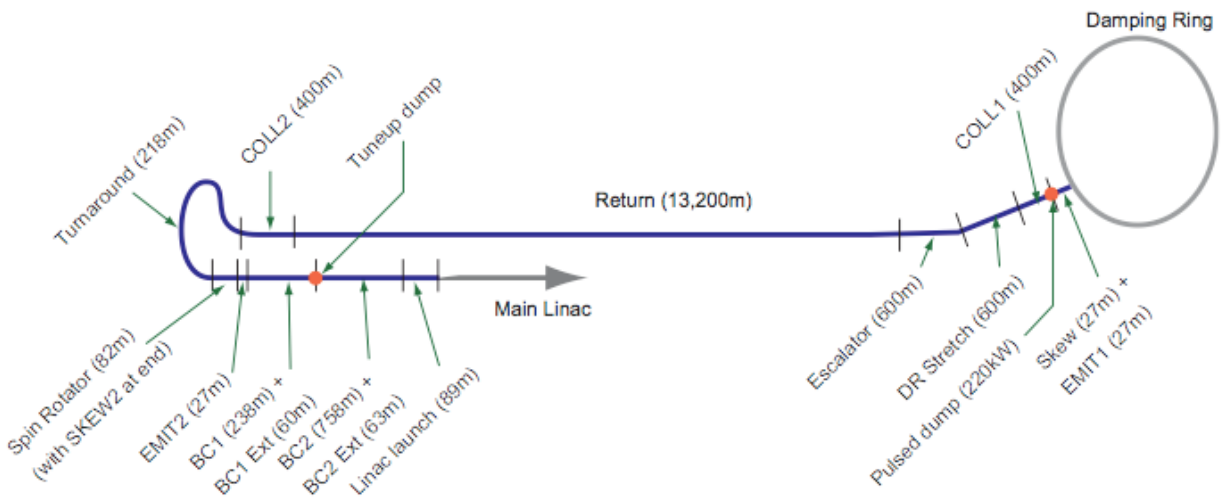

Figure 1.11: The approximate topology of the RTML layout including the beamline composition [34].

1.3.3 The Main Accelerators

Global accelerator research and development programs over the last decade have shown that two distinct technologies have the ability to operate reliably at the level required to achieve the baseline collision energy of $500GeV$ with an e^+e^- machine of around $30km$. These are room temperature copper structures operating at $11.4GHz$ (X-band) and $1.3GHz$ (L-band) superconducting niobium cavities. In 2004 the decision was taking to proceed with a design effort for the ILC based on superconducting accelerating technology.

The majority of the ILC tunnel length will be taken up by the superconducting accelerating cavities that form the main linacs. The total length of the machine is determined by the accelerating gradient that can be produced within these cavities. The current ILC design incorporates cavities that will be qualified to operate up to a gradient of $35MV/m$ which it is expected will produce an average gradient of around $31.5MV/m$ for the entire machine. However it is anticipated that further advances in the cavity design and production techniques may produce an eventual gradient of around $45MV/m$.

The superconducting RF cavities will be powered by $10MW$ Multi-Beam Kylstrons with each klystron driving 24 cavities. The cryomodules used to cool the accelerating components will each contain 8 cavities. Every fourth module also includes a quadrupole magnet which contains horizontal and vertical corrector windings and associated Beam Position Monitors (BPMs). A total of 1312 modules, containing 10496 superconducting RF cavities and 328 quadrupoles, are required to achieve collisions with centre-of-mass energies of $500GeV$.

The baseline ILC design incorporates acceleration cavities based on the TESLA design [35]. These cavities are 9-cell standing wave structures and are around $1m$ in length. The cavities are made from solid niobium and are bath-cooled by superfluid helium at $2K$. Figure 1.12 shows a prototype TESLA accelerating structure.

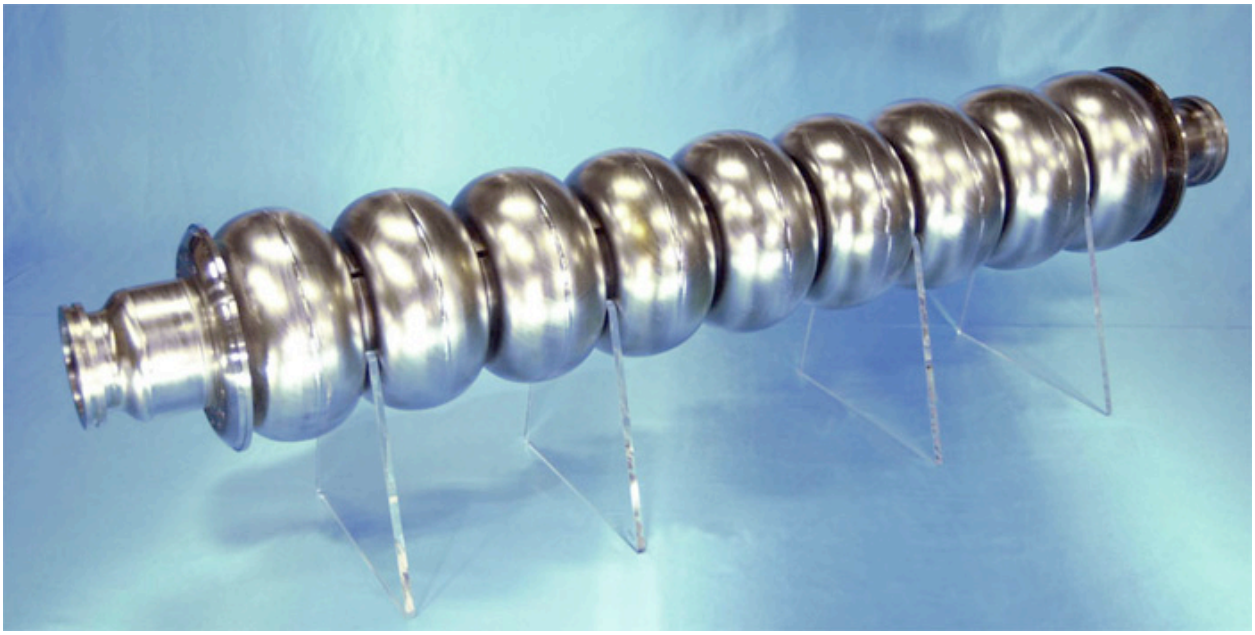

Figure 1.12: A prototype niobium 9-cell superconducting accelerating RF cavity which will form the basis of the accelerating structures used at the ILC [36].

1.3.4 The Beam Delivery System

A complete baseline configuration of the Beam Delivery System (BDS) has not yet been finalised since it requires close coordination with other areas of the design, most notably the damping rings. However the luminosity requirements produce strict constraints on the beam size and quality at the IP allowing for a detailed conceptual design to be developed.

The initial ILC specifications call for two interaction points to allow for results verification and independent physics studies to be carried out. The baseline multiple IP solution contains two interaction regions each with beam crossing angles of $14mrad$. Alternatives include solutions with 2 and $20mrad$ crossing angles. A further discussion is whether to have one large interaction region containing both detectors or two longitudinally separated detector halls. Clearly a single interaction region has benefits in terms of construction and initial

installation whereas separated detectors could provide the ability for one experiment to continue data taking whilst the other is undergoing maintenance or upgrade.

The current BDS optics configuration consists of: the linac (described in section 1.3.3); beam emittance, energy and betatron diagnostics located at the junction between the main linac and the entry to the BDS, this section of beamline measures the beam emittance using a laserwire system and monitors incoming energy and betatron orbit errors using BPM measurements; a coupling correction section; the tune-up and emergency extraction beamline which provides protection for BDS components via a system of replaceable collimators and allows for emergency beam extraction and dump when necessary; a beam switch yard; an upstream polarisation diagnostics section; a betatron and energy collimation systems consisting of spoiler-absorber pairs which are designed to survive the impact of errant bunches which escape from the emergency extraction line; an upstream energy spectrometer based on the 4-magnet chicane design used at LEP, which must be capable of making relative and absolute energy measurements of $\mathcal{O}(100ppm)$; the final focus with secondary clean-up collimation; the final doublet; the extraction beamline with downstream energy and polarisation diagnostics; and the beam dump which is based on a water vortex design used at the SLC. An overview of the current conceptual BDS design is shown in figure 1.13.

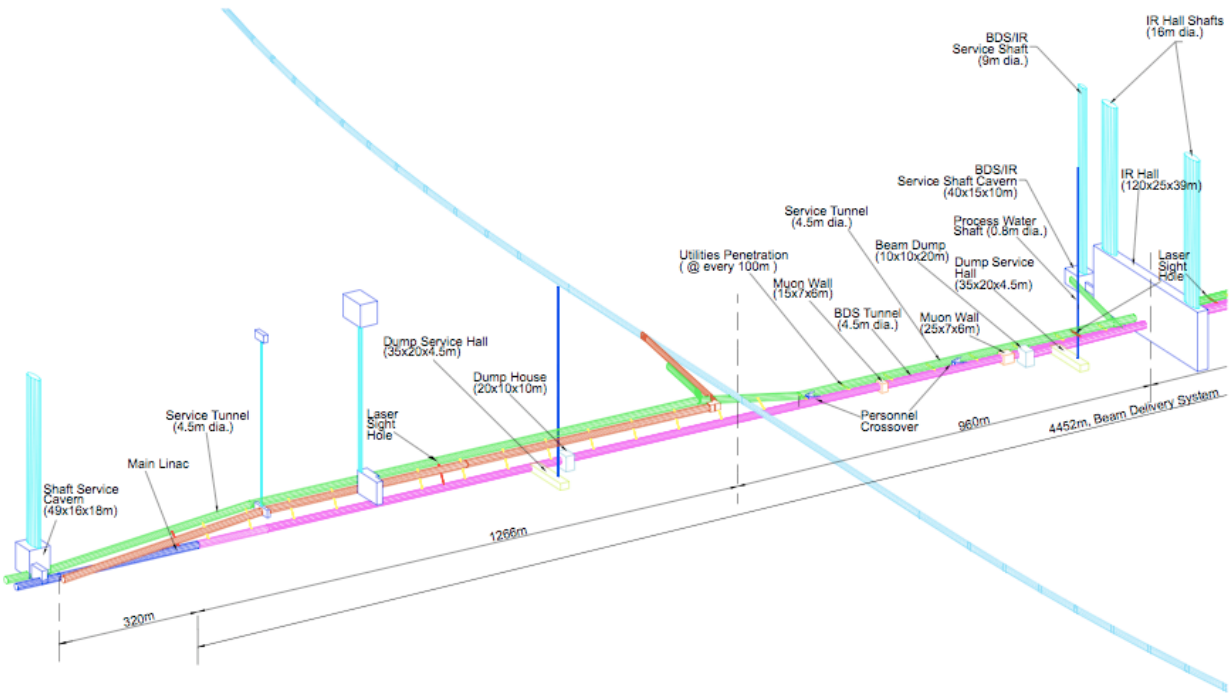

Figure 1.13: A graphical overview of the proposed beam delivery system for the ILC. The beam and service tunnels (magenta and green respectively), shafts, experimental hall are shown. The line crossing the BDS beamline at right angles is the damping ring which located $10m$ above the BDS tunnels [31].

1.4 Alignment of the ILC

The challenges associated with the beam emittance requirements at the ILC are much greater than those overcome at any previous particle accelerator. Therefore a more comprehensive alignment strategy is required which covers all aspects of machine construction and operation. The overall aim of the alignment process is to produce a machine capable of achieving the beam emittance, and therefore luminosity, requirements. The exact technical details of the process have not yet been decided, this section provides a conceptual overview.

The alignment process will consist of several stages. Throughout the construction phase a guidance system, based on standard surveying techniques and surface GPS measurements, will be employed to achieve the initial construction specifications. After the completion of tunnel construction, prior to accelerator module installation, a full survey will be carried out producing a reference coordinate system within the tunnel. This reference frame will be used throughout the installation phase to position and align modules and other components.

Since each module consists of multiple active components the position of the 'active centre' of each module with respect to the external markers has to be determined via a process known as *fiducialisation*. Knowledge of the positional relationship between the internal active components and external markers allows each module position to be adjusted so that the best global alignment can be achieved. The final stage in the alignment process makes use of beam-based alignment mechanisms to optimise the beam trajectory through to the IP.

The overall alignment tolerance budget was produced by analysing the accelerator physics. Each stage of the alignment process has been assigned a fraction of this global tolerance budget using estimates of what will be achievable with several years of R&D prior to commencing the construction of the ILC.

1.4.1 Tunnel Construction and Reference Survey

The construction of the tunnel and the corresponding effect on surveying and accelerator alignment is extremely dependant upon the final choice of location for the ILC. No decision has yet been taken regarding where the ILC should be constructed although several sample sites are currently under consideration. Potentially suitable sites have been proposed in Asia, Europe and North America. An overview of each of the proposed sites is given below outlining some of the potential benefits and drawbacks of each.

Asian Multiple sample sites are under consideration. The tunnel would be constructed within uniform solid rock away from active faults. Surface access to be provided via service tunnels around every $5km$, these would be used for accelerator installation as well as power delivery. The chosen site will be positioned away from large urban areas and heavy traffic routes to minimise human-made sources of vibration.

CERN French-Swiss Border. The site would make use of existing CERN infrastructure including currently installed $400kV$ electrical supply. The proposed deep tunnel configuration constructed within sandstone bedrock should produce a stable and water-

tight tunnel. The region is relatively geologically inactive meaning stability should be acceptable. The detector facilities could be housed on the current LHC site.

DESY Northern Germany. The site would make use of existing DESY facilities including $110/220kV$ electrical supplies and local headquarters of potential ILC construction contractors and component suppliers. A shallow tunnel configuration could make use of planning permission already obtained for the TESLA project. The proposed tunnel would be placed in sand and be below the local water table for most of it's length. The proposed configuration is based on TESLA and could be extended up to $70km$ with access shafts around every $5km$.

FNAL Northern Illinois, USA. The site would make use of existing infrastructure and is close to large scale electricity production facilities. The proposed deep tunnel configuration would be constructed in the solid bed rock. The geology should provide a relatively dry and stable tunnel.

The final decision on the location of the ILC will require further detailed investigations of all proposed sites. These will include geological surveys including test bores and environmental impact studies. A summary of the current site proposals is given in table 1.5.

	Asian	**CERN**	**DESY**	**FNAL**
Accelerator Tunnel Diameter / m	3.2	3.2	3.2	4
Service Tunnel Diameter / m	4	4	4	4
Tunnel Depth / m	10 to 200	100 to 130	7 to 30	120 to 150
Rock Type	Granite	Molasse Sandstone	Quarternary sand	Galena Platteville Dolomite
Length of Site / km	$\geq$50	$\geq$50	$\geq$50	$\geq$50

Table 1.5: An overview of the preliminary design data for the currently proposed ILC sites [34].

The construction of the tunnel will be undertaken using tunnel boring machines. The details of the tunnel production will depend on the final site decision and complete specification of the ILC facility. The options for finishing the interior tunnels walls will primarily depend on the geology of the chosen site. In the case of hard bedrock a sealant may be applied to control water inflow. However for the European sites (tunnels constructed in sandstone or sand) precast watertight concrete sections will be laid in place during the tunnel excavation. The $6km$ tunnel that will contain the damping rings will be produced in the same fashion as the main accelerator tunnels. However investigation are underway at the European sites as to the feasibility of using existing tunnels (SPS and HERA) to house the ILC damping rings.

The tunnel alignment during construction will primarily rely on a geodetic network with reference points placed close to the access shafts with their positions determined from GPS measurements. Laser pointing measurements will be used to provide the required accuracy

during the boring stage in the sections between the access shafts. There are no guaranteed fixed points within the tunnel therefore after construction a full reference survey must be completed quickly and be repeated as necessary.

Ground Motion

The effects of ground motion caused by both natural and man-made sources must be properly understood to ensure successful ILC performance. These effects can produce beam emittance growth and could results in the complete misalignment of the beams. Investigation into the levels and time-dependence of ground motion at various sites (existing and proposed sites as well as control sites) have taken place [37]. Measurements were made using three axis seismometers allowing the Power Spectral Density (PSD) of the ground motion to be determined. The seismometers directly measure the velocity of motion in each direction however it is straightforward to extract the displacement PSD from the acquired results. The PSDs are integrated over large time periods ($\geq$15 minutes) to smooth the effects of single noise events. The total r.m.s. displacement over the whole frequency range was then found by taking the square root of the integrated displacement PSD. The integrated vertical ground motion spectra for existing high energy experiment sites at CERN, FNAL, HERA at DESY, the proposed TESLA site and a control site are shown in figure 1.14.

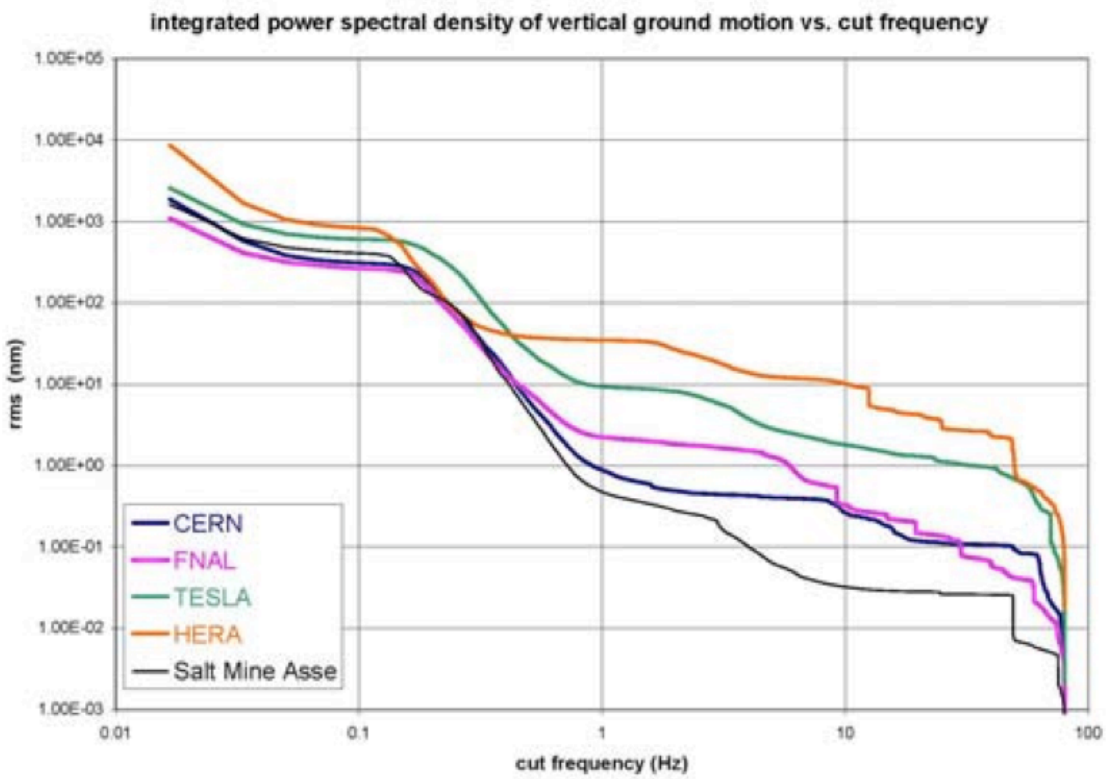

Figure 1.14: The integrated vertical ground motion spectra for existing high energy experiment sites at CERN, FNAL and HERA, the proposed TESLA site and a control site in the Asse rock salt mine in Germany [37].

Ground motion is usually divided into two regimes, 'slow ground motion' at frequencies less than $1Hz$ and 'fast ground motion' at higher frequencies which is normally dominated by man-made or *cultural* noise. Low frequency effects such as the microseismic peak present at 0.1 to $0.25Hz$ (due to coastal waves) are present at all sites. Changes in atmospheric conditions and Earth tides contribute at frequencies lower than this. In general the shape of the PSDs follows a random walk noise trend producing a $1/f^4$ behaviour at frequencies below $1Hz$. However in the higher frequency regime the dominance of cultural noise produces large site-to-site variations and a deviation away from the $1/f^4$ behaviour.

The motion of the ground at the ILC will have minimal impact on the survey of the tunnel and the alignment of the accelerator components. High frequency vibrations, both natural and man-made, will be too small in amplitude to affect the survey process on the scales required during construction phase. While the slower motions such as the settling of the site during the lifetime of the machine place a lower limit on the re-survey frequency.

1.4.2 Module Construction and Installation

The accelerator modules described in section 1.3.3 must be fabricated and aligned to high precision to achieve the required beam properties at the IP. Any misalignment of components results in beam trajectory errors which causes emittance growth. Dispersive emittance growth is produced by anomalous kicks from misaligned quadrupoles coupled with the non-zero energy spread of the beam. Furthermore quadrupoles rotated about the beam axis couple a fraction of the large horizontal emittance into the smaller vertical emittance. Wake-fields and cavity tilts also contribute to emittance growth. The tolerances of the active components with respect to the external fiducials of each module are given in table 1.6. The stated offset values correspond to the vertical with the horizontal tolerances being at least 3 times less stringent [38].

Degree of Freedom	**Value**	**with respect to**
BPM Offset / μm	300	module
Quadrupole Offset / μm	300	module
Quadrupole Roll / μrad	300	module
Cavity Offset / μm	300	module
Cavity Tilt / μrad	300	module
Module Offset / μm	200	perfect line
Module Tilt / μrad	20	perfect line

Table 1.6: The alignment tolerances of the active accelerator components within the main linacs [38].

Quadrupole Roll refers to rotations around the beam axis, since this is the most relevant rotation. For rotations about the axes perpendicular to the beam only the cavity rotation is relevant, however since there are many cavities in each module the module rotation is also an important parameter. As with the offset tolerances the rotational tolerances around the

vertical axis (yaw) are at least 3 times less than the tolerances about the horizontal axis (pitch). These transverse rotations are collectively referred to as tilts.

The horizontal and vertical beam emittance at damping ring extraction are $\gamma\varepsilon_x = 8\mu m$ and $\gamma\varepsilon_y = 20nm$ respectively. An emittance growth budget for the regions between the damping rings and the IP has been defined to ensure achievement of the target emittance at the IP, stated in table 1.2. The details are given in table 1.7 [33].

Machine Region	$\Delta\varepsilon_y$
RTML / nm	≤ 4
Main linac / nm	≤ 10
BDS / nm	≤ 6

Table 1.7: The vertical emittance growth budget for the regions between the damping rings and the IP [38].

The final alignment and fiducialisation of the individual active components is conducted after the strings of cavities have been moved to a final assembly area and have been attached to the Helium Gas Return Pipe (HGRP). The HGRP forms an integral part of the structure of the module. The module is then moved and installed using the external reference markers, indicated on the right of the body of the module in figure 1.15, to recover the alignment of the active components.

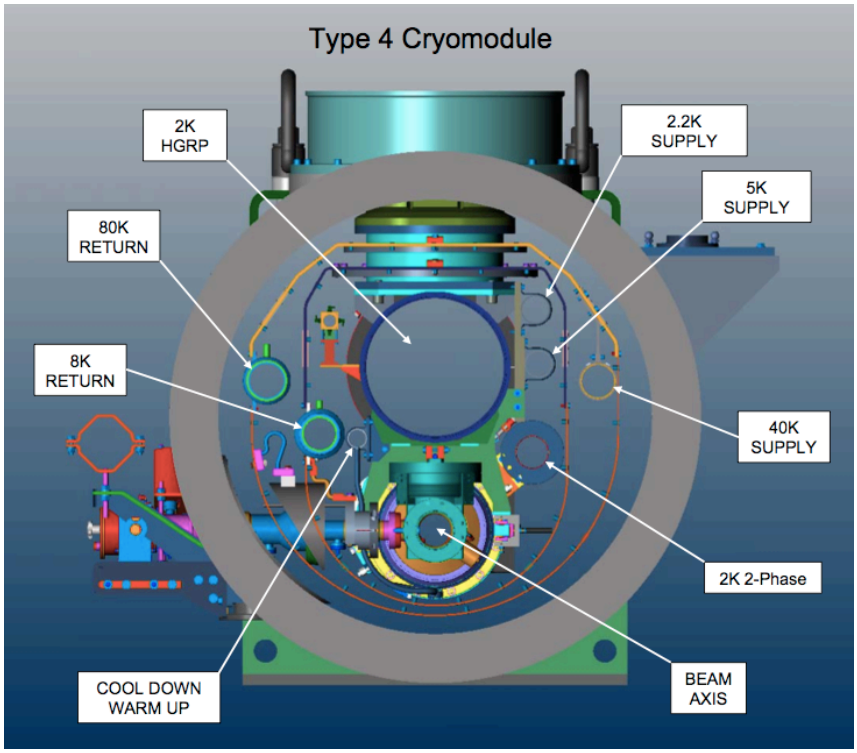

Figure 1.15: A cross-sectional view of an accelerator module, the Helium Gas Return Pipe (HGRP) is shown along with the position of the external reference marker. The other Helium cryosystems are also labelled [33].

The requirements for the alignment of each accelerator module are defined in terms of the mean deviation from a best fit straight line over any baseline section of tunnel. The length of the chosen baseline is often referred to in terms of the betatron wavelength of the machine. These requirements are $\leq 200\mu m$ in the vertical and $\leq 500\mu m$ in the horizontal over a baseline of $600m$. Machine simulations indicate that such an installation accuracy allows beam-based alignment to converge to an acceptable emittance orbit over a majority of seed machines.

The modules are aligned with respect to the tunnel reference markers during a process referred to as a *stake-out*. This involves using an additional survey instrument to determine the module positions and orientations with respect to the previously determined positions of tunnel reference markers. During this procedure the relevant length scales are significantly less than the those in the full tunnel survey and hence classical optical survey techniques may be used. Since the position of each module can be determined with respect to several tunnel reference markers the accuracy of the tunnel survey will be maintained during this coordinate transfer.

1.4.3 Stabilisation

A fast beam-beam intra-train feedback system is included in the baseline ILC configuration along with slower train-by-train feedback. These systems use a combination of BPMs and kickers to help to redress luminosity degradation resulting from train-to-train variations of beam offset and angle. Additional active stabilisation methods will also be employed to stabilise critical components, such as the chromaticity correcting sextupoles and the final doublet, on time scales of a few seconds or less. These may include accelerometers placed on the cryostats and fixed frequency interferometric systems monitoring the motion of critical components with respect to external references. A combination of these methods is necessary to ensure the luminosity requirements are met.

1.5 The Rapid Tunnel Reference Surveyor

The requirement to completely survey a tunnel around $30km$ in length to an accuracy of $200\mu m$ over $600m$ in the vertical, and $500\mu m$ over $600m$ in the horizontal presents a significant challenge. The extremely long tunnel and the speed at which the survey must completed excludes the use of portable open-air optical survey methods. The highest achievable accuracy using a single open-air optical measurement is around $4.5mm$ over $600m$ due to a typical vertical temperature gradient within the tunnel[5] of approximately $0.1K/m$. A full survey must be undertaken prior to accelerator installation and the entire process must be repeated approximately annually. These restrictions make an automated survey solution highly desirable. The cost of installing a static measurement system throughout the tunnel could be prohibitively large hence a portable survey system is preferred.

[5]The presence of a vertical temperature gradient also introduced problems associated with calibration due to thermal expansion.

The LiCAS Rapid Tunnel Reference Surveyor (RTRS) involves the installation and survey of a reference coordinate system throughout the tunnel. Such a tunnel-wide reference system provides multiple benefits. The survey process can be automated with greater ease since markers on the tunnel wall can be regularly spaced, whereas for various reasons the markers placed on the accelerator components will be irregularly positioned. Once in place the tunnel reference system can be used numerous times to determine the position of accelerator components with respect to the tunnel and each other. The tunnel reference system can also be partially or wholly re-surveyed and updated with minimal interference with other activities taking place within the tunnel.

A coordinate convention has been defined for use within the tunnel. The local tunnel direction is labelled as z with the direction normal to z and horizontal being labelled x and the direction normal to both z and x being labelled as y. This system is illustrated in figure 1.16. Translations and rotations of the cars or the train within this system are labelled as dx, dy, dz and $rot\text{-}x$, $rot\text{-}y$, $rot\text{-}z$ respectively. The errors on translation are labelled as $\sigma(dx)$ or sigma-X while the errors on the rotations are referred to as $\sigma(rot\text{-}x)$ or sigma-A, sigma-B and sigma-C for rotations about the x, y and z axes respectively. The measurements made by the RTRS provide a complete reference coordinate system within the tunnel.

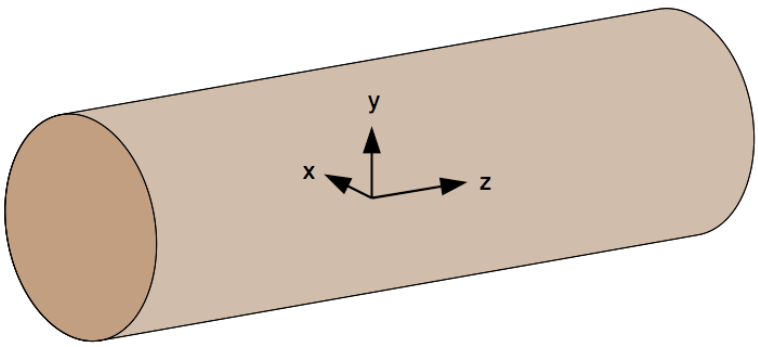

Figure 1.16: An illustration of the coordinate system defined for use within the tunnel.

1.5.1 System Overview

The RTRS is a train comprised of measurement cars which are capable of surveying regularly spaced markers placed on the tunnel wall. The train contains an internal measurement system which allows the position and orientation of each car to be determined with respect to the other cars in the train. The relative positions of these cars can be adjusted by $\pm 25mm$ and $\pm 2°$ in all directions to produce an optimal measurement configuration.

The survey markers are placed on the tunnel wall at regular intervals with their separation matching that of the measurement cars. When the train stops the position of the marker directly in front of each car is determined in 3 dimensions. The train is moved along the tunnel one marker at a time so each car determines the position of each marker[6]. Using the

[6]The positions of the markers at the extremes of any survey section will not be determined by every car.

information from the internal measurement systems this overlapping technique allows the sets of positions determined at each train stop to be combined. The measurements made at previous stops can be propagated assuming that the markers are stable on the time scale of the survey. Thus a full 3 dimensional reference coordinate system is built up throughout the entire tunnel. An illustration of the overlapping measurement technique that will be employed by the RTRS is given in figure 1.17.

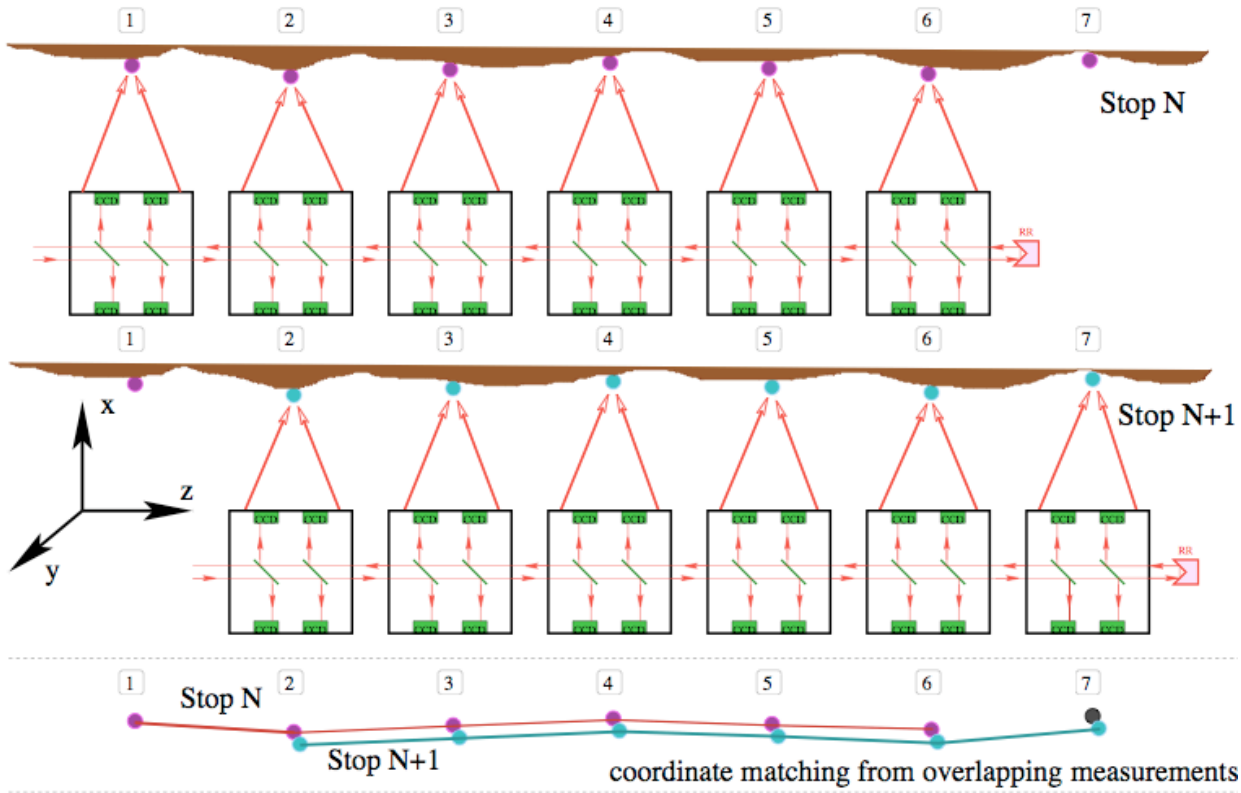

Figure 1.17: An illustration of the survey technique to be employed by the LiCAS RTRS. The measurements made by the internal systems at Stop N and Stop N+1 allow the wall marker positions to be combined [39].

Initially a 3-car prototype RTRS system will be produced to test the measurement systems within the train setting. The design model of the 3-car prototype RTRS is shown in figure 1.18. This prototype RTRS will incorporate measurement systems which have been designed to allow the global survey requirements to be achieved. The system proposed for use in the survey and alignment of the ILC will contain 6 measurement cars providing increased redundancy and higher accuracy.

1.5.2 The Measurement Systems

There are three independent measurement systems present in the RTRS. Together these systems overconstrain the 6 degrees of freedom of each car and the 3 degrees of freedom of the markers placed on the tunnel wall. The main measurement systems that are described in this section are shown in figure 1.19.

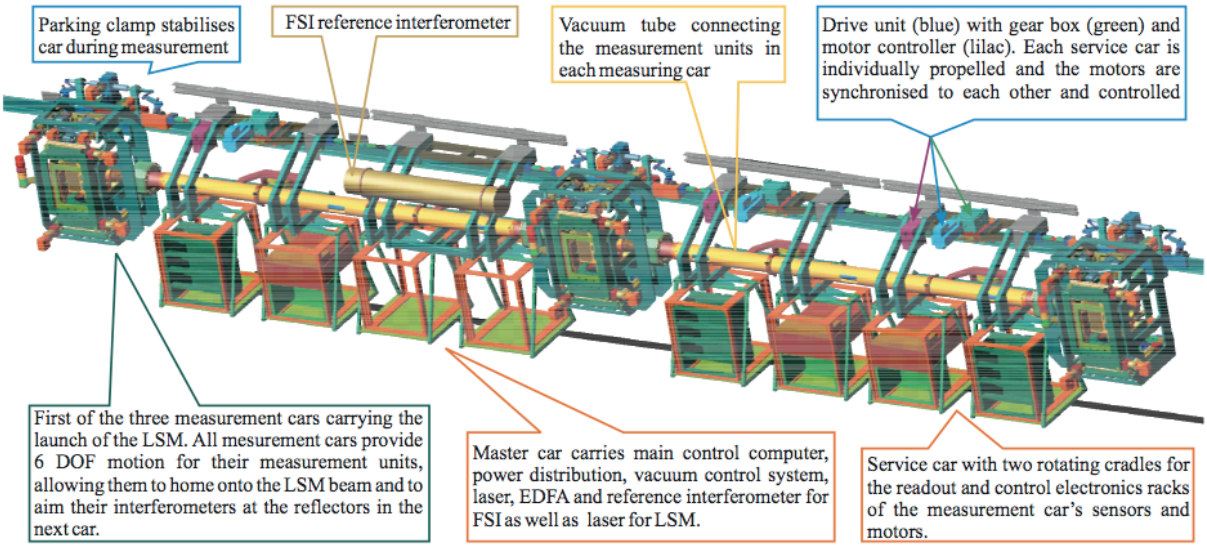

Figure 1.18: The full design model of the prototype 3-car RTRS including the service and master cars which contain the equipment required to operate the measurement systems [40].

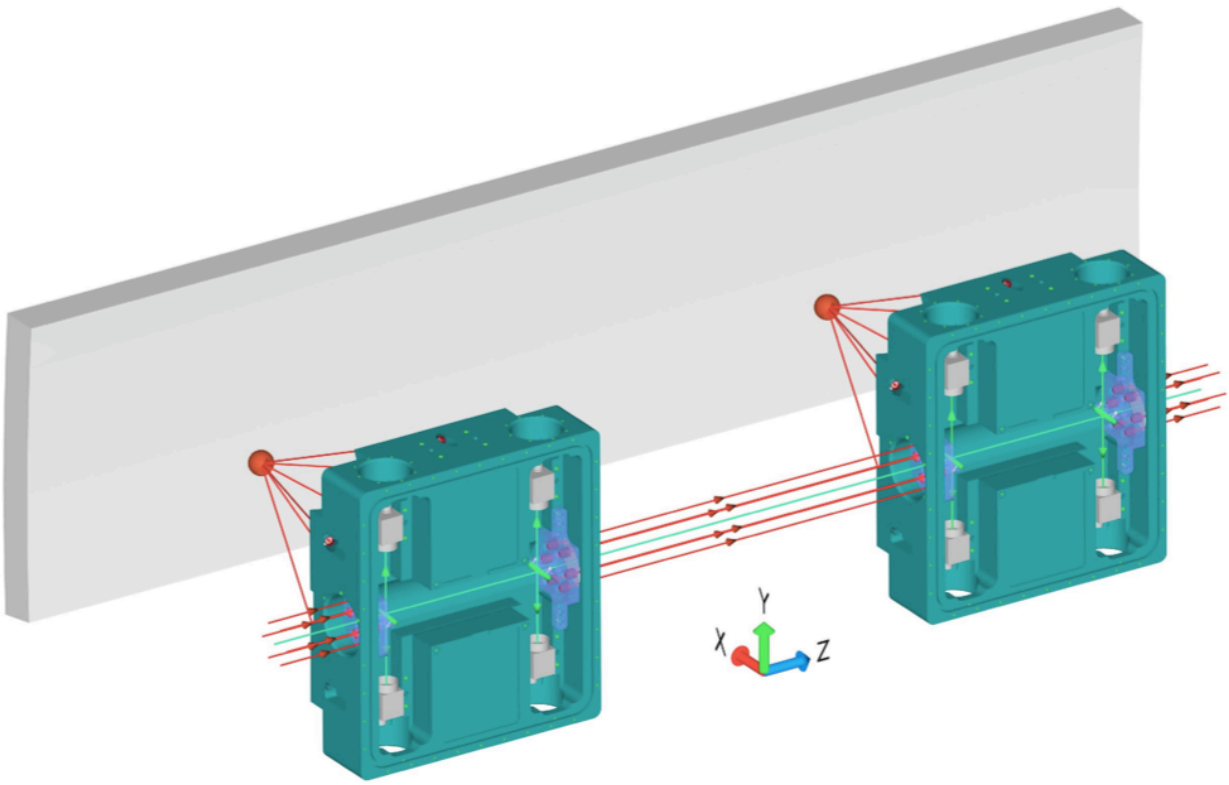

Figure 1.19: An illustration of the RTRS measurement systems. The LSM beam is shown in green with the FSI measurement lines shown in red, the tilt sensors are not shown.

The Laser Straightness Monitor

The Laser Straightness Monitor (LSM) provides a local straightness reference throughout the train. The LSM consists of a laser beam that is propagated from the first car via a vacuum tube that runs through the centre of the train to the final car where it is returned by an adjustable mirror. This produces two parallel straight beams which pass through each car in the train. The LSM beam is shown as a green line in figure 1.19. By placing a pair of beam splitters in each car both the outward and returned beams can be viewed using the 4 CCD cameras within each car. Measurements of the positions of the beam spots overconstrain the dx, dy, $rot\text{-}x$ and $rot\text{-}y$ degrees of freedom of each car.

The LSM system is capable of producing micron precision measurement of translations and microradian precision measurements of rotations. These measurements are made by isolating the positions of the spots produced by the two LSM beams on a CCD image. A complete model of the LSM geometry is used to fit the eight measurements allowing the relevant 4 degrees of freedom to be determined.

The Tilt Sensors

Each measurement car will be equipped with two orthogonally arranged, DC operated gravity referenced inclinometers with a range of 1° and a resolution of 0.1 arc seconds. These will be used as nulling devices only and have a settling time of $2s$. The output voltage signal will be digitised to 16 bit resolution. Only the measurement of $rot\text{-}z$ contributes to the survey measurements thus maintaining independence from the local geoid shape. The $rot\text{-}x$ levelling is only used to simplify the pre-alignment of the RTRS. The coarse range levelling adjustment is undertaken using measurements made by a dual axis tilt sensor with a 20° range, a resolution of 0.0125° and a settling time of $0.5s$.

The Frequency Scanning Interferometry Systems

Frequency Scanning Interferometry (FSI) is an absolute distance measurement technique that is capable of producing micron accuracy over distances of several metres. There are two FSI subsystems within the RTRS, one forming part of the internal measurement system and the other being the external marker measurement system. Details of how the measurements are made and the specifics of the system implementations are given in Chapter 2.

The internal FSI measurement system consists of six parallel absolute distance measurement interferometers, shown as red lines between the two measurement cars in figure 1.19. These interferometers measure the car separation. They provide a set of redundant measurements of dz and are also sensitive to $rot\text{-}x$ and $rot\text{-}y$.

The external FSI system also consists of six absolute measurement interferometers which form a hexagonal based pyramid with the marker on the tunnel wall at the apex. These are also shown as red lines in figure 1.19 and provide 6 independent distance measurements from known fixed points on each car to the survey markers on the tunnel walls. This set of

six measurements allows for the determination of the marker position in 3 dimensions with respect to the measurement car.

1.5.3 Preliminary System Simulations

The system performance of the RTRS was simulated by G. Grzelak [39]. The propagation and correlation of measurement errors was studied to asses the ability of the system to achieve the required alignment performance. An opto-geometrical model of the RTRS was produced, using the SIMULGEO package [41], to study the propagation of measurement errors to wall marker position uncertainties during a tunnel survey. As a preliminary benchmark of the RTRS performance simulations were undertaken using a nominal LSM and FSI measurement precision of $1\mu m$. These initial results provide a link between the ILC machine requirements, the RTRS system requirements and the requirements of the individual FSI and LSM measurement systems.

The error propagation as the train progresses along the tunnel was investigated by simulating the measurement precision at overlapping train positions. A total of 20 train stops were simulated which corresponds to $90m$ of fully surveyed tunnel. The measurements at each train stop are coupled to the previous stop via 5 overlapping wall markers. The expected wall marker position determination errors for the simulated $90m$ survey are shown in figure 1.20 as a function of wall marker number.

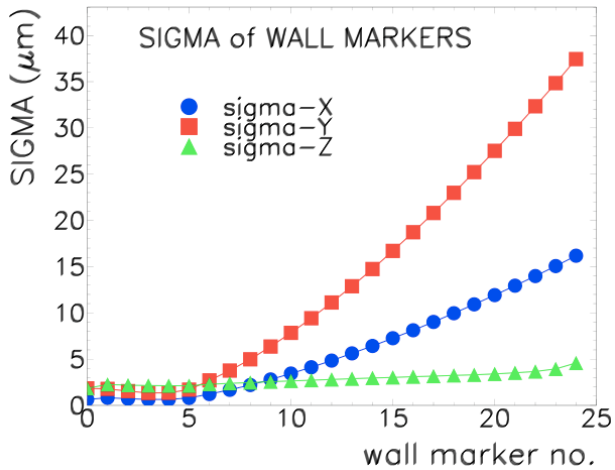

Figure 1.20: Results of a simulation of a survey of $90m$ of tunnel. The precision of wall marker position determination is shown as a function of marker number [39].

The SIMULGEO calculations provided very precise results since the model was an exact opto-geometrical representation of the survey procedure. However such an approach was very time and computer resource intensive when simulating large tunnel surveys. The results shown above required over 34 hours of CPU time on a $2GHz$ machine with the dimensions of the manipulated matrices approaching $\mathcal{O}(10^5)$. The numerical complexity scales like N^2, were N was the number of coordinates involved hence a complete simulation of a $600m$ tunnel section would have required around 8 weeks of CPU time.

Due to these extremely limiting computational requirements another method was developed. A simplified analytical formula base on a random walk model was derived to extrapolate the SIMULGEO results over long tunnel sections[7]. The form used is given in equation 1.15.

$$\sigma_{xy,n} = \sqrt{l^2\sigma_\alpha^2\frac{n(n+1)(2n+1)}{6} + \sigma_{xy}^2\frac{n(n+1)}{2}}, \quad \sigma_{z,n} = \sqrt{\sigma_z^2\frac{n(n+1)}{2}} \tag{1.15}$$

where n is the wall marker index and l is the effective step length of the random walk (the car separation distance). The error parameters: the angular error, σ_α; the transverse errors, σ_{xy}; and the longitudinal error, σ_z are illustrated in figure 1.21.

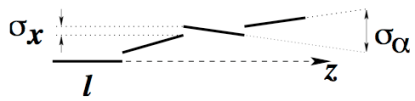

Figure 1.21: The random walk model for the error propagation for the position of the accelerator components. The terms σ_{xy}, σ_α and l are those used in equation 1.15

The approximate asymptotic behaviours of the uncertainties defined in equation 1.15 are

$$\sigma_{xy,n} \sim n^{3/2}, \quad \sigma_{z,n} \sim n. \tag{1.16}$$

The rapid growth of the errors in the transverse directions, and to a lesser extent in the longitudinal direction, is due to the fact that the position determinations are highly correlated. The precision to which the position of the nth marker can be determined is highly dependant upon the precision of all previous measurements.

The SIMULGEO simulation results of the $90m$ tunnel survey were fitted using equation 1.15 to determine σ_α, σ_{xy} and σ_z. The extracted fit values were then used to extrapolate the results over a $600m$ tunnel section. These extrapolated results are shown in figure 1.22 and relate to the precision of the determination of the nth reference marker with respect to the 1st. However this measure of alignment quality does not provide a direct link to the global ILC alignment requirements. The required parameter is the mean deviation of each accelerator component from a best fit straight line to the positions.

To predict the alignment deviation of accelerator components from a straight line a series of random walk trajectories were produced using the parameters extracted from fitting the SIMULGEO results. A linear fit to each trajectory allowed the corresponding residuals to be calculated. The calculated RMS values from the residuals to the fits provide a measure of the precision of the entire alignment process. The oscillations of the generated trajectories were much smaller than would be expected from a completely random process as a consequence of the large correlation between adjacent measurements. A summary of the results for the predicted horizontal and vertical accelerator component alignment precision is given in figure 1.23. These results predict that an alignment precision of $\mathcal{O}(50\mu m)$ in the horizontal and $\mathcal{O}(100\mu m)$ in the vertical is feasible over a $600m$ tunnel section[8].

[7]The random walk model implemented contained both angle and position memory.

[8]This investigation only provides information on the statistical errors and does not take into account the systematic errors introduced during the survey process.

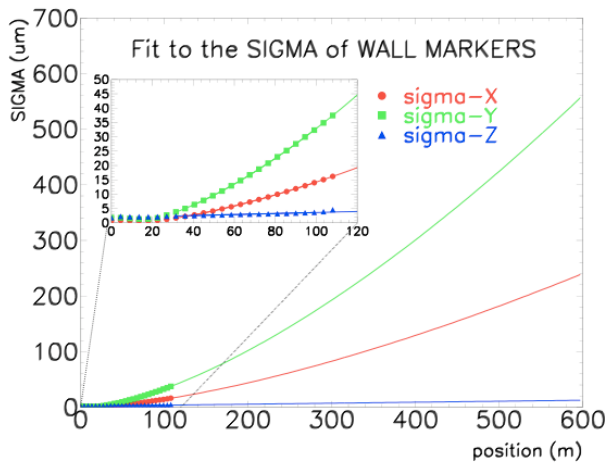

Figure 1.22: The SIMULGEO results for the full RTRS simulation with the extrapolation to a 600m tunnel section using the random walk model [39].

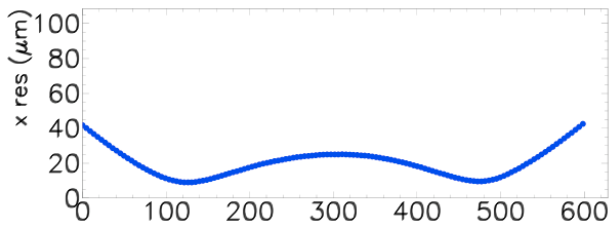

(a) RMS of the vertical residuals of simulated random walk trajectories.

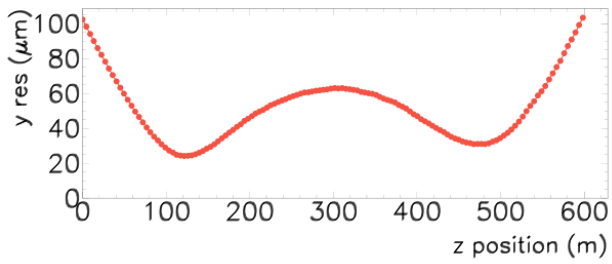

(b) RMS of the horizontal residuals of simulated random walk trajectories.

Figure 1.23: The RMS of the vertical and horizontal residuals of simulated random walk trajectories for a 600m tunnel section [39].

1.6 Summary

The study of physics beyond that currently encompassed within the Standard Model requires experimental investigations of TeV energy particle collisions. A complete picture of what physics exists at the TeV scale will require data from both hadron collisions, such as those that will be produced at the LHC, and from lepton collisions. The ILC will produce $500GeV$ e^+e^- collisions and must be a linear machine at these beam energies to limit the dissipative effects of synchrotron radiation. The study of physics beyond the Standard Model also requires an extremely high luminosity facility. The linear configuration removes the ability to recycle the beams however this also removes the need to maintain beam integrity after the collision. Extremely low emittance beams must be produced at the ILC and focused to nanometer spot sizes at the IPs to achieve the required luminosity. These increased beam emittance requirements mean that alignment is more critical and will therefore have to be considered during design and construction.

The LiCAS RTRS is a survey implementation based on FSI absolute distance and laser straightness monitor measurement techniques that have been designed to achieve the ILC reference survey requirements. Initially a 3-car prototype RTRS will be produced to examine the survey technique. The laboratory developed measurement systems will be integrated into this prototype. Preliminary simulations of a 6-car RTRS system indicate that a measurement precision of $\pm 1\mu m$ and $\pm 1\mu rad$ for all individual measurement systems will be necessary to achieve the ILC global survey requirements.

Chapter 2

FSI System Description

2.1 Introduction

This chapter details the specifics of the hardware implemented and techniques developed during the initial investigations of the absolute distance measurement systems for the prototype RTRS. An overview of the measurement technique is presented followed by a detailed description of the hardware components used to produce, acquire and digitise the interferometric signals. Additional hardware systems, such as environmental sensing and motion stages, are also described along with a definition of the data storage system.

2.2 FSI and LiCAS

The absolute distance measurement systems employed within LiCAS make use of Frequency Scanning Interferometry. This section outlines both the principles of the measurement process and the specifics of the implementations within the RTRS measurement systems.

2.2.1 FSI Basic Principles

An interference signal is produced by coherent phase differences between multiple interferometer beams from the same source[1]. The generation of an interference signal is describe here using classical electromagnetic theory in terms of a plane polarised electric field represented by amplitude and phase, as dealt with in [42]. However this description is in agreement with the predictions of more advanced quantum mechanical treatments of interference (see [43] for example).

The generation of an interferometric fringe pattern can be modelled by considering monochromatic light in the form of a plane wave with initial electric field amplitude E_0

[1] A phase difference is said to be coherence if it is maintained for much longer than the detector response time. Incoherent phase difference arise continually within the any light beam but are lost during the averaging of the detection process and so do not result in observable fringes.

travelling towards a beam splitter as shown in figure 2.1. The waves are separated by the beam splitter and travel along different interferometric paths before being recombined producing an interference pattern with is recorded at the detector. If the lengths of the different paths are d_1 and d_2 the electric field of the plane waves arriving at the detector from each path can be written in the form:

$$E_1 = a_1 E_0 e^{i(\omega t - k d_1)} \tag{2.1}$$

$$E_2 = a_2 E_0 e^{i(\omega t - k d_2 + \phi_0)} \tag{2.2}$$

where a_1 and a_2 are the amplitude coupling constants for the two paths and ϕ_0 is a general phase offset. If the fields in the two paths have the same polarisation the intensity of the interference pattern in a medium with electromagnetic impedance Z is given by

$$I = \left(\frac{1}{2Z}\right)(E_1 + E_2)(E_1 + E_2)^* \tag{2.3}$$

$$= \left(\frac{E_0^2}{2Z}\right)(a_1^2 + a_2^2 + 2a_1 a_2 \cos\Phi) \tag{2.4}$$

where the phase term is given by

$$\Phi = k(d_1 - d_2) + \phi_0 \tag{2.5}$$

$$= 2\pi\left(\frac{\Delta d}{\lambda}\right) + \phi_0 \tag{2.6}$$

where Δd is the optical path difference (OPD) of the interferometer and λ is the vacuum wavelength of the light, which is related to the wavevector k by

$$\lambda = \frac{2\pi}{k}. \tag{2.7}$$

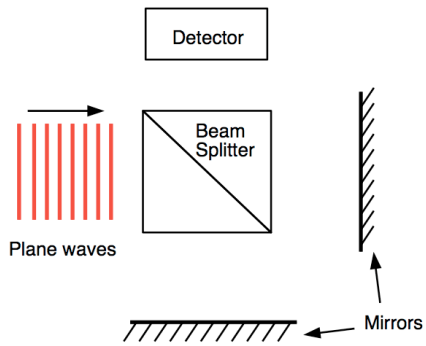

Figure 2.1: Interference fringe production from monochromatic plane wave in an amplitude splitting two beam interferometer.

In general the interferometers used within LiCAS can be thought of as single path two beam interferometers. This results from setting one of the optical path lengths to zero allowing the length of the second optical path to be directly access from a measurement of the OPD. A schematic of the LiCAS interferometer geometry is shown in figure 2.2.

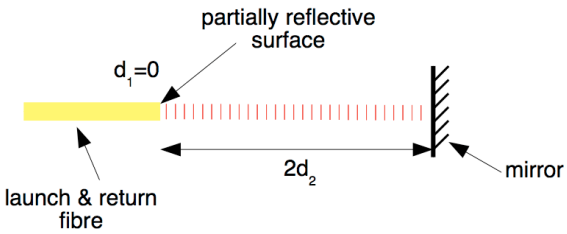

Figure 2.2: A schematic view of the LiCAS single path two beam interferometer geometry.

The process of Frequency Scanning Interferometric length measurement involves obtaining the phase advance within an interferometer during a laser frequency scan. The measurement method employed throughout this investigation involves the comparison of the phase advance in two or more interferometers. By feeding multiple interferometers simultaneously with light from a common source and defining one interferometer as a reference the length ratio of the two interferometers can be determined. For a reference interferometer with optical path difference L the phase of the detected reference signal is given by

$$\Phi = \left(\frac{2\pi}{c}\right)\nu L. \tag{2.8}$$

Likewise the phase of a second, measurement, interferometer of OPD D is given by

$$\Theta = \left(\frac{2\pi}{c}\right)\nu D. \tag{2.9}$$

Where in both cases ν is the optical frequency of the light fed into the interferometers and c is the speed of light.

If $\Delta\Phi$ and $\Delta\Theta$ are the phase advances induced in the reference interferometer and measurement interferometer respectively by tuning through a frequency interval of $\Delta\nu$. Then the ratio of the OPDs of the interferometers, q, is given by the ratio of the phase advances

$$q = \frac{\Delta\Phi}{\Delta\Theta} = \frac{L}{D}. \tag{2.10}$$

This holds under the assumptions that both interferometers have fixed OPDs throughout the laser scan and that there is no dispersion introduced within either interferometer. The second assumption can be achieved by placing both interferometers inside a vacuum. Hence, if the OPD of the reference interferometer is known prior to the laser scan then the OPD of the measurement interferometer can be obtained straightforwardly by calculating the phase ratio of the two interferometers.

This technique has many advantages. There is no requirement for any knowledge of measurement interferometer OPD prior to the scan taking place. The absolute phase of either of the interferometers does not enter into the calculations, only the phase advance (the relative phase change) of each during the laser scan is required. Also, the dynamic range is extremely large, and is in principle only restricted by the coherence length of the

tuneable laser source[2]. However, in practice limited knowledge of the measurement length is required so that the interferometric signal can be fully characterised during acquisition and digitisation, see sections 2.4 and 3.4.

Interferometer Drift

These arguments on the effects of interferometric drift during a laser scan were first made by Coe [44] and are re-expressed here. If the OPD of the reference interferometer drifts by ΔL, whilst the laser scans through the tuning interval $\Delta\nu$, then the phase advance is instead given by equation 2.11.

$$\Delta\Phi = \left(\frac{2\pi}{c}\right)(L\Delta\nu + \langle\nu\rangle\Delta L + \Delta\nu\Delta L) \tag{2.11}$$

The first part of the second bracketed term is the *intended* phase shift due to the applied change in laser output frequency (where in this case L is the scan average OPD). The second part of the second bracketed term is the *unwanted* phase shift due to interferometer OPD drift (where $\langle\nu\rangle$ is the scan average laser output frequency).

If the tuning interval is large enough such that

$$\left|\frac{\Delta\nu}{\langle\nu\rangle}\right| > \left|\frac{\Delta L}{L}\right| \tag{2.12}$$

then the phase shift terms in equation 2.11 descend in the order

$$|L\Delta\nu| > |\langle\nu\rangle\Delta L| > |\Delta\nu\Delta L|\,. \tag{2.13}$$

Similarly, if the measurement interferometer OPD drifts by ΔD during the same laser scan then the phase advance is given by equation 2.14.

$$\Delta\Theta = \left(\frac{2\pi}{c}\right)(D\Delta\nu + \langle\nu\rangle\Delta D + \Delta\nu\Delta D) \tag{2.14}$$

As with the reference interferometer phase advance the first two parts of the second bracketed term related to the *intended* and *unwanted* phase advances respectively. Also, as above, if

$$\left|\frac{\Delta\nu}{\langle\nu\rangle}\right| > \left|\frac{\Delta D}{D}\right| \tag{2.15}$$

then the phase shift terms in equation 2.14 again descend in the order

$$|D\Delta\nu| > |\langle\nu\rangle\Delta D| > |\Delta\nu\Delta D|\,. \tag{2.16}$$

For the purposes of explaining the error due to interferometer drift the $\Delta\nu\Delta L$ and $\Delta\nu\Delta D$ terms will be neglected here, since

$$\left|\frac{\Delta\nu}{\langle\nu\rangle}\right| \ll 1 \quad \& \quad \left|\frac{\Delta L}{L}\right| \ll 1 \quad \& \quad \left|\frac{\Delta D}{D}\right| \ll 1 \tag{2.17}$$

[2]Typically the coherence length of modern tuneable laser source can be several kilometres.

which is the case in all examples presented in this study[3]. The measured phase ratio is therefore given by

$$q = \frac{\Delta\Phi}{\Delta\Theta} = \frac{\left(\frac{2\pi}{c}\right)\left[L\Delta\nu + \langle\nu\rangle\Delta L\right]}{\left(\frac{2\pi}{c}\right)\left[D\Delta\nu + \langle\nu\rangle\Delta D\right]} \tag{2.18}$$

cancelling the common $\left(\frac{2\pi}{c}\right)$ terms and dividing numerator and denominator by $\Delta\nu$ this becomes

$$q = \frac{L + \left(\frac{\langle\nu\rangle}{\Delta\nu}\right)\Delta L}{D + \left(\frac{\langle\nu\rangle}{\Delta\nu}\right)\Delta D} = \frac{L\left[1 + \left(\frac{\langle\nu\rangle}{\Delta\nu}\right)\left(\frac{\Delta L}{L}\right)\right]}{D\left[1 + \left(\frac{\langle\nu\rangle}{\Delta\nu}\right)\left(\frac{\Delta D}{D}\right)\right]}. \tag{2.19}$$

This can be simplified using the approximation

$$\left(\frac{1+a}{1+b}\right) \approx 1 + a - b \tag{2.20}$$

providing $a, b \ll 1$. Neglecting all terms beyond first order this gives

$$q = \left(\frac{L}{D}(1 + \Omega\epsilon)\right) \tag{2.21}$$

where

$$\Omega = \frac{\langle\nu\rangle}{\Delta\nu} \tag{2.22}$$

and

$$\epsilon = \frac{\Delta L}{L} - \frac{\Delta D}{D}. \tag{2.23}$$

Hence a relative interferometer drift ϵ leads to an error in the apparent OPD ratio which is magnified by the factor Ω. For the LiCAS FSI systems a factor of $\Omega \approx 50$ is typical. This corresponds to an actual change in interferometer OPD of approximately $20nm$ during a laser scan producing a $1\mu m$ systematic error in the determined OPD.

2.2.2 The FSI Implementations

The two FSI measurement systems within the RTRS have significantly different distance and acceptance requirements. Thus the implementation specifics of each have been developed independently with decisions made corresponding to the different system priorities.

The External FSI System

The external FSI system uses 6 measurement interferometers to determine the distances to a retroreflector markers positioned on the accelerator tunnel wall. These measurements are subsequently combined to reconstruct the marker positions in 3D space with two-fold redundancy. The 6 external FSI measurement interferometers are shown as red lines in figure

[3] If instead $\left|\frac{\Delta\nu}{\langle\nu\rangle}\right|$ were to approach unity, the drift error would diminish and the presence or absence of the second order terms becomes irrelevant. The second order terms would only be significant if the corresponding conditions, given by equation 2.12 or equation 2.15, were not satisfied.

1.19. The nominal geometric distance between an interferometer launch and a tunnel wall is $450mm$. Due to the tunnel construction tolerances the retroreflector markers may only be positioned with a tolerance of $\pm 25mm$ in any direction of the ideal measurement position for a car at any train stop. Hence the external FSI system must be capable of accurately measuring the position of the markers anywhere inside a relatively large volume. The radius of the patrol field of the beam must be $\geq 33.2mm$ at $450mm$, this is illustrated in figure 2.3.

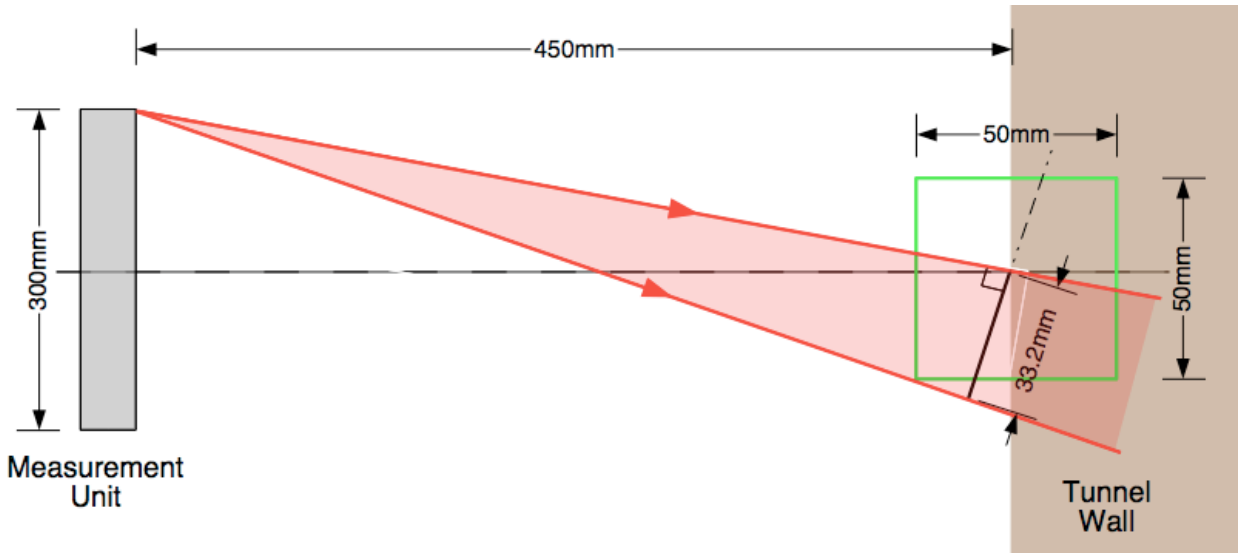

Figure 2.3: Diagram showing the patrol region in which the external FSI system must be able to make length measurements. Not to scale.

It is clear that using a simple, fully collimated solution in this case would be an extremely complex optical challenge. The lenses would need to be around $80mm$ in diameter meaning that vibration and thermal stabilisation would be difficult to achieve at the required level. Even if such a lens could be operated in an ideal environment aberrations would still limit the measurement accuracy of the interferometers. Many other solutions were considered including: a smaller diameter lens producing a divergent beam; a parabolic mirror providing a fully collimated beam; a zone plate to illuminate the patrol region via beam diffraction; and rotatable wedges to allow a small collimated beam to be steered.

Zemax [45] simulations of a system consisting of a smaller lens, approximately $25mm$ in diameter, with a fibre launch displaced from the focal point, thus illuminating the patrol field with a divergent beam, were carried out by R. Bingham [46]. The fraction of interferometer long arm returned light coupled back into the optical fibre, when the retroreflector was at the edge of the patrol region, using such a system was calculated to be 6.5×10^{-9} as compared to the peak value of 1.1×10^{-9} from a bare fibre launch with no lens [47]. The simulated fractional return power for the bare fibre launch solution is shown in figure 2.4 as a function of interferometer OPD and in figure 2.5 as a function of transverse retroreflector displacement.

Since these simulations indicated that a standard lens system producing a divergent beam would only provide a factor of ~ 6 increase in long arm recoupled power the external FSI system design was finalised with the inclusion of bare fibre launches. This would simplify

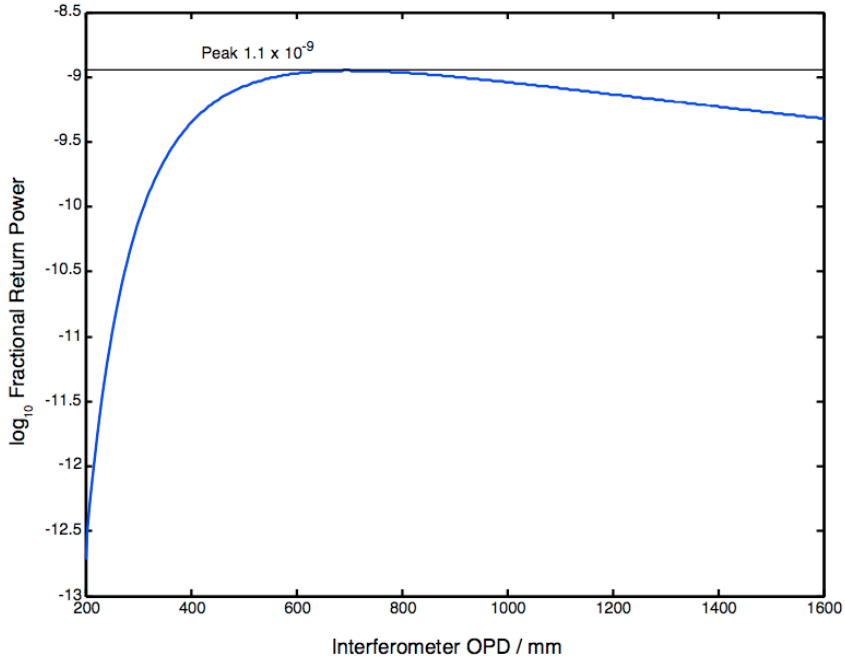

Figure 2.4: Simulated returned power fraction for a bare fibre launch as a function of interferometer OPD (which corresponds to twice the length shown in figure 2.3). The retroreflector was simulated to be maximally displaced ($33.2mm$) from the interferometer launch axis [47].

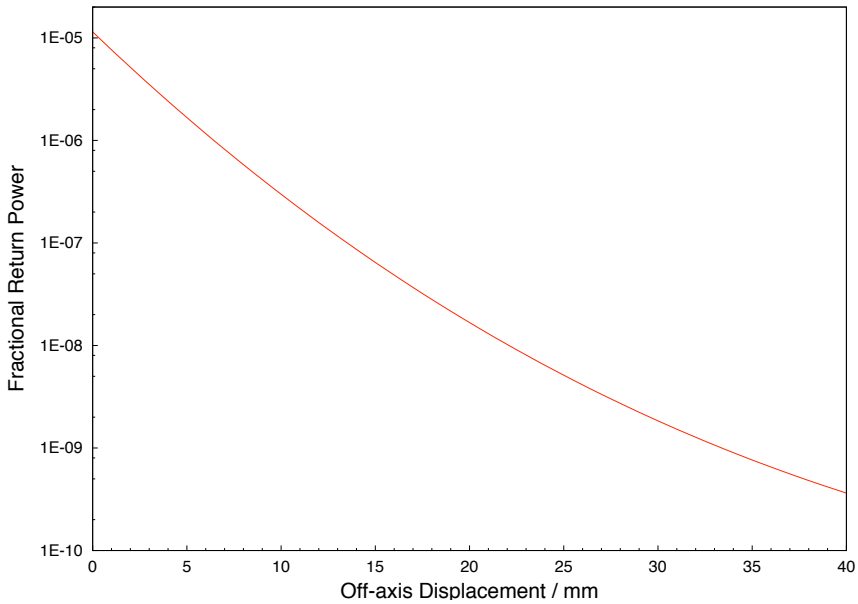

Figure 2.5: Simulated returned power fraction for a bare fibre launch as a function of transverse retroreflector displacement.

the optics system considerably however greater effort needed to be spent developing high gain, low noise photo detection electronics and an analysis technique capable of accurately determining interferometer OPDs from very low quality signals.

An illustration of the retroreflectors proposed as wall markers for the external FSI system is shown in figure 2.6. These markers are standard surveying corner-cube retroreflectors mounted into 1.5 inch spheres. They will also serve as markers for other surveying systems within the accelerator tunnel.

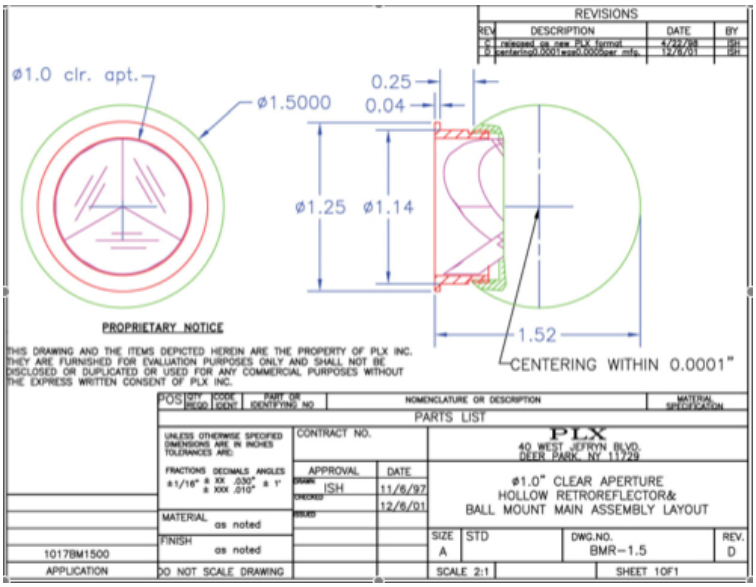

Figure 2.6: Technical drawing of the PLX 1.5 inch sphere mounted corner-cube retroreflectors proposed as survey markers in the ILC tunnel [48].

Both the defocused lens and the bare fibre launch solutions are susceptible to retroreflector defects. In the geometric optics approximation only the ray that travels from the fibre launch to the vertex of the retroreflector is returned and recoupled into the fibre. Rays that strike elsewhere within the acceptance region are displaced and do not return into the fibre. Hence, in the case of non-collimated light, the size of the retroreflector (i.e. the acceptance) has no effect on returned power. Therefore, within this approximation, if the retroreflector has a defect at the vertex no light is recoupled and we must rely on diffraction effects to produce a signal. If d is the defect diameter and L is the distance from the virtual fibre image to the retroreflector the approximate condition to ensure operation within the far-field regime (i.e the beam spread due to diffraction exceeds the diameter of the defect) is given by

$$d < \sqrt{L\lambda} \tag{2.24}$$

where λ is the wavelength of the incident light [42].

For a defocused single lens external FSI line, with a lens of focal length of $100mm$ and an aperture of $25mm$, with a fibre displaced from the focal point by $20mm$ the virtual fibre image to retroreflector separation is around $1400mm$. Hence the maximum tolerable defect size at the vertex is around $1.5mm$ (assuming $\lambda = 1550nm$). For a bare fibre launch with $L \approx 500mm$ the maximum tolerable defect size is around $0.9mm$. The use of non-collimated

light effectively places a lower limit on the length of an FSI interferometer for which an acceptable return signal can be produced for a given defect size.

Preliminary laboratory studies using bare fibre interferometers suggest that a minimum launch-to-retroreflector separation of around $200mm$ is required for the losses due to defects at the vertex not to be dominant [49]. At this distance defects of approximately $0.5mm$ contribute to the loss of return power.

The Internal FSI System

The internal FSI system consists of 6 interferometer launches on one car which measure the distance to 6 retroreflectors positioned on an adjacent car. These interferometers are housed within the vacuum tube that passes between the cars which also contains the LSM beams. The internal FSI measurement interferometers are shown as red lines between the two cars in figure 1.19. The nominal separation of the centres of the cars is $4.5m$.

To provide the long arm return power needed to make measurements over $4.5m$ a single lens collimation system is employed. This solution is acceptable in this case since the requirements for illumination area are much smaller than in the external FSI system. Using a single lens to fully collimate the beam serves dual purposes: light is concentrated onto the retroreflector and so more light is returned towards the launch; and the lens effectively increases the collection area of the returned light that will be coupled back into the fibre.

The fully collimated internal FSI interferometers typically produced a long arm fractional return power of around 10^{-3} during the laboratory investigations. The internal FSI system uses 0.5 inch sphere mounted corner-cube retroreflectors which are similar in specification to those in the external FSI system, see figure 2.6, but $1/3^{rd}$ of the size [50]. The problems of retroreflector defects are less serious in the internal FSI system because of the use of collimated beams and the longer path lengths. Similarly defects in the collimation lens within the internal FSI system would have to be very large to cause serious problems.

2.3 Laboratory Equipment

The laboratory equipment described in this section was used to undertake proof-of-concept investigations and to develop the system hardware and techniques required for the FSI measurement system within the prototype RTRS. The details of the aims of each investigation and the specifics of equipment configurations are given in Chapter 5.

An overview of the laboratory FSI system is presented in figure 2.7. The optical fibre connections are represented as yellow lines with the 50Ω (BNC) connections, used to transfer the acquired signals into the DAQ computer, and the GPIB connections, used to send control signals to the light sources, shown as blue and green lines respectively. Descriptions of the laser, EDFA, and optical fibres are given in sections 2.3.1, 2.3.2 and 2.3.3 respectively along with details of how these components were used. Sections 2.3.4 and 2.3.5 deal with the reference and measurement interferometers used within the laboratory FSI system.

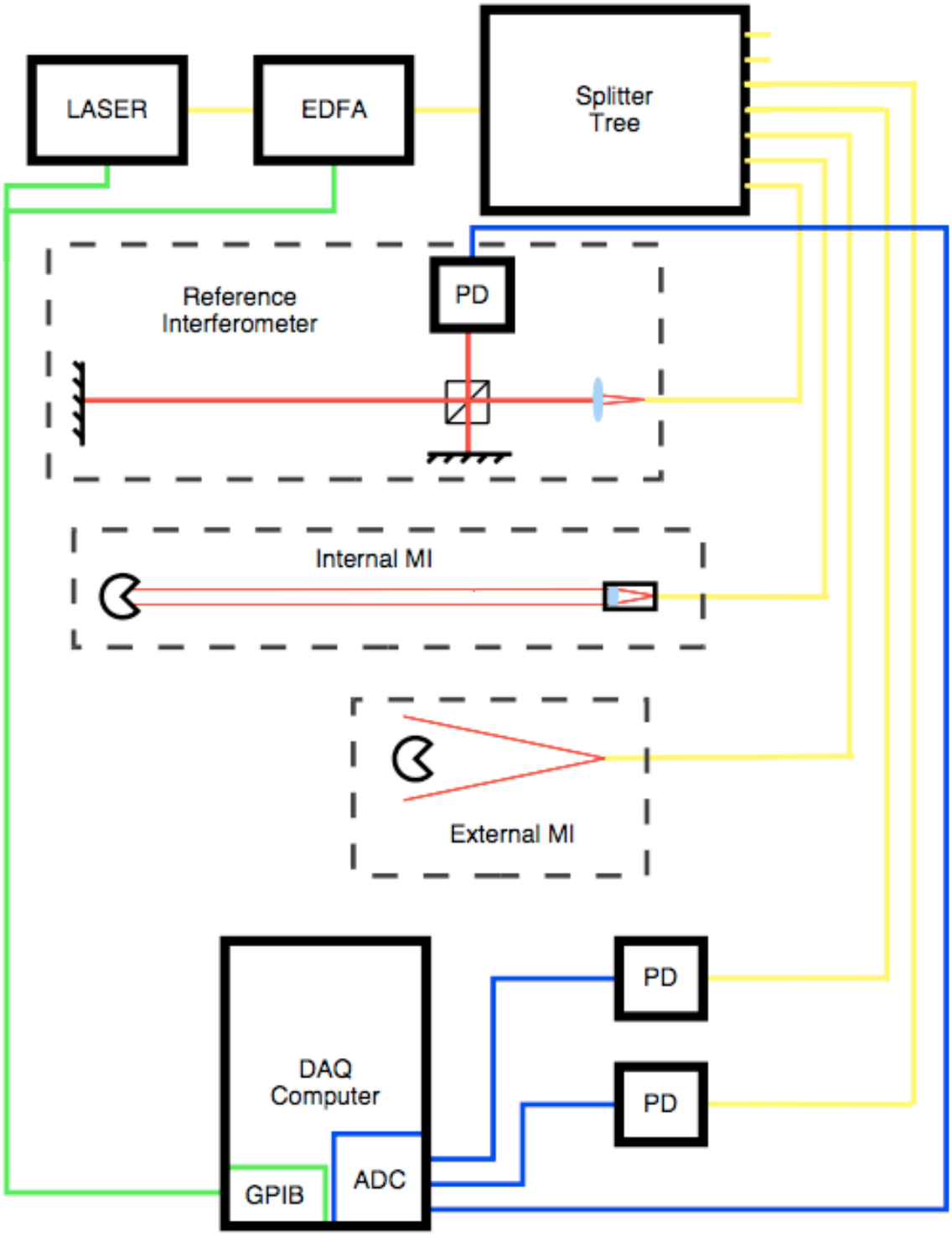

Figure 2.7: An overview of the laboratory FSI system. The yellow lines represent optical fibre connections with the blue and green lines corresponding to 50Ω (BNC) and GPIB connections respectively. The laser, EDFA, reference interferometer and measurements interferometers are described in sections 2.3.1, 2.3.2, 2.3.4 and 2.3.5 respectively. A description of the data acquisition procedure is given in section 2.4.

2.3.1 The Tuneable Laser

The laser used in the laboratory FSI systems was an Agilent 81642A tunable laser module. This type of laser was developed for testing components in optical networks. Over the past decade the increase in requirements for high speed data transfer via dense wavelength division multiplexing has drastically reduced the cost of tunable laser technology. The increased availability and relatively low cost of telecommunications technology was the main driver for the wavelength band choice for the FSI systems. Other technological advances at these wavelengths have also been employed and are described in section 2.3.2.

The tunable laser module was capable of producing light in the range $1510nm$ to $1640nm$, and could be tuned mode-hop free over a wavelength band of $50nm$ within this range. However the normal mode of operation throughout these investigations was to work in the telecoms C-band tuning from $1535nm$ to $1565nm$. This represented an optical frequency change of $3.75THz$ ($195.30THz$ to $191.55THz$). The maximum tuning speed was $40nm/s$ ($5THz/s$) allowing a scan to be completed in around $0.75s$. The large frequency change and high tuning speed significantly reduced the adverse effects of interferometer drift during a scan. The Ω factor, from equation 2.22, for a nominal laser scan was 51.6. Thus a real interferometer OPD change of approximately $19.4nm$ was required during a scan to produce an error in a determined OPD of around $1\mu m$. This corresponds to a rate of change of temperature of approximately $580\mu K/s$, assuming a coefficient of thermal expansion of $10ppm/K$ (i.e. steel) and an interferometer length of $5m$. This is far greater than the rate of change of temperature expected either in the laboratory or within any part of the accelerator tunnel which are expected to be no larger than $150\mu K/s$.

Some interferometric drift did result from the fact that the refractive index of the the transmission medium varied with wavelength. The refractive index of air is around $25ppb$ different for the end point wavelengths of a nominal laser scan. The drift errors resulting from this variation are given in table 2.1. The systematic error refers to the total drift resulting from the variation in refractive index due to the wavelength change during a nominal scan. The scan-to-scan variation relates to variation in drift resulting from the uncertainties in absolute wavelength of the end points of each scan. This systematic error can be completely eliminated by placing the interferometers inside a vacuum.

OPD / m	**Systematic Error** / μm	**Scan-to-Scan Variation** / nm
1.0	1.290	0.6
4.7	6.037	2.9
9.0	11.610	5.6

Table 2.1: Estimated drift errors resulting from the variation in the refractive index of air as a result of wavelength change during a nominal laser scan.

The relevant specifications of the Agilent 81642A tuneable laser source are given in table 2.2. The tunable laser module produced light of varying wavelength by modifying the laser cavity size during a scan. Ideally this would provide a linear change in frequency with respect to time. However the mechanism employed to control the rate of change of cavity

size produced an additional sinusoidal variation in the laser frequency output as a function of time. The extracted variation in output frequency during a nominal laser scan is shown in figure 2.8 with the corresponding rate of change of laser output frequency[4] shown in figure 2.9.

Parameter	Value	Notes
Wavelength Range / nm	1510 to 1640	-
Wavelength Resolution / pm	0.1	$12.5MHz$ @ $1550nm$
Absolute Wavelength Accuracy / nm	± 0.015	-
Relative Wavelength Accuracy / pm	± 7	typically ± 3
Wavelength Repeatability / pm	± 1	typically ± 0.5
Wavelength Stability / pm	$< \pm 1$	typical, 24hrs at const. temp.
Tuning Speed / nm/s	0.5/5/10/20/40	-
Linewidth / kHz Effective Linewidth / MHz	100 > 50	typical, coherence control off typical, coherence control on
Output Power / mW	≥ 5 ≥ 2 ≥ 0.2	peak, typical 1530 to $1610nm$ 1510 to $1640nm$
Power Stability / dB Power Stability / dB	± 0.01 ± 0.03	1 hour typical, 24hrs
Power Repeatability / dB	± 0.01	typical
Power Linearity / dB	± 0.3	typical
Signal to Spontaneous Emission / dB	≥ 27	typical, 1530 to $1610nm$
Relative Intensity Noise / dB/Hz	-0.01	typical, 1530 to $1610nm$

Table 2.2: The specifications of Aglient 81642A tuneable laser source used in the laboratory FSI system [51].

From figures 2.8 and 2.9 it is clear that the global laser output frequency variation was approximately linear in time. A linear fit to the extracted laser tuning curve produced a frequency change rate of $5.17744 \pm 2.6 \times 10^{-5} THz/s$, the RMS of the residuals to this fit were $3.8GHz$ ($\sim 20ppm$). A further quadratic fit produces a global rate of change of frequency of $4.99587 \pm 3.1 \times 10^{-5} THz/s$ with RMS of the residuals being $640MHz$ ($\sim 3ppm$). The residuals to both fits are shown in figure 2.10. Further investigation of the extracted laser tuning curve on smaller time scales revealed the effect of the mechanism used to control the tuning rate. Periodic variations in the output frequency with amplitude of around $250MHz$ can be seen with a frequency of around $1.6kHz$. These variations are illustrated in figure 2.10c. These oscillations in extracted tuning rate correspond to the observed variations in the rate of change of frequency of around $3THz/s$ with a period of around $625\mu s$. While the large scale patterns, due to the laser not tuning linearly in frequency with respect to time, seen in figures 2.10a and 2.10b were broadly reproducible from scan to scan whilst the small scale patterns, caused by the feedback mechanism, seen in figure 2.10c were not reproducible.

[4]The rate of change of frequency was determined by the ratio $\frac{\Delta\nu}{\Delta t}$ for neighbouring points and therefore is susceptible to noise within the acquired signal.

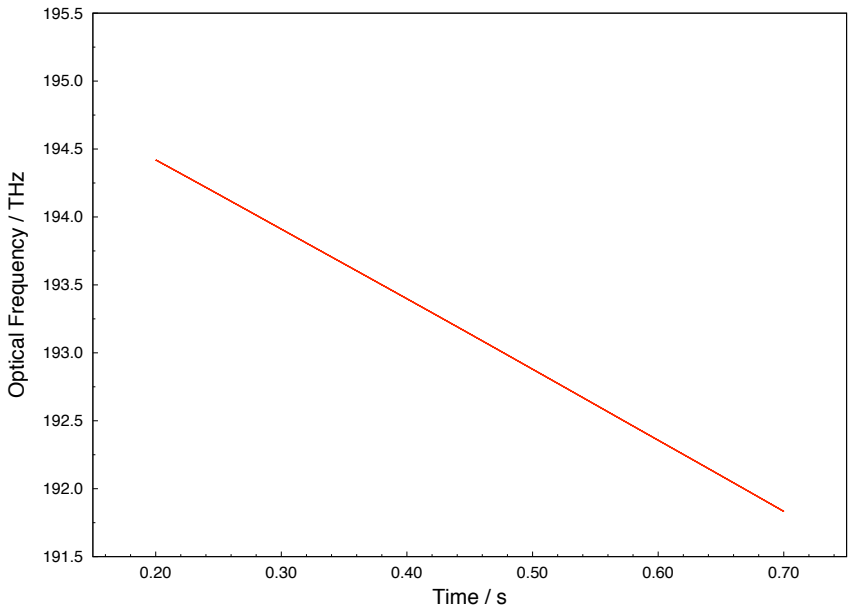

(a) The variation of laser output frequency extracted from the measured phase advance in the Michelson Reference Interferometer during a nominal laser scan.

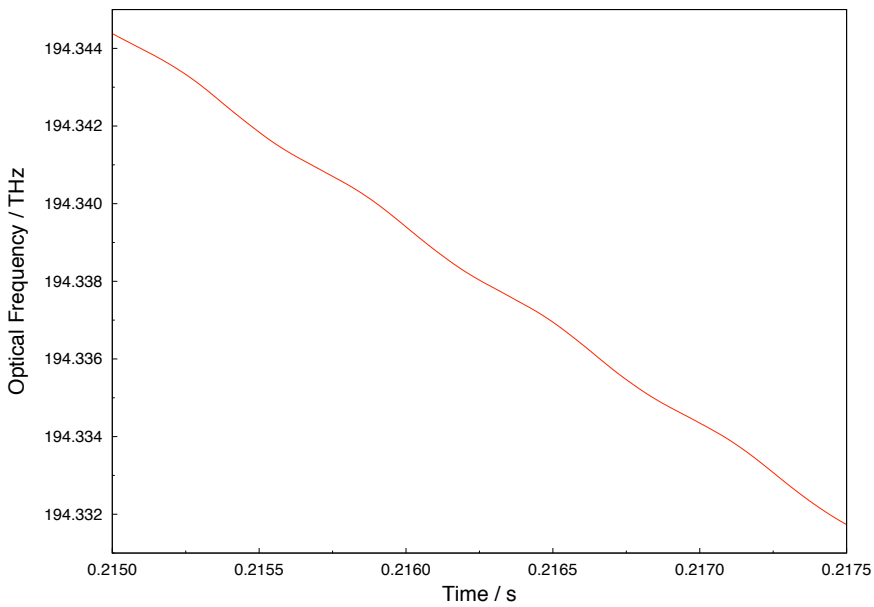

(b) A zoom section showing the oscillations of the output laser frequency.

Figure 2.8: The laser output frequency variations during a nominal laser scan with a zoom showing the oscillations of the output laser frequency.

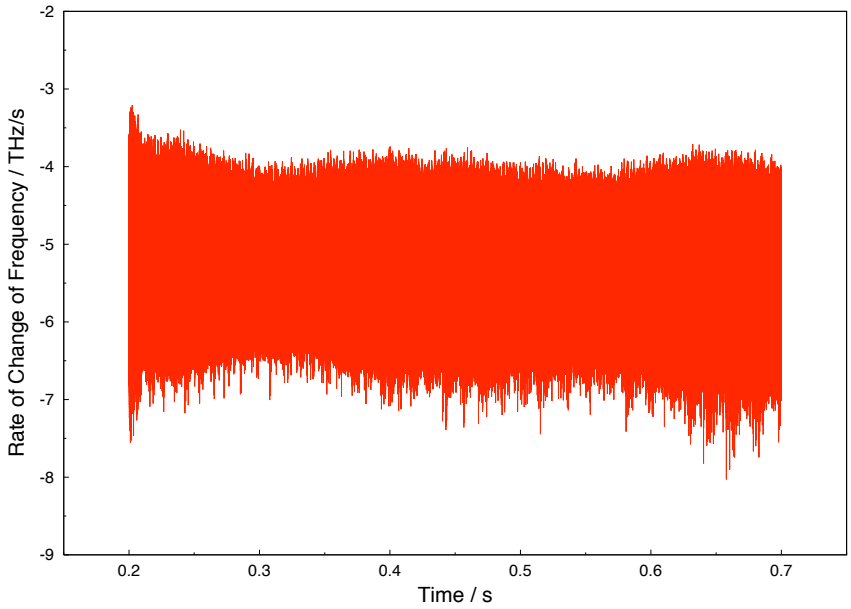

(a) The extracted rate of change of the laser output frequency during a nominal laser scan.

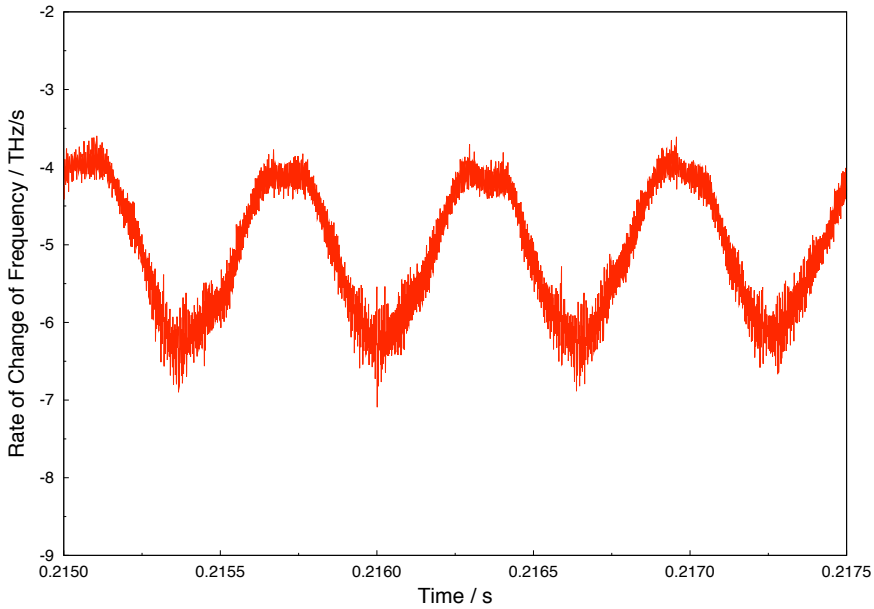

(b) A zoom section showing the oscillation of the rate of change of output laser frequency.

Figure 2.9: The rate of change of the laser output frequency during a nominal laser scan with a zoom showing the oscillation of the rate of change of output laser frequency.

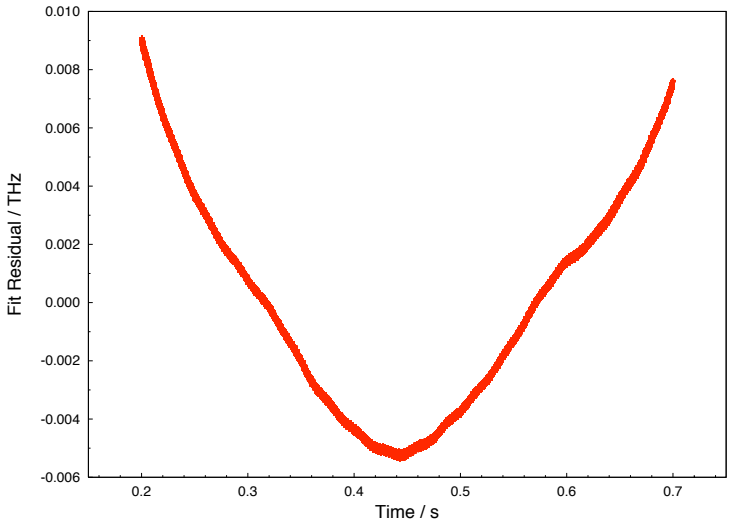

(a) The residuals from a linear fit.

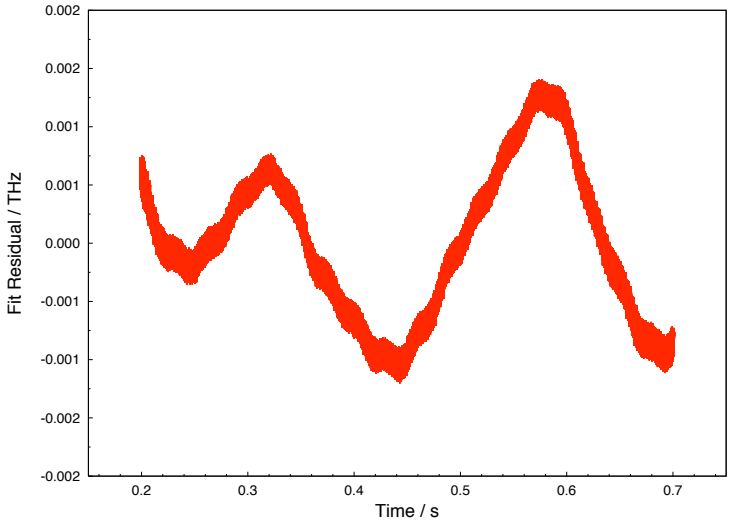

(b) The residuals from a quadratic fit.

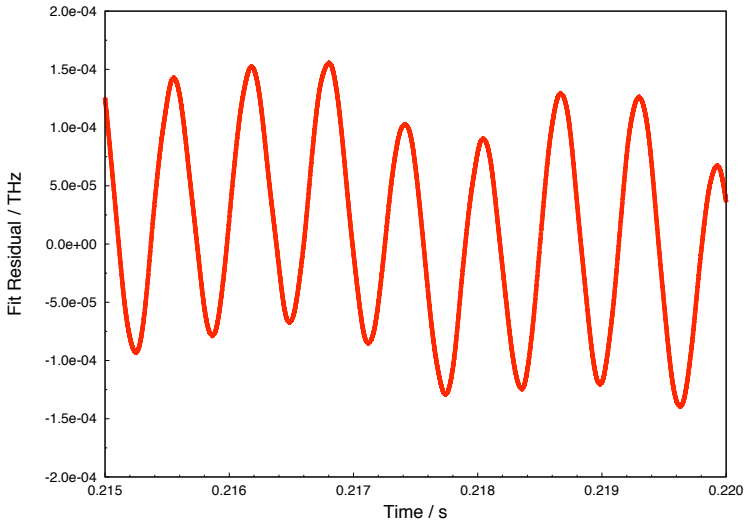

(c) A zoom of a section illustrating the oscillations in laser output frequency.

Figure 2.10: The residuals of a linear and a quadratic fit to the extracted laser output frequency as a function of time for a nominal laser scan. A zoom section is also shown to illustrate the output frequency oscillations

To analyse the tunable laser source noise response with respect to frequency during a nominal laser scan the output of the laser was passed directly into an AC coupled photodetection unit. The detection system had an input frequency range of $1.5kHz$ to $1MHz$ and the signal was digitised at a rate of $2MHz$. The resultant acquired data was transformed using a standard Discrete Fourier Transform (DFT) method. The spectrum of the output of the laser during a nominal scan is shown in figure 2.11.

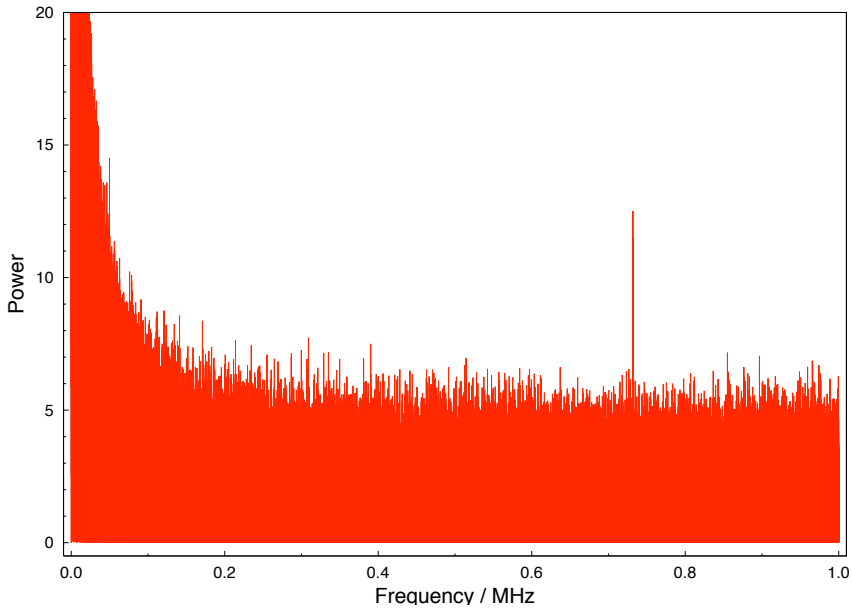

Figure 2.11: The extracted spectrum from a directly digitised nominal laser scan.

The spectrum shows the expected peak at low frequency[5] but levels off and exhibits an approximately frequency independent response at frequencies greater than $100kHz$. The only noticeable feature at higher frequencies is a narrow peak at around $720kHz$ which corresponds to an interferometer OPD of around $43.2m$ and is significantly above the fringe rate of any interferometers used within the laboratory investigations.

2.3.2 The Erbium Doped Fibre Amplifier

An independent amplification stage was coupled to the output of the tuneable laser source which allowed the intensity of light launched into the interferometers to be measured and controlled. This Erbium Doped Fibre Amplifier (EDFA) provided scalability to the FSI system allowing multiple additional interferometers to be incorporated into the internal or external systems with minimal disruption.

When light in the wavelength range $1456nm$ to $1643nm$ passes through an optical fibre with a core doped with Erbium 3+ ions amplification can take place if the fibre is also 'pumped' with light of wavelength around $980nm$. The process works by exciting the $4f$ inner electrons of the Er^{3+} ions and stimulating their decay. The 'pump' photons of wavelength

[5]The low frequency peak is a result of an approximately constant DC offset within the acquired signal.

$980nm$ excite electrons out of the $^4I_{15/2}$ ground state[6] into the $^4I_{11/2}$ state which rapidly decay down into the metastable $^4I_{13/2}$ state which has a comparatively long lifetime of $14ms$. With enough applied pump power a population inversion can be produced. This population inversion is subsequently depleted by signal photons which stimulate the electrons to decay producing another identical photon [52]. The relevant energy level of Er^{3+} in silicate glass are shown in figure 2.12. Since the Erbium ions are placed in a glass environment the $^4I_{13/2}$ state is very broad[7] and so provides gain over a large frequency range. The typical gain curve of an Erbium doped fibre is shown in figure 2.13 with the telecoms C-band, in which the laboratory FSI systems operated, indicated.

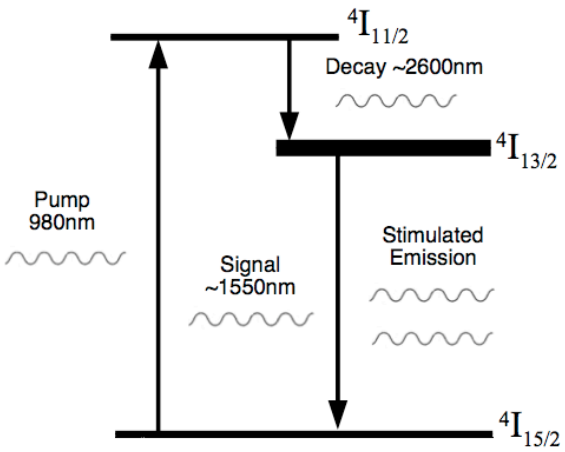

Figure 2.12: The Erbium 3+ ion energy levels, within silicate glass, relevant to the light amplification process at around $1550nm$.

EDFA Noise Production Mechanisms

There are a number of potential sources of noise present in the output of the optical amplification process. These are characterised by the Noise Figure, NF, which is defined in equation 2.25 in decibel units [53].

$$NF = 10\log_{10}(F) = 10\log_{10}\left(\frac{SNR_{in}}{SNR_{out}(\nu, f)}\right) \tag{2.25}$$

The noise factor, F, can be defined via measurable parameters by using Poisson statistics. The input SNR can be expressed in terms of the input signal photocurrent, i_{in}, and the variance of the received photocurrent noise, $\Delta^2 i_{noise}$.

The mean input signal photocurrent is given by

$$\langle i_{in} \rangle = \mathcal{R} P_{in} \tag{2.26}$$

[6]In standard spectroscopic notation states labelled I correspond to a principle quantum number of 7.
[7]The crystal structure of silicate glass broadens the spectral line of electron states of the Er^{3+} ions.

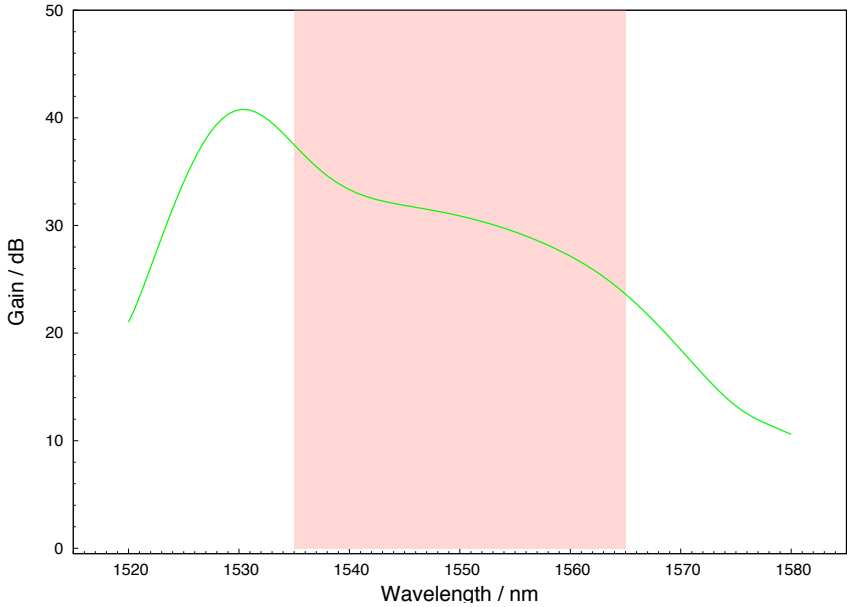

Figure 2.13: A typical gain curve of an Erbium doped fibre pumped at $980nm$ for low power inputs. The telecoms C-band in which the laboratory FSI system operated is indicated in red.

where $\mathcal{R}$ is the DC responsivity of the photodetector, given by equation 2.27 and P_{in} is the optical input power in W.

$$\mathcal{R} = \frac{\eta q}{h\nu} \tag{2.27}$$

where η is the photodetector quantum efficiency, q is the charge produced by the photodiode and $h\nu$ is the photon energy in J (i.e. ν is the optical frequency in Hz).

The variance of the received photocurrent noise is found by integrating the received intensity noise spectrum over the bandwidth of interest, equation 2.28.

$$\langle \Delta^2 i_{noise} \rangle = \mathcal{R}^2 \int_{B_e} S_P(f) df \tag{2.28}$$

where $S_P(f)$ is the power spectral density, in W^2/Hz, of the undesired power fluctuations accompanying the signal, B_e is the photodetector bandwidth in Hz, and f is the electrical baseband frequency in Hz. Since the SNR is defined in terms of power levels of the photocurrent it is a ratio of electrical rather than of optical power levels. Therefore the input SNR becomes

$$SNR_{in} = \frac{\langle i_{in} \rangle^2}{\langle \Delta^2 i_{noise} \rangle} = \frac{\mathcal{R}^2 P_{in}^2}{2q\mathcal{R}P_{in}B_e} = \frac{\eta P_{in}}{2h\nu B_e}. \tag{2.29}$$

The output SNR can be determined using the same relationship

$$SNR_{out} = \frac{\langle i_{out} \rangle^2}{\langle \Delta^2 i_{out} \rangle} \tag{2.30}$$

where

$$\langle i_{out} \rangle = \mathcal{R}GP_{in} \tag{2.31}$$

and

$$\langle \Delta^2 i_{out} \rangle = \mathcal{R}^2 B_e [S_e(\nu, f) + \eta^{-1} S_{shot}] \tag{2.32}$$

where G is the gain and $S_e(\nu, f)$ and S_{shot} are the spectral noise density contributions from *excess* and shot sources respectively in units of W^2/Hz.

Shot noise from the source laser will be amplified along with the signal. The shot-noise spectral density due to the signal power P_{in} is given by equation 2.33.

$$S_{shot} = 2h\nu G P_{in} \tag{2.33}$$

Spontaneous decays also occur from the $^4I_{13/2}$ state producing photons that do not correspond to a signal photon. These spontaneously emitted photons are then amplified by subsequent Er^{3+} ions producing *Amplified Spontaneous Emission* (ASE). The *signal-spontaneous* spectral noise density depends upon the product of the optical signal and the ASE spectral density, ρ_{ASE}. At baseband frequencies below $\sim 50GHz$ the signal-spontaneous noise density is given by equation 2.34. In this frequency regime signal-spontaneous noise in the dominant source of excess noise.

$$S_{sig-sp} = 4\rho_{ASE} G P_{in} \tag{2.34}$$

Therefore the output SNR becomes

$$SNR_{out} = \frac{\langle i_{out} \rangle^2}{\langle \Delta^2 i_{out} \rangle} = \frac{\mathcal{R}^2 G^2 P_{in}^2}{\mathcal{R}^2 B_e [S_e(\nu, f) + \eta^{-1} S_{shot}]} = \frac{G P_{in}}{2B_e [2\rho_{ASE} + \eta^{-1} h\nu]}. \tag{2.35}$$

Hence the ratio of the SNRs is given by

$$F = \frac{SNR_{in}}{SNR_{out}} = \frac{\frac{\eta P_{in}}{2h\nu B_e}}{\frac{G P_{in}}{2B_e[2\rho_{ASE} + \eta^{-1} h\nu]}} = \frac{2\eta\rho_{ASE}}{Gh\nu} + \frac{1}{G}. \tag{2.36}$$

Which leads to the noise figure

$$NF = 10 \log_{10} \left(\frac{2\eta\rho_{ASE}}{Gh\nu} + \frac{1}{G} \right). \tag{2.37}$$

The form of the noise figure given in equation 2.37 provides information on the optimum mode of operation of the EDFA. Unlike many other types of amplification device the relative amount of noise produced during this type of optical amplification process scales inversely with the gain. Since the population inversion must become depleted by either stimulated or spontaneous photon emission a higher gain will reduce the number spontaneous emissions and so reduce the noise. The EDFA in the laboratory FSI system was provided with a minimal power input of around $-2dBm$ from the tuneable laser producing an output power of $18dBm$ therefore it operated at close to maximum gain[8].

The specifications of the Keopsys KPS-BT-C-21-Bo-FA EDFA used in the laboratory FSI system are given in table 2.3. An analysis of the frequency dependance of the light passed

[8]The dBm unit refers to an absolute decibel scale with $0dBm$ referenced to $1mW$.

into the interferometers was undertaken by acquiring the output of the EDFA with an AC coupled photodetector. The detection system had an input frequency range of $1.5kHz$ to $1MHz$ and the signal was digitised at $2MHz$. The acquired data set was transformed using a DFT in the same way as the laser output. The EDFA output spectrum, which is actually the combined output of the laser and the EDFA, for a nominal laser scan is shown in figure 2.14 with the ranges of the two FSI implementations indicated.

Parameter	Value	Notes
Wavelength Range / nm	1535 to 1565	-
Saturated Output Power / dBm	21	$P_{in} = 0dBm$
Optical Input Power / dBm	-3 to 3	-
Noise Figure / dB	< 7	$P_{in} = -3dBm@1550nm$
Small Signal Gain / dB	> 30	$P_{in} = -30dBm@1550nm$
Gain Variation / dB	< 1.5	$P_{in} = 0dBm$
Polarisation Dependent Gain / dB	< 0.5	-
Polarisation Mode Dispersion / ps	< 1	-
Optical Isolation / dB	> 30	-
Return Loss / dB	> -40	-

Table 2.3: The specifications of the Keopsys KPS-BT-C-21-Bo-FA EDFA used in the laboratory FSI system [54].

The EDFA output spectrum shows a similar noise response to the laser spectrum at low frequency and appears very similar at frequencies less than $300kHz$. Peaks that do not appear in the laser spectrum can be seen at $290kHz$, $320kHz$, $490kHz$, $520kHz$, $570kHz$ and $820kHz$ which correspond to OPDs of approximately $17.4m$, $19.2m$, $29.4m$, $31.2m$, $34.2m$ and $49.2m$ respectively. These peaks all fall well outside the measurement range of the FSI systems. The peak at $720kHz$ that is present in the laser spectrum has increased in height but remains very narrow. However apart from these narrow peaks the flat noise response is maintained up to the Nyquist frequency of $1MHz$. The implications of the relatively large noise level in the frequency region of the external system, indicated in green in figure 2.14, are discussed in Chapter 3. The spectral form of the combined output of the laser and EDFA was reproducible however it is most likely that the features seen result from the specific hardware used. Therefore any other laser modules or amplification stages will require further spectral investigation.

2.3.3 Optical Fibres

The optical fibres used throughout the laboratory FSI systems were Corning SMF-28 [55]. These fibres are a telecommunications industry standard and are mass produced consistently to an extremely high standard. The connections between fibres within the distribution system were either fusion spliced, as within the splitter trees, or butted faces filled with index matching gel. All fibres were terminated with angle polished connectors (APC) which

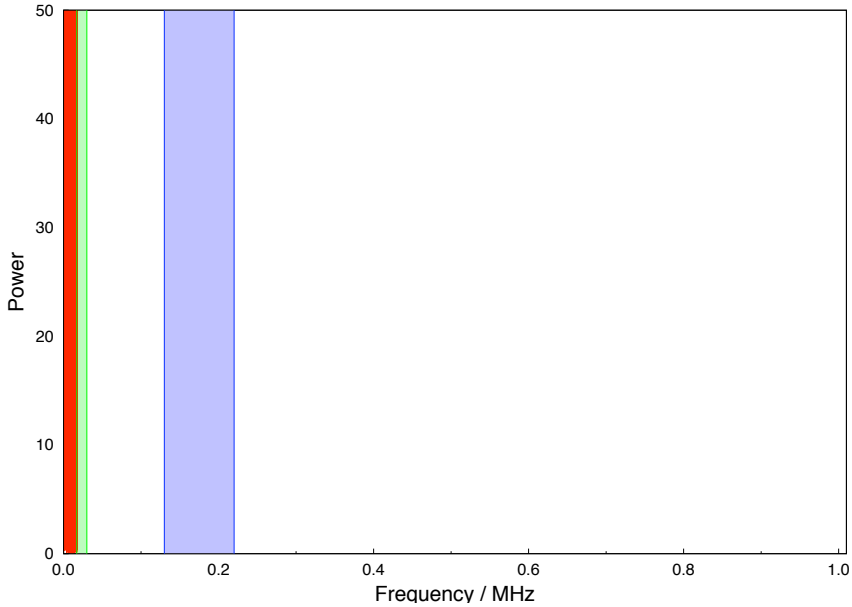

Figure 2.14: The extracted spectrum of a directly digitised EDFA output. The external and internal fringe frequency regions are indicated in green and blue respectively.

significantly reduced the effects of reflections at the fibre terminations[9]. Table 2.4 gives the specifications of the Corning SMF-28 optical fibre used within the laboratory FSI system.

Parameter	**Value**
Attenuation @ $1550nm$ / dB/km	≤ 0.22
Mode Field Diameter @ $1550nm$ / μm	10.4 ± 0.8
Zero Dispersion Wavelength / nm	1302 to 1322 to 1313 (typical)
Zero Dispersion Slope / $ps/(nm^2km)$	≤ 0.092 to 0.086 (typical)
Polarisation Mode Dispersion / $ps/\sqrt{km}$	0.2
Operating Temperature / °C	-60 to $+85$
Temperature Induced Attenuation / dB/K	≤ 0.05
Numerical Aperture	0.14
Effective Group Refractive Index @ $1550nm$	1.4682
Refractive Index Difference	0.36% (typical)

Table 2.4: The specifications and characteristics of the Corning SMF-28 optical fibre used in the laboratory FSI system [55].

When the fibres are used to launch light into free space they produce a Gaussian illumination field. The intensity with respect to angle is determined by the Numerical Aperture (NA) which is defined in equation 2.38.

$$NA = n_i \sin \theta_{max} \tag{2.38}$$

[9]By polishing the termination at 8° from the perpendicular the reflections produced at the polished face are not coupled back into the fibre.

where n_i is the refractive index of the incident medium and θ_{max} is the half angle measured to the point where the intensity has fallen to $1/e^2$, see figure 2.15.

Light was launched into the interferometers from the delivery fibre termination. Each fibre launch was either a straight polished connector (SPC) or an angle polished connector. The short arm interferometric reflection was provided either by the fibre termination itself or by an additional reflective surface. When an APC launch is used Snell's Law dictates that the illumination field is not centred on the axis of the fibre core since this is no longer normal to the polished face. The effect of using an APC terminated fibre to launch light into air is also illustrated in figure 2.15.

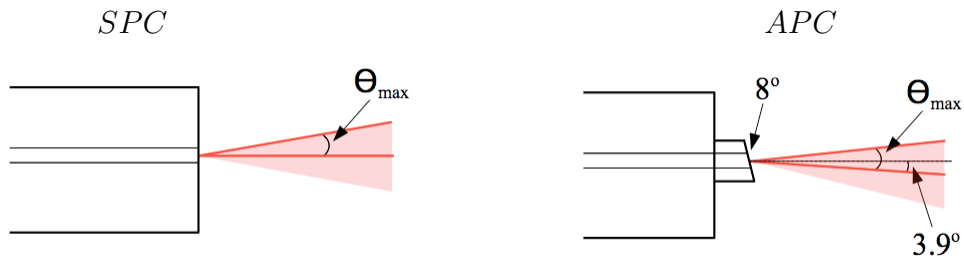

Figure 2.15: An illustration of the light cones produced by launching from SPC and APC fibre terminations.

2.3.4 Reference Interferometers

In the laboratory a Michelson style geometry was used for the purposes of a reference interferometer. The set-up was very similar to the interferometer used in the Michelson-Morley experiment with two arms at right angles to each other [56]. In the case of the Michelson Reference Interferometer used throughout the following investigations both the OPD and frequency variation rate were maximised to produce the highest possible fringe frequency. A schematic representation of the Michelson Reference Interferometer used in the laboratory is shown in figure 2.16.

The choice of a Michelson style interferometer as the primary reference interferometer was mainly due to the extremely clean interference signal that could be achieved. The fact that the photodetector acquired the signal from within the interferometer, rather than the light being recoupled into a fibre, meant that only interference fringes relating to the two interferometer arms were acquired. This was a necessary requirement for any signal that was to undergo phase analysis of the type described in section 3.3 since the phase extraction algorithm could be adversely affected by superpositions of sinusoids with differing frequencies. One of the major drawbacks of using such a configuration was the difficulty in thermal stabilisation. Since the two arms were perpendicular any thermal gradients present within the material onto which the mirrors were mounted would induce variations in interferometer OPD. Rather than applying a complicated stabilisation system for the initial laboratory tests post-analysis corrections were made using the temperature measurements taken of the optical table on which the interferometer was situated.

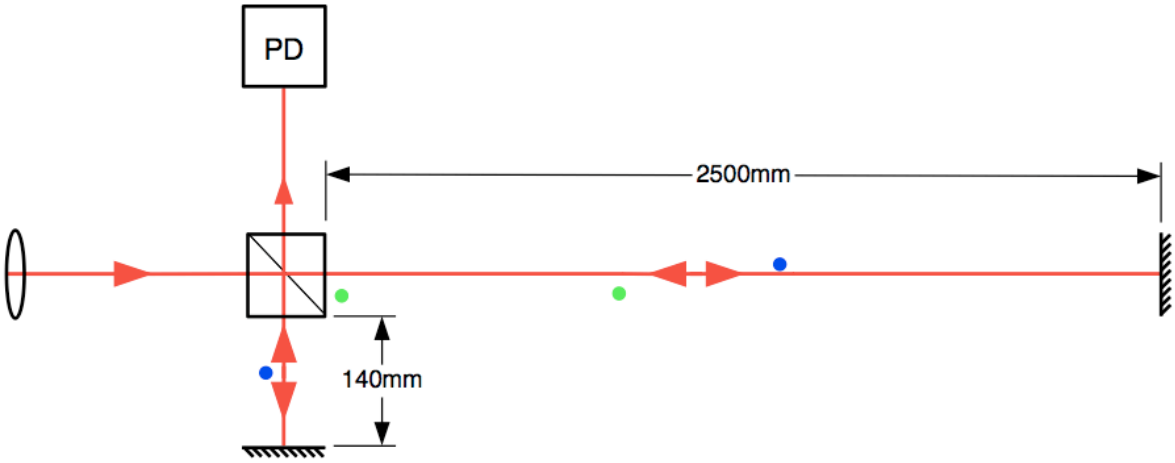

Figure 2.16: A schematic representation of the Michelson Reference Interferometer used in the laboratory FSI system. The blue and green circles indicate the approximate positions of the surface and air temperature sensors respectively. Not to scale.

A second interferometer, the Short Reference Interferometer (SRI), was designed to serve as an independent reference length. This interferometer had the same basic geometry as the measurement interferometers, describe in section 2.3.5. The design incorporated a temperature compensation mechanism which reduced the effects of temperature induced OPD variations. This was achieved by mounting the retroreflector on a rod which would thermally expand in the opposite direction to the tube that formed the body of the SRI. Hence upon a temperature increase the end plates became further apart but the OPD remained constant. A schematic diagram of the SRI is shown in figure 2.17.

By choosing the materials for the tube and the rod such that the products of the length and the coefficient of thermal expansion (CTE) were equal, see equation 2.39, changes in the SRI OPD due to thermal variations could be compensated for.

$$L_{tube}CTE_{steel} = L_{rod}CTE_{nylon} \tag{2.39}$$

Within the SRI the tube was made from steel and the rod from nylon so that the ratio of CTEs was predicted to be approximately 10. Thus with a tube of length $550mm$ and a rod of length $55mm$ the SRI had a nominal OPD of around $990mm$.

To achieve optimal OPD stability over a given temperature range an iterative fine tuning process is required. This procedure will involve acquiring interferometric data from the SRI allowing the OPD variation as a function of temperature to be determined. This information can then be used to estimate the change in rod length required to improve the performance of the compensation system. The initial step of this procedure is presented in section 5.2.1. This method will be restricted by the measurement accuracy of the FSI system, however this can be overcome by using the SRI as a fixed frequency interferometer during applied temperature variations. The use of a frequency stabilised laser would allow the variations in SRI OPD as a function of temperature to be determined with higher accuracy.

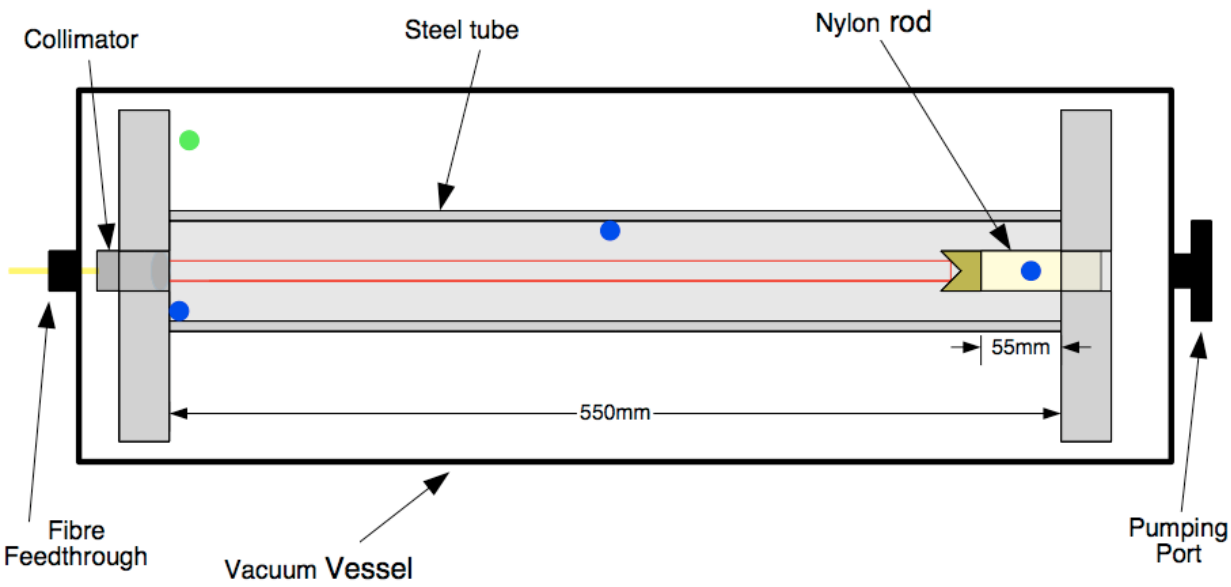

Figure 2.17: A schematic diagram of the Short Reference Interferometer illustrating the active thermal compensation components. The positions of the surface and air temperature sensors are indicated with blue and green dots respectively. Not to scale.

2.3.5 Measurement Interferometers

The bulk of the interferometers within the laboratory FSI system were of unknown OPD. The principle job of these interferometers was to measure the distance between a launch position and the apex of a retroreflector. This was achieved by measuring the OPD of the interferometer where the position of the short arm interferometric reflection had been determined. Hence the geometric distance from the surface providing the short arm reflection to the apex of the retroreflector is half the measured interferometer OPD (assuming a unit refractive index, $n = 1$).

The measurement interferometers used the same fibre for delivery and return of the light, unlike other FSI based distance measurement systems [44][57]. This reduced the problems associated with multiple short arm paths and in the case of bare fibre launches it ensured that the interferometric short arm was effectively zero. However this method does introduce some problems in terms of accessing the returned light with a suitable detector. This problem was solved by delivering the light to the interferometer by way of a 50/50 fibre splitter[10] instead of a single path fibre. Although this meant that four times as much power was required per interferometer, since 50% was effectively lost on each pass through the splitter, it did provide a means of return by simply connecting a photodetector to the input leg of the splitter that was not connected to the light source. A schematic representation of the single fibre delivery and return method is shown in figure 2.18.

[10]By placing the cores of two fibres adjacent to one-another transmitted light can be shared. If relatively large lengths of fibre core are positioned in this was the light passed into either fibre will be split approximately equally between the two output fibres.

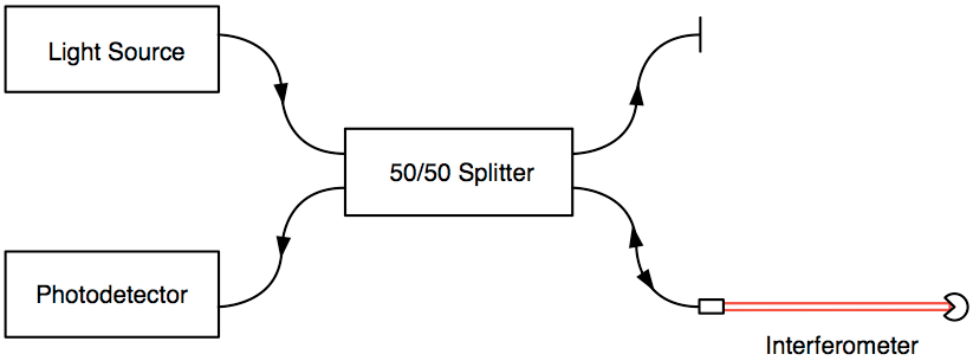

Figure 2.18: A schematic representation of an interferometer launch using a 50/50 fibre splitter. The same fibre is used to launch and collect the interferometric light.

The second output leg of the fibre splitter provided a useful diagnostic and power measurement channel. However it was not used to deliver light into a second interferometer since the signals from both would have been superimposed at the photodetector and could not then have been decoupled after digitisation. Another potential problem was returned light propagating back towards the laser source. This was resolved by the use of an isolator within the laser. By using multiple 50/50 fibre splitters fusion spliced into a tree multiple interferometers could be fed and read out using light from the same source.

Collimated Interferometer Launch Options

As discussed in section 2.3.3 there were two distinct fibre termination types used to launch light into the interferometers. The SPC terminated fibres were more easily incorporated into the internal collimated interferometers since the large polished face, see figure 2.15, simplified the positioning of the fibre termination with respect to the lens. The SPC termination also provided a suitable short arm interferometric reflection.

The integration of APC terminated fibres into the internal collimated interferometers, on the other hand, was not so straightforward. The relatively small angle polished face, illustrated in figure 2.15, could not be used to accurately position the fibre core with respect to the lens. Hence each APC launch had to be individually adjusted to ensure the light was adequately collimated. Since APC terminations are designed to limit the coupling of surface reflected light back into the fibre an additional partially reflective surface was required to provide a suitable interferometric reflection. The additional reflective surface was made up of a glass beam splitter fixed in front of the lens. The face nearest the lens was anti-reflection coated and was held in place with UV curing glue. After adjustment this beam splitter provided a short arm reflection approximately 10% of the level seen with the SPC configuration. Figure 2.19 shows a schematic representation of the SPC and APC collimation solutions.

Despite being more complicated the APC configuration provided potential benefits over the simpler SPC configuration. Since the interferometric short arm reflection is produced

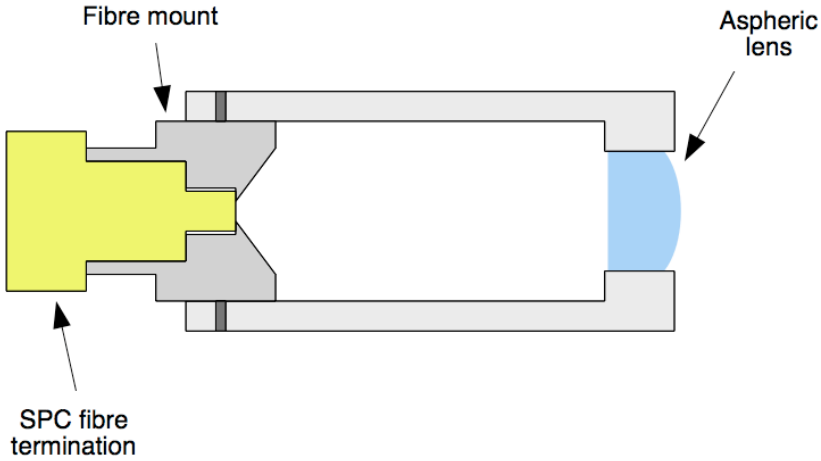

(a) The SPC fibre termination collimation solution.

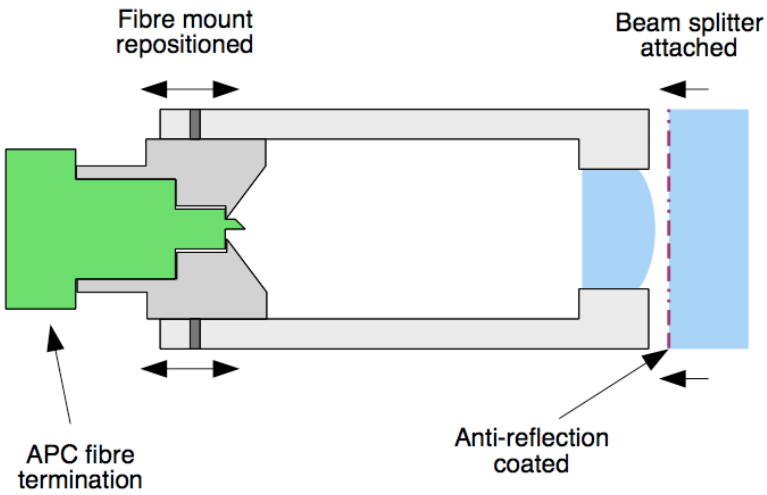

(b) The APC fibre termination collimation solution.

Figure 2.19: Schematic views of the internal FSI system collimation solutions. In both cases the fibre termination remained detachable from the collimation unit. Not to scale.

by the last glass-air interface all paths outside of the interferometer are common to both arms which is not strictly the case with the SPC configuration. This removed potential problems that could arise in a system with no independent frequency measurement device. Chromatic aberrations can result in shifts of the interferometric signal frequencies which may subsequently be incorrectly interpreted as OPD variations within the interferometer.

The production of the APC launch units involved the precise positioning and fixing of optical and mechanical components. The production involved two stages: positioning of the fibre termination with respect to the lens to produce an adequately collimated output; and fixing the beam splitter in front of the lens so as to provide a suitable reflection.

The APC fibre termination was positioned at the focal point of the collimating lens via a manual motion stage. The light output was then viewed using an IR sensitive camera to ensure an acceptable level of collimation. The fibre mount was then glued in place, although the fibre was still detachable from the launch unit. The unit was then repositioned to allow

for light to be launched vertically. The beam splitter was placed in front of the collimating lens with the anti-reflection coated side nearest to the lens. A low viscosity UV curing adhesive was applied to the back of the beam splitter and the barrel of the launch unit. Adjustments were made to the position of the beam splitter with the effect on the amount of recoupled power monitored. Once the optimum beam splitter position had been achieved the adhesive was cured using UV light from an LED source. The launch units were allowed to fully cure for 48 hours prior to incorporation into interferometers.

In the investigations presented in sections 5.4 and 5.5 the collimation units were positioned side-by-side and since each used a difference surface to provide a short arm interferometric reflection different nominal values of OPD were produced. The relative positions of the two interferometric reflective surfaces and the points at which the collimation units were fixed to the optical table are illustrated in figure 2.20.

The lenses used in the collimation units were made from Corning CO550 glass [58]. The stated CTE is $15ppm/°C$ and the stated refractive index variation as a function of temperature is $-11ppm/°C$. Therefore these effects partially compensate for one another. The OPD increase within an SPC launched interferometer, due to the lens being in the optical path, as a result of thermal expansion of the lens was expected to be around $60nm/°C$. The expected OPD decrease as a result of refractive index variations with temperature was approximately $70nm/°C$. Hence a resultant OPD decrease of around $10nm/°C$ was expected.

In addition to the drift error resulting from the wavelength induced refractive index variation of the air within the optical paths, described in section 2.3.1, the lens within optical path of an SPC launched interferometer also produces a drift error. The refractive index of the collimation lens varied by around $227ppm$ during a nominal laser scan. The estimated systematic drift error and scan-to-scan variation introduced by the lens within the optical path are shown in table 2.5. Unlike the case of the error caused by the air this drift error is only present within SPC launched interferometers. This error was approximately constant throughout the investigations it was not corrected for. However since it is a systematic effect the error on the measurement accuracy can be removed by subtracting the calculated drift error from the measured OPD of an interferometer using an SPC launch.

	Systematic Error	**Scan-to-Scan Variation**
SPC Launch	$74\mu m$	$36nm$

Table 2.5: Estimated drift errors resulting from lens dispersion of an SPC launched interferometer as a result of the wavelength change during a nominal laser scan.

The external bare fibre interferometers use an APC fibre termination to launch the light. These were chosen, instead of SPC terminations, because the much lower level of recoupled reflected light from the polished face provides a much more suitable short arm interferometric reflection. This produced a more accessible signal since the high-gain, low-noise electronics would saturate due to the high power inputs produced by a large short arm reflection.

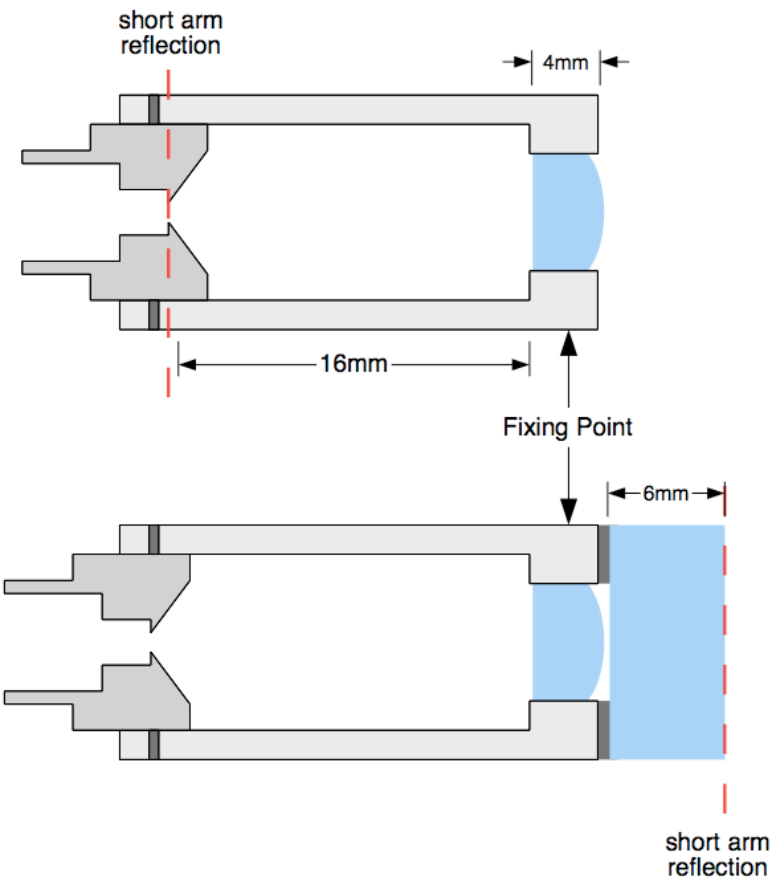

Figure 2.20: An illustration of the relative positions of the SPC and APC launches and the corresponding short arm interferometric reflective surfaces. The points used to fix the units to the optical table are also shown. Expansion of the material beyond the short arm reflective surface contributes to variation of the OPD. Not to scale.

2.3.6 Thermometry

The temperature measurement system used throughout the laboratory investigations comprised of Pt100 platinum resistance sensors, in-house developed custom signal shaping electronics, and 16-bit IOTECH ADCs. Two 8 channel systems were produced allowing 16 simultaneous temperature measurements to be made of the reference system, the measurement system and the ambient laboratory environment. The sensors locations are listed in table 2.6, channels 1 to 8 correspond to signal shaping box 1 and 9 to 16 to signal shaping box 2.

The Sensors

Platinum resistance sensors were chosen because of their excellent long term stability and repeatability as well as flexibility of implementation. Two formats of sensors were used within the system depending upon the specific application. The first type consisted of a pure platinum wire wound into spiral and located in a high purity alumina rod. These were used to measure air temperatures within the experimental set-up and generally within the

Channel	Sensor Position
1	SRI Metal Centre
2	SRI Metal Launch
3	SRI Nylon Rod
4	SRI Air
5	MI Air Launch
6	MI Metal Centre 1
7	MI Metal Centre 2
8	MI Air Retro
9	Michelson Air Beam Splitter
10	Michelson Metal Short Arm
11	Michelson Air Long Arm
12	Michelson Metal Long Arm
13	Signal Shaping Box 1
14	Signal Shaping Box 2
15	Low-end Reference Resistor
16	High-end Reference Resistor

Table 2.6: Positions of the temperature measurement sensors.

laboratory. The second type were formed from flat ceramic pads onto which tracks had been printed with platinum-rich ink. These were used for surface temperature measurements.

The performance of the Pt100 sensors is primarily determined by the temperature dependant resistive properties of platinum. Both types of sensor exhibit the same nominal performance characteristics with the resistance at 0°C stated as $100.00 \pm 0.06\Omega$ which corresponds to a temperature uncertainty of ± 0.15°C. The form of the resistance dependance with temperature of platinum is given in equation 2.40.

$$R(\vartheta) = R_0 \left(1 + A_{90}\vartheta + B_{90}\vartheta^2 + C_{90}\vartheta^3 \times (\vartheta - 100)\right) \tag{2.40}$$

where $R_0 = 100\Omega$, $A_{90} = 3.9083 \times 10^{-3}K^{-1}$, $B_{90} = -5.775 \times 10^{-7}K^{-2}$ and $C_{90} = -4.183 \times 10^{-12}K^{-4}$ [59]. The stated Pt100 resistance values at various temperatures are shown in figure 2.21. The main difference between the two sensor types was the response time. However, as described in section 2.4, only measurements of thermal variations over relatively large time scales were undertaken. The implementation of a calibration procedure for the signal shaping electronics allowed for consistent measurement to be made with multiple sensors.

The Signal Shaping Electronics

Each sensor was used in a 4-wire configuration and was read out via custom built signal shaping electronics[11]. The electronics were designed to produce an output of 0 to $10V$ relating to a measured temperature of 20°C to 30°C, although negative voltage outputs,

[11]The readout circuit was based upon a system developed for the ATLAS semiconductor tracker FSI alignment system and was originally designed by D. F. Howell.

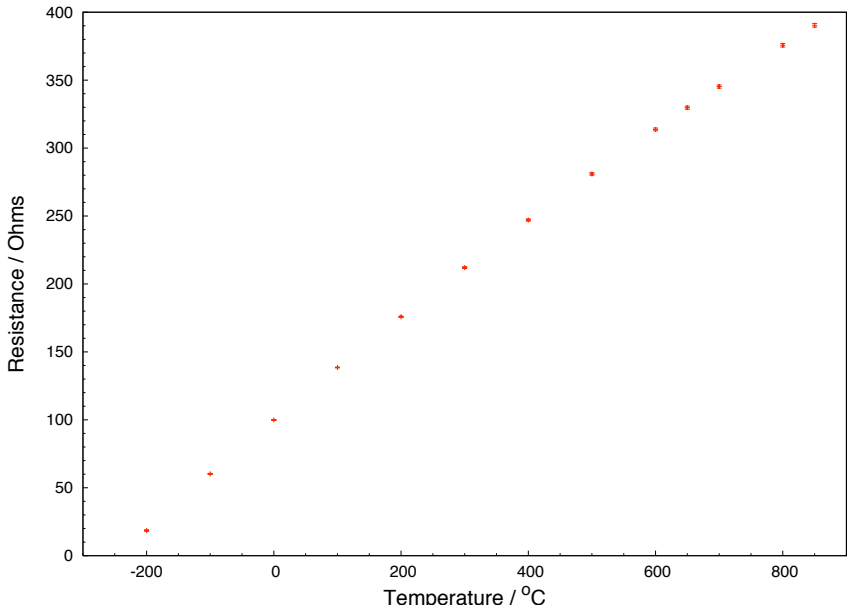

Figure 2.21: The resistance response of the Pt100 sensors with respect to temperature.

relating to temperatures less than 20°C, were produceable. Hence, to first order, a $1mV$ change of the output related to a $1mK$ temperature change. A schematic representation of the front end of the signal shaping board is shown in figure 2.22.

Non-linearities in the resistance response of the Pt100 sensors with respect to measured temperature and variations in the output voltage of the signal shaping boards due to ambient temperature changes meant that calibration with precision end point resistors was necessary.

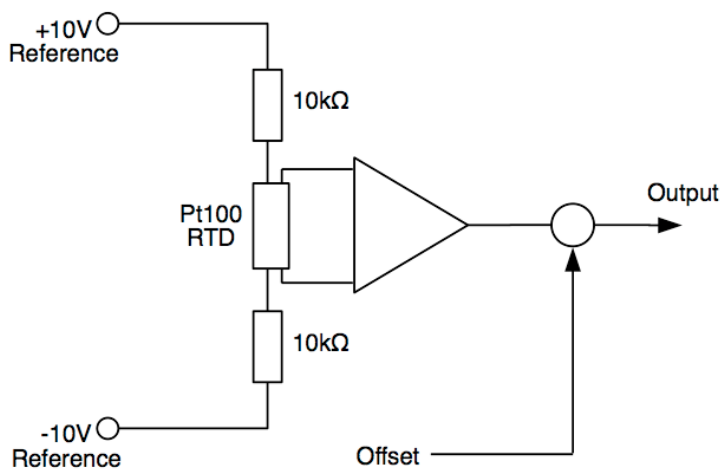

Figure 2.22: A schematic representation of the custom temperature signal shaping electronics. The $10k\Omega$ resistors shown are 0.1% absolute resistance tolerance, $3ppm/°C$ temperature coefficient precision resistors.

Thermometry ADCs

The outputs of the signal shaping boards were digitised using 16-bit IOTECH ADCs [60]. The ADCs digitisation range was set to $\pm 10V$ which meant that the least significant bit corresponded to a temperature of approximately $0.5mK$. The presence of noise from sources such as the power supplies and from the general laboratory environment as well as the ADC itself was estimated to give a temperature measurement uncertainty of around $5mK$.

The Calibration Process

The temperature measurement system was calibrated using combinations of high precision resistors (0.1% absolute resistance tolerance, $3ppm/°C$ temperature coefficient) which produced resistance values equivalent to that of the Pt100 sensors at approximately 20°C and 30°C. The 4-wire calibration resistance values were measured using a Keithley 2000 digital multimeter, at a temperature of 21.5°C. The resistance values are shown in table 2.7 along with the corresponding temperatures. Variable resistors placed within the signal shaping electronics allowed for offset and gain adjustment so that the correct outputs were produced for the two end-point calibration resistances.

Resistance / Ω	**Temperature / °C**
107.751 ± 0.004	19.889 ± 0.010
111.611 ± 0.002	29.838 ± 0.004

Table 2.7: Measured reference resistance values (at 21.5°C) and corresponding Pt100 temperatures used in the calibration of the signal shaping electronics.

Temperature Data Acquisition

The resistance of the Pt100 sensors placed in various positions around the experimental set-up varied as a function of temperature according to equation 2.40. The custom made thermometry signal shaping electronics produced a voltage output that corresponds to the resistance of the sensor. The conditioned output signals were passed into the ADCs via shielded BNC cables. The IOTECH ADCs were controlled by the master DAQ computer using a GPIB link. The ADCs were initialised before the start of the laser scan to acquire continuously at $20Hz$. Upon receiving a trigger signal issued by the laser at the start of each scan 30 pre-trigger and 30 post-trigger values were acquired. These values were read out from the ADC buffer memory into the memory of the master DAQ computer via the GPIB link and written to disk in tab delimited ASCII format. The temperature values quoted throughout this investigation are the mean of these 60 acquired values.

2.3.7 Motion Stages

The motion stages used during the laboratory investigations were MICOS Ultra Precision Stages [61]. These stages were designed for applications such as wafer fabrication, fibre alignment and automated precision robotics where sub-micron accuracy is required. Throughout the research and development of the measurement systems these motion stages were used in single or multiple axis configurations to allow the measurement techniques to be studied. They may also be used for RTRS calibration by placing a complete measurement unit upon multiple stages in a configuration that reproduces the 6 degrees of freedom present during full operation as part of the train in the working tunnel environment. Table 2.8 contains the specifications of the UPM-160 Ultra Precision Linear Stages used during this investigation.

Parameter	**Value**
Bi-directional Repeatability / μm	± 0.1
Accuracy per $50mm$ / μm	± 0.25
Straightness / Flatness / μm	$< \pm 0.5$
Pitch / μrad	$< \pm 15$
Yaw / μrad	$< \pm 20$
Closed-Loop Resolution / μm	0.005 to 0.1

Table 2.8: Specifications of MICOS UPM-160 Ultra Precision Linear Stages used during this investigation [61].

2.4 Data Acquisition

The software used for component control and data acquisition was composed of three distinct segments. These were: the interferometric signal acquisition and corresponding component control; the environmental data acquisition; and the motion stage control and read-out. These segments were integrated into a single software package capable of controlling the relevant equipment and acquiring data within the laboratory. Figure 2.23 shows a screenshot of data acquisition and control software used in the laboratory to acquire the data presented in this investigation.

2.4.1 Interferometric Signal Data Acquisition

The most fundamental piece of the DAQ package was the light source control and interferometric signal acquisition software. The tuneable laser source and the EDFA were controlled by the master DAQ computer via a GPIB link. This allowed parameters such as the end-point wavelengths and tuning speed of a laser scan to be set remotely. The output power of the EDFA, and so the launched power into each interferometer, could also be controlled in a similar fashion. The control software issued a set of initialisation commands which switched both instruments to remote control and set all relevant parameters for the user defined scan.

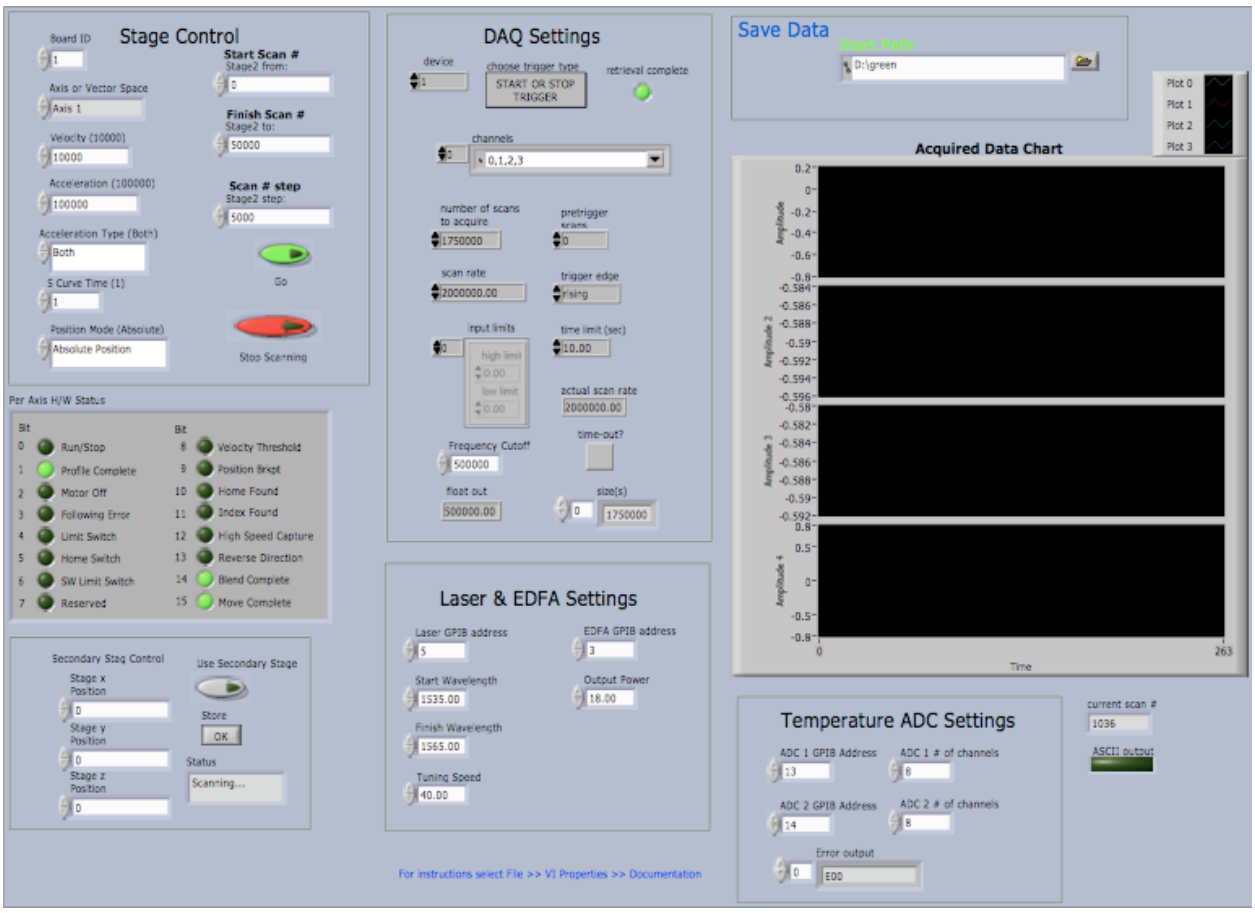

Figure 2.23: A screenshot of the front panel of the data acquisition and control software used in the laboratory.

Both instruments then waited for a further command from the master DAQ computer before commencing the laser scan. Once this command was received the laser produced a trigger signal and proceeded with the scan for which it had been previously initiated.

The output of the laser was passed via a fibre patch cable into the EDFA. After amplification the light was transported via a second patch cable into the fibre splitter tree. Light from the output of one of the branches of the splitter tree was then fed into an interferometer, the details of the interferometers used are given in section 2.3.4 and 2.3.5. In general the interferometers in the laboratory investigations were pre-aligned by viewing the interferometric signal on a digital oscilloscope in real-time prior to data acquisition.

The return signal from the interferometer was propagated back along the delivery fibre into the splitter tree and was accessed via the second input leg of the delivery fibre splitter as shown in figure 2.18. This signal was then passed into a custom made photodetection unit. Each unit used an InGaAs diode to output an electrical signal which was proportional to the optical input. Two types of amplification electronics for the photodetection units were designed. The first type operated with the reasonably large optical signals produced by the internal measurement interferometers. This type of detector was rated to accept optical inputs from around $100nW$ up to $200\mu W$ and operated in the frequency range $1.5kHz$ to

$1MHz$ producing an AC coupled output in the range $\pm 5V$. These detectors were used to acquire the interferometric data presented throughout this investigation. The second type of photodetection unit used a low-noise, high-gain amplification system which allowed the low quality signals produced by the external, bare fibre, interferometers to be acquired. These units were designed to cope with optical inputs from around $5pW$ up to $100nW$ and operated in the range $8kHz$ to $20kHz$. The output was also AC coupled and in the range $\pm 1V$.

The amplified and conditioned output signals of the photodetection units were then passed via BNC cables into the NI BNC-2110 I/O connector block. The signals from several inputs were passed via a SCSI cable to the NI PCI-6115 (12 bit, 10MSample/s) ADC card within the master DAQ computer. The relevant specifications of the ADC card are shown in table 2.9 for the standard laboratory DAQ configuration. 1.75 million data points were digitised at a sampling rate of $2MHz$ for each interferometric channel. This data was passed into the master DAQ computer main system memory via the PCI bus. The interferometer signal data was written to disk using a standard C binary disk IO function which provided both speed and reliability.

Parameter	**Value**
Input Resolution / mV	0.48
Output Noise / mV	0.60
Temperature Stability / $\mu V/°C$	± 35
Timing Accuracy / %	0.01

Table 2.9: The specifications of the National Instruments PCI-6115 12 bit 10MSamples/s ADC card used to acquire interferometric signal within the laboratory [62].

2.4.2 Triggering and Timing

The ADCs in the system were initialised by the software but required a trigger signal to begin the acquisition process. The laser was configured to produce a $5V$ TTL trigger output upon the start of each laser scan. This was distributed to all instruments requiring such a timing signal via BNC cables.

The data acquisition process involved in taking a single laser scan's worth of data took around $6s$. In this time the laser, EDFA and ADCs were initialised; the laser scan was started; the ADCs were triggered and the acquisition was commenced; the digitised data was passed into the main system memory of the master DAQ computer and written to disk in various formats. This process was basically sequential and was not optimised since many of the instruments and components within the laboratory system will not be present in the prototype RTRS and so any optimisation would have been largely irrelevant.

The data runs acquired for this investigation fall, on the whole, into one of two categories. Sequential scans involved acquiring one scan directly after the previous one had been completed. Other runs were acquired to study longer term effects and so groups of scans were acquired sequentially followed by substantial intervals. During the long term studies

presented in Chapter 5 groups of four sequential scans were acquired followed by intervals of around 300 seconds.

2.4.3 File Naming and Directory Structure

A strict directory structure and file naming system formed the basis of the interface between the data acquisition and analysis software packages. The conventions were designed to produce minimal coupling between the two packages and to allow a smooth transition from offline to online analysis in the future.

The top level directory was defined by a run number and contained one or more digitised laser scans. The run number had to be unique and was usually the date of acquisition in the form *yymmdd* although any unique number could be used. Also contained within this top level directory was the human written 'analysis parameters' file which was read prior to starting the analysis and controlled which scans were to be analysed and also defined various relevant parameters. The files relating to each scan were contained in sub-directories which were labelled with a scan number. Each scan number must also be unique (within each run) and was usually incremented from zero.

The directory structure and file naming below this level was such that analysis of multiple scans within a run could be performed sequentially by providing the analysis software with a run number and a range of scan numbers. Within each scan directory there were two sub-directories containing files relating to the acquired data and the output of the analysis, these are the *rawData* and the *analysisOutput* directories respectively. An illustration of the directory structure for an acquired run is shown in figure 2.24.

The files in the rawData directories were created at the time of scan acquisition and contained information on interferometer intensities as well as data relating to acquisition time, temperatures and stage positions. The files held within these directories were only read during the analysis process and never modified. Details of the files stored in the rawData directory are given in table 2.10a.

The analysisOutput directories became populated during the analysis process with the types of files written being determined by parameters within the analysis program. Some of these files were appended to if subsequent secondary analysis took place. Details of the files that may be written by the analysis software into this directory are given in table 2.10b.

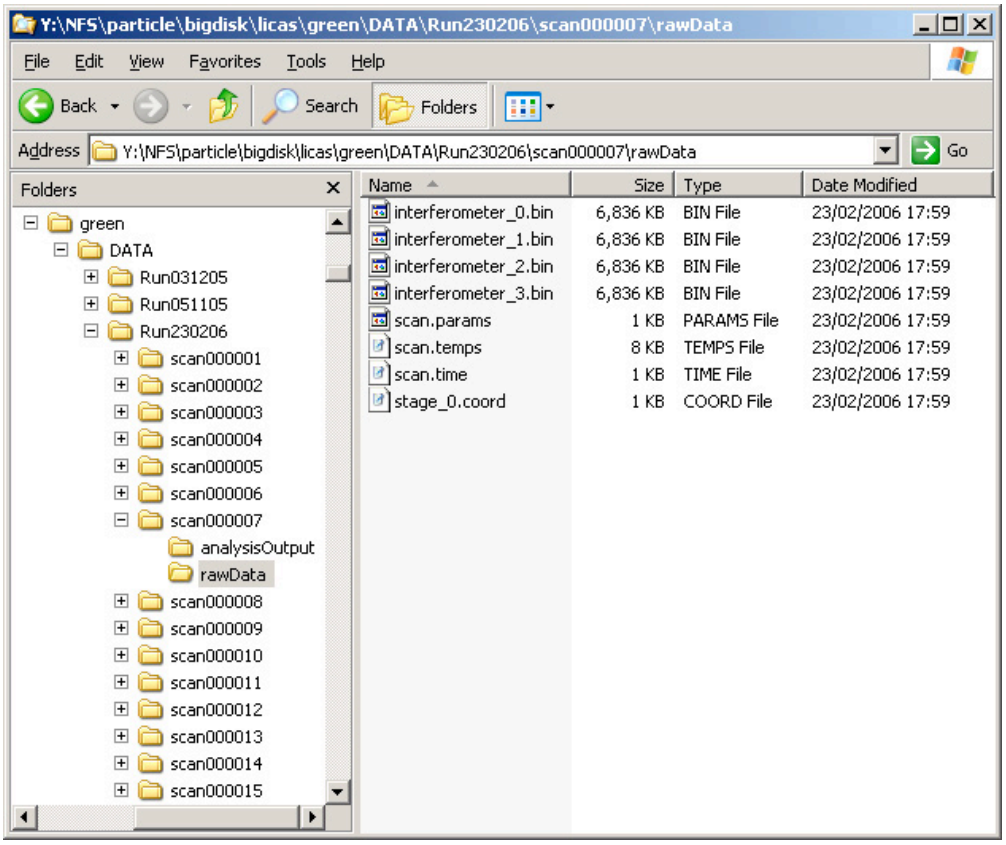

Figure 2.24: The directory structure of an acquired laboratory data run.

File Name	Description of Contents	Extension
scan.params	details of the acquired scan	*.params*
scan.time	acquisition time of the scan	*.time*
scan.temps	acquired temperature data	*.temps*
interferometer_n	acquired intensity data for interferometer n	*.bin* or *.ascii*
stage_i	position of stage i at the point of acquisition	*.coord*

(a) Files relating to acquired raw data.

File Name	Description of Contents	Extension
analysisXXXXXX	global analysis results for the entire scan	*.out*
refAnalysisXXXXXX_n	analysis parameters and outputs for the reference	*.log*
miAnalysisXXXXXX_n	analysis parameters and outputs for the MIs	*.log*
miXXXXXX_n.peaks	details of the identified MI spectral peaks	*.peaks*
miXXXXXX_n.freq	examined frequencies of the spectral analysis	*.freq*
miXXXXXX_n.spec	spectral powers relating to examined frequencies	*.spec*
refXXXXXX_n.wrap	Carré extracted phase of the reference	*.wrap*
refXXXXXX_n.unwrap	phase advance of the reference	*.unwrap*

(b) Files relating to the outputs of the analysis procedure.

Table 2.10: Definition and description of the files relating to the acquired raw data and the outputs of the analysis procedure.

Chapter 3

Data Processing and Analysis

3.1 Introduction

This chapter outlines how the interferometric signals were processed and analysed. The different procedures for dealing with the reference and measurement interferometer data are discussed along with the details of interferometer OPD determination. A description of the applied post-analysis OPD correction techniques, using environmental data, is also provided.

An overview of the analysis procedure is presented in figure 3.1. The processes contained within the blue blocks relate to data preparation and are described in section 3.2. The steps in the yellow block represent the Phase Analysis process. These are described in section 3.3 and are undertaken only on the data acquired from the nominated reference interferometer. The steps in the red block correspond to the Spectral Analysis procedure and are described in detail in section 3.4. The green block represents the Length Determination processes which are detailed in section 3.5. Both the Spectral Analysis and the Length Determination procedures are undertaken on all acquired interferometric signal within each scan.

3.2 Data Preparation

The primary concern of the first stage of post-acquisition data processing was to ensure that the recorded data for all interferometers within each laser scan represented the signal produced by that interferometer and was independent of unwanted laser effects or DAQ timing variations. This was achieved by cutting the first 400 000 and last 350 000 data points from each interferometric signal which resulted in data sets containing 1 000 000 points. Figure 3.2 shows an entire acquired interferometer signal with the positions of the low and high cuts indicated.

The removal of data from both ends of each data set was primarily pragmatic since the laser tuning rate at the extremities of a scan was far from ideal and laser mode-hops were common. Applying the same cuts to all data sets within each scan maintained the acquisition timing correlation between the data sets which ensured consistency since light of the same

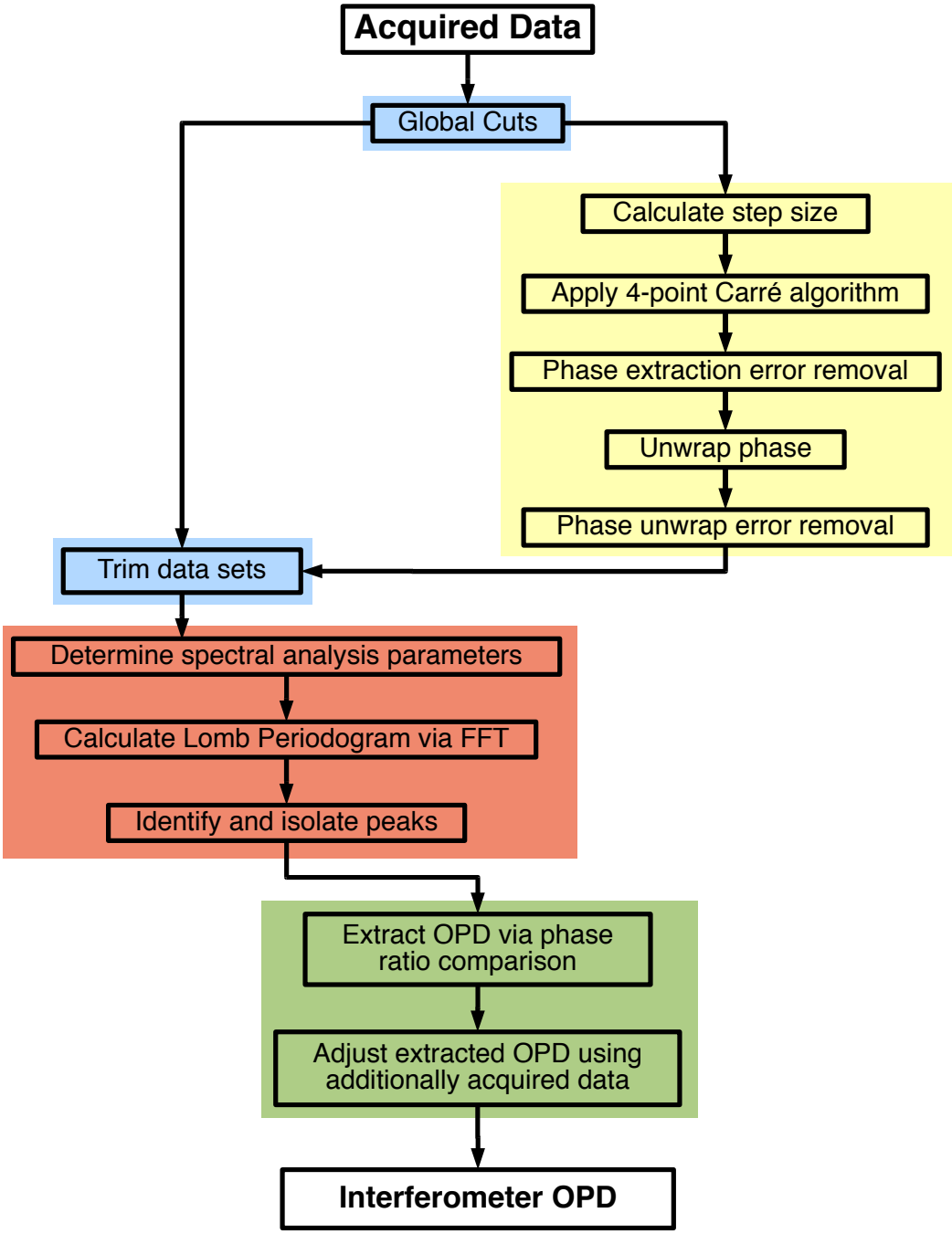

Figure 3.1: A flow chart illustrating the steps required to determine the interferometer OPD from the measurement and reference interferometer data sets. The yellow, red and green blocks relate to the Phase Analysis, Spectral Analysis and Length Determination processes respectively.

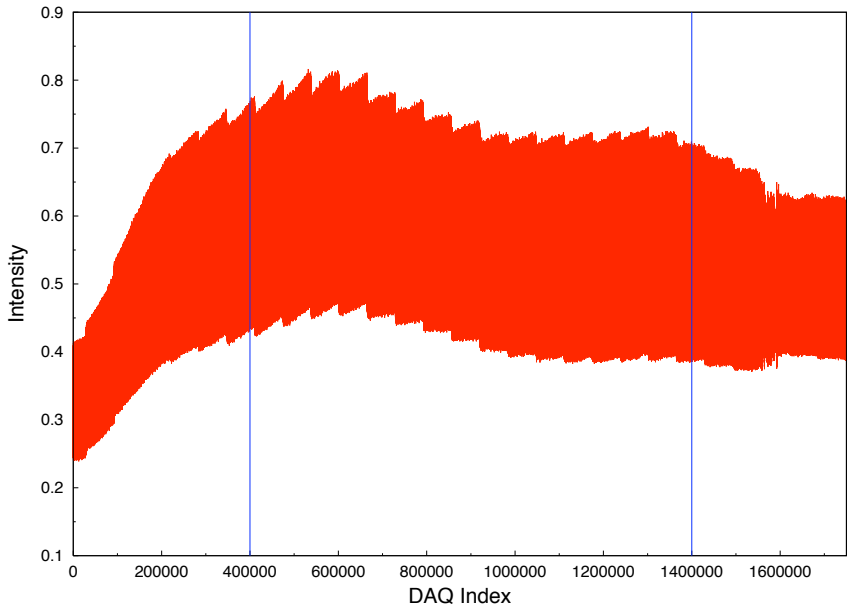

Figure 3.2: An entire acquired Michelson Reference Interferometer signal with the nominal cut positions indicated in blue.

optical frequency was entering each interferometer at any given time. Accurate knowledge of the end point optical frequencies, however, was no longer available since the tuning of the laser was non-linear and non-repeatable. This uncertainty could be removed by the addition of an external optical frequency measurement system, such as a series of etalons as used in other FSI systems [44]. Such a system would allow the data cuts to be defined in terms of optical frequency rather than acquisition time.

The data analysis and interferometer OPD determination procedures described in this chapter do not require the direct measurement of the time dependance of the optical frequency changes, since a mapping from time to optical frequency is provided via the reference interferometer. The requirements of the analysis procedure with respect to the positioning of the cuts was negligible provided consistency was maintained throughout the acquired data of each scan. It was necessary to match the DAQ indices of the extracted reference interferometer phase advance values and of the acquired measurement interferometer intensity values for the analysis process to produce a true phase ratio. Details of how this DAQ index correlation was ensured via a data trimming implementation are given in section 3.4.3.

3.3 Phase Analysis

The extraction of the phase advance within the reference interferometer as a function of time, $\Phi(t)$, provides information on how the laser output frequency, $\nu(t)$, varied with time during each scan. This output is referred to as the laser tuning curve. It is clear from equation 2.8 that $\Phi(t)$ is proportional to $\nu(t)$ assuming that the reference interferometer OPD, L, remains constant throughout the laser scan. As described in section 2.3.1 the

mechanism used to control the laser tuning rate produced a non-linear tuning curve which was also non-reproducible from scan to scan. By using the reference interferometer to access the laser frequency it is possible to produce a mapping from the time domain to the optical frequency domain. This mapping is unique to each laser scan and when used to convert the acquired measurement interferometer data into a function of laser frequency the problems of non-linearity and non-reproducibility of laser tuning are removed.

The process of extraction of the phase advance within the reference interferometer, and therefore indirectly of optical frequency change, is described in this section. The details of how the time to optical frequency mapping was implemented and the effects this had on the rest of the analysis process are discussed in sections 3.4 and 3.5.

3.3.1 The Carré Phase Extraction Implementation

The Carré phase extraction formula determines a mean phase value from four detector intensity values taken from a sinusoidally varying signal [63]. The phase is stepped by a the same amount, α_s, between the measurements which lie symmetrically about ϕ_{mid}. Hence the four measured values can be written in the form shown in equations 3.1, 3.2, 3.3 and 3.4.

$$I_1 = I_0 \left[1 + \gamma \cos\left(\phi_{mid} - \frac{3}{2}\alpha_s\right)\right] \tag{3.1}$$

$$I_2 = I_0 \left[1 + \gamma \cos\left(\phi_{mid} - \frac{1}{2}\alpha_s\right)\right] \tag{3.2}$$

$$I_3 = I_0 \left[1 + \gamma \cos\left(\phi_{mid} + \frac{1}{2}\alpha_s\right)\right] \tag{3.3}$$

$$I_4 = I_0 \left[1 + \gamma \cos\left(\phi_{mid} + \frac{3}{2}\alpha_s\right)\right] \tag{3.4}$$

where I_0 is the DC signal intensity and γ is the signal visibility. The Carré extracted phase is then given by equation 3.5.

$$\phi_{mid} = \arctan\left[\frac{\sqrt{[3(I_2 - I_3) - (I_1 - I_4)][(I_2 - I_3) + (I_1 - I_4)]}}{(I_2 + I_3) - (I_1 + I_4)}\right] \tag{3.5}$$

For any given value of α_s a correction to the extracted result ϕ_{mid} is required due to the loss of information created by taking the positive definition of the square root in the numerator of equation 3.5. This information loss problem was resolved by Coe [44] by using knowledge of the value of the phase step size to redefine the expression for ϕ_{mid} to produce equation 3.6.

$$\phi_{mid} = \arctan\left[\frac{\tan(\frac{1}{2}\alpha_s)[(I_2 - I_4) + (I_1 - I_3)]}{(I_2 - I_4) - (I_1 + I_3)}\right] \tag{3.6}$$

where

$$\alpha_s = \arccos\left[\frac{1}{2}\left(\frac{I_1 - I_4}{I_2 - I_3} - 1\right)\right] \tag{3.7}$$

This modification allows the phase to be extracted unambiguously for any value of α_s.

The 4-point Carré phase extraction algorithm provides an efficient way to extract the phase advance from the reference interferometer signal. The first step in the process was to accurately estimate the optimum step size[1] so that the phase extraction algorithm received the correct input intensities. This was done by splitting the data set into equal segments and estimating the number of fringes in each data segment. The size of the segments were chosen such that they contained several laser tuning rate oscillations but that the overall DC level change was low ($\lesssim 5\%$). This allowed thresholds to be set at 80% of the RMS value above and below the mean level of the data segment. A section of reference interferometer data is displayed in figure 3.3a with the thresholds shown in blue.

The fringe count was incremented when three data points above the upper threshold were followed, not necessarily immediately, by three data points below the lower threshold followed by one further data point above the upper threshold. Three points were required outside the respective thresholds (rather than just one or two) to remove spurious fringe counting problems caused by noise fluctuations. Identifying the number of threshold crossings within each segment produced a count of the number of full fringes present.

An estimate of the number of fringes present within each data segment allowed an estimation of the phase advance per point to be made. Therefore the increment in DAQ index required to produce the optimum phase step could be calculated. Thus an optimum Carré phase extraction step size was calculated for each data segment in terms of DAQ Index. A mean value of the number of data points to step through was then calculated for the entire data set.

The automation of the calculation of α_s allowed the correct reference interferometer intensity values to be passed into the Carré phase extraction formula, equation 3.6. Thus the phase extraction process produced a value of interferometer phase for each acquired intensity. However since the phase extraction formula only used four intensity inputs to calculate each phase value no information on the total phase advance was available. The extracted phase values from the 4-point Carré algorithm all fall within the region $-\pi \leq \phi \leq \pi$. These values are referred to as the *wrapped* or *folded* phase. The relation between the input intensities and the output phase values is shown in figure 3.3.

3.3.2 Phase Unwrapping

To produce a true representation of the optical frequency variation during a scan the phase change as a function of time within the reference interferometer must be made continuous. This process of removing the discontinuities from the extracted phase output of equation 3.6 is referred to as *unwrapping*.

The procedure starts with the extracted *wrapped* phases values, ϕ_i, from an entire data set. To unwrap the phase an order number, the unwrapping index u_i, is added to each extracted phase value to produce the unwrapped phase, $\Phi_i[u_i]$. The unwrapping index started at zero and was incremented each time the extracted phase went through a falling

[1] The optimum step size was estimated to be around 110° by Coe [44] which corresponds to the 4 intensity values approximately spanning one complete cycle of the acquired signal.

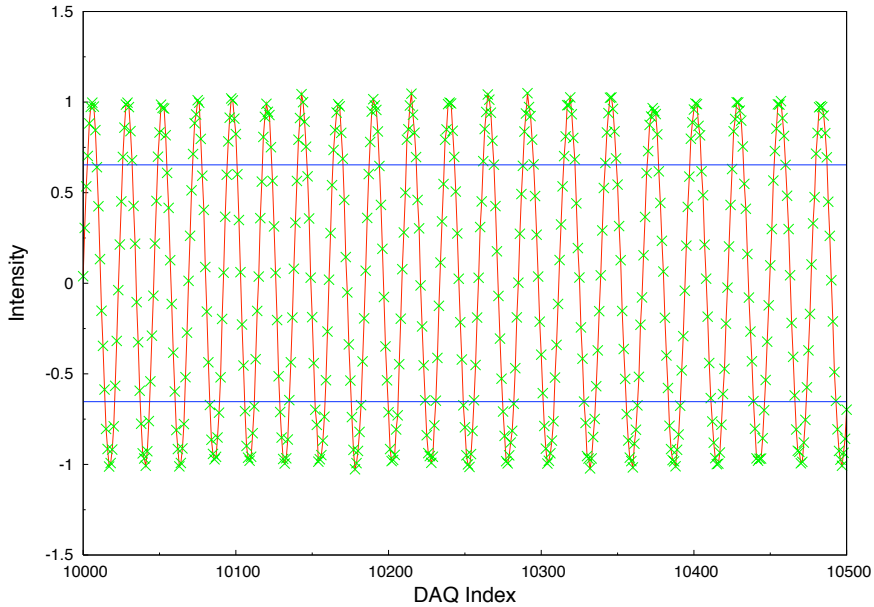

(a) The input data points passed to the Carré phase extraction algorithm. The thresholds used during the step size calculation are shown in blue.

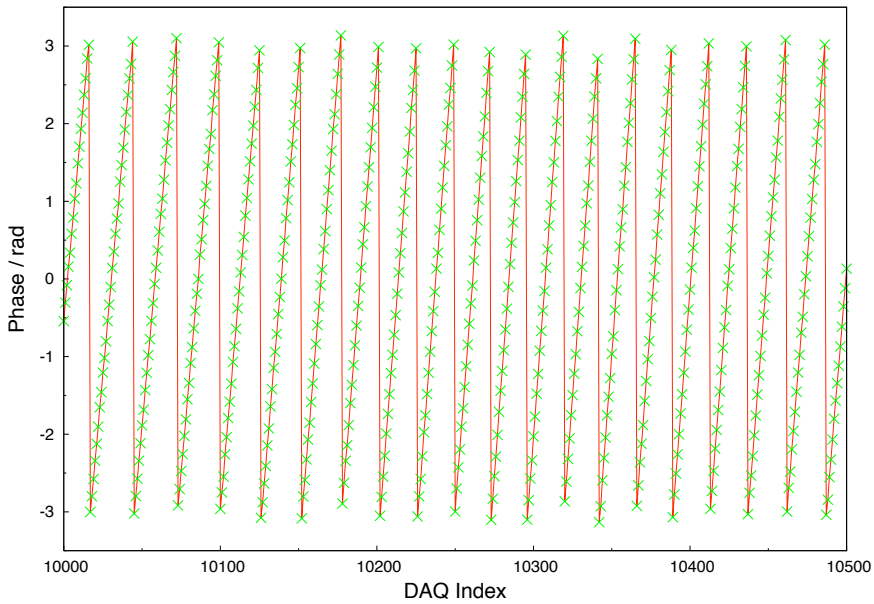

(b) The extracted phase output from the Carré phase extraction algorithm.

Figure 3.3: Reference interferometer data points past to the 4-point Carré phase extraction algorithm and the corresponding wrapped phase output.

edge ($+\pi$ to $-\pi$) and decremented each time upon a rising edge ($-\pi$ to $+\pi$). The latter should not occur in a nominal laser scan.

The boundary between one cycle and the next was recognised by looking at the difference between neighbouring extracted phase values ϕ_i and ϕ_{i-1}. Whenever the absolute difference between the two points was greater than π a cycle boundary was assumed to have been crossed and the unwrapping index was altered accordingly. The unwrapping proceeded by induction, using the following algorithm:

$$\begin{gathered} u_1 = 0 \\ \text{if } (\phi_i - \phi_{i-1}) < -\pi \text{ then } u_i = u_{i-1} + 1 \\ \text{if } (\phi_i - \phi_{i-1}) > +\pi \text{ then } u_i = u_{i-1} - 1 \\ \text{else } u_i = u_{i-1}. \end{gathered}$$

Applying this procedure to the extracted phase values from a complete reference interferometer data set produced the continuous phase advance as a function of time, $\Phi(t)$, over the course of the laser scan, equation 3.8.

$$\Phi_i = 2\pi u_i \times \phi_i \tag{3.8}$$

Hence the optical frequency variations of the light used to produce the interferometric signals within the measurement interferometers, $\nu(t)$, was also produced. The phase advance from a reference interferometer data set during a nominal laser scan is shown in figure 3.4. This phase advance was used to extract the laser tuning curve shown in section 2.3.1.

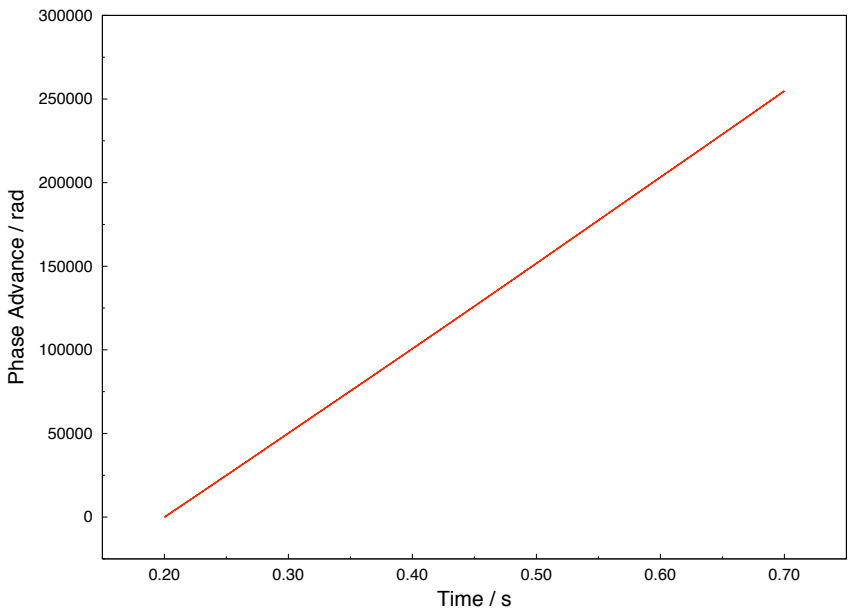

Figure 3.4: The phase advance witnessed within the Michelson Reference Interferometer during a nominal laser scan.

3.3.3 Extraction and Unwrapping Error Removal

The presence of phase errors within the output of the Carré analysis of the reference interferometer signal have a cumulative effect on the entire analysis process. These errors must be identified and corrected. There are two main types of error which occur during the Phase Analysis process.

Extraction Errors

The 4-point Carré phase extraction algorithm used the standard C mathematics library `acos()` function which returns NaN (Not a Number) in the case of input values outside the range ± 1, since this refers to output values in the complex plane. Such input values could be produced due to the presence of noise on the reference interferometer signal or by the incorrect intensity values being passed into the Carré algorithm. The phase extraction set these NaN values to 0 and used an error flag to indicate at which DAQ indices this type of error had occurred. Errors of this form were most commonly found near the transitions between phase cycles. An illustration of two instances of phase extraction errors is provided in figure 3.5.

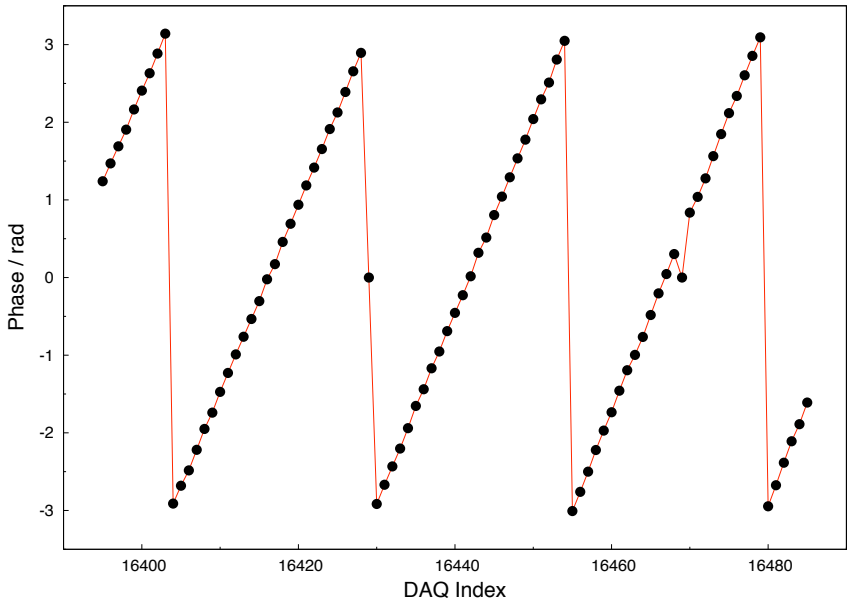

Figure 3.5: An illustration of the two instances of phase extraction errors produced by the 4-point Carré phase extraction implementation.

Extraction error removal was undertaken directly after the completion of the phase extraction process, prior to phase unwrapping. The most frequent form of this type of error was characterised by a zero value of extracted phase, $\phi_i = 0$, accompanied by a sign change from ϕ_{i-1} and ϕ_{i+1}. Errors of this type were removed by resetting ϕ_i using the condition:

$$\text{if } (\pi - |\phi_{i-1}|) > (\pi - |\phi_{i+1}|) \text{ then } \phi_i = \pi$$
$$\text{else } \phi_i = -\pi.$$

The second, and much less frequently occurring, instance of this type of extraction error was characterised by a zero value of extracted phase with no associated sign change in the extracted phase values directly before and after it. This type of error was produced when $I_1 - I_4 = 0$ and $I_2 - I_3 = 0$ which also resulted in a NaN output which was again set to 0. In this case the incorrect zero value of extracted phase was removed and replaced with a value inferred, by linear interpolation, from the neighbouring phase values.

In general consecutive errors were very rare and were treated individually. The total number of extraction errors produced during the phase extraction of an reference interferometer data set containing 10^6 data points was typically around 6000. This corresponds approximately to one extraction error every 10 fringes. A second examination of the phase values after extraction error removal was used to confirm the success of the error removal process.

Unwrapping Errors

This type of error was introduced by the incorrect assignment of cycle boundaries during the initial phase unwrapping process. If the absolute difference in the extracted phase values ϕ_i and ϕ_{i-1} was less than π a cycle boundary would not have been detected. This was caused by the extraction error removal algorithm not completely eliminating the first type of extraction error. In this case the unidentified phase discontinuity produced during the extraction process remained present in the unwrapped data set. Hence all subsequent values of the unwrapping index would be incorrect. Thus large artificial discontinuities in the calculated laser tuning curve could be created. An illustration of a phase unwrapping error is provided in figure 3.6.

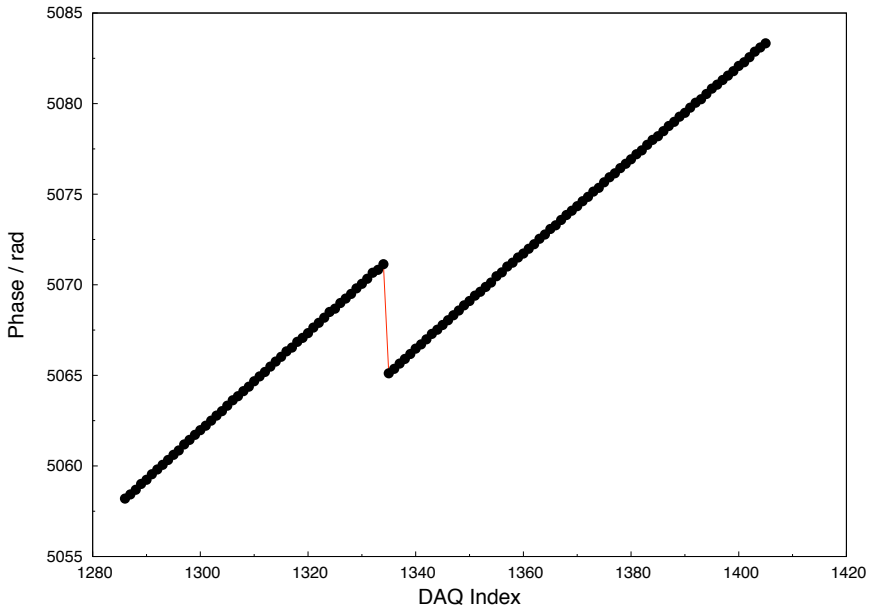

Figure 3.6: An illustration of phase unwrapping error produced by failing to remove a discontinuity in the output of the 4-point Carré phase extraction algorithm.

These errors could only be removed by the direct study of the unwrapped data sets since the employment of an error flagging technique was not possible. Error identification and subsequent correction was undertaken in an iterative manner. A copy of the unwrapped phase data was made at the beginning of each error removal iteration and used for error identification whilst corrections were applied to the original data. This precaution was required since simultaneous identification and correction of errors within a single data array introduced the risk of the application of unnecessary and repeated corrections. A correction of π was added to all subsequent unwrapped phase values if the following condition was met:

$$(\Phi_i - \Phi_{i-1}) < 0.$$

The removal of the errors introduced during the phase extraction and unwrapping processes provided a continuous description of the phase advance within the reference interferometer during each laser scan. A histogram of the phase advance per point $(\Phi_i - \Phi_{i-1})$ for an acquired reference interferometer data set is shown in figure 3.7. Such plots provide verification that no errors from the phase analysis process remain since there are no entries relating to values of $+\pi$, $-\pi$ or 0.

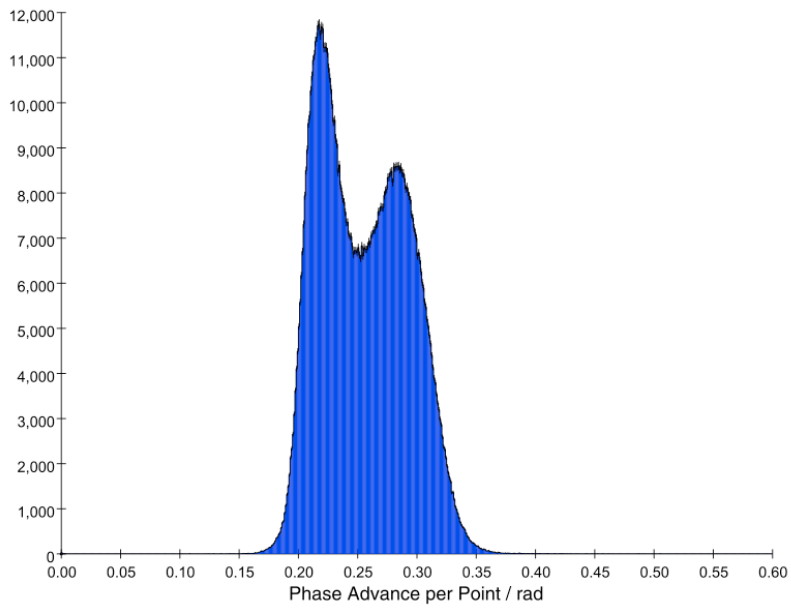

Figure 3.7: A histogram of the phase advance per point $(\Phi_i - \Phi_{i-1})$ of a Michelson Reference Interferometer data set after phase extraction, unwrapping and error removal.

The shape of the phase advance per point distribution seen in figure 3.7 provides information on the way in which the laser tunes during the scan. The width indicates the scale of laser tuning rate variations during the scan, which is approximately 40%. The two distinct peaks are a results of the laser tuning curve oscillations around the global tuning rate, as described in section 2.3.1 and shown in figure 2.10. The larger peak at the lower phase advance values corresponds to the valleys of these oscillation where the tuning rate is lowest. In these regions the phase advance per point is lowest and the statistics are highest.

3.4 Spectral Analysis

The spectral analysis procedure formed the fundamental basis of the investigation into the periodic signals present within the interferometric data. This section outlines why a spectral analysis method was chosen as well as describing the capabilities of the algorithms used to deal with data that was not evenly sampled. The implementation specifics of the analysis procedure and the process of identification of signal peaks within the output spectra are also discussed.

3.4.1 Advantages of Spectral Analysis

The variety of FSI implementations within LiCAS pose several significant problems with respect to data analysis. There are two distinct length scales: the first with OPDs of around $1m$ requiring a large dynamic range (due to the large acceptance requirements) and interferometric length determination from very low quality signals; the second with OPDs of around $9m$ where, although high quality signals can be expected, multiple interferometric lengths may well be present within each signal[2]. Spectral analysis lends itself as a more natural solution to these problems than purely analytical phase extraction or the sine fitting methods employed in previous FSI signal analysis systems [44][57].

The advantages of spectral analysis when compared to sine fitting, i.e. chi-squared minimisation of a function of the form shown in equation 3.9 are as follows.

$$I = a + b\sin(\Phi + \phi_0) \tag{3.9}$$

In the case of spectral analysis the determination of the parameter of interest, Φ (the phase advance within the interferometer during a laser scan) is isolated from other aspects of the signal and is not dependant on the correct determination of a (the DC amplitude) or b (the AC amplitude). Also multiple phase advance rates, corresponding to different OPDs, can be simultaneously extracted from a single data set, which is not possible with sine fitting methods due to seeding requirements. Moreover, the ability to isolate a signal peak within a spectrum is only affected by the presence of noise within the immediate vicinity. Thus white noise sources such as the photodiode and the digitisation process have a much smaller effect upon the output of the analysis process. Finally all FSI data can be analysed using a single analysis technique, with only minimal analysis parameter modifications[3], simply by identifying signal peaks in different parts of the resultant spectra.

3.4.2 Spectral Analysis of Unevenly Sampled Data

Due to the need to transform the acquired interferometric signals from the time domain to the reference interferometer phase domain, so as to remove the effects of variations in

[2]Additional reflective surfaces within the vacuum tube containing the interferometers produce secondary, low-level signals which are superimposed onto the desired interferometric signal. These signals have a large visibility in the internal systems since the short arm reflection is strong.

[3]The modifications to analysis parameters serve primarily to limit unnecessary computations.

the laser tuning rate on periodicity, the inputs to the spectral analysis become unevenly sampled. This immediately rules out many potential time series analysis methods including the employment of a wavelet transform or a straightforward Fourier transform.

The spectral analysis of the interferometric data, $I(\Phi)$, requires an extension of the discrete Fourier transform (DFT), shown in equation 3.10, to allow for unevenly sampled data.

$$DFT(\omega) = \sum_{n=0}^{N-1} I(\Phi_n) e^{-i\omega\Phi_n} \tag{3.10}$$

for signals sampled at Φ_n where $(n = 0, 1, 2, \ldots, N-1)$[4] and ω is the *angular phase ratio* which is the phase ratio, as defined in equation 2.10, divided by 2π.

However, the periodogram resulting from equation 3.10 is not invariant under a translation in Φ. This limitation can be removed by modifying the definition of the periodogram to obtain an expression for a zero-mean series. This method was first suggested by Lomb [64] and is equivalent to evaluating the signal in terms of sines and cosines only at the points where the signal was sampled. Thus the *Lomb Normalised Periodogram*, given in equation 3.11, computes the spectral power as a function of angular phase ratio.

$$P(\omega) \equiv \frac{1}{2\sigma^2} \left(\frac{\left[\sum_n (I_n - \bar{I}) \cos\omega(\Phi_n - \varphi)\right]^2}{\sum_n \cos^2\omega(\Phi_n - \varphi)} + \frac{\left[\sum_n (I_n - \bar{I}) \sin\omega(\Phi_n - \varphi)\right]^2}{\sum_n \sin^2\omega(\Phi_n - \varphi)} \right) \tag{3.11}$$

where $I_n \equiv I(\Phi_n)$. The mean and variance of the signal are found by the usual formulas,

$$\bar{I} \equiv \frac{1}{N} \sum_{n=0}^{N-1} I_n \qquad \sigma^2 \equiv \frac{1}{N-1} \sum_{n=0}^{N-1} (I_n - \bar{I})^2 \tag{3.12}$$

and φ is defined by

$$\tan(2\omega\varphi) \equiv \frac{\sum_n \sin(2\omega\Phi_n)}{\sum_n \cos(2\omega\Phi_n)}. \tag{3.13}$$

An equivalent result can be obtained by fitting a least squares model of the form of equation 3.14 to the data for each given angular phase ratio, ω.

$$I(\Phi) = a\cos(\omega\Phi) + b\sin(\omega\Phi) \tag{3.14}$$

For this reason the Lomb periodogram is also referred to as the *Least Squares Periodogram*. A full derivation of the Lomb Periodogram is provided in Appendix C.

Spectral analysis of unevenly sampled data also allows for the examination of angular phase ratios higher than the Nyquist critical angular phase ratio[5]. In an evenly sampled data set, $I_n = I(n\Delta)$ where $n = \ldots, -3, -2, -1, 0, 1, 2, 3, \ldots$ and Δ is the sampling interval, the Nyquist critical angular phase ratio is given by equation 3.15.

$$\omega_c \equiv \frac{1}{2\Delta} \tag{3.15}$$

The Lomb method weighs the data per value instead of per interval as with a Fourier transform and so removes the sharp cut-off behaviour at the highest angular phase ratios present in the evenly sampled case.

[4] If $\Phi_{n+1} - \Phi_n = const$ then equation 3.10 becomes the standard DFT equation for evenly sampled series.

[5] This is equivalent to the Nyquist critical frequency of a signal sampled at equally spaced time intervals.

3.4.3 The Spectral Analysis Implementation

The implementation of the analytical form of the Normalised Lomb Periodogram is uncomplicated although the algorithm is extremely slow. It is not unusual to examine $\mathcal{O}(2N)$ angular phase ratios and for each combination of data point and angular phase ratio four trigonometric calls must be made to evaluate equations 3.11 and 3.13. Hence the operation count can approach several hundred times N^2. Replacing the trigonometric calls with recurrences only reduces this by a factor of four[6]. Thus the unmodified normalised Lomb periodogram can only be implemented sensibly for data sets where $N \lesssim 1000$. Applying such an algorithm to a data set containing $\mathcal{O}(10^6)$ points would require approximately 150 hours of CPU time on a $2GHz$ Pentium 4 machine.

An implementation was required which maintained the properties of the Lomb Periodogram but with a lower operation count, hopefully approaching $N \log N$. This would be practical for data sets containing $\mathcal{O}(10^6)$ points. The chosen spectral analysis implementation uses the FFT algorithm to reduce the operation count. Such an approach was first proposed by Press and Rybicki [65]. This solution retains the attributes of the Lomb method since it uses the outputs of the FFT algorithm to actually evaluate equations 3.11 and 3.13.

The four trigonometric sums in equation 3.11 can be simplified via the use of the product-to-sum trigonometric identities:

$$\sum_{n=0}^{N-1}(I_n - \bar{I})\cos\omega(\Phi_n - \varphi) = C_I \cos\omega\varphi + S_I \sin\omega\varphi \tag{3.16}$$

$$\sum_{n=0}^{N-1}(I_n - \bar{I})\sin\omega(\Phi_n - \varphi) = C_I \cos\omega\varphi - S_I \sin\omega\varphi \tag{3.17}$$

$$\sum_{n=0}^{N-1}\cos^2\omega(\Phi_n - \varphi) = \frac{N}{2} + \frac{1}{2}C_2\cos(2\omega\varphi) + \frac{1}{2}S_2\sin(2\omega\varphi) \tag{3.18}$$

$$\sum_{n=0}^{N-1}\sin^2\omega(\Phi_n - \varphi) = \frac{N}{2} - \frac{1}{2}C_2\cos(2\omega\varphi) - \frac{1}{2}S_2\sin(2\omega\varphi). \tag{3.19}$$

Where

$$C_I \equiv \sum_{n=0}^{N-1}(I_n - \bar{I})\cos(\omega\Phi_n) \qquad S_I \equiv \sum_{n=0}^{N-1}(I_n - \bar{I})\sin(\omega\Phi_n) \tag{3.20}$$

and

$$C_2 \equiv \sum_{n=0}^{N-1}\cos(2\omega\Phi_n) \qquad S_2 \equiv \sum_{n=0}^{N-1}\sin(2\omega\Phi_n). \tag{3.21}$$

In the case of evenly spaced Φ_ns two complex FFTs can be used to evaluate C_2 and S_2. Therefore C_I and S_I can be found using the half angle identities and φ from equation 3.13. Thus to employ the FFT algorithm in the evaluation of equations 3.20 and 3.21 a reverse interpolation process is required.

[6]Replacing the trigonometric calls in this way is also only possible for a linear sequence of examined angular phase ratios.

During reverse interpolation values at arbitrary points are replaced with a set of function values on a regular mesh, rather than using a set of function values on a regular mesh to accurately approximate arbitrary points as in standard interpolation. This must be done in such a way so as to produce sums over the regular mesh that are an accurate approximation of the sums over the original arbitrary points.

The function to be reverse interpolated, $I(\Phi)$, is known only at discrete, unevenly sampled points I_n, whilst the function $g(\Phi)$ can be evaluated anywhere, i.e. $\cos(\Phi)$. Hence the Lagrange interpolation gives an approximation of the form shown in equation 3.22.

$$g(\Phi) \approx \sum_k w_k(\Phi) g(\hat{\Phi}_k) \tag{3.22}$$

where $\hat{\Phi}_k$ is a sequence of evenly spaced points on a regular mesh and $w_k(\Phi)$ are the interpolation weights. A sum of interest can then be evaluated using the scheme shown below

$$\sum_{n=0}^{N-1} I_n g(\Phi_n) \approx \sum_{n=0}^{N-1} I_n \left[\sum_k w_k(\Phi_n) g(\hat{\Phi}_k) \right] = \sum_k \left[\sum_{n=0}^{N-1} I_n w_k(\Phi_n) \right] g(\hat{\Phi}_k) \equiv \sum_k \hat{I}_k g(\hat{\Phi}_k) \tag{3.23}$$

where

$$\hat{I}_k \equiv \sum_n I_n w_k(\Phi_n) \tag{3.24}$$

The accuracy of equation 3.22 depends only upon the fineness of the mesh with respect to the function $g(\Phi)$. The spacing of the points Φ_n within the function $I(\Phi)$ does not affect the accuracy. Therefore the accuracy of equation 3.23 also has this property.

Prior to any data set being spectrally analysed a subtlety regarding the mapping from the time to the laser frequency domain must be addressed. Due to the way in which the 4-point Carré phase extraction algorithm operates it is not possible to calculate a phase value for every acquired intensity value. The number of extracted phase values was less than the number of acquired intensity values by the number of DAQ indices relating to the separation of the first and last point used in each 4-point Carré calculation (i.e. $3 \times \alpha_{step}$, where α_{step} is the Carré step size in units of DAQ index). This typically results in a discrepancy of around 15 to 20 points for each data set. The ability to remove the correct intensity values in each data set before commencing the spectral analysis relies on specific knowledge of the Carré step size used during the phase extraction process. This information allows intensity values from the beginning and end of the interferometer data set to be discarded thus maintaining the data integrity with respect to acquisition time correlation.

The separation of the examined angular phase ratios is controlled by an externally set parameter. The `freqStep` parameter provides direct control of the resolution of the spectral analysis output. The correspondence between this parameter and the theoretical length resolution is described in section 3.5.1. As well as defining the resolution of the analysis procedure the total size of continuous memory required to implement the spectral analysis algorithm is also determined by `freqStep` and the highest examined angular phase ratio[7].

[7]The bulk of the continuous memory requirement comes from the use of the FFT and only by using a single block of memory can an operation count of approaching $N \log N$ be achieved.

The definition of the value of `freqStep` along with knowledge of the reference interferometer OPD and an estimation of the measurement interferometer OPD allows the other relevant spectral analysis parameters to be calculated. The average Nyquist angular phase ratio for the input data is calculated by modifying equation 3.15 to take into account the non-linear advance in reference phase, equation 3.25.

$$\langle \omega_c \rangle = \frac{1}{\frac{2}{N}\sum_n \Phi_n - \Phi_{n-1}} \tag{3.25}$$

The lowest independent angular phase ratio examined is such that the data contains one full cycle. The mean of the input data set was subtracted in equation 3.11 since the zero-angular phase ratio piece of the data was of no interest[8]. Unlike a simple Fourier approach higher independent angular phase ratios are not simply integer multiples of $1/\Phi_{tot}$, where Φ_{tot} is the total reference interferometer phase advance within the data set[9]. Since the presence of any peak is of interest oversampling is introduced to sample more finely than intervals of $1/\Phi_{tot}$. This results in sample points being closer to the top of any peak. The oversampling factor, `ofac`, was determined using equation 3.26.

$$\texttt{ofac} = \frac{2\langle \omega_c \rangle}{N \times \texttt{freqStep}} \tag{3.26}$$

It was also necessary to specify the highest angular phase ratio to examine, ω_{hi}. This involved the relative highest examined angular phase ratio parameter, `hifac`, which defines ω_{hi} in terms of the average Nyquist angular phase ratio. The `hifac` parameter was determined using equation 3.27,

$$\texttt{hifac} = \frac{\omega_{hi}}{\langle \omega_c \rangle} = \frac{1.2}{2\pi}\frac{D}{L}\frac{1}{\langle f_c \rangle} \tag{3.27}$$

where the factor of 1.2 was introduced to ensure the signal peak was fully contained within the spectra. The number of different output angular phase ratios produced, N_p, is then given by equation 3.28.

$$N_p = \frac{\texttt{ofac} \times \texttt{hifac}}{2} N \tag{3.28}$$

After the completion of the initial parameter calculations the average and variance of each input data set are calculated to ensure that the data is suitable for the subsequent analysis. Once the data integrity is confirmed by a non-zero value of variance the data is mapped onto an evenly spaced mesh, the resolution of which is determined by `freqStep`, using the Lagrange interpolation scheme described above. The evenly spaced interpolated data is then conditioned by the application of a Bartlett (triangular) window, this involves multiplying each point by B_n where

$$B_n = 1 - \left| \frac{n - \frac{1}{2}N}{\frac{1}{2}N} \right| . \tag{3.29}$$

[8]The zero-angular phase ratio piece is equivalent to the mean of the data set.

[9]Φ_{tot} is equivalent to the period of the data set measured in units of reference interferometer phase advance.

The conditioned data is then transformed via a standard bit reversing FFT algorithm. Thus the terms in equations 3.20 and 3.21 are evaluated. These results are then substituted back through equations 3.16 to 3.19 to evaluate equations 3.11 and 3.13 which produces a value of spectral power for each examined angular phase ratio.

After the completion of the calculations the output arrays are checked and $NULL$ entries arising from the reverse interpolation and oversampling processes are removed. The mean level and standard deviation of the spectral power data are then calculated. The subsequent steps in the analysis procedure involve the identification and isolation of spectral peaks.

3.4.4 Spectral Peak Identification

The properties of a signal peak in the output spectra depend upon many factors which are determined primarily by the input data. Since, ideally, a monochromatic sinusoid containing around 10^5 cycles will be transformed the resultant spectral peak should approximate to a delta function. Nevertheless as would be expected from the discrete Fourier transform of a sinusoid inside a triangular envelope the peak has the form of $sinc^2$ and is finite in both height and width [66].

A spectral peak of interest was defined as three or more consecutive examined angular phase ratios with power values at least 5σ above the mean spectral level. Figure 3.8 shows a Short Reference Interferometer signal peak with the threshold level shown in blue.

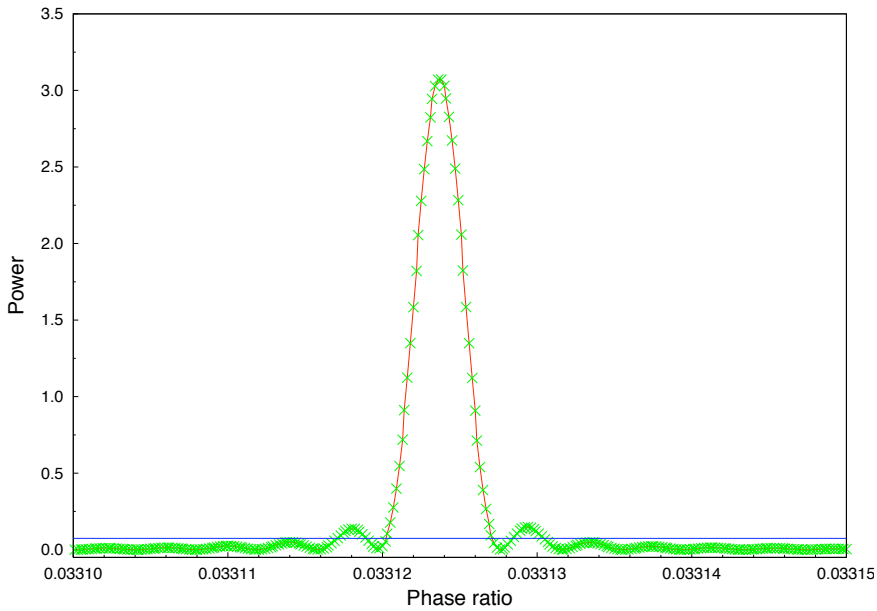

Figure 3.8: An identified peak in the output spectrum of an analysed Short Reference Interferometer data set. The 5σ threshold level is shown in blue.

After the spectral analysis of the input data and the calculation of the mean and standard deviation of the output spectrum a spectral peak threshold level is set. The spectrum is then investigated for groups of examined angular phase ratios with power values above the

threshold level. All identified peaks, with the exception of the lowest frequency peak[10] were subsequently fitted to improve the precision of the determination of the mean angular phase ratio.

The peak fitting process begins with an estimation of the width by determining the distance to the spectral mean level on either side of the peak. The points that form the isolated peak are then fitted using a standard Marquardt non-linear least square fitting technique [67]. This process uses chi-squared minimisation to calculate best fit values for the peak height, width and mean angular phase ratio by fitting a function of Gaussian form[11] shown in equation 3.30.

$$P = ae^{-\left(\frac{\omega-b}{c}\right)^2} \tag{3.30}$$

where P and ω are the spectral power and angular phase ratio respectively. The fitted coefficients, a, b and c, relate to the peak height, mean position and width respectively. Uniform errors were used throughout the peak fitting process. The fitted peak height provides information on the fraction of total signal power present at that examined angular phase ratio. The width provides information on the number of cycles present in the raw data and the extent of effective OPD variations of the interferometer during the scan.

The error on the mean peak position determined from the fit can be used to provide an estimate of the statistical error on the OPD determination. This estimate is used as a indicator of the single measurement uncertainty in Chapter 5. A more reliable evaluation of the OPD determination error would be provided by also including the values, and errors, of the fitted peak width. This improvement was not undertaken since the performance of the analysis was assessed via the use of simulations, see Chapter 4.

The calculated peak width also contains a component resulting from *power leakage* into adjacent bins which is unavoidable during the spectral analysis process. Power leakage occurs since the convolution theorem states that the Fourier transform of the product of data with a window is equal to the convolution of the Fourier transform of the data with the Fourier transform of the window. Since in the case of any discrete data set the window must begin at zero, rise to a maximum and fall back to zero the resultant Fourier transform will contain side lobes. The Bartlett window, given in equation 3.29, was chosen since this maximised the distance between the main peak and the first side lobes. This made the process of isolating and fitting the resultant spectral peaks easier.

3.5 Length Determination

The final stage of the analysis procedure is to convert a mean angular phase ratio obtained during the fitting process into an interferometer OPD. This process involves the comparison of calculated interferometer phase advance rates, as describe in section 2.2.1, along with the addition of corrections determined from additionally acquired data.

[10] This peak is not fitted since it is always present and it provides no additional information.
[11] The central peaks of the $sinc^2$ were assumed to approximately Gaussian.

3.5.1 Length Calculation

The spectral analysis procedure described in the previous section calculates the phase advance rate induced in a measurement interferometer during a laser scan as a function of the rate of reference interferometer phase advance. This was a results of the mapping of the measurement interferometer data set into a function of laser frequency via the use of the extracted reference interferometer phase advance. Thus the number of cycles occurring in 2π reference phase advance gives us directly the phase ratio q, defined in equation 2.10. Hence the ratio of reference interferometer OPD to measurement interferometer OPD can be determined by

$$q = \frac{L}{D} = 2\pi\omega \tag{3.31}$$

where ω is the calculated mean angular phase ratio at the signal peak.

It follows from equation 3.31 that when a reference interferometer data set is spectrally analysed the calculated angular phase ratio should be $\omega_{ref} = 1/2\pi$. Since the length ratio in this case is exactly unity there will be exactly one complete cycle in every 2π radians of phase advance. Since the phase ratio of two interferometers is equal to the length ratio, equation 2.10, it must also be true that the ratio of the calculated angular phase ratios of two interferometers is also equal to the ratio of interferometer OPDs. Equation 3.32 describes how the OPD of a measurement interferometer, D, is calculated from the results of the spectral analysis of the acquired reference and measurement interferometer data.

$$D = L\frac{q_{ref}}{q_{MI}} = L\frac{\omega_{ref}}{\omega_{MI}} \tag{3.32}$$

The theoretical length resolution of the analysis process depends upon the value of `freqStep` and the length of the reference interferometer. Thus the effective length increment that corresponds to `freqStep` can be found from

$$\Delta L = \frac{\texttt{freqStep}}{2\pi} L. \tag{3.33}$$

This means that for a reference interferometer with an OPD of $4.7m$, as used throughout the laboratory FSI investigations, and an analysis implementation using a `freqStep` value of 2×10^{-7} the nominal length resolution was around $0.03\mu m$. This resolution may be further improved by the fitting procedure applied to the identified spectral peaks.

3.5.2 Length Corrections

The effect of optical path length variations due to changes in the refractive index of the air within the interferometers was modelled and corrected for. These corrections are limited since the RTRS FSI systems will contain an evacuated reference and evacuated internal interferometers leaving only the minimal effects on the external interferometers to be corrected. The applied corrections assume dry air with standard composition of CO_2 and no atmospheric contaminants, such as oil vapour. The basis of the applied corrections come

from the Edlén equation [68] which was subsequently modified and corrected by Birch and Downs [69][70].

The corrections are applied by determining the refractivity, ρ, which is the departure of the refractive index from unity. The refractivity of the air within the interferometers was calculated using equation 3.34.

$$\rho_{air} \equiv n_{air} - 1 = \left(\frac{Z_{sa}T_{sa}}{Z_{air}T_{air}}\right)\left(\frac{k_1}{k_0 - \sigma^2} + \frac{k_3}{k_2 - \sigma^2}\right).10^{-8} \tag{3.34}$$

where Z_{sa} and Z_{air} are the compressibilities of standard air and air respectively and are found from equation 3.35; T_{air} is the air temperature in K, $T_{sa} = 288.15K$; $k_0 = 238.0185\mu m^{-2}$; $k_1 = 5792105\mu m^{-2}$; $k_2 = 57.362\mu m^{-2}$; $k_3 = 167917\mu m^{-2}$; and σ is the wavenumber (the reciprocal of the vacuum wavelength) in μm^{-1}.

$$Z = 1 - \left(\frac{P}{T}\right)\left(a_0 + a_1\vartheta + a_2\vartheta^2\right) \tag{3.35}$$

where P is the pressure in Pa; T is the temperature in K; $a_0 = 1.58123 \times 10^{-6}KPa^{-1}$; $a_1 = -2.9331 \times 10^{-8}Pa^{-1}$; $a_2 = 1.1043 \times 10^{-10}K^{-1}Pa^{-1}$; and ϑ is the temperature in °C.

The coefficients used are taken from Ciddor [71] since these are the most up to date and are valid into the infrared therefore providing the best description for wavelengths around $1550nm$. They are also valid for a wide range of CO_2 concentrations and humidity values which is important for measurements undertaken in a tunnel since the atmospheric conditions may well vary more significantly than in a laboratory. The calculated values of the coefficients assume 0% humidity with a CO_2 composition of $450ppm$ at standard atmospheric pressure ($101.325kPa$).

The primary correction was for changes in refractive index as a function of temperature. The temperature range investigated was 18 to 26°C which was standard operating range for the laboratory. Figure 3.9 shows the calculated refractivity, as a function of temperature for the investigated range with the results of a linear fit to calculated refractivity values shown in table 3.1. These results predict approximately a $0.9ppm/°C$ decrease in the refractivity of the air within the laboratory.

Parameter	**Value**
Gradient / ppm/K	-0.90663 ± 0.00072
Intercept / K	286.747 ± 0.016

Table 3.1: The results of a linear fit to calculated refractivity as a function of temperature.

Each calculated MI OPD was corrected via the use of equation 3.36.

$$D_{corr} = L\left(\frac{\omega_{ref}}{\omega_{MI}}\right)\left[1 + \rho(\vartheta_{ref}) - \rho(\vartheta_{MI})\right] \tag{3.36}$$

where ϑ_{ref} and ϑ_{MI} were the scan averaged air temperatures, in °C, within the Michelson Reference Interferometer and the measurement interferometer respectively.

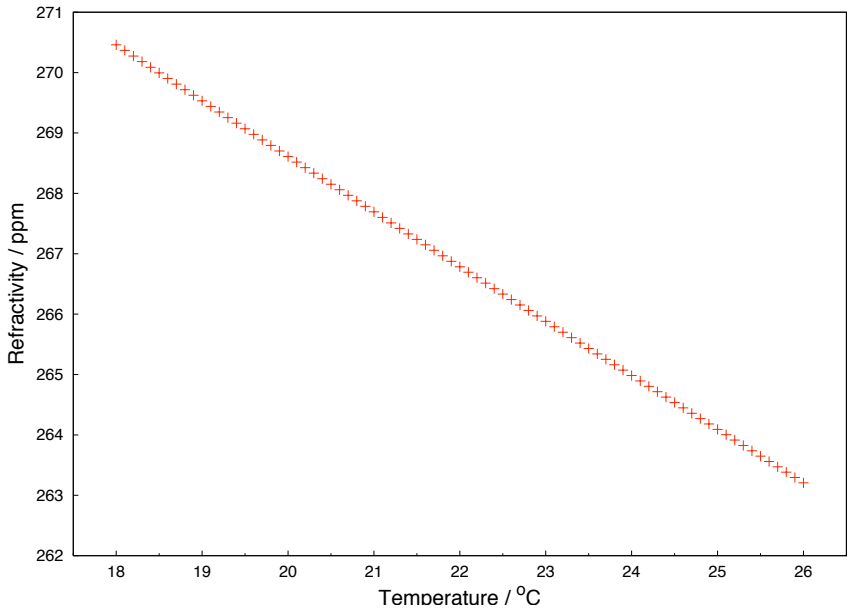

Figure 3.9: The calculated refractivity of air as a function of temperature for the nominal operating range within the laboratory.

The refractive index also varied as a function of pressure. The pressure range investigated was 960 to 1040$mBar$ which was the atmospheric pressure range expected within the laboratory. Figure 3.10 shows the calculated refractivity as a function of atmospheric pressure for the investigated range with the results of a linear fit to calculated refractivity values shown in table 3.2. These results predict approximately a 0.27$ppm/mBar$ increase in the refractivity of the air within the laboratory.

Parameter	Value
Gradient / $ppm/mBar$	$0.265204 \pm 2.534 \times 10^{-7}$
Intercept / $mBar$	-0.107685 ± 0.0002535

Table 3.2: The results of a linear fit to calculated refractivity as a function of atmospheric Pressure.

The refractivity dependance upon water vapour content within the air was also investigated. The absolute refractivity of water vapour at the standard conditions (20°C, 1333Pa) was calculated using equation 3.37.

$$\rho_{ws} \equiv n_{ws} - 1 = 1.022(w_0 + w_1\sigma^2 + w_2\sigma^4 + w_3\sigma^6).10^{-8} \tag{3.37}$$

where $w_0 = 295.235\mu m^{-2}$; $w_1 = 2.6422\mu m^{-2}$; $w_2 = -0.032380\mu m^{-4}$; $w_3 = 0.004028\mu m^{-6}$; and σ is the wavenumber in μm^{-1}. Once again the coefficients are taken from Ciddor [71].

The refractivity of wet air is given by equation 3.38.

$$\rho_{RH} = \rho_{air}(1 + RH\rho_{ws}) \tag{3.38}$$

where RH is the relative humidity in %. The calculated refractivity as a function of relative humidity is shown in figure 3.11. The results of a linear fit to the calculated data are given

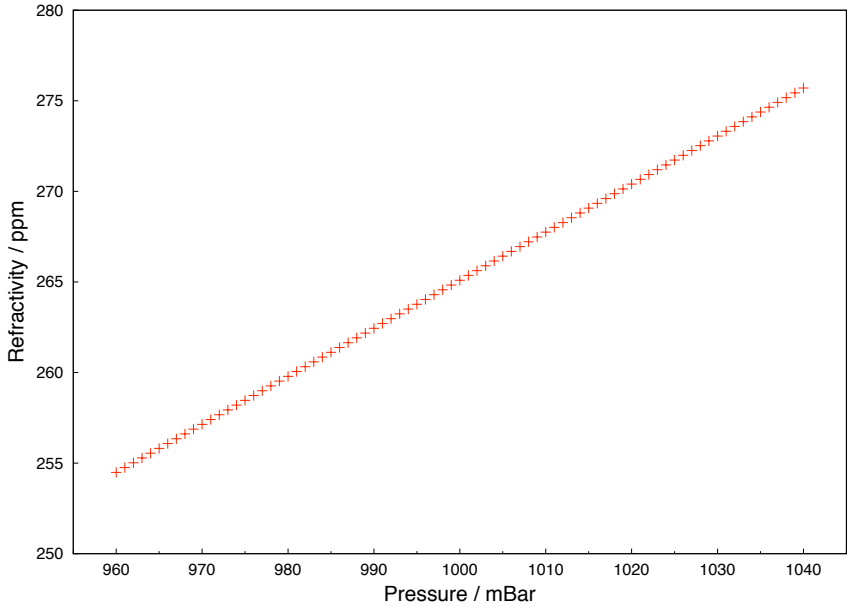

Figure 3.10: The calculated refractivity of air as a function of atmospheric pressure for the range expected within the laboratory.

in table 3.3. These results predict approximately a $30ppb/\%$ increase in the refractivity of air with respect to relative humidity. No corrections for variations in the water vapour content of the laboratory air were applied in this investigation since the variation was expected to be low and the dependance is weak.

Parameter	Value
Gradient / $ppm/\%$	$0.0302849 \pm 8 \times 10^{-7}$
Intercept / K	$273.26 \pm 1 \times 10^{-5}$

Table 3.3: The results of a linear fit to calculated refractivity values as a function of the relative water vapour content of the laboratory air.

The effects of variations in the CO_2 content of air have not been accounted for in this investigation. No relevant data was acquired within the laboratory and so no corrections were applied. However the effects of CO_2 concentration variations are expected to be much greater within the enclosed accelerator tunnel and so a correction of the form shown in equation 3.39 may be required for the open air measurements.

$$\rho_{axs} \equiv n_{axs} - 1 = \rho_{air}[1 + 0.534 \times 10^{-6}(x_c - 450)] \tag{3.39}$$

where ρ_{air} is the refractivity of air, determined from equation 3.34, and x_c is the measured concentration of CO_2 in ppm.

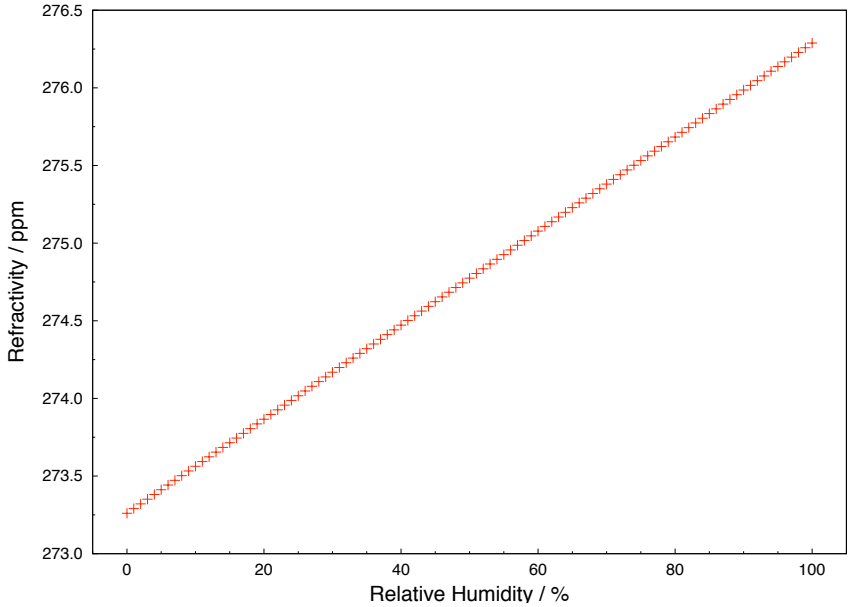

Figure 3.11: The calculated refractivity of air as a function of the relative water vapour content of the laboratory air.

3.6 Summary

An overview of the implemented analysis procedure is given in figure 3.1. The Phase Analysis process produces a continuous record of the phase advance within the reference interferometer during each laser scan. This provides a method of mapping the data acquired in all other interferometers into the laser frequency domain. This removes the effects of laser tuning rate variations during the scan. The implemented algorithm requires a high quality continuous interferometric signal to perform adequately. Other phase determination methods are currently being investigated which should prove to be more robust with respect to noise and signal discontinuities.

The application of the Spectral Analysis procedure allows the periodic components of the acquired interferometric signals to be evaluated. This technique will allow extremely low strength periodic signals to be resolved. The use of the reference interferometer phase advance mapping provides direct access to the interferometer phase ratio from the resultant spectral output. The calculated interferometer OPDs are then modified using additionally acquired environmental data.

Chapter 4

Evaluation of Analysis and OPD Determination Techniques

4.1 Introduction

This chapter describes the development of software designed to test and verify the analysis implementation before providing a full evaluation of the analysis performance in a both nominal and extraordinary circumstances. This process involved the simulation of data representative of that acquired within the laboratory and the RTRS. The comparison of simulated and extracted values allowed the determination of the expected measurement precision, accuracy and resolution as well as providing a means of investigating the systematic effects introduced during the analysis.

4.2 Data Simulation

The data simulation software performed two roles. Firstly it was used to produce simplified data throughout the development of the analysis process for the purpose of debugging. This simulated data was not necessarily fully characteristic of acquired data. The second role was to simulate data that corresponded as closely as possible to laboratory data. This allowed the performance of the analysis to be assessed via the comparison of extracted values with input parameters.

The simulation process was designed to produce output data files that contained the simulated intensities of one or more interferometers along with the corresponding parameter and log files. Various other outputs from the simulations could also be written to file. To do this initial parameter values had to be defined, these were chosen to reflect the parameters that could be controlled when configuring an experimental investigation in the laboratory. The inputs required by the simulation software are given below.

Interferometer OPD This parameter was the primary factor in determining the frequency of the simulated interferometric signal.

Laser Parameters The start and finish wavelengths of the laser scan and the global rate of change of the wavelength. Together these parameters determined the period of the simulated laser scan.

Number of Data Points This determined the DAQ rate since the scan period was defined by the laser parameters.

Interferometer Signal-to-Noise Ratio This parameter allowed the high signal quality of the internal system and the low quality signals of the external system to be investigated as well as providing a means of determining the limits of the analysis.

For each point the simulation code used these predefined inputs to calculate a phase and an intensity value. The first step in the process was to determine the local laser tuning rate, i.e. the instantaneous rate of change of frequency. To 1st order this was the same as the predefined global tuning rate however the fluctuations of this rate which were produced by the FSI laser were modelled and are describe in detail in section 4.2.1. Having determined the actual tuning rate the optical frequency at time t and the change in frequency during the interval $t = 0$ to t was determined using equations 4.1 and 4.2.

$$\nu|_t = \nu|_{t-\Delta t} - \frac{\partial \nu}{\partial t}\Delta t \tag{4.1}$$

$$\Delta\nu|_t = \nu|_{t=0} - \nu|_t \tag{4.2}$$

where $\frac{\partial \nu}{\partial t}$ is the actual tuning rate and Δt is the time interval between data points[1].

The phase at time t was subsequently calculated using equation 4.3 and the intensity from equation 4.4 which both follow directly from equation 2.8 discussed in section 2.2.1.

$$\Phi|_t = \left(\frac{2\pi}{c}\right)\Delta\nu|_t L \tag{4.3}$$

$$I|_t = \cos\left(\Phi|_t\right) + noise \tag{4.4}$$

details of the *noise* factor are described in section 4.2.2.

4.2.1 Laser Tuning Curve Model

The aim of the laser tuning curve model was to reproduce the output frequency time dependance of the FSI laser. This allowed for the verification of the algorithms within the phase analysis process with respect to the laser tuning curve parameters. It also provided details of the regime in which the spectral analysis should be independent of the details of laser tuning curve.

[1]During nominal laser operation, described in section 2.3.1, tuning occurred in the direction of increasing wavelength, and therefore decreasing frequency. This convention was maintained in equations 4.1 and 4.2 and throughout the simulation process for consistency.

The global tuning rate, $\frac{\partial\nu}{\partial t}|_{global}$, was modified by the addition of a sinusoidal variation of the form shown in equation 4.5 to produce the actual tuning rate $\frac{\partial\nu}{\partial t}$.

$$\frac{\partial\nu}{\partial t} = \left.\frac{\partial\nu}{\partial t}\right|_{global} \times \left[1 + a\sin\left(\frac{n\Delta t}{\tau} + \phi\right)\right] \tag{4.5}$$

where a is the amplitude of oscillation about the global tuning rate; n is the DAQ index; Δt is the time interval between data points; τ and ϕ are the period and the phase of the oscillations respectively. The calculated value of the actual rate of change of frequency was then used in equation 4.1 and the simulation of interferometer intensity proceeded as described above.

The values of the parameters used to model the laser tuning curve variations were extracted from data acquired using the laboratory FSI laser, see section 2.3.1. An arbitrary value was chosen for the phase, ϕ. The parameter values used to simulate the data presented in this chapter are shown in table 4.1.

Parameter	**Value**
a	5×10^{-5}
τ / μs	630
ϕ	1.3094

Table 4.1: The parameter values, relating to equation 4.5, used to model the variations in laser tuning rate during the simulation of interferometric data.

The effect of the addition of a sinusoidal variation to the global rate of change of frequency on the output intensity of an interferometer is illustrated in figure 4.1. Figure 4.1a shows simulated data produced with a linear tuning rate whilst figure 4.1b shows simulated data where the sinusoidal modification to the tuning rate has been introduced. To illustrate the affect of the sinusoidal variation the difference is shown in figure 4.1c. The areas where the sign of the difference is predominantly the same indicates when the sinusoidal variation has produced the greatest deviations from the linear tuning rate case.

4.2.2 Noise Model

Noise was introduced to the simulated interferometric signals by the addition of Gaussian weighted random deviations. The relative noise level was scaled by the predefined interferometer signal-to-noise ratio. This simple noise model provided acceptable simulated interferometric signals despite not fully characterising the complexities of the noise produced within the light source and amplifier since the Phase Analysis procedure (detailed in section 3.3), where noise may significantly effect results, was only performed on reference interferometer data where an extremely clean, high quality signal can be guaranteed. The output values of the Spectral Analysis, described in section 3.4, were only effected by noise at frequencies close to that of the signal. Therefore the overall OPD determination ability was unaffected by the presence of noise at frequencies away from the interferometric signal frequency.

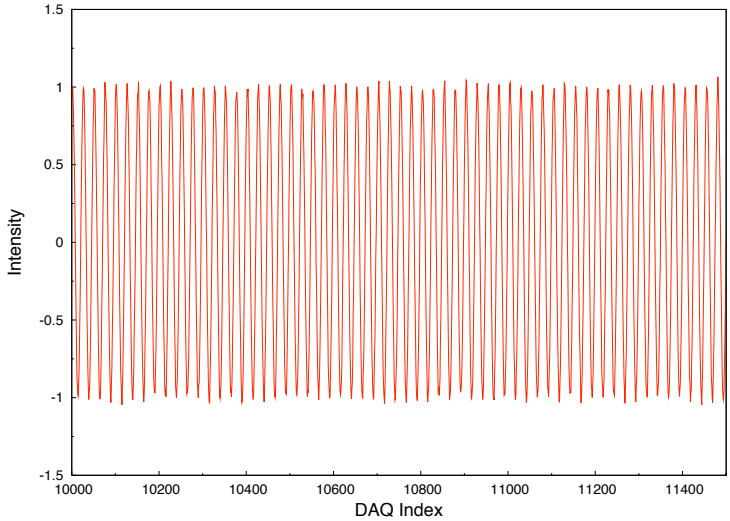

(a) Signal produced with a linear tuning rate.

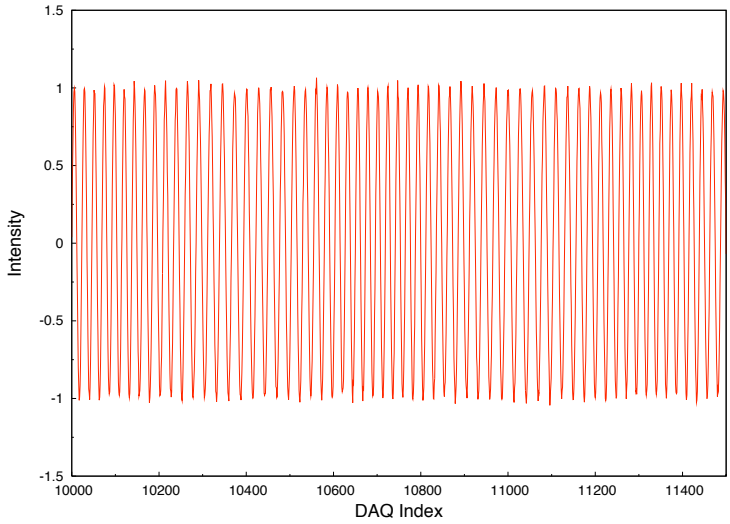

(b) Signal produced with a sinusoidal tuning curve variation.

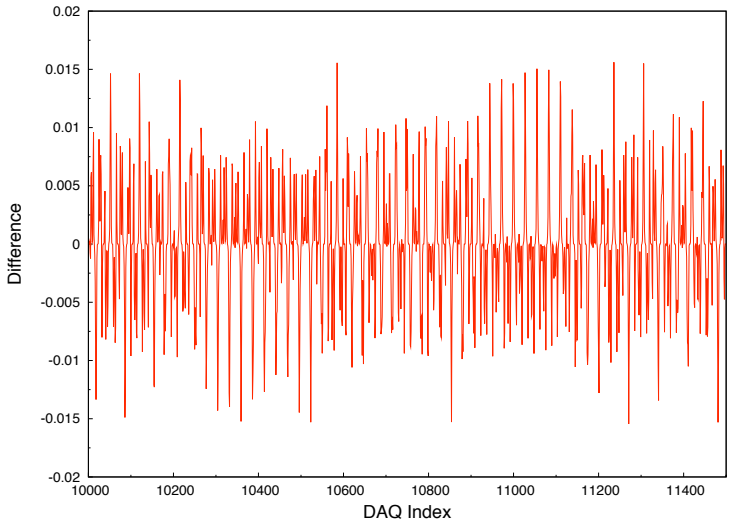

(c) Difference between the two signals.

Figure 4.1: A comparison between simulated reference interferometer data with linear and sinusoidal oscillating laser tuning curves.

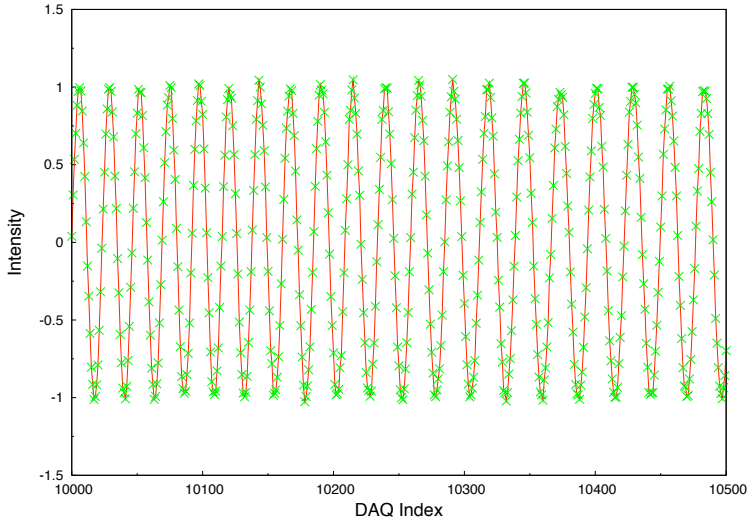

(a) A simulated reference interferometer signal with an OPD of $4.7m$ and SNR of 40.

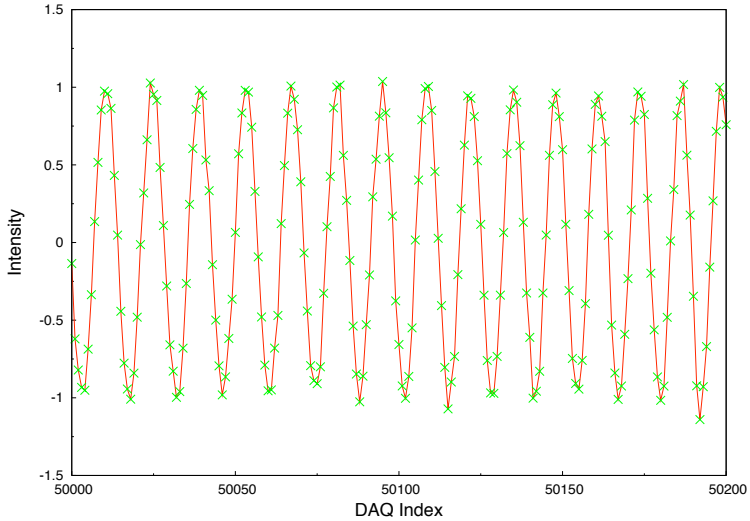

(b) A simulated internal interferometer signal with an OPD of $9.0m$ and SNR of 20.

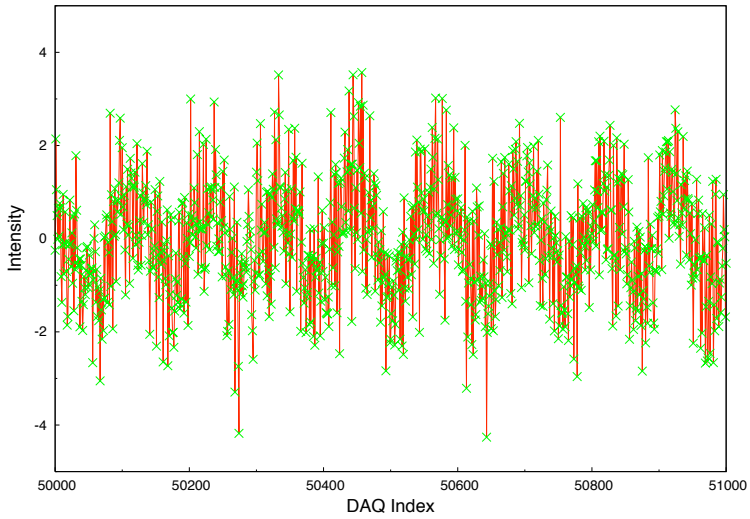

(c) A simulated external interferometer signal with an OPD of $0.9m$ and SNR of 1.

Figure 4.2: Comparison of simulated reference, internal and external interferometric signals.

The post-interference noise sources, such as the photodetector and the digitisation process, have been considered to be Gaussian. Hence, the *noise* in equation 4.4 is a Gaussian distributed random number scaled by the inverse of the input signal-to-noise ratio for each simulated interferometer. The SNR values used during nominal simulations were 40, 20 and 1 for the reference, internal and external interferometers respectively. The fringe patterns produced from such a simulation are shown in figure 4.2

4.3 Nominal Performance Characterisation

The first stage in the evaluation of the analysis procedure involved using simulated data to determine the nominal performance characteristics. The three performance measures used are described below.

Precision A measure of the extent to which the analysis produced the same result given identical simulation OPDs. This measure may also be referred to as the *repeatability* or the *reproducibility*. The precision was quantified by the standard deviation from the mean of a set of measurements with identical OPDs, $\sigma(D)$.

Accuracy A measure of the degree to which the analysis produced a result that conformed with the simulated OPD. The accuracy was quantified by the deviation of the mean of a set of measurements from the true value[2], $\langle D \rangle - D_{true}$.

Resolution A measure of the ability of the analysis to identify a variation in the simulated OPD. The resolution was quantified by evaluating the smallest increase in input value that the analysis could correctly identify as an OPD increase.

The precision investigations provided information on the inherent scan-to-scan fluctuations in determined OPD results. The accuracy studies produced a measure of the potential of the analysis to correctly determine interferometer OPDs. The presence of systematic effects introduced by the analysis were also evaluated within the accuracy investigation. The smallest detectable OPD variation was estimated by the investigations into resolution. These investigations involved the production of simulated laser scans that represented data acquired under nominal operating conditions for both the internal and external measurement systems. The scan and interferometer parameters used to produce the simulated data are given in tables 4.2 and 4.3 respectively[3].

4.3.1 Precision

The precision of the analysis process was investigated by simulating multiple scans with identical input parameters, only the random number seeds used to generate the noise were

[2]This is equivalent to the deviation of the mean of the residuals from zero.

[3]The value of external SNR used corresponds to the expected value for a transverse retroreflector displacement of around $25mm$.

Parameter	Value
Initial Wavelength / nm	1535
Final Wavelength / nm	1565
Global Tuning Rate / nm/s	40
Number of Points Simulated	1 500 000
Effective DAQ Rate / MHz	2

Table 4.2: Scan input parameters used to simulate data for the characterisation of nominal FSI analysis performance.

	Reference	Internal	External
Simulated OPD / m	4.700000	8.999998	0.899998
SNR	40	20	1

Table 4.3: Interferometer input parameters used to simulate data for the characterisation of nominal FSI analysis performance. The SNR values are estimates based on preliminary laboratory investigations.

varied from scan-to-scan. The determined interferometer OPDs were then compared to the simulated values. A total of 100 scans were simulated using the parameters given in tables 4.2 and 4.3. Each scan contained a reference and two measurement interferometers, one internal and one external.

Internal MI Precision

The determined OPD variations of the simulated internal interferometer are shown in figure 4.3 with the input OPD value indicated by the green line. A histogram of the determined OPD variations is displayed in figure 4.4. The mean value of determined OPD, the standard deviation from the mean and the sigma of the projection are given in table 4.4. The shift between the mean determined and simulated OPD is also shown as a comparison for the investigation presented in section 4.3.2.

Parameter	Value
Mean Determined OPD / m	8.999 997 962
Standard Deviation / μm	0.052
Sigma of Projection / μm	0.061
Mean Shift from Simulated OPD / μm	-0.038 ± 0.052

Table 4.4: Results of simulated internal interferometer OPD determination precision.

The standard deviation of the determined OPD values for the simulated internal FSI system indicates the analysis process exceeded the precision implied from the `freqStep` parameter value of 2×10^{-7}. As described in section 3.5.1 the separation of examined angular phase ratios within the spectral analysis process relates to OPD increments of around

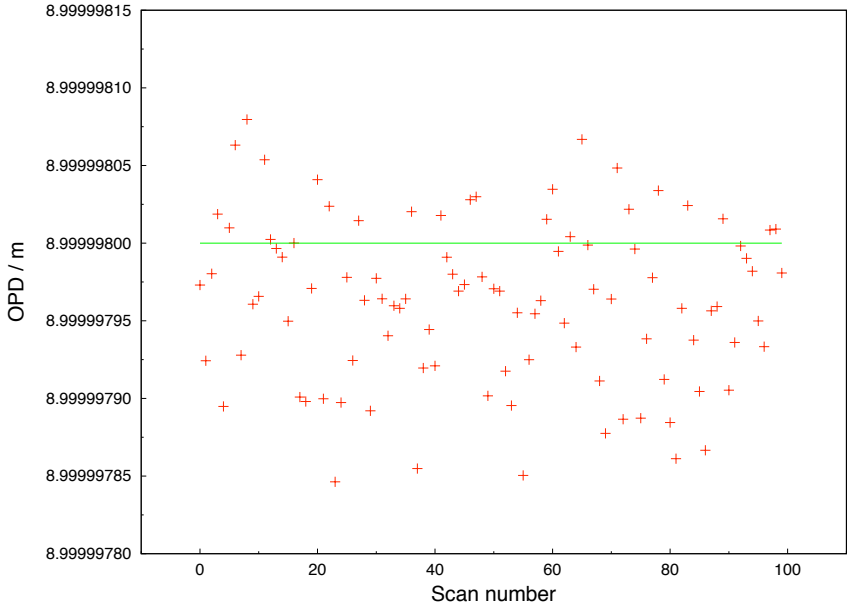

Figure 4.3: The OPD variations for 100 simulated laser scans of an internal interferometer produced using the input parameters given in tables 4.2 and 4.3. The green line indicates the simulated OPD.

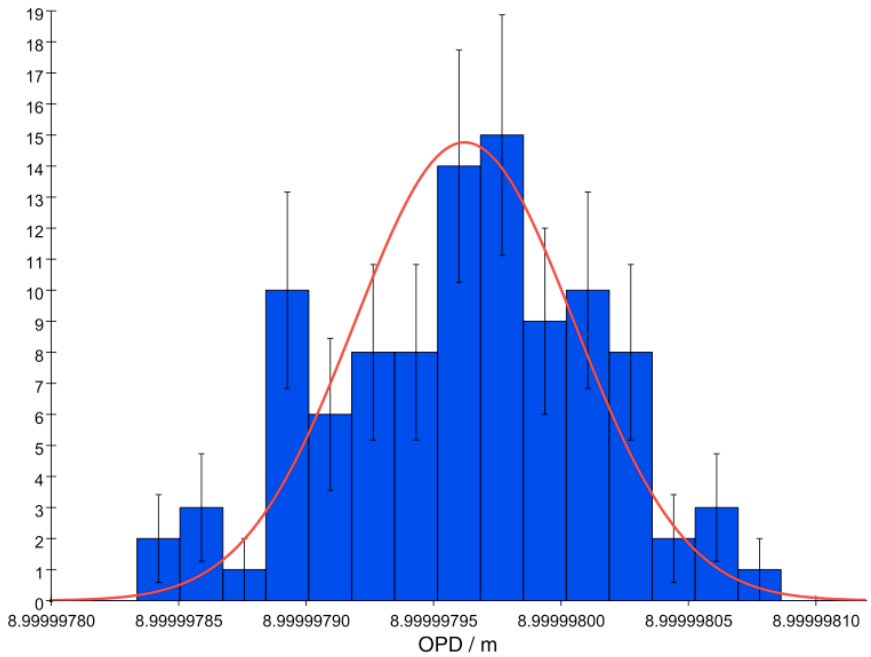

Figure 4.4: The projected histogram of determined OPDs for 100 simulated laser scans of an internal interferometer produced using the input parameters given in tables 4.2 and 4.3.

$0.06\mu m$ for the internal system. This nominal limit was exceeded by fitting the resultant spectral peaks to determine the mean position more precisely. Hence for interferometer signals relating to an OPD of $9m$ with a signal-to-noise ratio of 20 the expected nominal OPD determination precision can be achieved.

External MI Precision

The determined OPD variations of the simulated external interferometer are shown in figure 4.5 with the input OPD value indicated by the green line. A histogram of the determined OPD variations is displayed in figure 4.6. The mean value of determined OPD, the standard deviation from the mean and the sigma of the projection are given in table 4.5. The shift between the mean determined and simulated OPD is also shown as a comparison for the investigation presented in section 4.3.2.

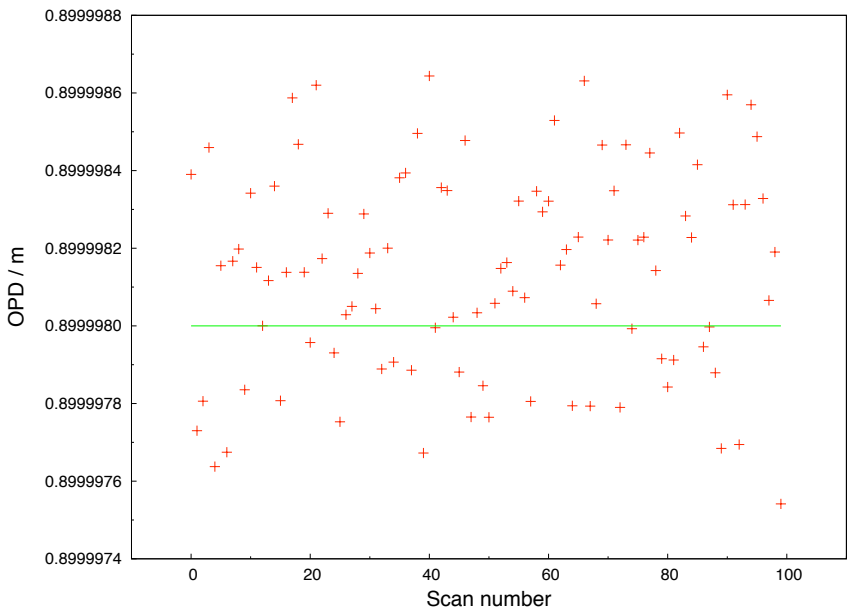

Figure 4.5: The OPD variations for 100 simulated laser scans of an external interferometer produced using the input parameters given in tables 4.2 and 4.3. The green line indicates the simulated OPD.

Parameter	Value
Mean Determined OPD / m	0.899 981 360
Standard Deviation / μm	0.266
Sigma of Projection / μm	0.298
Mean Shift from Simulated OPD / μm	0.136 ± 0.266

Table 4.5: Results of simulated external interferometer OPD determination precision.

The lower precision of the external FSI lines is due to the increased level of noise present within the signals. The larger standard deviation from the mean determined OPD and sigma

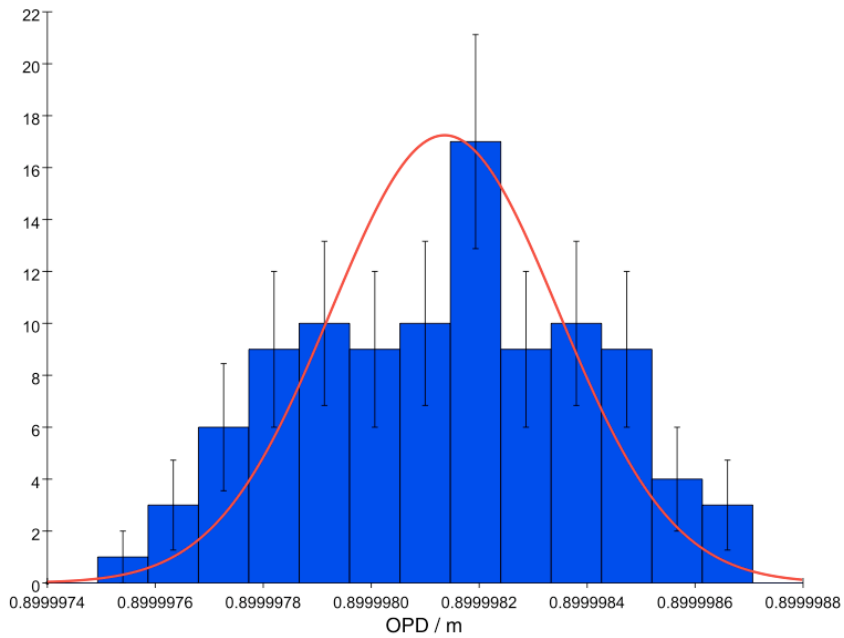

Figure 4.6: The projected histogram of determined OPDs for 100 simulated laser scans of an external interferometer produced using the input parameters given in tables 4.2 and 4.3.

of projection indicates that the examined angular phase ratio separation during the spectral analysis process is not the dominant factor in OPD determination precision when operating in the high noise regime. Hence a decrease in the `freqStep` parameter will not improve the interferometric OPD determination performance in this case. Further investigation into the effects of decreased signal-to-noise ratio on the OPD determination capabilities of the analysis are given in section 4.4.

4.3.2 Accuracy

The accuracy of the analysis process was investigated by simulating multiple laser scans with input OPD values modified from scan-to-scan (the noise random number seeds were also varied). The determined OPDs were then compared with the inputs to the simulation. A total of 200 scans were simulated with the input OPD varied in $100nm$ increments over a total range of $1\mu m$, producing 20 scans at each input OPD value.

Internal MI Accuracy

The correlation between the input and determined OPDs for the simulated internal system is shown in figure 4.7, the errorbars represent the standard deviation from the mean determined OPD of the 20 data sets simulated at each OPD. The results of the linear fit to the data, shown in green, are given in table 4.6. Figure 4.8 shows the difference be determined and input OPDs.

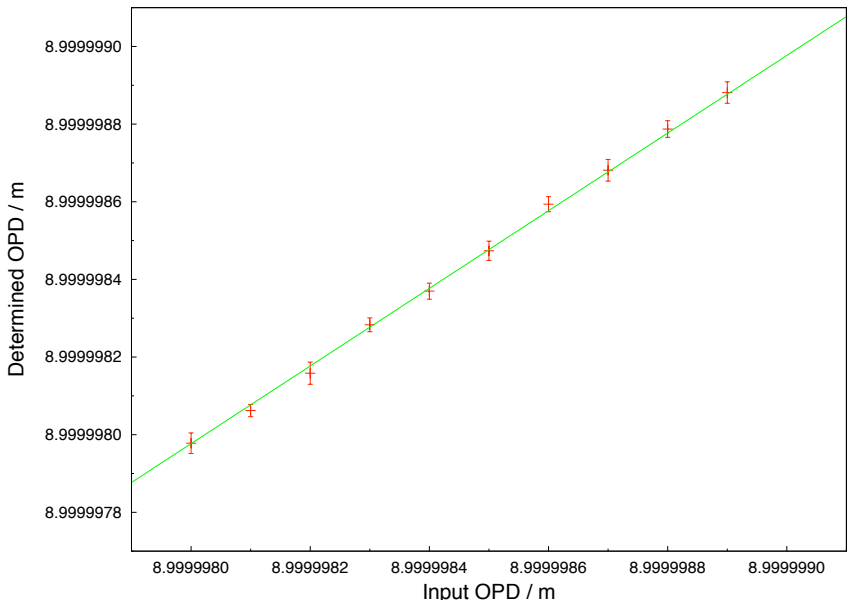

Figure 4.7: The correlation between simulated and determined OPDs for 200 simulated laser scans of an internal interferometer with input OPD increments of $100nm$. The green line indicates the best fit straight line.

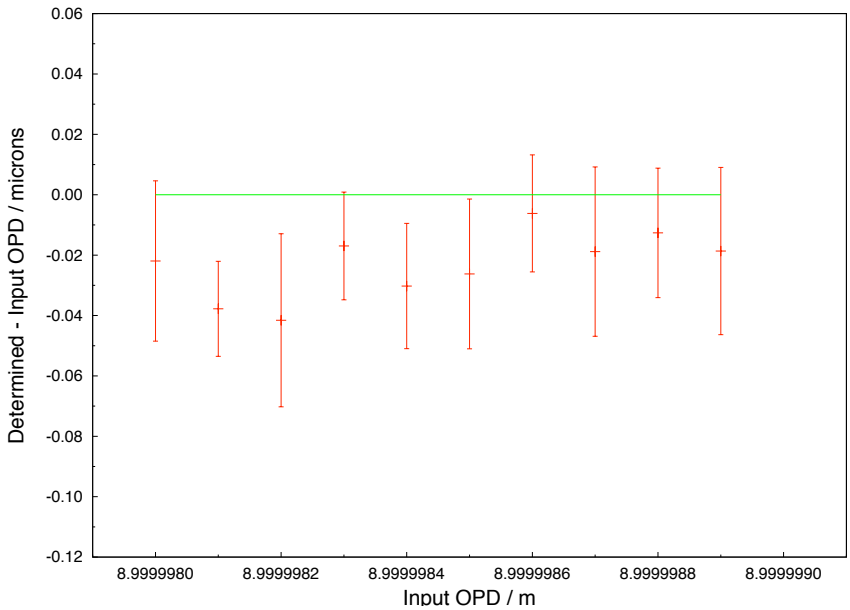

Figure 4.8: The difference between determined and input OPDs for simulated internal interferometer with input OPD increments of $100nm$.

Parameter	Value
Gradient	0.999997 ± 0.012851
Intercept / μm	2.173 ± 1.157
RMS of Residuals / μm	0.012
Mean Shift from Simulated OPD / μm	-0.023 ± 0.011

Table 4.6: Results of simulated internal interferometer OPD determination with varied input OPD values.

The fitted gradient to the determined OPD data is consistent with unity which indicates the analysis process successfully determined the simulated OPD increments. The intercept value is insignificant since the range of fitted data is very small and extremely far from the origin. The RMS of the residuals to the straight line fit shows the correlation between determined and simulated OPD was $12nm$ which corresponds to around $1.5ppb$. This provides a measure of the statistical error, however there exists an absolute difference between the simulated and determined OPDs of $23nm$ which corresponds to approximately $3.8ppb$.

External MI Accuracy

The correlation between the input and determined OPDs for the simulated external system is shown in figure 4.9, the errorbars represent the standard deviation from the mean determined OPD of the 20 data sets simulated at each OPD. The results of the linear fit to the data, shown in green, are given in table 4.7. Figure 4.10 shows the difference be determined and input OPDs..

Parameter	Value
Gradient	0.999958 ± 0.031974
Intercept / μm	0.506 ± 2.879
RMS of Residuals / μm	0.029
Mean Shift from Simulated OPD / μm	0.106 ± 0.027

Table 4.7: Results of simulated external interferometer OPD determination with varied input OPD values.

The gradient of the fit to the determined OPD data is consistent with unity which indicates the analysis process successfully determined the simulated OPD increments. The RMS of the residuals to the straight line fit shows the correlation between the determined and simulated OPDs was $29nm$ which corresponds to around $32ppb$. This provides an measure of the statistical error, however there exists an absolute difference between the simulated and determined OPDs of $106nm$ which corresponds to approximately $150ppb$.

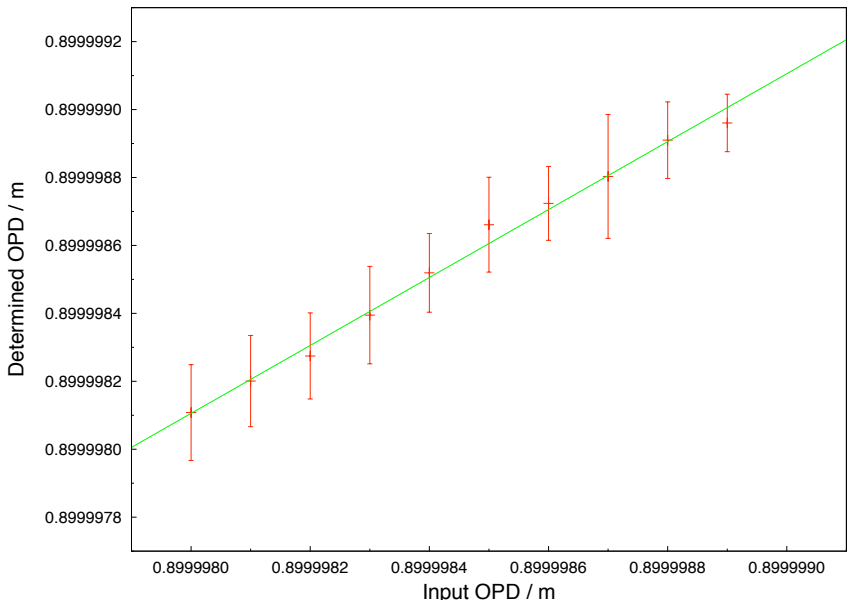

Figure 4.9: The correlation between simulated and determined OPDs for 200 simulated laser scans of an external interferometer with input OPD increments of $100nm$. The green line indicates the best fit straight line.

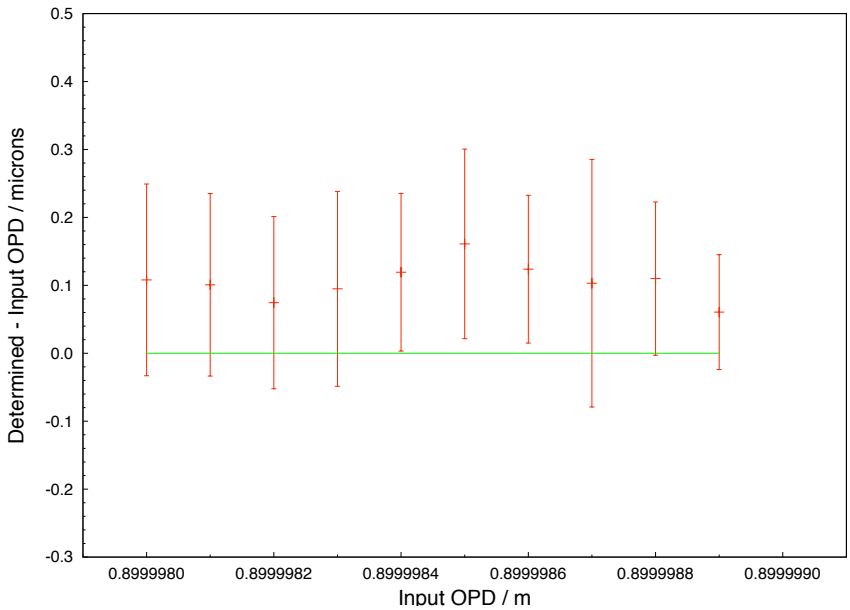

Figure 4.10: The difference between determined and input OPDs for simulated external interferometer with input OPD increments of $100nm$.

Systematic Effects

To investigate the difference between input and determined OPDs as a function of OPD internal interferometers were simulated with OPDs ranging from 0.5 to 9.5m. Figure 4.11 shows the difference between determined and simulated OPDs as a function of OPD over this range. The errorbars represent the standard deviation from the mean determined OPD of 20 simulated scans. The green line indicates a linear fir to the data.

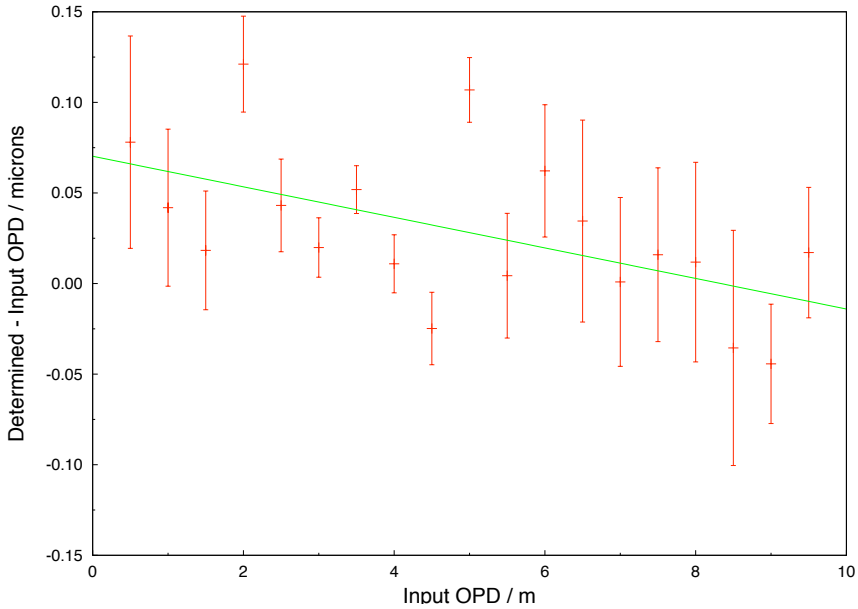

Figure 4.11: The difference in determined and simulated OPDs as a function of input OPD for simulated internal interferometers. The green line indicates a linear fit to the data.

The results of a linear fit to the difference between the determined and simulated OPDs as a function of OPD are given in table 4.8. These results provide confirmation that there is a systematic difference between the determined and simulated OPDs which is a function of interferometer OPD. This is consistent with the mean shift from simulated OPD values presented in the previous investigations.

Parameter	**Value**
Gradient / nm/m	-8.4 ± 3.1
Intercept / nm	70 ± 18
RMS of Residuals / nm	37
Mean Shift from Simulated OPD / nm	28 ± 43

Table 4.8: The linear fit results for the difference between the determined and input OPD as a function of OPD.

4.3.3 Resolution

The resolution of the analysis was evaluated in two ways. A value of the resolvable OPD variation given N measurements of each OPD, for both the internal and external systems, was predicted using the values of measurement precision calculated in section 4.3.1. Multiple sets of scans were also simulated with differing input OPDs to assess the ability of the analysis to identify OPD variations. Each set contained 100 scans which were produced with the same input OPD value. The simulated OPDs were incremented by a constant amount between each of the sets of scans. The gradient of the OPD variations between neighbouring sets of scans was found by dividing the mean OPD change observed within N scans by the constant input OPD increment, equation 4.6.

$$gradient = \frac{\langle \Delta D \rangle}{\Delta D_{true}} \tag{4.6}$$

The error on the gradient was given by the standard deviation of calculated gradients resulting from multiple simulations at constant OPD increments. An OPD increment was deemed to be resolved if the calculated gradient was positive and not compatible with zero.

Predicted Resolution

In the absence of any systematic error an OPD variation can be considered to be resolved if inequality 4.7 is satisfied.

$$\sigma(\langle D \rangle|_N - \langle D + \Delta D \rangle|_N) < \Delta D \tag{4.7}$$

where $\langle D \rangle$ is the mean determined OPD, N is the number of measurements, D is the true OPD and ΔD is the OPD variation.

Under the assumption that

$$\sigma(\langle D \rangle|_N) = \sigma(\langle D + \Delta D \rangle|_N) \tag{4.8}$$

and that the error on the mean of a set of N measurements scales as

$$\sigma(\langle D \rangle|_N) = \frac{1}{\sqrt{N}}\sigma(D) \tag{4.9}$$

where $\sigma(D)$ is the error on a single measurement (i.e. the precision). The resolution is predicted to be determined by the precision of the measurement system and the number of combined measurements. Therefore a variation in interferometer OPD is predicted to be fully resolved when N is sufficiently large such that

$$\sqrt{\frac{2}{N}}\sigma(D) \leq \Delta D_{true} \tag{4.10}$$

where ΔD_{true} is the true OPD variation.

The predicted resolutions of the measurement systems were estimated from the precision values found in section 4.3.1. The resolution of a single measurement was equal to the precision multiplied by a factor of $\sqrt{2}$. The resolution was expected to improve by a factor of $\frac{1}{\sqrt{N}}$ as more measurements were combined. The predicted measurement resolution values of the internal and external systems are given in table 4.9.

No. of Measurements	Internal Resolution	External Resolution
1	$73.5nm$	$376nm$
10	$23.3nm$	$119nm$
50	$10.4nm$	$53.2nm$
100	$7.35nm$	$37.6nm$

Table 4.9: The predicted resolutions for the internal and external FSI measurements systems for various numbers of measurements.

Internal MI Resolution

The investigation into the internal MI resolution involved simulating sets of scans with OPD increments of $10nm$ and $2nm$. The determined OPDs are shown in figure 4.12 as a function of simulated OPD value. Each displayed value is the mean of the determined OPDs of 100 simulated scans with the errorbars being the standard deviation from the mean. The determined OPDs are consistent with the input OPDs within the systematic uncertainties expressed in section 4.3.2. The standard deviation of each group of scans corresponds well with the value of internal MI measurement precision quoted in section 4.3.1. The mean and standard deviation of the OPD variation gradients, between the neighbouring sets of scans in figure 4.12, are given in table 4.10.

OPD Increment	Mean Gradient	Standard Deviation of Gradient
$10nm$	1.305	0.463
$2nm$	0.815	2.706

Table 4.10: The mean and standard deviation of the calculated OPD variation gradients for increments of $10nm$ and $2nm$ as part of the internal MI resolution investigation.

The calculated errors on the OPD variation gradient as a function of number of measurements are shown in figure 4.13 for both the $10nm$ and $2nm$ increment investigations. In both cases the expected $\frac{1}{\sqrt{N}}$ behaviour is present and the errors tends to zero as N is increased. A more insightful indicator of the resolution of the analysis is provided by looking at the difference between the OPD variation gradient and the error on the gradient. In the regime where an induced OPD variation has been fully resolved the gradient will approach 1 and the error will tend to 0, hence the difference will tend to 1. In the case of an unresolved OPD variation the difference should be significantly less than 1. A given increment is considered resolved when this indicator is positive. The difference between the calculated OPD variation gradient and the error on the gradient is shown in figure 4.14 as a function of the number of measurements.

The results of the investigation into internal MI resolution suggest that interferometer OPD variations of approximately $10nm$ can be resolved by the analysis with approximately 32 measurements. The simulated data sets with smaller OPD increments indicated that $2nm$ variations in OPD were beyond the resolution of the current implementation for a set of 100 measurements. This is consistent with the predictions given in table 4.9. The error

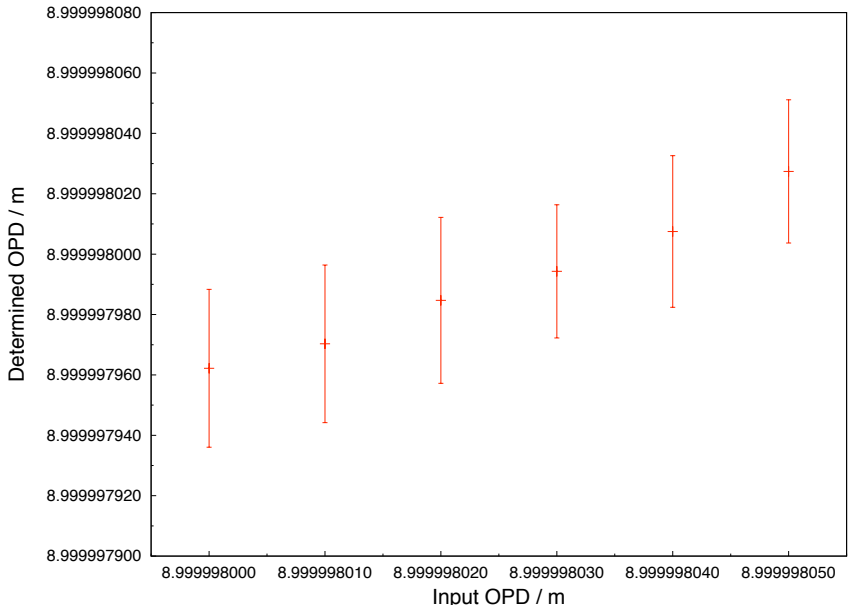

(a) Mean determined OPDs of groups of 100 scans for $10nm$ OPD increments.

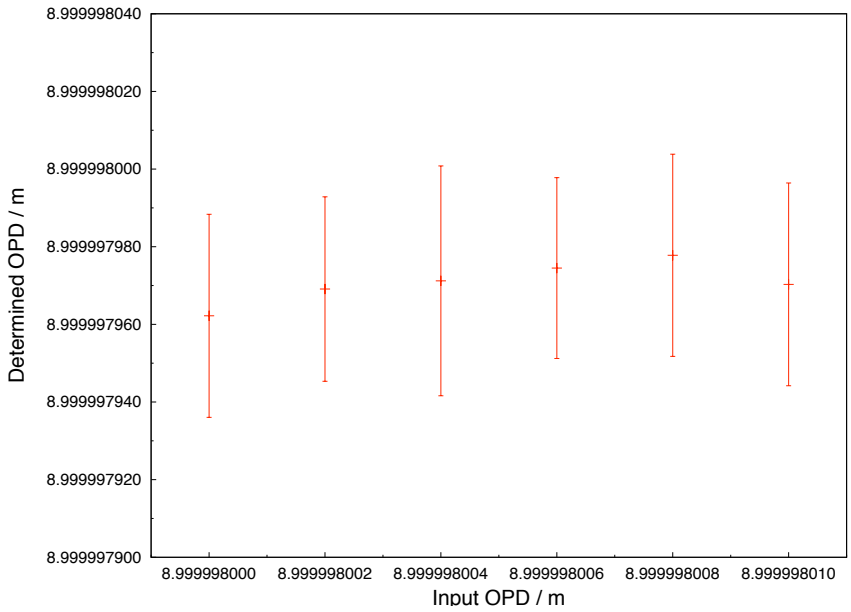

(b) Mean determined OPDs of groups of 100 scans for $2nm$ OPD increments.

Figure 4.12: The mean determined OPDs for groups of 100 scans as a function of simulated OPD values for increments of $10nm$, (a), and $2nm$, (b), as part of the internal MI resolution investigation.

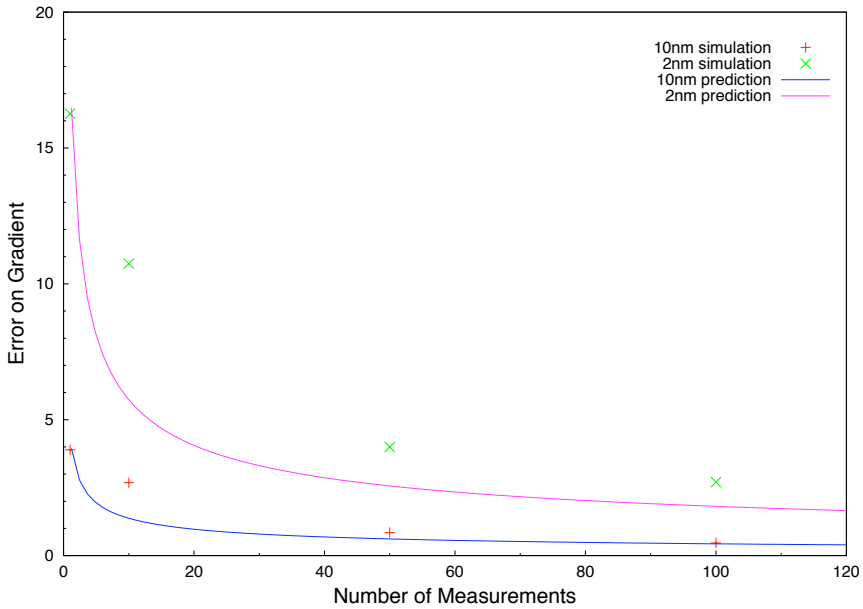

Figure 4.13: The calculated error on the gradient of the OPD variation as a function of the number of measurements for a series of simulated internal MIs with OPD variations of $10nm$ and $2nm$.

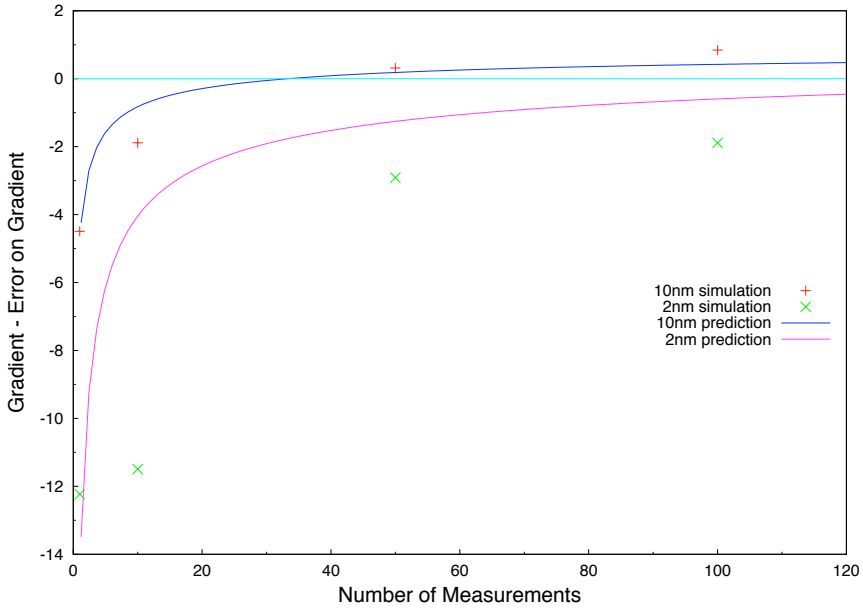

Figure 4.14: The difference between the determined gradient of the OPD variation and the error on the gradient as a function of the number of measurements for a series of simulated internal MIs with OPD variations of $10nm$ and $2nm$.

on the calculated OPD variation gradient decreases as $\frac{1}{\sqrt{N}}$ as expected in the case of OPD increments of $10nm$ and $2nm$ for sets of up to 100 measurements. An increase in measurement resolution beyond $\Delta D \approx 10nm$ is unnecessary since a fixed frequency interferometric system would be better suited to resolving OPD changes of $\mathcal{O}(1nm)$ if this were required.

External MI Resolution

To investigate the external MI resolution sets of scans with OPD increments of $100nm$ and $10nm$ were simulated. The determined OPDs are shown in figure 4.15 as a function of simulated OPD. The OPD values displayed are the mean of 100 simulated scans with the errorbars indicating the standard deviation from the mean. The determined OPDs are consistent with the simulated OPD values within the systematic uncertainties presented in section 4.3.2. The standard deviation of each group of simulated scans agrees well with the precision value quoted in section 4.3.1. The mean values of the gradient, between the neighbouring sets of scans in figure 4.15, are given in table 4.11.

OPD Increment	**Mean Gradient**	**Standard Deviation of Gradient**
$100nm$	0.919	0.206
$10nm$	1.521	2.818

Table 4.11: The mean and standard deviation of the calculated OPD variation gradients for increments of $100nm$ and $10nm$ as part of the external MI resolution investigation.

The calculated error on the OPD variation gradient as a function of number of measurements is shown in figure 4.16. The data clearly exhibits the expected $\frac{1}{\sqrt{N}}$ behaviour and the error tends to zero as N increases. Once again a more insightful indicator of the resolution is provided by the difference between the OPD variation gradient and the error on the gradient. This difference will approach 1 when an OPD variation is fully resolved and be significantly less than 1 for an unresolved OPD variation. The difference between the calculated OPD variation gradient and the error on the gradient is shown in figure 4.17 as a function of the number of measurements.

The results of the investigation into the resolution of the external measurement system suggest that OPD variations of approximately $100nm$ can be resolved by the analysis from a set of around 20 measurements. The simulated data sets with smaller OPD increments indicated that $10nm$ variations in OPD were beyond the resolution of the current analysis for a set of 100 measurements. This is consistent with the predictions given in table 4.9. The expected $\frac{1}{\sqrt{N}}$ decrease of the error on the calculated OPD variation gradient is observed for OPD increments of $100nm$ and $10nm$ for sets of up to 100 measurements. A further increase in resolution is not required since resolving OPD changes of $\mathcal{O}(10nm)$ from open air measurements is not practical. An additional measurement technique will be necessary if such a resolution is required.

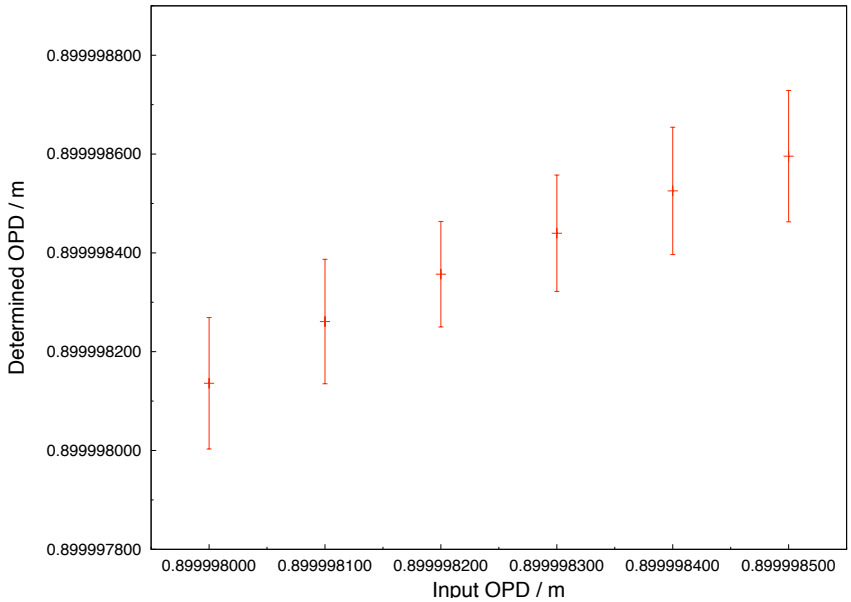

(a) Mean determined OPDs of groups of 100 scans for 100nm OPD increments.

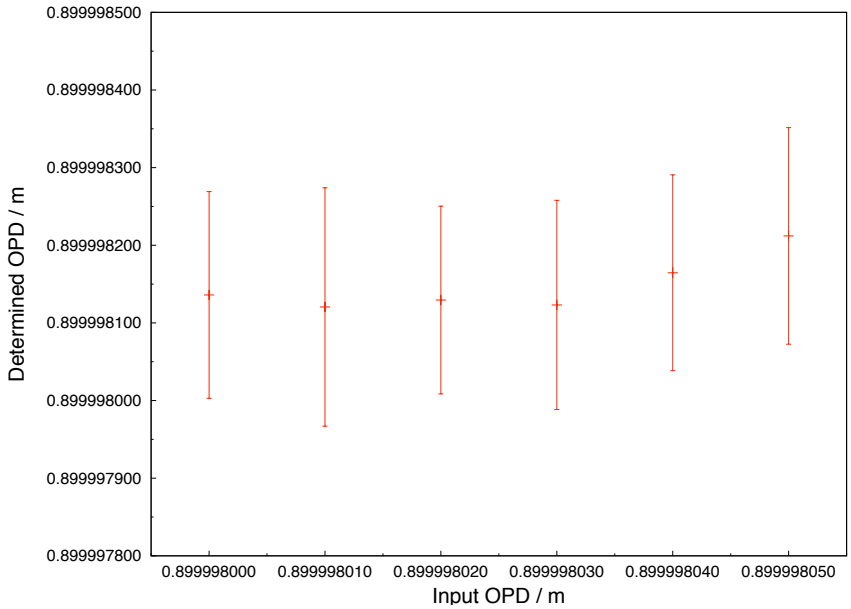

(b) Mean determined OPDs of groups of 100 scans for 10nm OPD increments.

Figure 4.15: The mean determined OPDs for sets of 100 scans as a function of simulated OPD values for increments of 100nm, (a), and 10nm, (b), as part of the external MI resolution investigation.

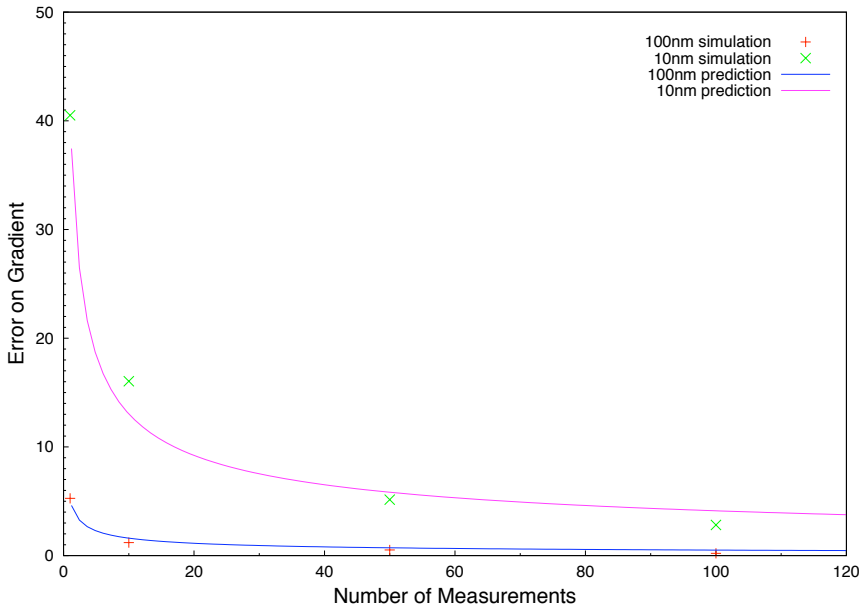

Figure 4.16: The calculated error on the gradient of the OPD variation as a function of the number of measurements for a series of simulated external MIs with OPD variations of $100nm$ and $10nm$.

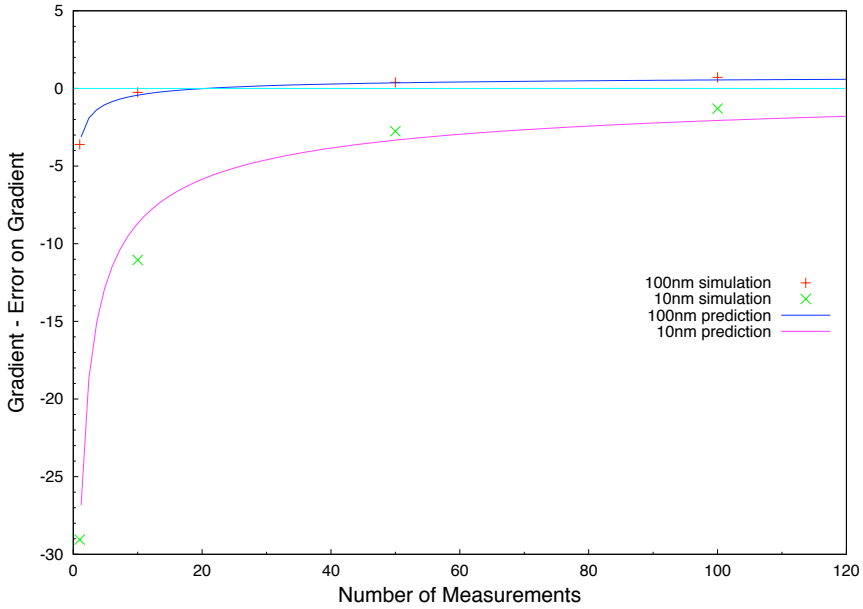

Figure 4.17: The difference between the determined gradient of the OPD variation and the error on the gradient as a function of the number of measurements for a series of simulated external MIs with OPD variations of $100nm$ and $10nm$.

4.4 OPD Determination from Low Quality Data

The affect of increasing interferometric noise level is studied in this section. The investigations presented here were designed to determine the performance of the analysis in conditions outside the expected nominal operating regimes. The purpose of these investigations was to gain a more complete understanding of the analysis by identifying the acceptable operating range of the measurement systems with respect to noise.

4.4.1 Affect of Noise within Measurement Interferometer Signals

The results presented in section 4.3.1 suggest that the nominal OPD determination precision of the analysis can be achieved when analysing signals with SNR of 20 whilst a reduced precision can be expected when analysing signals with SNR of 1. To investigate the affect of intensity noise on the performance of the analysis more thoroughly groups of 20 external scans were simulated with the same OPD for input SNR values from 20 to 0.05. The difference between the mean determined and simulated OPD for each of the SNR values is shown in figure 4.18, the errorbars represent the standard deviation from each mean determined OPD.

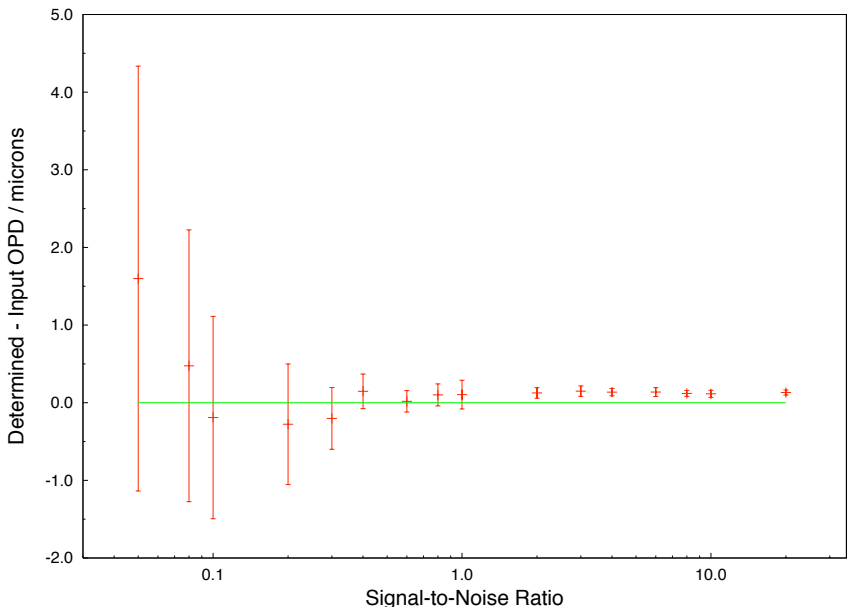

Figure 4.18: The difference between determined and input OPDs for simulated laser scans as a function of relative noise level.

The results shown in figure 4.18 indicate that the OPD determination precision of the analysis is approximately constant with respect to intensity noise level down to SNR of around 2. The measurement precision in this region is around $0.1\mu m$. The standard deviation of the groups of 20 simulated scans exceeds $1\mu m$ for signals with SNR of 0.2. At greater relative noise levels the OPD determination precision becomes further degraded. However in all cases the mean determined OPD is consistent with the input OPD after taking into account the systematic shift introduced by the analysis, as described in section 4.3.2.

The difference between the mean determined and simulated OPD was approximately constant with respect to noise down to SNR values of around 0.8. The magnitude of the difference between the mean determined and simulated OPD is around $0.12\mu m$ down to SNR values of around 1, this is consistent with the results given in table 4.7. At higher noise levels a greater fluctuation in the shift from the simulated OPD can been seen. However at SNR of less than 1 the values of OPD difference are consistent with the values seen in the lower noise cases. At SNR values less than 0.1 the magnitude of the difference fluctuates more widely and exceeds $1\mu m$.

This difference, however, is not the dominant source of error in the high noise regime since the OPD determination precision is approximately $5\mu m$. There appears to be no additional systematic error introduced as a function input SNR and so the measurement accuracy should be regained simply by acquiring more data sets from interferometers producing low quality signals.

The relationship between the input value of SNR, which is described in section 4.2.2, and the spectral SNR, which is the ratio of spectral peak height to the mean level of the entire spectrum, is shown in figure 4.19. It is clear that at low noise levels the spectral SNR should be approximately constant since the height of the spectral signal peak is determined by the number of acquired fringes, and the amplitude of the signal, whilst the background level resulting from the noise is significantly less than the signal peak height. Hence the mean spectral level is dominated by the signal peak and so the spectral SNR remains constant. As the noise level increases there is a corresponding decrease in spectral SNR. In the very high noise regime the spectral background level approaches the signal peak height since the power present at the signal frequency is no greater than that at all other frequencies. Thus the spectral SNR tends to 1 as the input signal-to-noise ratio approaches 0.

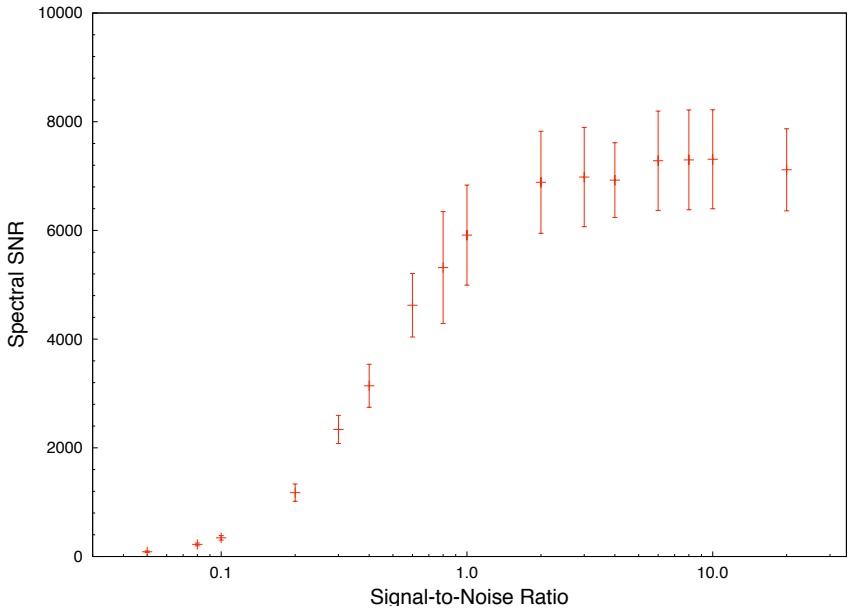

Figure 4.19: The spectral SNR (signal peak height compared to mean spectral level) as a function of input signal-to-noise ratio for a simulated external interferometer.

For signal SNR values above 2 the spectral SNR is approximately constant, in this region the OPD determination precision is $\leq 0.1\mu m$. The drop off in spectral SNR from 2 to 0.1 corresponds to the observed deterioration in OPD determination precision in the same region. The spectral SNR approaches 1 for very low signal SNR. For spectral SNR values below 100 the corresponding OPD determination precision is around $5\mu m$. The OPD determination precision as a function of spectral SNR is shown in figure 4.20.

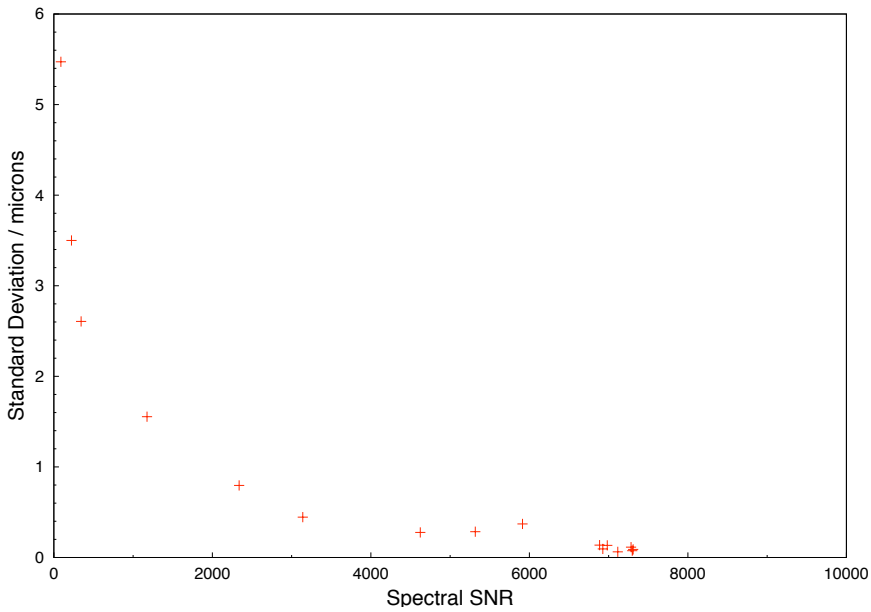

Figure 4.20: The OPD determination precision as a function of spectral SNR (signal peak height compared to mean spectral level) for a simulated external interferometer.

4.4.2 Affect of Noise within Reference Interferometer Signals

Quantifying the affects of the presence of noise within reference interferometer signals is much more complicated. Although the automated Carré step size algorithm, described in section 3.3.1, is capable of dealing with low levels of noise it is not able to cope with large amounts of noise or discontinuities within the reference interferometer signal. Hence poor quality signals may well produce inaccurate step size calculations which directly affects the ability of the Carré phase extraction algorithm to correctly assign phase values. This clearly will also have a detrimental effect on the phase unwrapping process. The extraction and unwrapping error removal algorithms were only designed to correct isolated errors and not to reconstruct large sections of incorrectly calculated phase advance values. Hence they can rapidly become overwhelmed and may potentially descend into infinite loops whilst struggling to provide corrected phase values. Consequently, without an accurate representation of the laser tuning during a scan obtained from the reference interferometer phase advance data, a successful outcome from spectral analysis process is impossible.

A fundamental underlying principle of the FSI process as a whole is that the chosen reference interferometer data contains a well sampled, clean and continuous interferometric

signal. In the laboratory and in the RTRS this must be achieved for the FSI measurement systems to function adequately. Providing an interferometer from which a suitable signal can be acquired must be achieved through specific mechanical and electronic design efforts. The current analysis procedure does not contain any scan rejection functionality however discarding acquired scans which contain low quality reference interferometer signals may well be the only way of dealing with these exceptional circumstances.

4.5 Summary

The investigations described in this chapter deal with the performance characterisation of the FSI analysis procedure. A software simulation of the laser system was created to produce simulated interferometric signals with which to test the analysis. Nominal characterisation of OPD determination precision (repeatability), accuracy and resolution were undertaken for both the internal and external FSI systems. A summary of the results from these investigation is shown in table 4.12.

Investigated Parameter	**Value**
Internal FSI Precision / μm	0.038(syst) + 0.052(stat)
Internal FSI Accuracy / μm	0.023(syst) + 0.012(stat)
Internal FSI Resolution / μm	0.074 @ $N = 1$ ≈ 0.007 @ $N = 50$
External FSI Precision / μm	0.136(syst) + 0.266(stat)
External FSI Accuracy / μm	0.106(syst) + 0.029(stat)
External FSI Resolution / μm	0.376 @ $N = 1$ ≈ 0.068 @ $N = 50$

Table 4.12: A summary of the nominal performance of the analysis for the internal and external FSI systems.

The performance of the analysis was also investigated under conditions outside the normal operating regimes to identify potential failure criteria. The ability to correctly determine the OPD of an interferometer from signals with large amounts of intensity noise was assessed. This investigation revealed that the analysis can successfully determine OPDs with a precision greater the $1ppm$ ($\leq 1\mu m$ in $1m$) for signals with SNR of 1 and remains operable down to SNR of 0.05. High noise levels appear to produce no additional systematic effects hence the OPD determination precision should be recoverable by combining the results from multiple measurements of interferometers which produce low quality signals.

Chapter 5

Laboratory Interferometer OPD Determination

5.1 Introduction

The results of OPD determination from interferometric signals acquired within the laboratory are presented in this chapter. Investigations into reference interferometer stability on various time scales are presented as well as investigations into measurement interferometer OPD determination precision and resolution. The investigations undertaken were designed to provide proof-of-concept results and to confirm the ability of the FSI implementations to perform at the levels required within the prototype RTRS.

The OPD results presented throughout this chapter have been determined via a comparison with a second OPD. Since no absolute length calibration of any of the laboratory interferometers was undertaken prior to these investigations the absolute errors on the OPDs are unknown. However the Michelson Reference Interferometer was initially installed with a nominal OPD of $4.7m$. Hence this acted as the benchmark for the length measurement process within the laboratory FSI system.

5.2 Reference Interferometer Stability

This section describes investigations into the stability of the two reference interferometers, described in section 2.3.4, over time scales of a few minutes and 24 hours. Stability studies over longer periods would have required absolute length calibration of the interferometers which was not possible prior to this investigation. The Michelson Reference Interferometer signal was used during the Phase Analysis process, as described in section 3.3. Hence instabilities within this interferometer affected the results obtained from all other interferometers within the system. Therefore understanding the behaviour of this interferometer is vital to meeting the measurement requirements of the system as a whole. The Short Reference Interferometer was a prototype of a stabilised reference interferometer design proposed for the prototype RTRS FSI system. It was included in the laboratory system primarily to test the

design concept and as an independent witness length. The thermal compensation mechanism within the SRI should remove temperature induced expansion effects, on the measurement scale of the FSI system, once correctly tuned. These preliminary investigations represent the first iteration in the tuning process of this mechanism.

The changes in arm lengths of the Michelson Reference Interferometer due to thermal expansions were corrected for via the use of measurements of the surface temperature of the optical table. The resultant changes in SRI OPD as a function of temperature variations were corrected for via the use of surface temperature measurements of the passive thermal compensation elements. The rate of change of the temperature of these components was also monitored. Measurements of the temperature variations of the air enclosed within both interferometers were used to correct for the effects of refractive index variations, as described in section 3.5.2.

5.2.1 Stability Over 24 Hours

The stability of the OPDs of the two reference interferometers over a period of around 24 hours was investigated by acquiring 4 consecutive laser scans at intervals of approximately 5 minutes. The OPD of each interferometer was calculated by comparison with the fully corrected OPD of the other reference interferometer. The observed OPD variations of the interferometers are shown in this section before and after the application of corrections. The ratio of the OPDs of the two interferometers is displayed as an indication of the performance of the corrections.

The Michelson Reference Interferometer

Due to the relatively large thermal mass of the optical table variations in the interferometer arm lengths resulting from thermal fluctuations were expected to have occurred slowly. The temperature variations of the optical table, on which the Michelson Reference Interferometer was placed, and the air within the optical paths are shown in figure 5.1 as a function of time. The observed maximum temperature change of around 1.3°C should correspond to around a $65\mu m$ variation in OPD due to thermal expansion and a $5\mu m$ OPD variation due to the change in the refractive index of the air. The effect of refractive index variation is expected to have occurred on a shorter time scale than the thermal expansion effects.

The maximum rate of change of temperature observed during a 24 hour period was approximately $50\mu K/s$ which relates to a maximum rate of change of interferometer OPD of around $2.8nm/s$, assuming a CTE of the optical table of $12ppm/K$. This corresponds to a maximum drift error of around $109nm$ for a nominal scan.

The Michelson Reference Interferometer OPD variations before and after corrections are shown in figure 5.2 for a period of approximately 24 hours. A histogram of the fully corrected Michelson Reference Interferometer OPD is shown in figure 5.3 with the calculated mean and standard deviation of the uncorrected and fully corrected OPDs along with the sigma of a Gaussian fit to the projection given in table 5.1.

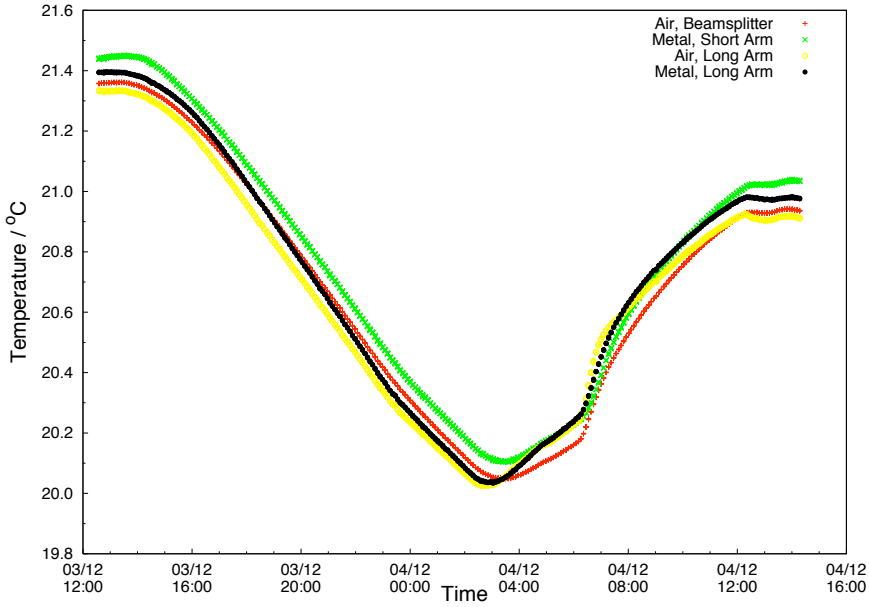

Figure 5.1: Temperature variations of the steel optical table and air within the Michelson Reference Interferometer over a period of around 24 hours.

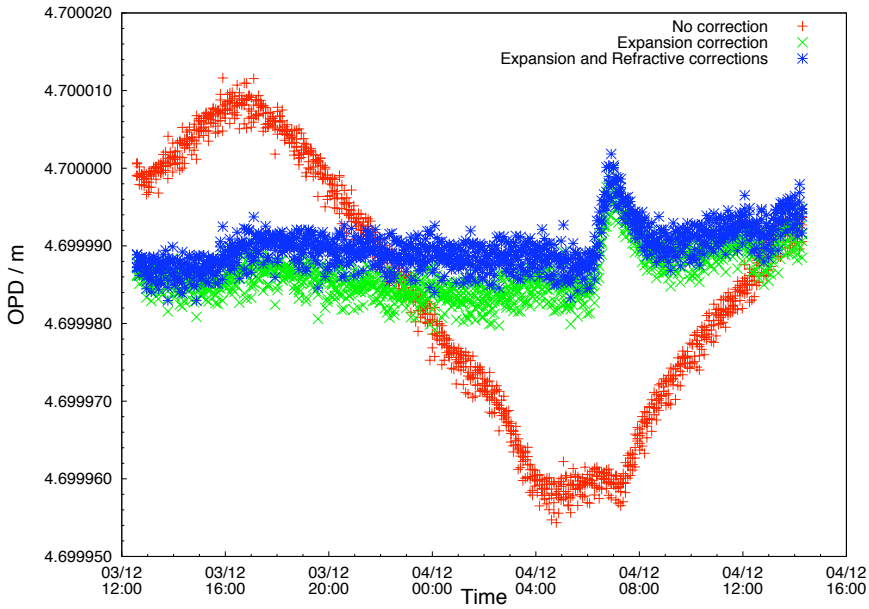

Figure 5.2: The OPD variations of the Michelson Reference Interferometer before and after the applications of corrections as a function of time over a period of around 24 hours.

The uncorrected OPD values, displayed in red in figure 5.2, clearly show the effects of temperature variations on the Michelson Reference Interferometer. The observed change in interferometer OPD was around 55μm which corresponds well to the expected value of OPD variation due to thermal effects. The corrected OPD values, shown in blue in figure 5.2, display an approximately constant behaviour throughout the 24 hour period. The observed OPD variations are a combination of variations within the SRI OPD that could not be corrected for and residual effects within the Michelson Reference Interferometer that were not corrected. The spike at around 04/12 07:00 was a result of a SRI OPD change which was caused by a large thermal gradient to which the SRI thermal compensation mechanism was unable to react.

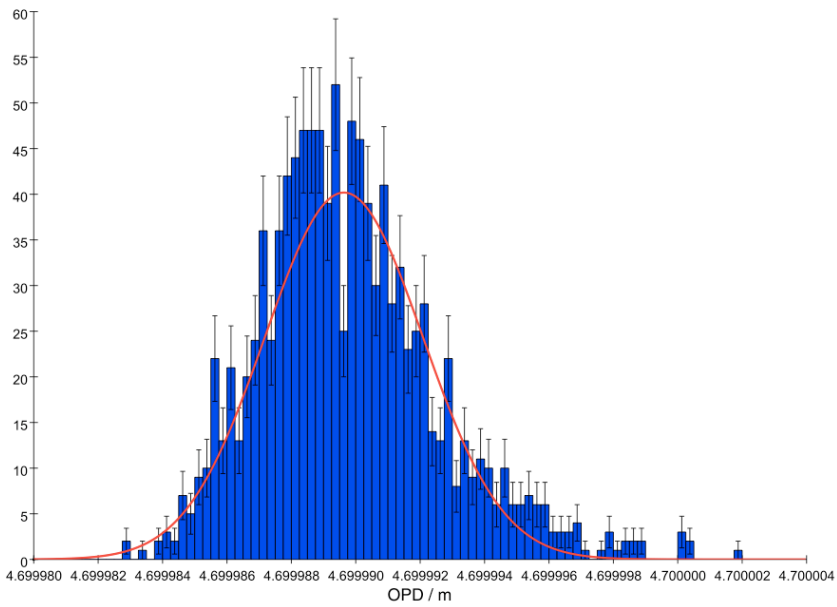

Figure 5.3: Histogram of the corrected OPD of the Michelson Reference Interferometer over a period of around 24 hours.

	Uncorrected	**Fully Corrected**
Mean OPD / m	4.699 983 924	4.699 989 781
OPD Standard Deviation / μm	16.468	2.804
Sigma of Projection / μm	-	3.457

Table 5.1: The results of the investigation into the stability of the Michelson Reference Interferometer over a period of around 24 hours.

The results given in table 5.1 clearly illustrate the improvement in OPD stability after the application of the expansive and refractive corrections. The fully corrected standard deviation result corresponds to a Michelson Reference Interferometer stability of around 600ppb.

The Short Reference Interferometer

As with the case of the Michelson Reference Interferometer the low rate of change of temperature and the relatively large thermal mass of the SRI were expected to limited the effects of thermal expansion to relatively long time scales. The measured temperature variations within the SRI during the acquisition period are shown in figure 5.4. The temperature induced OPD variations were dependant upon the temperature differential between the steel body of the interferometer and the nylon rod that formed the retroreflector support[1]. This temperature difference is displayed in figure 5.5. The maximum OPD variation due to the observed temperature change of around 2°C was estimated to be approximately $12\mu m$ as a result of thermal expansion, assuming an effective CTE of $6ppm/K$. However the performance of the nominally configured temperature compensation mechanism was difficult to anticipate prior to data acquisition.

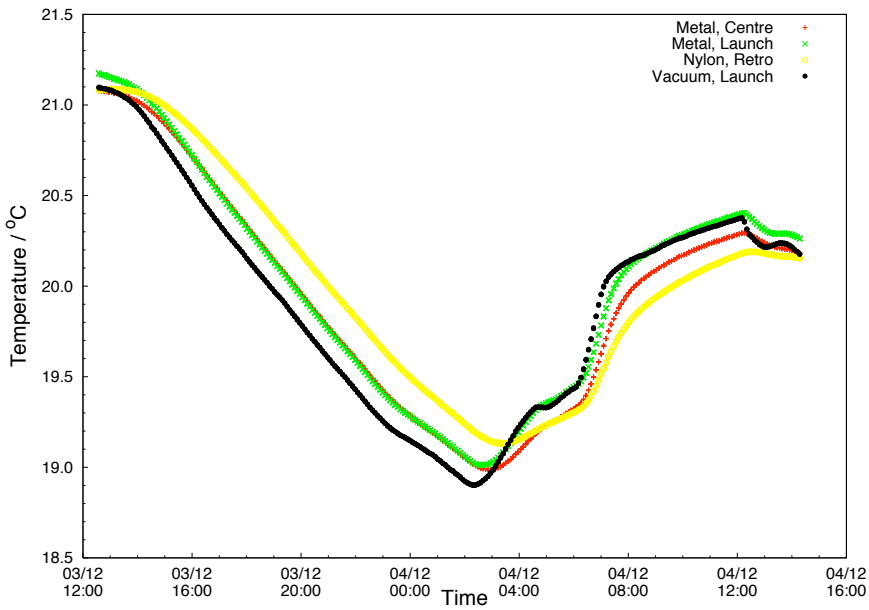

Figure 5.4: Temperature variations of the compensation components and the air within the SRI over a period of around 24 hours.

A maximum rate of change of temperature of around $150\mu K/s$ was observed which relates to a rate of change of OPD of around $0.9nm/s$, assuming an effective CTE of $6ppm/K$ for the nominally configured thermal compensation mechanism. This corresponds to a maximum drift error of around $39nm$ for a nominal scan. However for the majority of the acquisition period the rate of change of temperature was several times lower than the maximum.

The stability of the SRI, along with the performance of the nominally configured temperature compensation mechanism, was investigated over a period of around 24 hours by acquiring groups of 4 consecutive laser scans at intervals of approximately 5 minutes. The analysis of the OPD variations produced by temperature changes provided information which

[1]The temperature difference discussed here is the scan average measured temperature of the steel tube minus the scan averaged measured temperature of the nylon rod.

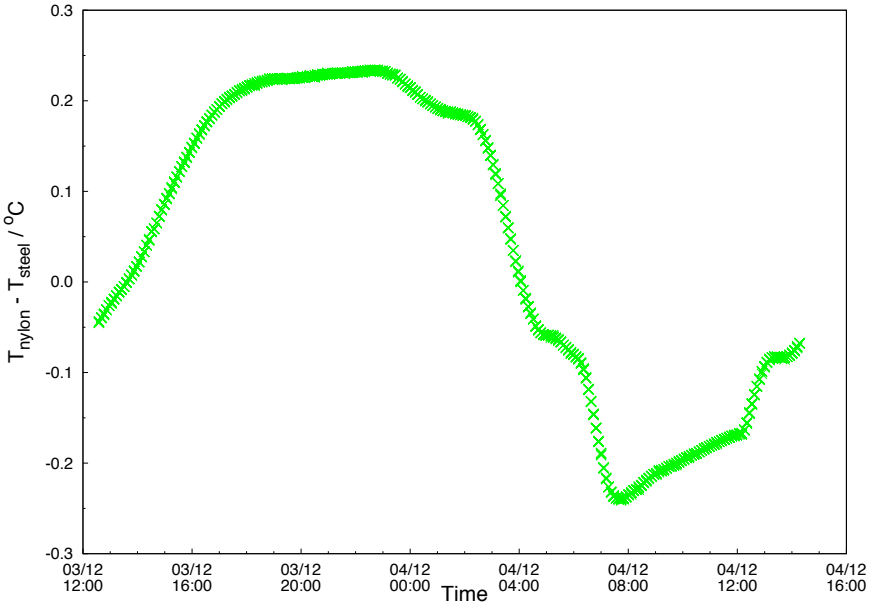

Figure 5.5: Measured temperature difference between the steel body of the SRI and the nylon rod on which the retroreflector was mounted over a period of around 24 hours.

could be used in the fine tuning of the temperature compensation system. Prior to commencing the data taking process the SRI was evacuated to a pressure of approximately $13Pa$ (0.013% standard atmospheric pressure). The vacuum pump was not left running during the investigations to remove the possibility of vibrations affecting the acquired signals.

The observed increase in uncorrected OPD as a function of time over the 24 hour period seen in figure 5.6 was caused by the pressure inside the SRI vessel slowly increasing. The observed OPD increased by approximately $45\mu m$ over the 24 hour period. The lack of experimental data relating to the air refractivity variations at such low pressures made the determination of the leak rate difficult. However an estimated leak rate of around $0.6Pa/s$ was obtained by using the coefficients for standard atmospheric pressure given in section 3.5.2. This leak rate corresponds to a pressure increase of around $50kPa$ over the 24 hours period which produced the observed OPD increase. The effect on the SRI OPD of this deterioration in vacuum level were corrected for by assuming a constant leak rate.

The OPD variations, after the removal of the vacuum deterioration effects, are displayed in figure 5.7 both before and after the application of the correction for thermal effects. A histogram of the fully corrected OPD is shown in figure 5.8. The mean and standard deviation of the SRI OPD before and after thermal corrections along with the sigma of a Gaussian fit to the projection given in table 5.2.

The OPD variations before the application of the corrections for thermal effects, shown in red in figure 5.7, show that a negative temperature difference (the temperature of the nylon rod was greater than that of the steel tube) produced an increase in OPD. While a positive temperature difference correspondingly produced a decrease in OPD. This leads to the conclusion that the effective length of the nylon rod must be increased since it was not compensating sufficiently for the thermally induced length changes of the steel tube. The

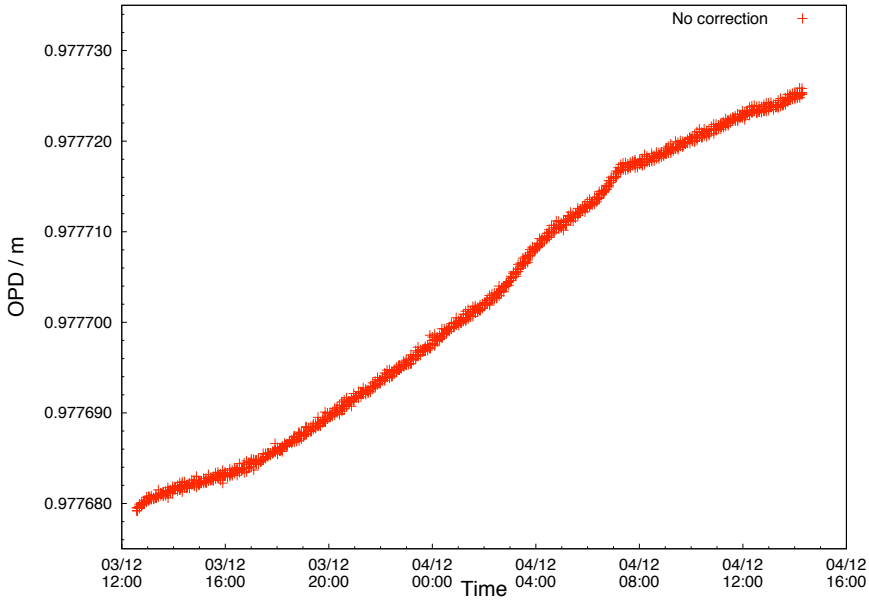

Figure 5.6: Observed OPD variations of the SRI as a function of time over a period of around 24 hours before the application of any corrections.

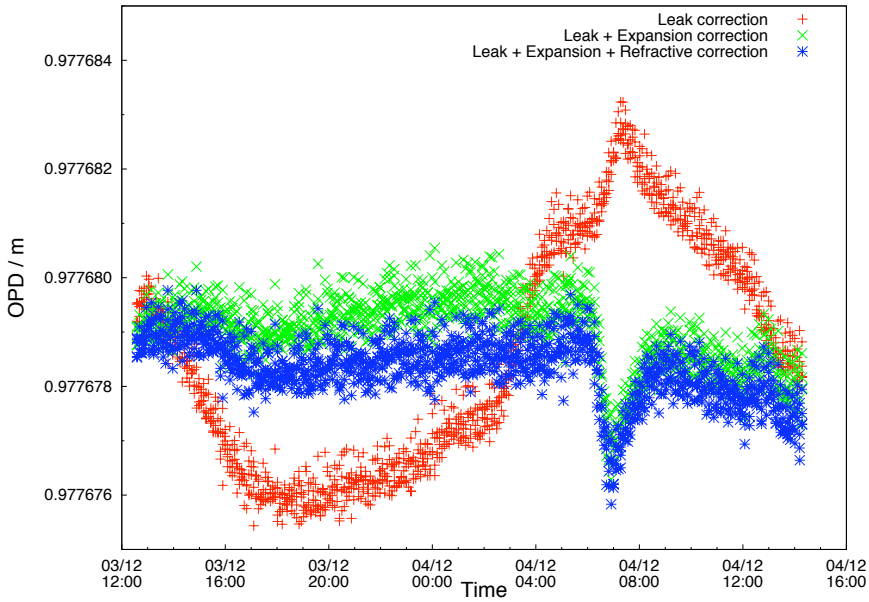

Figure 5.7: The OPD variations of the SRI before and after the applications of corrections for thermal effects as a function of time over a period of around 24 hours.

observed variation in SRI OPD was around $6\mu m$ as a results of a temperature difference variation of around 0.5°C. Therefore an increase in the effective length of the nylon rod by an estimated $1.4mm$ is required.

	Uncorrected	**Fully Corrected**
Mean OPD / m	0.977 678 587	0.977 678 344
OPD Standard Deviation / μm	2.086	0.585
Sigma of Projection / μm	-	0.589

Table 5.2: The results of the investigation into the stability of the SRI over a period of around 24 hours.

The SRI OPD variations after the application of the corrections, shown in blue in figure 5.7, exhibit an approximately flat behaviour as a function of acquisition time. A global OPD change of around $2\mu m$ was observed over the 24 hour period. The sharp decrease in observed OPD at around 04/12 07:00 was caused by the presence of a large thermal gradient. Around this time the temperature within the SRI varied at a rate of approximately $150\mu K/s$. The compensation components reacted to this thermal gradient at different speeds producing a relatively large but short term variation of the SRI OPD. Such an effect will be avoided in the future by thermally insulating the SRI vacuum vessel.

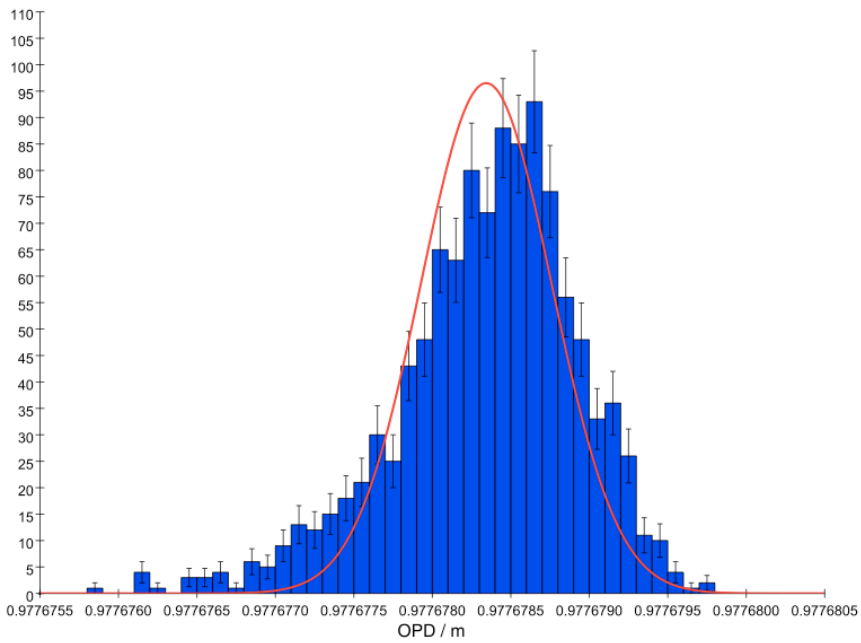

Figure 5.8: Histogram of the corrected OPD of the SRI over a period of around 24 hours.

The results shown in table 5.2 illustrate the improvement in SRI OPD stability after the application of the corrections for thermal effects. The fully corrected standard deviation result corresponds to a SRI stability of around $600ppb$. This resultant instability correlates with that seen in the previous investigation and is most likely the results of air turbulence within the Michelson Reference Interferometer.

The Reference Interferometer OPD Ratio

The performance of the corrections was assessed by taking the ratio of the reference interferometer OPDs. This not only allowed the effectiveness of the corrections to be evaluated but also provided an indication of the resultant relative instability due to additional effects. Figure 5.9 shows the OPD ratio before and after the applied corrections in red and blue respectively. The calculated rate of change and the RMS variation of reference interferometer OPD ratio were determined by linear fits to this data and are given in table 5.3.

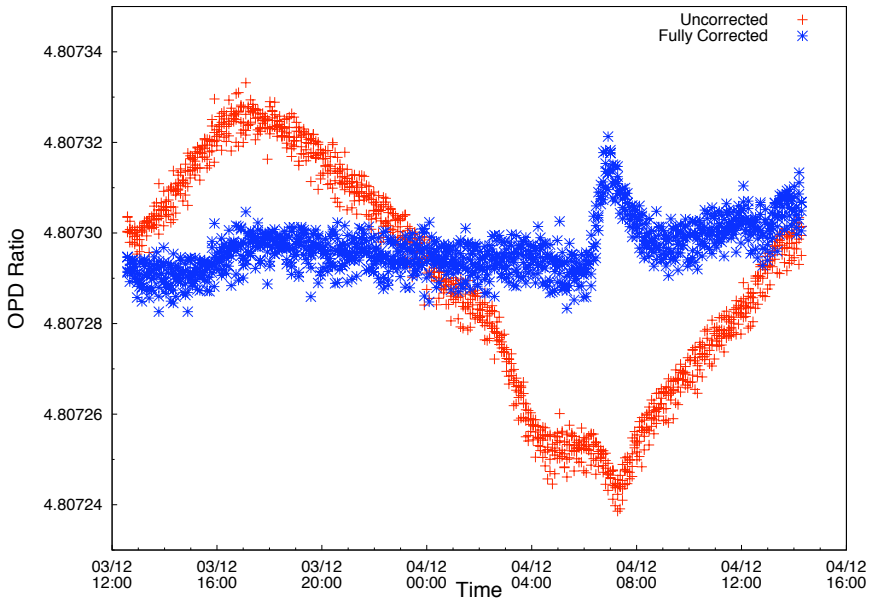

Figure 5.9: The ratio of the reference interferometer OPDs before (red) and after (blue) the application of corrections over a period of around 24 hours.

	Uncorrected	**Fully Corrected**
Rate of Change of OPD Ratio / ppb/s	-0.475 ± 0.018	0.135 ± 0.005
RMS of Residuals / ppb	1611	487

Table 5.3: Results determined from linear fits to the uncorrected and fully corrected reference interferometer OPD ratio data over a period of around 24 hours.

The results shown in table 5.3 show that the corrections did improve the relative rate of change of OPD of the two reference interferometers. The corrections also produced a decrease in the RMS variation of the OPD ratio. Although in the uncorrected case the RMS of the deviations from a straight line is not a particularly relevant parameter since the variations are obviously systematic being dominated by thermal expansion. The application of the corrections clearly had an effect on the long term relative stability of the two reference interferometers. The resultant relative instability of the two interferometers was around 500ppb, this is believed to be primarily due to air turbulence within the Michelson Reference Interferometer.

5.2.2 Stability Over 20 Minutes

The stability of the OPDs of the two reference interferometers over a period of around 20 minutes was investigated by acquiring 200 consecutive laser scans. The OPD of each interferometer was calculated by comparison with the fully corrected OPD of the other reference interferometer. The OPDs of the interferometers are shown in this section before and after correction. The length ratio of the two interferometers is also displayed as an indication of the performance of the corrections.

The Michelson Reference Interferometer

The Michelson Reference Interferometer OPDs are shown in figure 5.10 before and after correction as a function of acquisition time. Histograms of the uncorrected and fully corrected Michelson Reference Interferometer OPDs are shown in figure 5.11. The calculated mean and standard deviation of the OPDs along with the sigma of a Gaussian fit to the projections of the uncorrected and fully corrected OPDs are given in table 5.4.

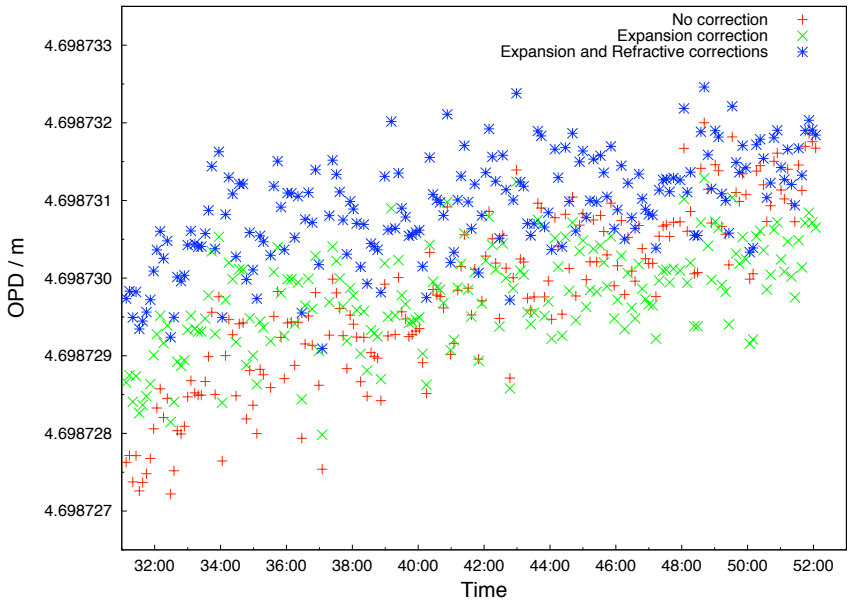

Figure 5.10: The OPD variations of the Michelson Reference Interferometer before and after the application of corrections as a function of time over a period of around 20 minutes.

	Uncorrected	**Fully Corrected**
Mean OPD / m	4.698 729 765	4.698 730 900
OPD Standard Deviation / μm	1.121	0.688
Sigma of Projection / μm	1.159	0.939

Table 5.4: The results of the investigation into the stability of the Michelson Reference Interferometer over a period of around 20 minutes.

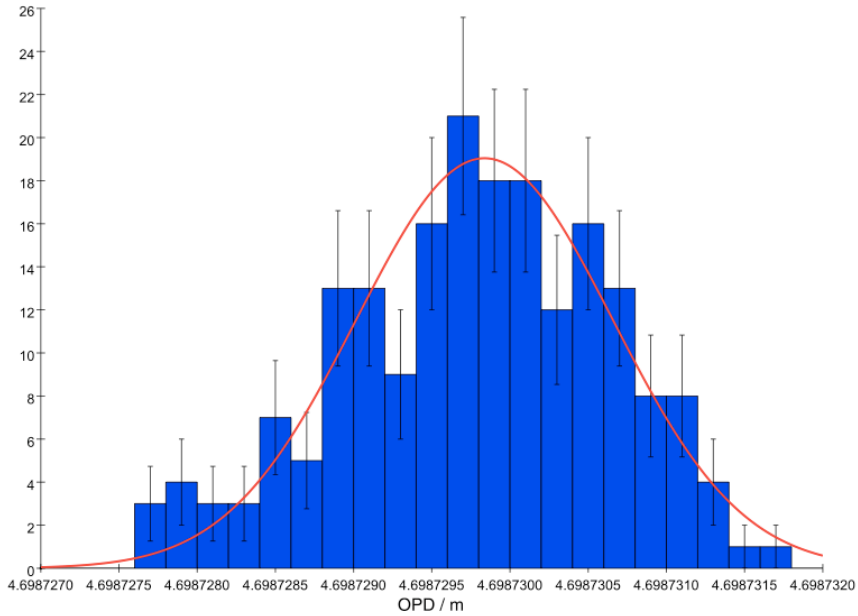

(a) Uncorrected OPDs of the Michelson Reference Interferometer.

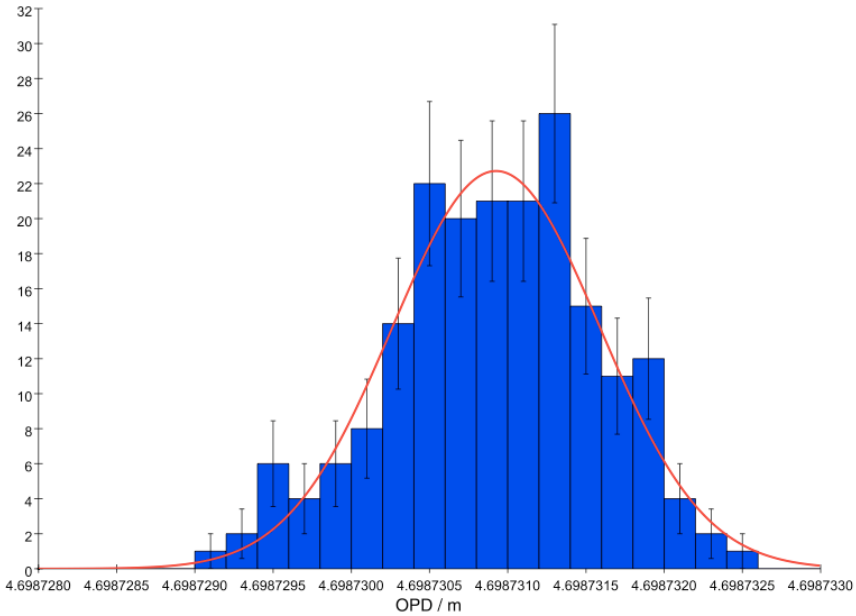

(b) Fully corrected OPD of the Michelson Reference Interferometer.

Figure 5.11: Histogram of the uncorrected and fully corrected OPD of the Michelson Reference Interferometer over a period of around 20 minutes.

The measured temperature variation within the Michelson Reference Interferometer during the 20 minute acquisition period was around 0.03°C. This relates to a total OPD variation due to thermal expansion during the investigation of around $1.7\mu m$. The corresponding rate of change of temperature of the table was approximately $25\mu K/s$ which corresponds to a drift error of around $55nm$. The calculated values of stability given in table 5.4 corresponds to a Michelson Reference Interferometer stability of around $146ppb$ over the 20 minute period.

The Short Reference Interferometer

The SRI OPDs are shown in figure 5.12, both before and after correction, as a function of acquisition time. Histograms of the uncorrected and fully corrected SRI OPDs are shown in figure 5.13. The calculated mean and standard deviation of the OPDs along with the sigma of a Gaussian fit to the projections of the uncorrected and fully corrected OPDs are given in table 5.5.

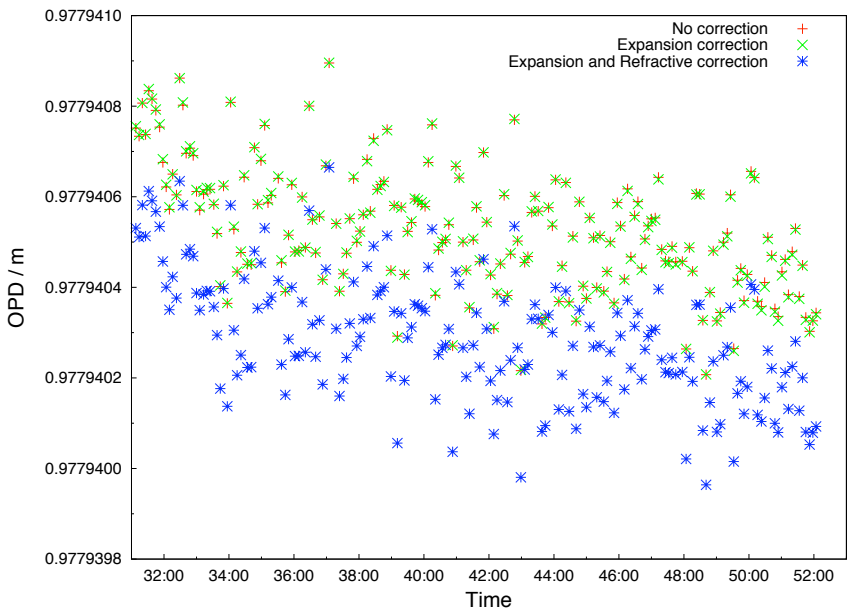

Figure 5.12: The OPD variations of the SRI before and after the applications of corrections as a function of time over a period of around 20 minutes.

	Uncorrected	**Fully Corrected**
Mean OPD / m	0.977 940 525	0.977 940 289
OPD Standard Deviation / μm	0.131	0.132
Sigma of Projection / μm	0.188	0.154

Table 5.5: The results of the investigation into the stability of the Short Reference Interferometer over a period of around 20 minutes.

The measured temperature variation within the SRI during the 20 minute acquisition period was around 0.04°C. This relates to a total OPD change of around $0.25\mu m$. The

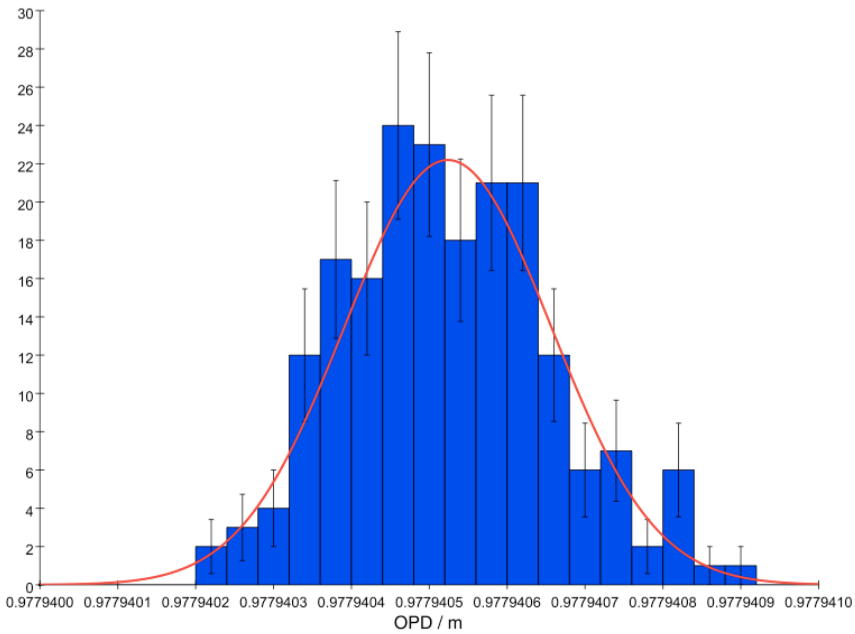

(a) Uncorrected OPD of the Short Reference Interferometer.

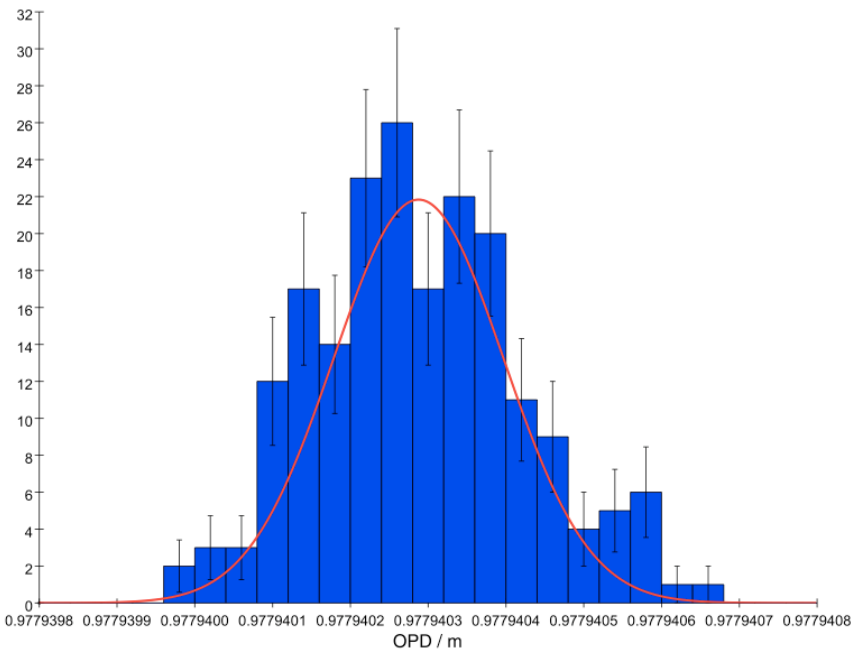

(b) Fully corrected OPD of the Short Reference Interferometer.

Figure 5.13: Histogram of the uncorrected and fully corrected OPD of the Short Reference Interferometer over a period of around 20 minutes.

corresponding rate of change of temperature within the interferometer of approximately $25\mu K/s$ which relates to a drift error of around $6nm$ for a nominal scan, assuming an effective CTE of $6ppm/K$. The calculated values of stability given in table 5.5 corresponds to a SRI stability of around $135ppb$ over the 20 minute period.

The Reference Interferometer OPD Ratio

The ratio of the OPDs of the reference interferometers was again used to evaluate the performance of the applied corrections. As before this provided information upon the effectiveness of the corrections and gave an indication of the resultant instability due to factors not present in the longer term stability investigation. Figure 5.14 shows the OPD ratio before and after corrections in red and blue respectively. The results of linear fits to the two sets of data are given in table 5.6.

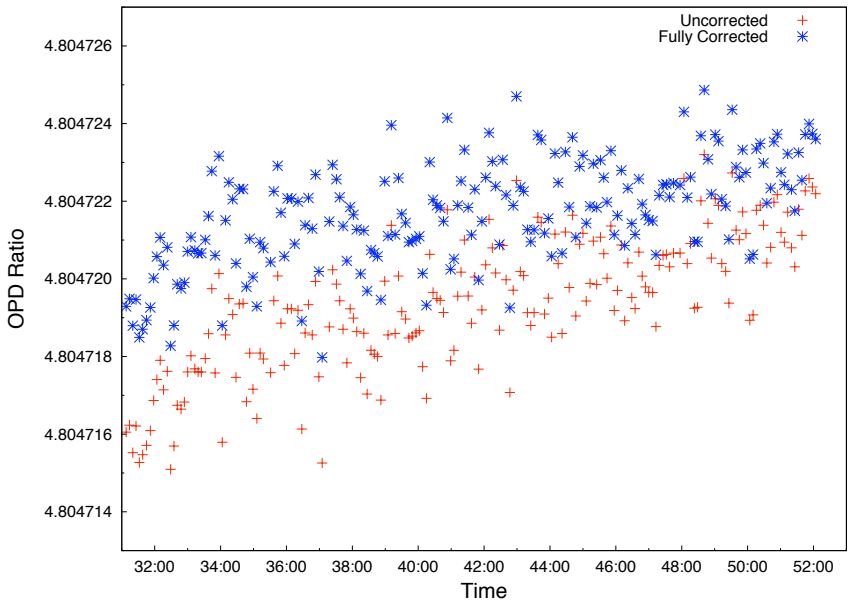

Figure 5.14: The ratio of the reference interferometer OPDs before (red) and after (blue) the application of corrections over a period of around 20 minutes.

	Uncorrected	**Fully Corrected**
Rate of Change of OPD Ratio / ppb/s	3.709 ± 0.216	2.230 ± 0.215
RMS of Residuals / ppb	111	110

Table 5.6: The results of linear fits to the uncorrected and fully corrected reference interferometer OPD ratio data over a period of around 20 minutes.

The results shown in table 5.6 indicate that the applied corrections did improve the relative rate of change of OPD of the two reference interferometers. However there was little decrease in the RMS variation of the OPD ratio after the application of the corrections. The effects dealt with by the applied corrections are more prominent on longer time scales. The

resultant relative instability of the two reference interferometers was around 110*ppb*, this was due to effects that were not corrected for. The application of corrections will also reduce the level of systematic error on the measurements. The dominant source of instability on the scan-to-scan time scale was air refractive index fluctuations over short distances caused by turbulence. This imposes the limit on the short term stability of open-air measurements.

5.2.3 Stability Conclusions

On the shortest relevant time scales, around a few seconds, the observed variations in OPD are dominated by air turbulence. Due to the short coherence time of this effect it is very difficult to correct for. Turbulence effects dominant on the scan-to-scan time scale and produce a limit on the single measurement precision of open air measurements. Over longer time scales the effects of atmospheric pressure changes have an increasing impact. These pressure changes induce OPD variations in open air interferometers which are not seen in evacuated interferometers. The effect of these pressure variations will be manifest as a lower stability in investigations conducted over longer periods. No OPD corrections for the effects of turbulence or atmospheric pressure variations were applied during these investigations.

The effects of thermal expansion and thermally induced refractive index variations have little impact on time scales of a few minutes but are much more important over time scales of several hours. These thermally driven variations are larger than the turbulence effects and correlate over much larger time scales. Over a period of around 24 hours the thermal expansion effects are approximately an order of magnitude greater than the effects produced by the refractive index variations.

A comparison of the reference interferometer OPD ratio on the two investigated time scales indicates that the applied corrections are most effective at compensating for longer term effects. Since the two reference interferometers were positioned in different parts of the laboratory their environments were expected not to correlate on time scales of a few minutes but to exhibit a much greater correlation over longer time scales. Hence it was expected that the correlation between the two reference interferometer OPDs would be greatest on longer time scales.

The dominant factors in resultant reference interferometer instability, after the application of the corrections, were turbulence and pressure variations inside the Michelson Reference Interferometer enclosure. These effects dominate on the short and long time scales respectively and are the main sources of the instabilities stated in tables 5.3 and 5.6. It is expected that evacuating both interferometers would increase the relative stability and improve the correlation between the results obtained on both time scales.

The performance of the evacuated and thermally compensating reference interferometer within the RTRS will require evaluation prior to integration. However it is expected to exceed the performance of the reference interferometer used during the laboratory investigations.

5.3 External Measurement Interferometer Performance

Several alternative designs for the external FSI system were investigated both analytically, as described in section 2.2.2, and experimentally. This section details the initial laboratory investigations that were undertaken to investigate the suitability and performance levels of the collimated and bare fibre options. The data presented in this section was acquired by Y. Han [72][73] and analysed by the author.

These investigations were preliminary and only interferometric signals were acquired with no additional environmental data. The uncorrected Michelson Reference Interferometer OPD was used during the determination of the measurement interferometer OPDs. Since the investigations were undertaken over periods of around 10 minutes the impact of environmental variations were assumed to be negligible. The most important area of examination was the response of the different interferometer concepts to transverse retroreflector displacement.

5.3.1 Collimated Measurement Interferometers

To investigate the potential for a collimated interferometer to produce a return signal as a function of transverse retroreflector position a single fibre interferometer was set-up using a $25mm$ diameter spherical lens with focal length $100mm$ to produce a collimated beam. The interferometric short arm reflection was provided by the SPC termination of the launch fibre. The collimating lens had both faces anti-reflection coated. The OPD was adjusted to around $1m$ and a 1.5 inch retroreflector was translated through the illumination field via a linear translation stage. An overview of the experimental setup is shown in figure 5.15. Single laser scans were acquired at $1mm$ intervals for displacements of $15mm$ either side of a nominal centre line of the interferometer. Figure 5.16 shows the OPD as a function of transverse off-axis distance of the retroreflector.

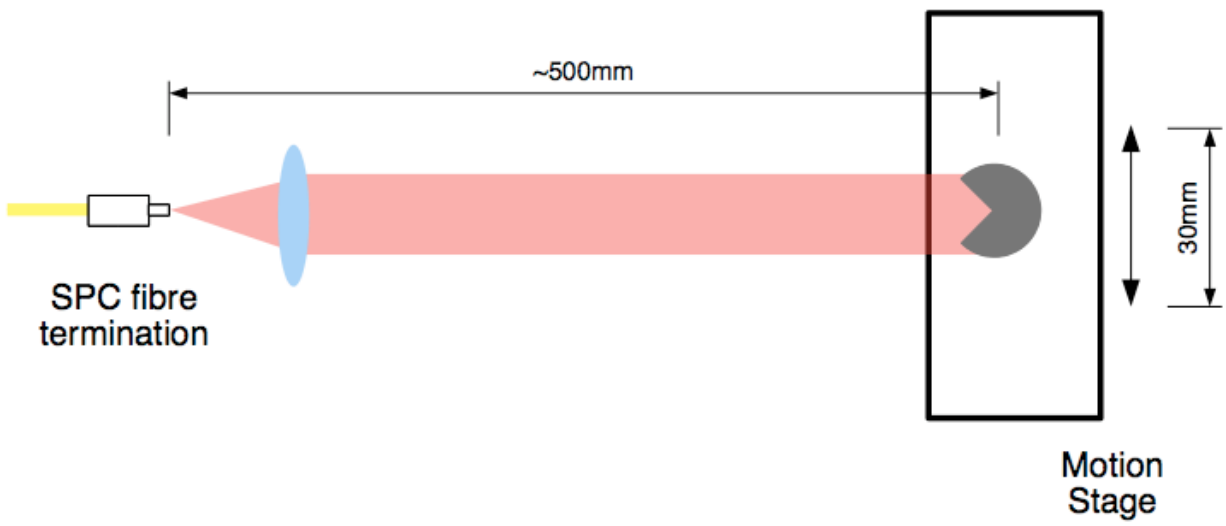

Figure 5.15: An overview of the collimated external MI experimental setup. Not to scale.

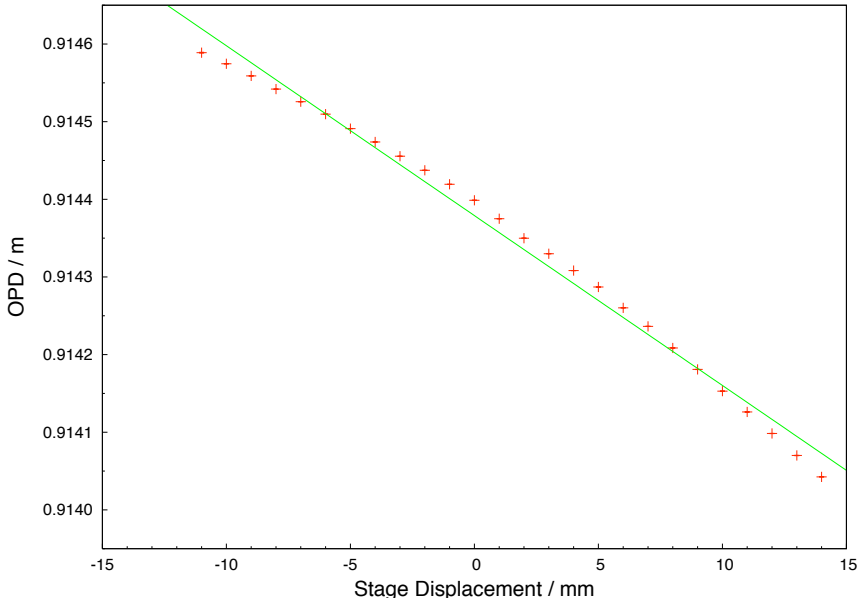

Figure 5.16: The OPD of an external MI illuminated with collimated light as a function of transverse retroreflector displacement. The green line is a linear fit to the data.

It is clear from the data displayed in figure 5.16 that the axis of motion of the linear translation stage on which the retroreflector was mounted was not perpendicular to the launch axis of the interferometer. Since the angle was small the gradient of a linear fit to the data, shown in green in figure 5.16, was used to determine the magnitude of this deviation from the normal. The results of the fit yield a deviation angle of approximately $22\mu rad$.

The data shown in figure 5.16 also indicates that the light was not fully collimated by the single lens. If this had been the case a plane wavefront would have been observed across the illumination field rather than the curved wavefront described by the data. The absence of a plane wave illumination can be accounted for by two factors. Firstly the fibre termination was placed at the nominally stated focal length away from the lens using a second manual linear translation stage. It is therefore likely that the launch point of the light was not positioned exactly at the focal point of the lens and thus produced a mildly divergent beam. This would produce an approximately spherical wavefront, with a large but finite radius of curvature, at the retroreflector.

The presence of aberrations, which are expected for non-optimally focused spherical lens, would result in a distorted wavefront as shown in figure 5.17 which shows the residuals of a linear fit to the OPD variation as a function of transverse retroreflector displacement. The form of the wavefront at the retroreflector is consistent with a classical focus error combined with with a typical spherical aberration. The signal peak height is displayed in figure 5.18 as a function of transverse retroreflector displacement. This was almost constant while the retroreflector was close to the interferometer axis. However a sharp cut-off exists as the displacement was increased in either direction.

The effect of the transverse displacement of a retroreflector with respect to the launch axis of a collimated interferometer is illustrated in 2D in figure 5.19. This model uses a simplified

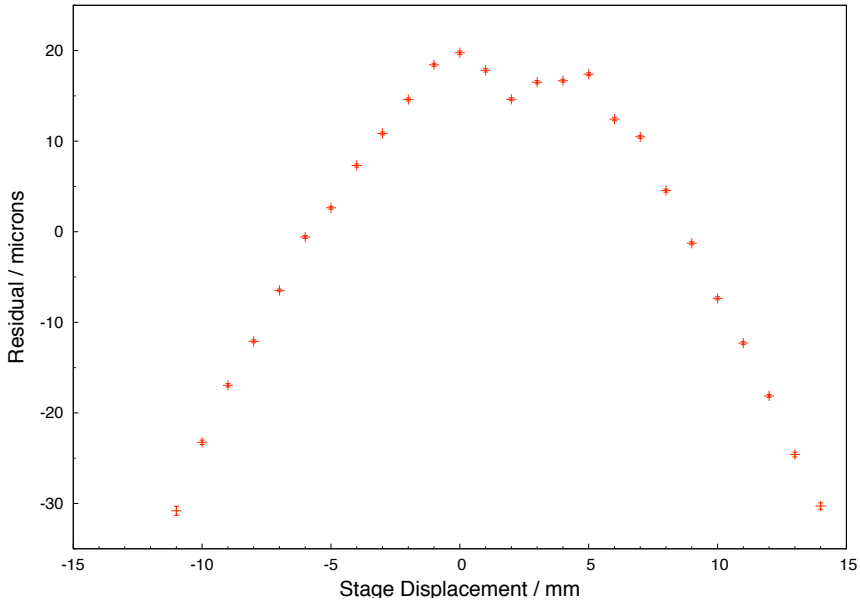

Figure 5.17: The residuals to a linear fit of the OPD of an external MI illuminated with collimated light as a function of transverse retroreflector displacement.

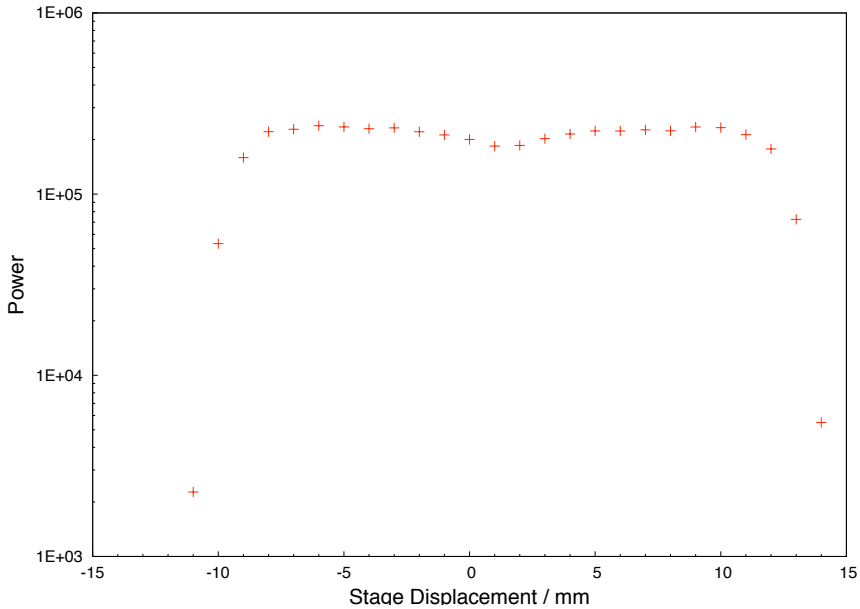

Figure 5.18: The height of the signal spectral peak of an external MI illuminated with fully collimated light as a function of transverse retroreflector displacement.

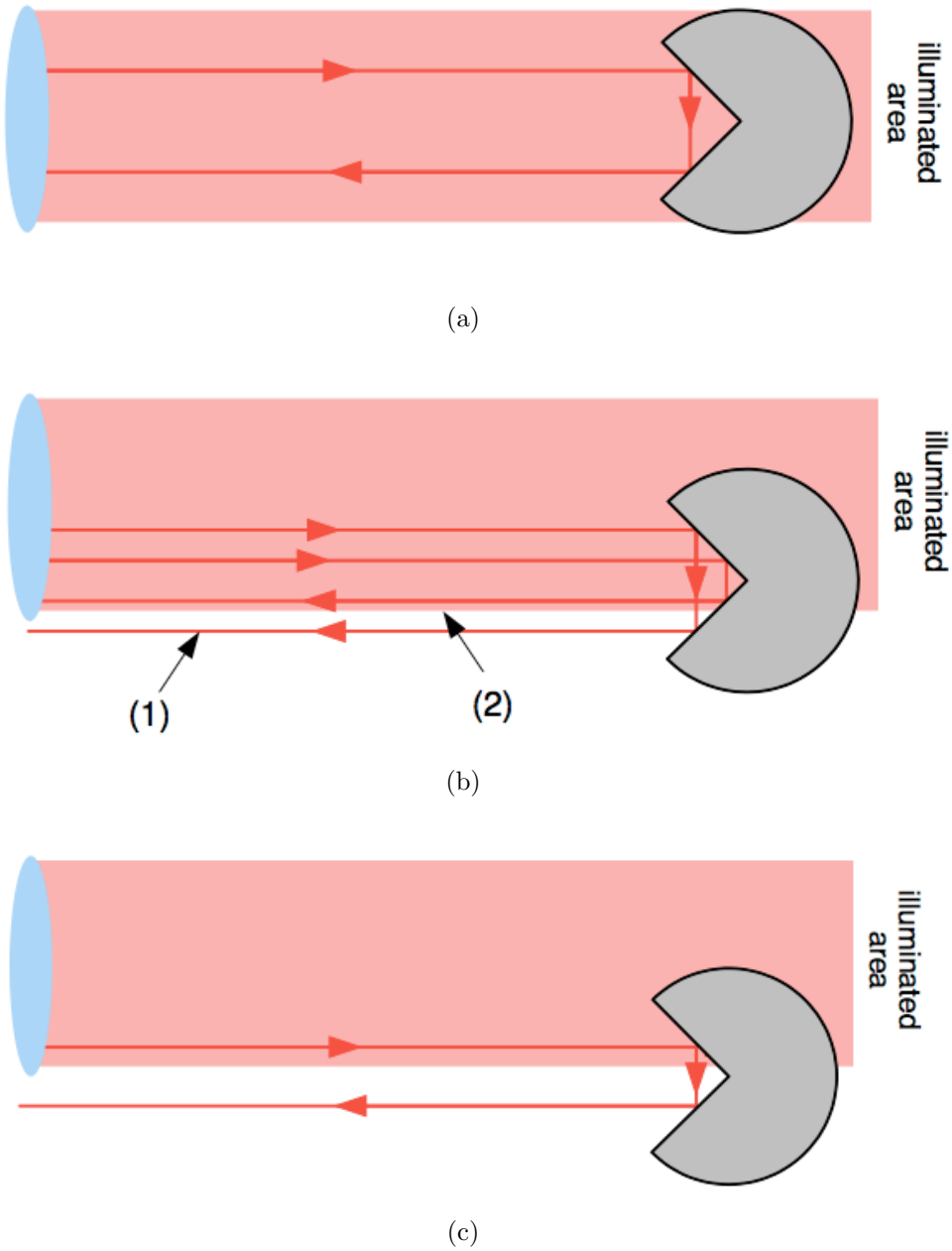

Figure 5.19: A 2D illustration of the production of long arm interferometric reflections as a retroreflector is transversely displaced.

top-hat intensity distribution and ignores divergence. When the entire acceptance region of the retroreflector is illuminated any ray entering will be reflected back and can be coupled back into the launch fibre, as shown in figure 5.19a. In this scenario the interferometric long arm, and therefore the visibility of signal, is maximised.

As the retroreflector is displaced away from the launch axis of the interferometer a portion of the retroreflector is no longer illuminated. Hence rays entering the retroreflector above the apex will be walked across as they are reflected and may be returned outside of the illumination area and so will not be coupled back into the launch fibre, ray (1) in figure 5.19b. However rays entering close to the apex, whilst also being walked as they are reflected, will be returned within the illumination area and so can be coupled back into the launch fibre, ray (2) in figure 5.19b.

Further off-axis displacement of the retroreflector eventually results in the situation where the apex no longer lies within the illumination field, figure 5.19c. In this case there is no ray that can enter the retroreflector and subsequently be coupled back into the launch fibre. Therefore the long arm interferometric reflection provided by the retroreflector, and hence the signal visibility, falls to zero. This accounts for the extremely sharp decline in the signal peak height seen in figure 5.18 as the transverse displacement is increased. The width of the high spectral peak plateau is around $25mm$ which corresponds well to the stated 1 inch clear aperture of the retroreflector used[2].

5.3.2 Bare Fibre Measurement Interferometers

The ability to determine OPDs from the interferometric signals produced from interferometers illuminated with light launched directly from an angle polished fibre termination was investigated as a function of transverse retroreflector displacement. The aim of this investigation was to confirm that such interferometers could be considered as an option for the external FSI system and hence justify further investigation and development of dedicated signal conditioning and amplification electronics.

The interferometer set-up consisted of an FC/APC terminated fibre launch and a 1.5 inch sphere mounted retroreflector which was translated across the illumination field using a linear motion stage. The interferometer OPD was set to around $800mm$ and laser scans were acquired at $5mm$ intervals from the nominal interferometer launch axis to a stage displacement of $40mm$. The APC termination was used to produce the short arm interferometric reflection and returned approximately $1ppm$ of the interferometer light input. This style of fibre termination was chosen to reduce the DC level of the interferometric signal and avoid saturation of the electronics.

An overview of the experimental setup is shown in figure 5.20. Groups of 5 scans were acquired at each retroreflector position, figure 5.21 shows the OPD as a function of transverse retroreflector displacement. The errorbars shown represent the standard deviation from the mean of the groups of measurements.

[2]The orientation of the three retroreflector mirrors with respect to the direction of translation also impacts on the amount of returned light.

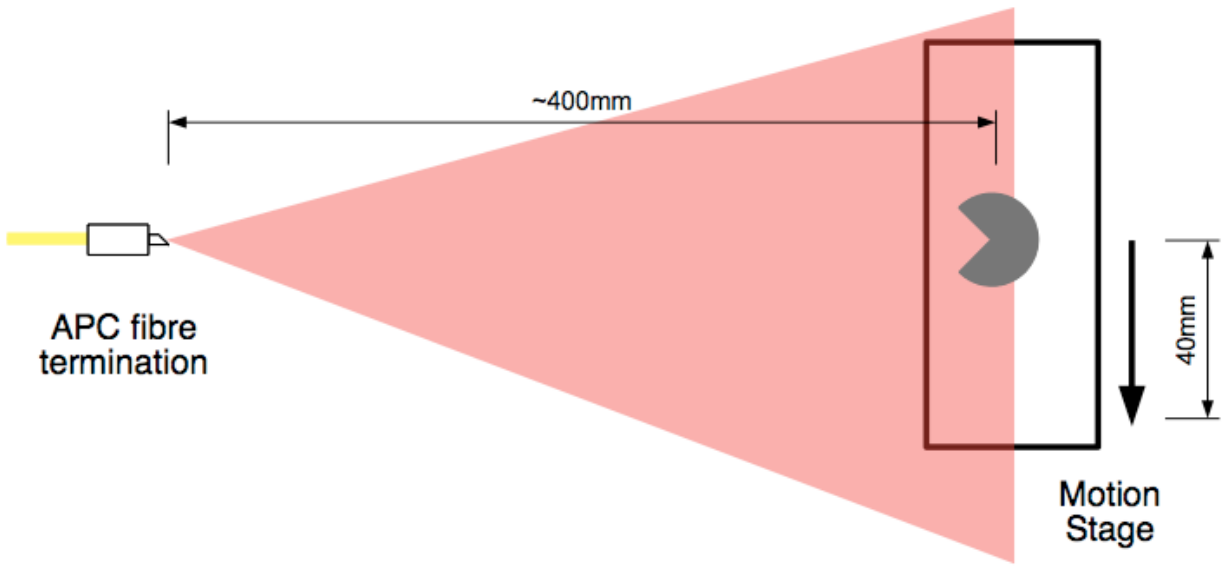

Figure 5.20: An overview of the bare fibre launch external MI experimental setup. Not to scale.

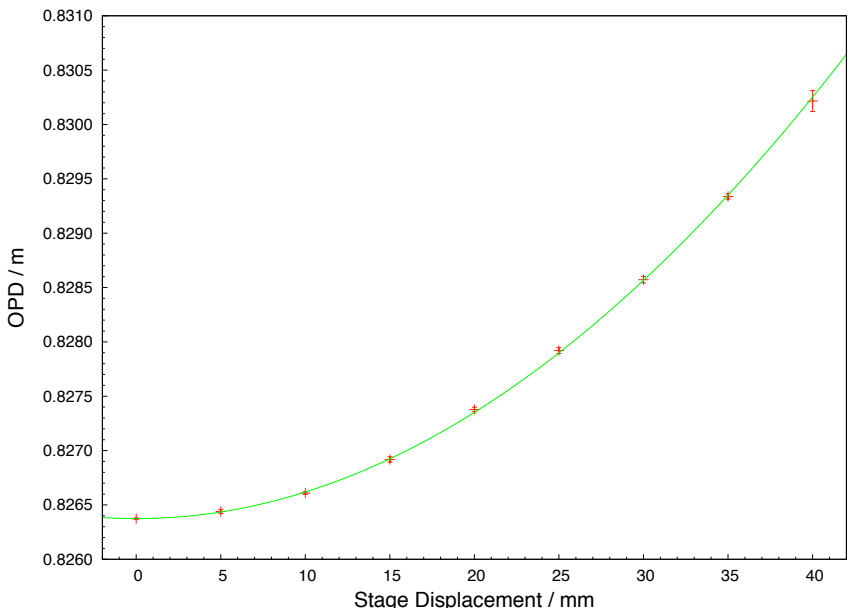

Figure 5.21: The OPD of an external MI illuminated with light launched from a bare fibre APC termination as a function of transverse retroreflector displacement. The green line is a parabolic fit to the data.

The observed increase in OPD as the retroreflector was displaced further from the interferometer launch axis is consistent with illumination by a spherical wavefront. This was expected since the bare fibre launch can be approximated to a point source with a Gaussian beam profile [42]. A parabolic fit to the data is shown as a green line in figure 5.21.

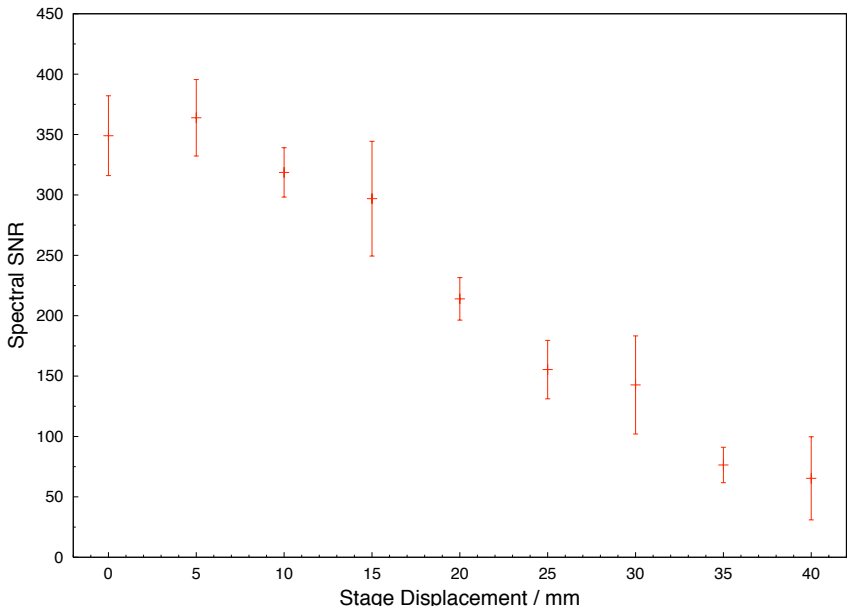

Figure 5.22: The spectral SNR of an external MI illuminated with light launched from a bare fibre termination as a function of transverse retroreflector displacement.

An indication of the strength of the recoupled signal returned from the retroreflector as a function of transverse retroreflector position is shown in figure 5.22. A signal peak that is ten times higher than the mean level of the spectrum can reliably be identified by the automated peak finder algorithm within the analysis process. Figure 5.22 clearly shows that although there was a significant reduction in spectral SNR as the retroreflector was moved further from the interferometer launch axis a signal capable of producing an identifiable spectral peak was still achieved at a transverse retroreflector displacement of $40mm$.

Figures 5.21 and 5.22 strongly indicate that the bare APC fibre termination launch method is a solution that can meet the transverse acceptance requirements of the external FSI system. Signal peaks can be identified within the spectra of acquired interferometer signals for off-axis distances greater than the required $32mm$ calculated in section 2.2.2. Nevertheless, further investigations are needed to confirm that the required OPD determination precision and resolution can be achieved with a system using this style of interferometer. Comparison with the simulations undertaken with low quality signals in section 4.4.1 indicates that the OPD determination precision at the extremes of the acceptance region would be around $\pm 3\mu m$. However it is expected that the spectral SNR can be further increased via the use of low-noise, high-gain signal acquisition electronics which were still under development at the time this data was acquired.

5.4 Internal Measurement Interferometer Precision

This section describes the investigations designed to study the performance of the collimated internal measurement interferometers over time scales of a few minutes and approximately 24 hours. Two distinct length scales were used to illustrate the scalability of the system. Initial studies were carried out with interferometers of around $1.6m$ OPD before the size was increased to the full RTRS OPD of approximately $9m$ in steps of around $1m$.

In the following investigations two parallel measurement interferometers were placed on an aluminium optical table inside a protective box designed to isolate the interferometers from the effects of environmental variations within the laboratory. These two interferometers represented one third of the RTRS internal FSI system. The interferometers differed in the way in which the light was launched and in the surfaces used to produce the short arm interferometric reflection.

One interferometer consisted of a FC/SPC launch with the short arm reflection produced by the fibre termination. The other used a FC/APC terminated fibre launch and had an additional glass beamsplitter after the collimator lens to provide the short arm reflection. Further details of the two types of launches are given in section 2.3.5. Both interferometers used identical lenses with the position of both fibre terminations adjusted to produce fully collimated outputs.

Throughout the following sections the two measurement interferometers are referred to as the *SPC-MI* and the *APC-MI* respectively. During the following investigations the fully corrected Michelson Reference Interferometer was used for OPD determination. The errorbars shown on single measurements are estimations of OPD determination uncertainty derived from the analysis, as described in section 3.4.4, and ignore experimental systematic effects. An overview of the internal MI experimental setup is shown in figure 5.23.

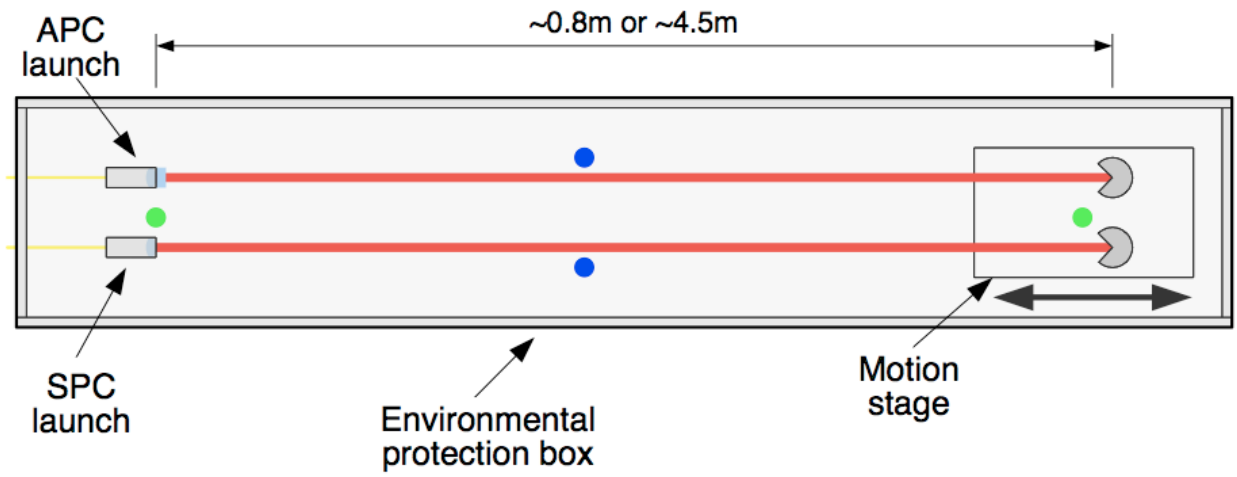

Figure 5.23: An overview of the internal MI experimental setup. Not to scale. The positions of the surface and air temperature sensors are indicated with blue and green dots respectively.

5.4.1 1.6m OPD Measurement Interferometers

As an initial investigation into the internal FSI system implemented in the laboratory a pair of MIs were prepared with OPDs of approximately $1.6m$. Interferometer signals and temperature measurements were acquired over a period of approximately 24 hours.

Groups of 4 laser scans were acquired at intervals of approximately 5 minutes for a period of around 24 hours. The observed temperature variations of the aluminium table and the air within the MIs over this period are shown in figure 5.24. The OPDs of the APC-MI and the SPC-MI are shown as a function of acquisition time in figures 5.25 and 5.26 respectively.

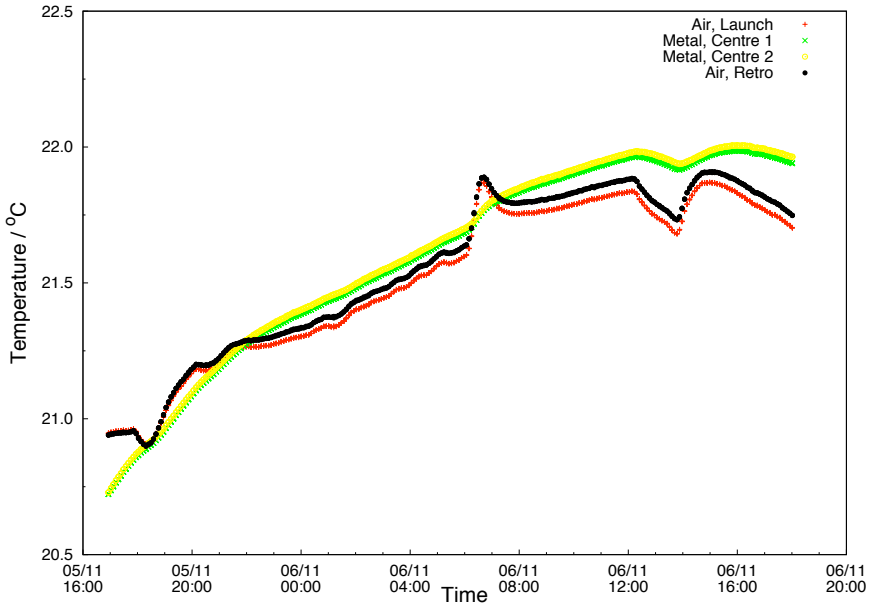

Figure 5.24: Observed temperature variations of the aluminium table and the air as a function of time for the $1.6m$ internal MIs.

The correlation between the temperature variations of the aluminium and the OPDs of the MIs is clear from comparison of figure 5.24 with figures 5.25 and 5.26. The two MIs were positioned as close to one another as possible to minimise the effects of differential refractive index variations. The maximum measured temperature variation during the 24 hour acquisition period was around 1.2°C which would have produced an OPD increase of around $44\mu m$ due to expansion of the optical table and around a $1.5\mu m$ decrease in OPD due to air refractive index variation. The observed changes in OPD within both the APC-MI and the SPC-MI agree well with these values.

The correlation between the OPDs of the two parallel MIs is shown in figure 5.27. This correlation disregards common effects such as thermal expansion and reference interferometer OPD changes. Hence it provides a very useful indicator of the true measurement precision of the laboratory FSI system. A straight line fit was applied to the APC-MI and SPC-MI OPD correlation data and the results are given in table 5.7. The residuals from the linear fit are shown in figure 5.28. The RMS of the residuals to the fit correspond to a correlation of around $160ppb$ in the OPDs of the two MIs.

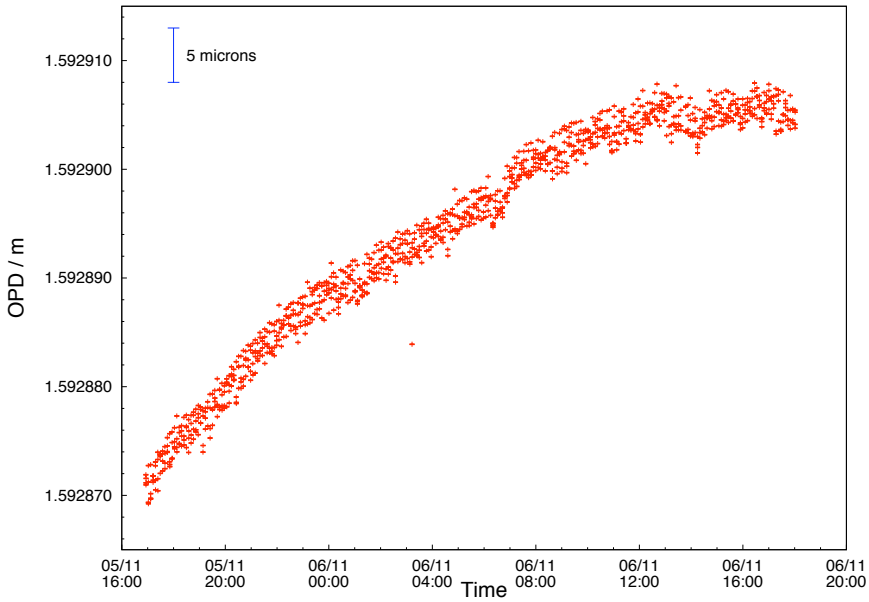

Figure 5.25: 1.6m APC-MI OPD as a function of time over a period of around 24 hours.

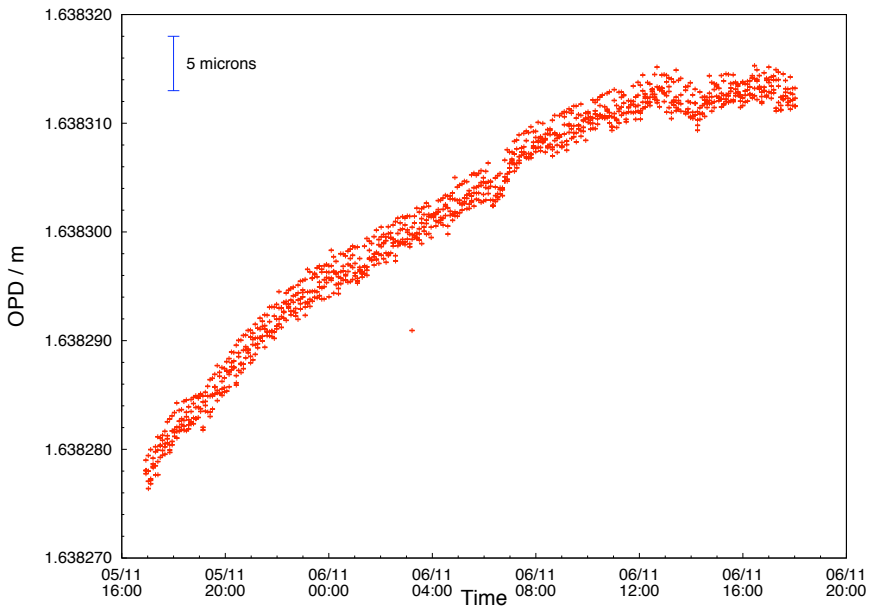

Figure 5.26: 1.6m SPC-MI OPD as a function of time over a period of around 24 hours.

Parameter	**Value**
Gradient	0.990832 ± 0.007342
Intercept / m	-0.030387 ± 0.001203
RMS of Residuals / μm	0.252

Table 5.7: The results of a linear fit to the 1.6m MI OPD correlation data over a period of around 24 hours.

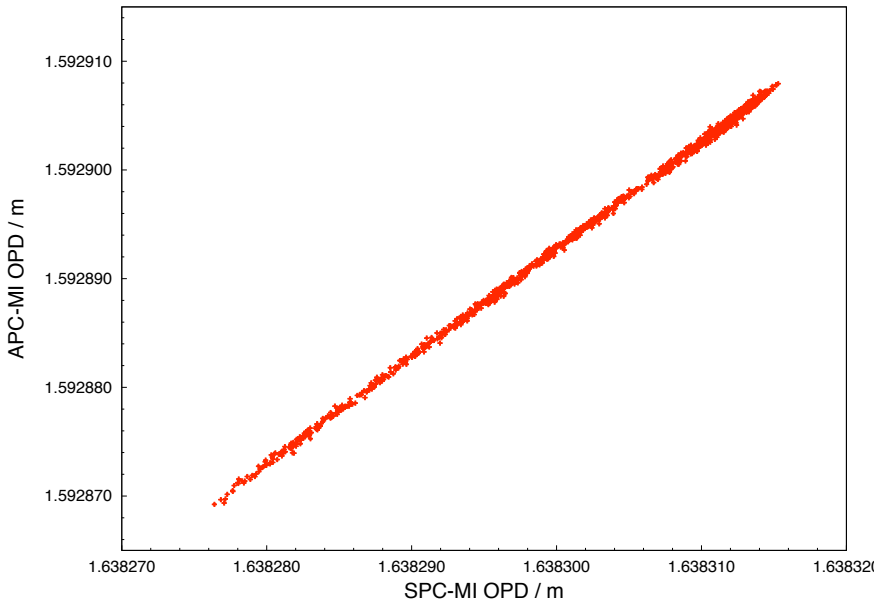

Figure 5.27: 1.6m MI OPD correlation over a period of around 24 hours.

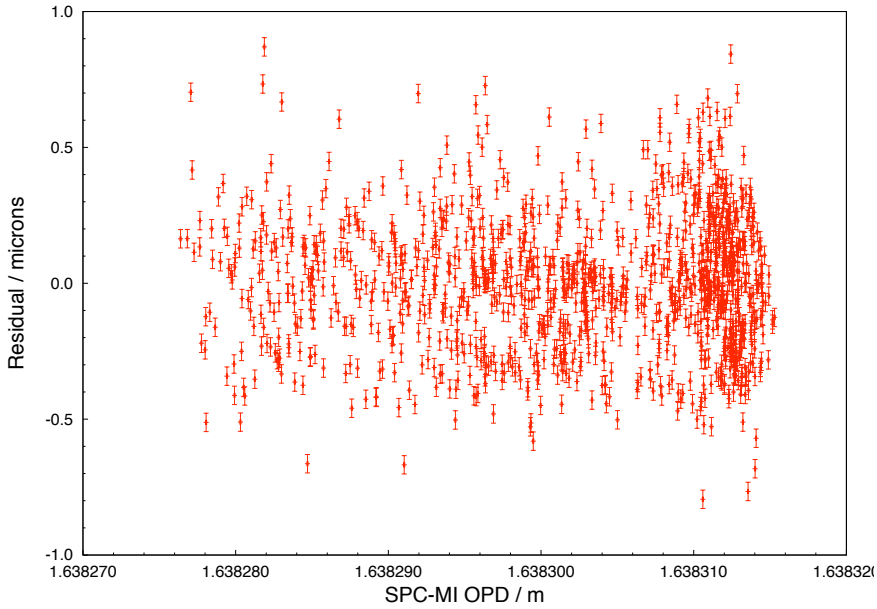

Figure 5.28: Linear fit residuals to the 1.6m MI OPD correlation over a period of around 24 hours.

5.4.2 Extension to Full Size Measurement Interferometers

After the preliminary investigations into the laboratory hardware and analysis software were completed the measurement interferometer OPDs were extended to the size required within the RTRS internal FSI measurement system. During this reconfiguration of the laboratory equipment data sets were acquired for intermediate OPDs to assess how the measurement precision would vary with the increase in OPD. The two MIs were configured with OPDs ranging from 1 to $9m$, in increments of approximately $1m$, and were subject to the same conditions as the previous investigation.

The standard deviations of a group of 20 scans for each acquired OPD are shown in figure 5.29 for both the APC-MI and the SPC-MI as a function of OPD. This plot clearly illustrates an approximately linear deterioration in OPD determination precision as a function of interferometer OPD. These results represent around a $1.3\mu m$ absolute length determination precision for the $4.5m$ long MIs in the laboratory FSI system.

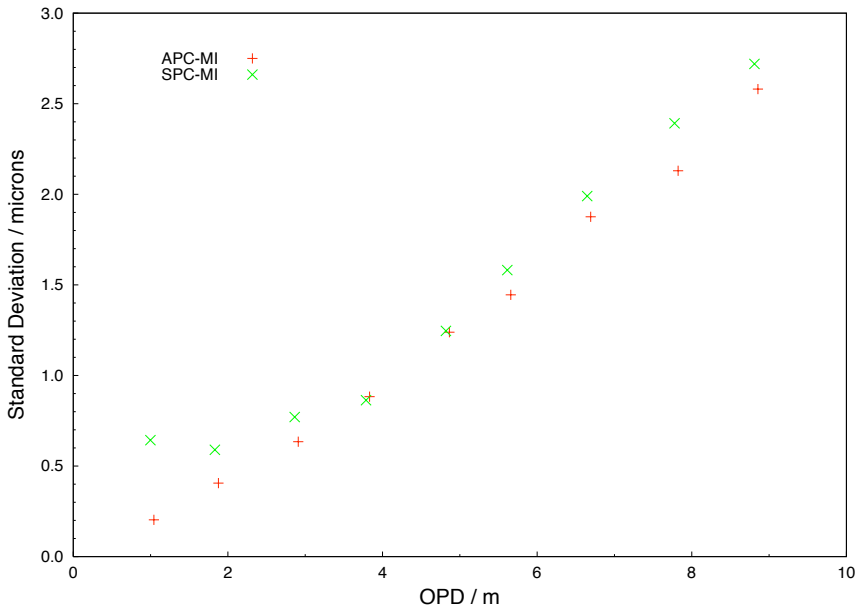

Figure 5.29: The standard deviation of the OPDs of 20 scans acquired for both the APC-MI and for the SPC-MI as a function of MI OPD.

The results of a linear fit to the correlation between the APC-MI OPD and the SPC-MI OPD are given in table 5.8. The gradient is consistent with the two MIs witnessing the same variations over the range of OPDs investigated. The large value of the RMS of the residuals is due to the reconfiguration of the MIs during each OPD increment. It is expected that this value would be less if the interferometer OPDs had been varied continuously by means of a translation stage rather than being manually reconfigured.

As a further indicator of the length determination precision the ratio of the OPDs of the APC-MI and the SPC-MI were evaluated. Figure 5.30 shows the standard deviation of the OPD ratios for the groups of 20 scans acquired at each length. These results indicate around a $120ppb$ relative length determination precision for OPDs of around $9m$ which corresponds

Parameter	Value
Gradient	$0.999911 \pm 9.82 \times 10^{-5}$
Intercept / m	$-0.045753 \pm 5.32 \times 10^{-5}$
RMS of Residuals / μm	332

Table 5.8: The results of a linear fit to the correlation of the APC-MI and the SPC-MI over a large range of OPDs.

to $0.54\mu m$ for the $4.5m$ long MIs in the laboratory FSI system. A more detailed investigation into the measurement precision on different time scales is given in the following section.

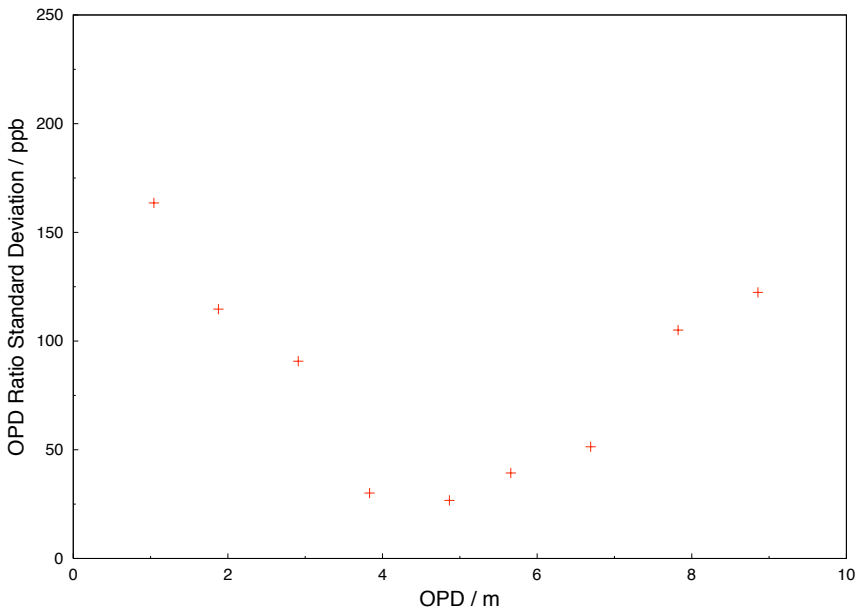

Figure 5.30: The standard deviation of the ratios of the OPDs of the APC-MI and the SPC-MI for groups of 20 scans acquired as a function of MI OPD.

5.4.3 9m OPD Measurement Interferometers

As a preliminary investigation into the performance of the RTRS internal FSI system a pair of MIs with OPDs of approximately $9m$ were prepared on the aluminium optical table in the laboratory. As with the previous investigations different launches were used in each interferometer. No vacuum system was installed, unlike in the RTRS design, however once again an environmental protection box completely enclosed both MIs.

Short Term Measurement Precision

The precision of the measurement procedure over a period of approximately 6 minutes was investigated by acquiring 50 consecutive laser scans. The OPDs of the APC-MI and the SPC-MI are shown as a function of acquisition time in figures 5.31 and 5.32 respectively.

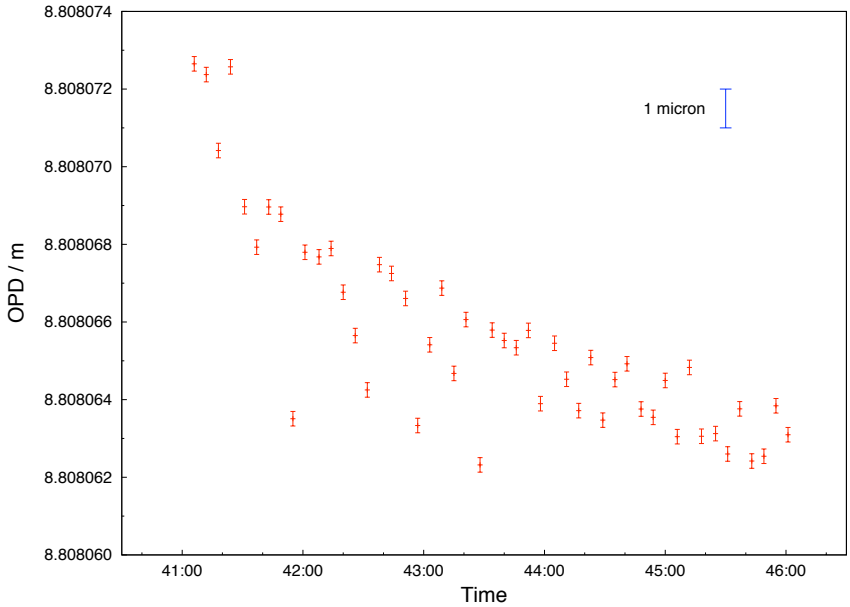

Figure 5.31: $9m$ APC-MI OPD as a function of time over a period of around 6 minutes.

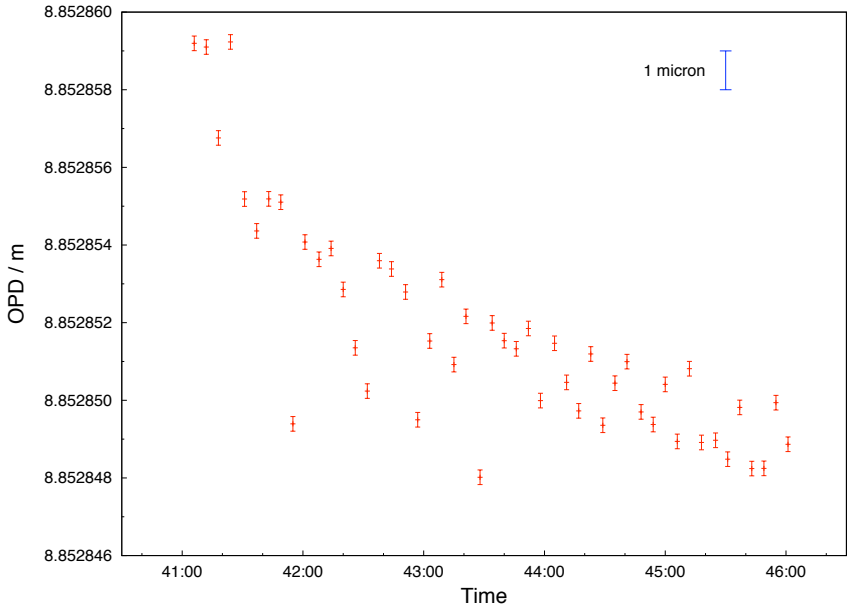

Figure 5.32: $9m$ SPC-MI OPD as a function of time over a period of around 6 minutes.

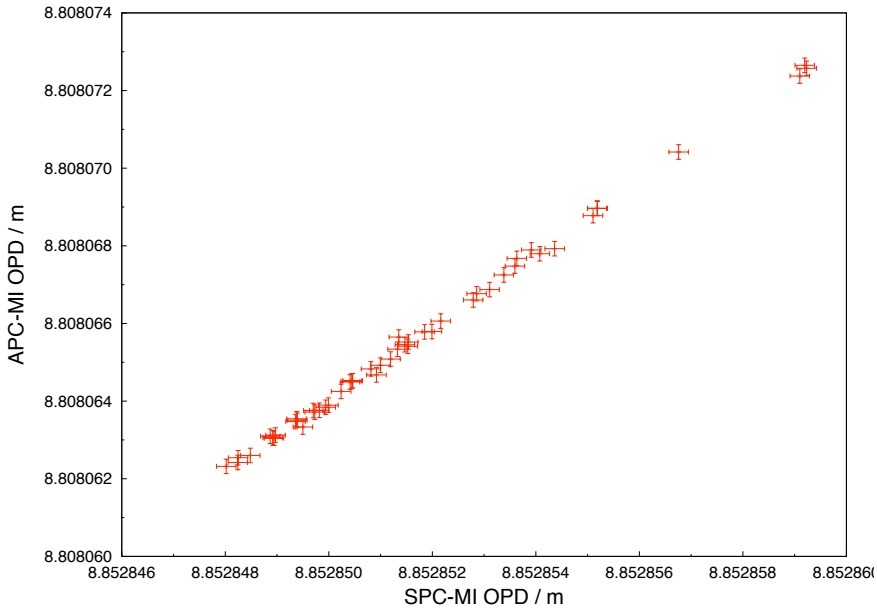

Figure 5.33: $9m$ MI OPD correlation over a period of around 6 minutes.

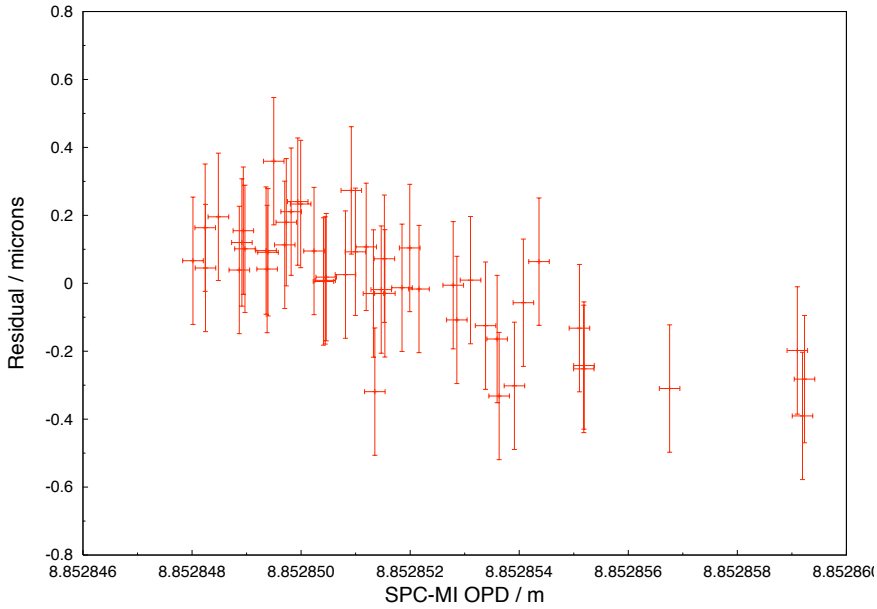

Figure 5.34: Linear fit residuals to the $9m$ MI OPD correlation over a period of around 6 minutes.

The correlation between the OPDs of the two interferometers is shown in figure 5.33. This allows the elimination of all effects which are common to both MIs including turbulence, hence it is equivalent to completely correcting both MI OPDs. A linear fit was applied to the correlation data with the results given in table 5.9. The residuals to the linear fit are shown in figure 5.34.

The calculated gradient of the linear fit is consistent with the two MIs observing the same OPD variations while the intercept indicates the absolute difference in OPD. This difference between the two MIs arose from the different ways in which the short arm interferometric reflections were produced. The calculated RMS of the residuals of the linear fit represents a correlation of around 26*ppb* between the OPDs of the two MIs during the acquisition period. This corresponds to a measurement precision of approximately $0.12\mu m$ in $4.5m$. The limiting factor in open-air interferometers on this time scale is air turbulence. Therefore the precision should be improved by placing the MIs inside a vacuum.

Parameter	**Value**
Gradient	1.000024 ± 0.011573
Intercept / m	-0.044997 ± 0.010252
RMS of Residuals / μm	0.228

Table 5.9: The results of a linear fit to the $9m$ MI OPD correlation data acquired over a period of around 6 minutes.

Long Term Measurement Precision

Both the precision of the measurement system and the ability to track the temperature induced length variations of the interferometers over a period of approximately 24 hours were investigated. Groups of 4 sequential laser scans were acquired at intervals of around 5 minutes producing a total of 1120 data sets. The observed temperature variations of the aluminium table and of the air at the launch and at the retroreflector are shown in figure 5.35 as a function of time.

The OPDs of the APC-MI and the SPC-MI are shown in figures 5.36 and 5.37 respectively. The correlation between the observed temperature variations of the aluminium optical table and the OPDs of the MIs is clear from the comparison of figures 5.35 with figures 5.36 and 5.37. As in the previous investigation the two the MIs were positioned as close to one another as possible to minimise the effects of differential OPD variations due to refractive index changes.

The temperature of the optical table varied by around 1.8°C during the period of the investigation producing approximately a $370\mu m$ variation in OPD due to expansion of the optical table. The observed air temperature variation, during the same period, of around 2.1°C would have produced a variation in interferometer OPD of approximately $17\mu m$. The variations in MI OPDs shown in figures 5.36 and 5.37 during the 24 hours period are consistent with these estimations.

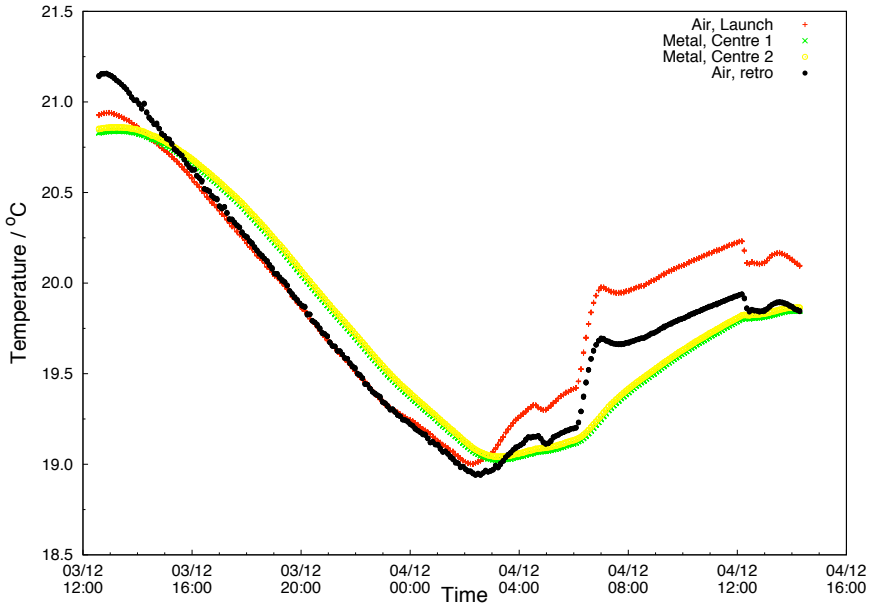

Figure 5.35: Observed temperature variations for the $9m$ MIs as a function of time over a period of around 24 hours.

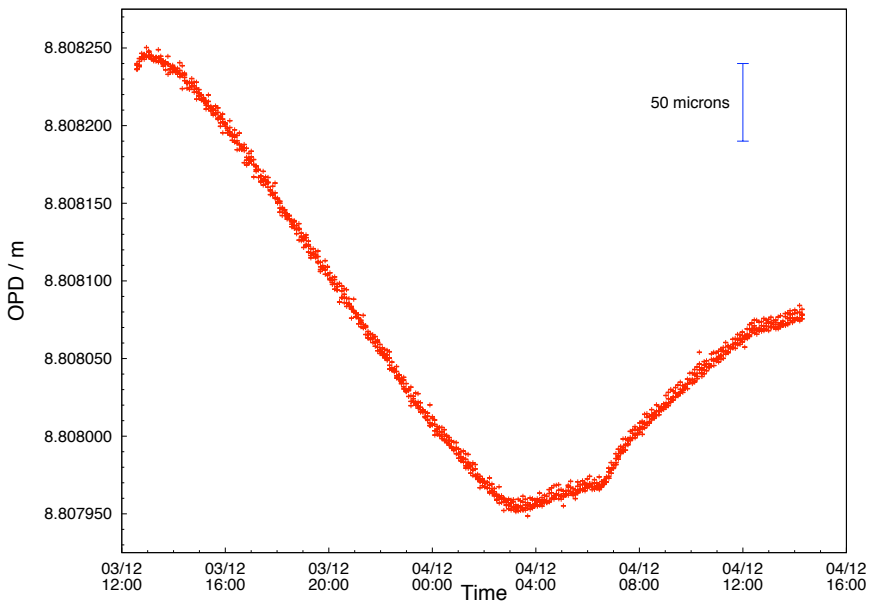

Figure 5.36: $9m$ APC-MI OPD as a function of time over a period of around 24 hours.

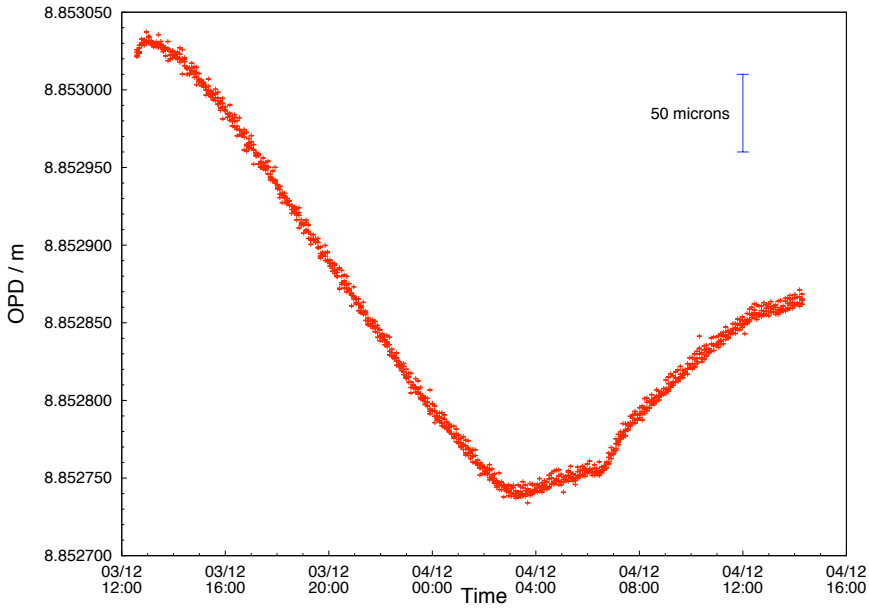

Figure 5.37: $9m$ SPC-MI OPD as a function of time over a period of around 24 hours.

As discussed previously in this section the correlation between the OPDs of the two MIs provides a more relevant indicator of the measurement precision. Once again the correlation between the determined OPDs of the two parallel measurement interferometers, shown in figure 5.38, was extremely good.

The degree to which the OPDs of the two MIs correlate gives a clear indication as to the level of precision of the measurement and analysis systems. The results of a linear fit to the correlation data are given in table 5.10 with the residuals to the fit shown in figure 5.39. The RMS of the residuals to the linear fit relates to a correlation of around $55ppb$ in the OPDs of the two MIs. This corresponds to a relative length measurement precision of approximately $0.25\mu m$ in $4.5m$.

Parameter	**Value**
Gradient	0.999912 ± 0.000174
Intercept / m	-0.044034 ± 0.001539
RMS of Residuals / μm	0.519

Table 5.10: The results of a linear fit to the $9m$ MI OPD correlation data over a period of around 24 hours.

The correlation between the measured table temperature and the OPDs for the APC-MI and the SPC-MI are shown in figure 5.40. These plots show that the observed MI OPD variations during the 24 hour period were primarily due to the expansion of the optical table as a result of temperature changes. These results include the corrections for the variations in the refractive index of the air. The departure from the linear behaviour seen at the greatest temperatures relates to the laboratory environment settling to an equilibrium after initiating the investigation.

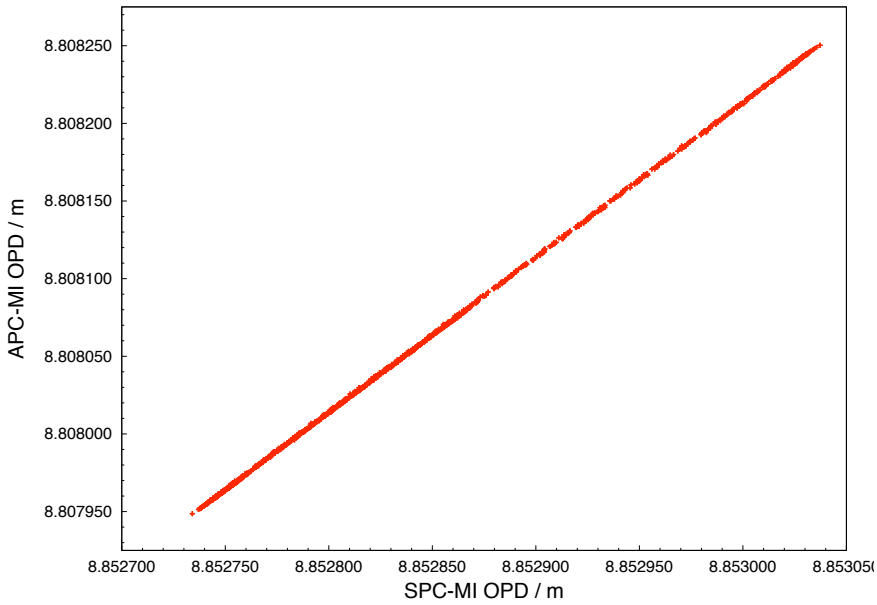

Figure 5.38: $9m$ MI OPD correlation over a period of around 24 hours.

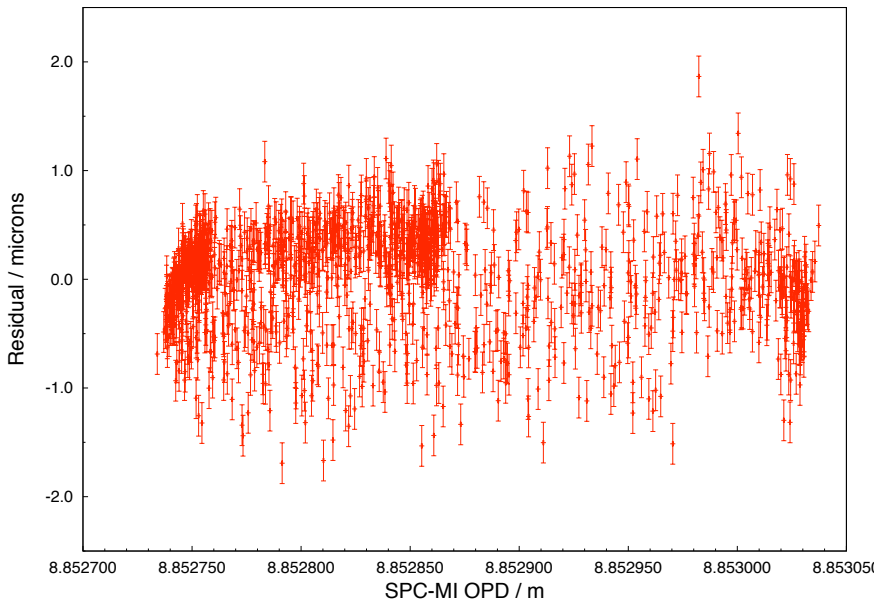

Figure 5.39: Linear fit residuals to the $9m$ MI OPD correlation over a period of around 24 hours.

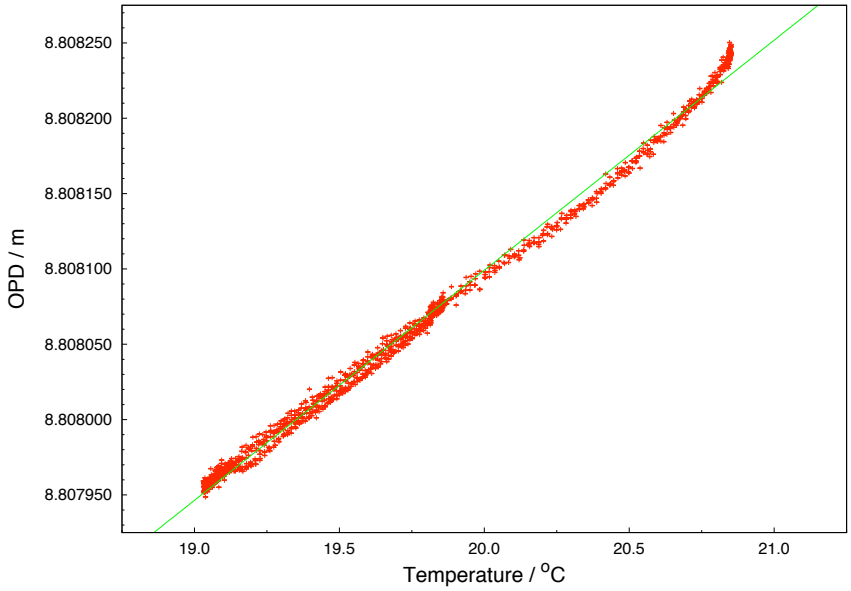

(a) $9m$ APC-MI OPD as a function of optical table temperature.

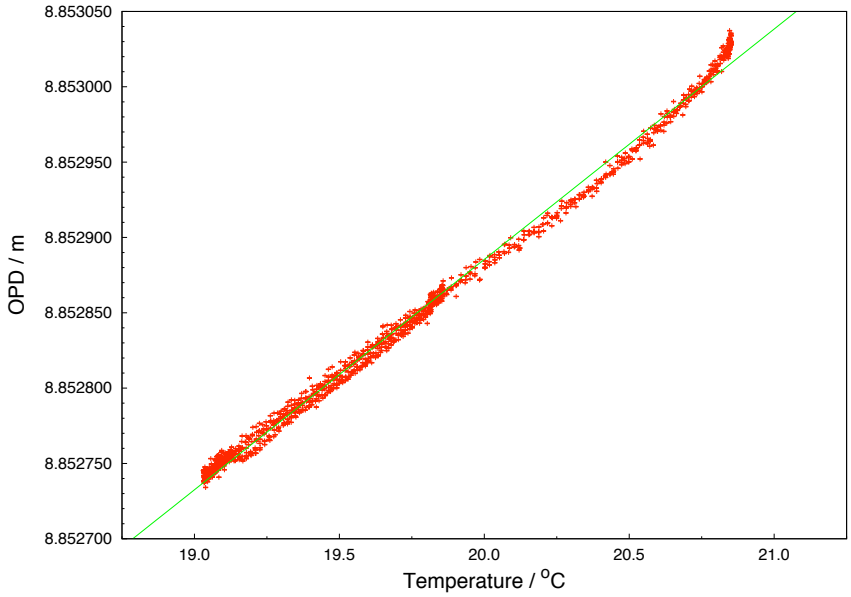

(b) $9m$ SPC-MI OPD as a function of optical table temperature.

Figure 5.40: The $9m$ MI OPDs as a function of measured optical table temperature. The green lines indicate the linear fits.

By applying linear fits to the OPD data, indicated by the green lines in figure 5.40, a values of the CTE of the aluminium optical table could be extracted. The gradient of the fits provides values for the OPD change of each interferometer per unit change in temperature. However the observed OPD changes within the MIs were also dependent upon thermal expansion within the reference interferometer as shown in equation 5.1.

$$\Delta D = D.CTE_{MI}.\Delta T - \Delta L \tag{5.1}$$

Hence the expansion of the Michelson Reference Interferometer per unit temperature change must be added to the calculated values of MI OPD change per unit temperature change. The expansion of the Michelson Reference Interferometer can be found from equation 5.2 and is approximately $52.2\mu m/°C$.

$$\Delta L = L.CTE_{ref}.\Delta T \tag{5.2}$$

Therefore dividing the sum of the gradient and the Michelson Reference Interferometer expansion per unit temperature by the mean OPD of the MI a value for the OPD change per unit change in temperature per unit OPD could be obtained for each MI. The details of the results of linear fits to the APC-MI and the SPC-MI OPDs as a function of temperature and the calculated CTE values are given in table 5.11. The calculated CTE values are comparable to the nominal CTE of aluminium which is $23.1\mu m/m/°C$ at $273K$ [74].

	APC-MI	**SPC-MI**
Gradient / $\mu m/°C$	152.702 ± 0.315	152.886 ± 0.313
Intercept / m	$8.805053 \pm 6.228 \times 10^{-6}$	$8.849833 \pm 6.198 \times 10^{-6}$
RMS of Residuals / μm	6.126	6.096
Mean OPD / m	$8.808066863 \pm 2.682 \times 10^{-6}$	$8.852853129 \pm 2.685 \times 10^{-6}$
CTE / $\mu m/m/°C$	23.260 ± 0.048	23.163 ± 0.047

Table 5.11: The results of the calculation of the CTE of the aluminium optical table from the acquired SPC-MI and APC-MI data sets.

5.5 Internal Measurement Interferometer Resolution

The resolution of the internal FSI measurement system was investigated by modifying the OPDs of the MIs. This was achieved by mounting the retroreflectors on a linear translation stage. The MI OPDs were incrementally changed over two different length scales. Initially the motion stage produced a total length change of $0.25mm$ in both interferometers with steps of $1.25\mu m$. This was designed to investigate the performance with OPD variations that should have been resolvable by the measurement system. Further data was acquired with the stage displaced by a total of $5\mu m$ in $25nm$ steps. These represented the smallest achievable length increments and produced OPD variations that were below the resolution of the measurement system. Together these two investigation provide a study of the measurement resolution of the internal FSI system for OPD variations in the range $50nm$ to $10\mu m$.

The OPDs for the parallel APC-MI and SPC-MI are shown in figures 5.41 and 5.42 respectively as a function of applied stage displacement over a range of $0.25mm$ in increments of $1.25\mu m$. A single measurement was acquired at each stage position. The effects of thermal expansion and variations in the refractive index of the air have been corrected for. The linear fit gradients of both MIs, given in table 5.12, are close to the expected value of 2 since the observed change in OPD should correspond to twice the applied stage displacement. Minor deviations from this behaviour may be explained by an error in the absolute reference OPD measurement or the axis of travel of the motion stage not being parallel to the measurement axes of the interferometers[3]. The RMS of the residuals to the linear fit was around $5\mu m$ for both interferometers. This is approximately the level of uncertainty expected as a result of air turbulence within the measurement and reference interferometers.

	APC-MI	**SPC-MI**
Gradient	1.974634 ± 0.005545	1.964011 ± 0.005161
Intercept / m	$8.834033 \pm 8.12 \times 10^{-7}$	$8.865473 \pm 7.54 \times 10^{-7}$
RMS of Residuals / μm	5.637	5.247

Table 5.12: The results of linear fits to the MI OPDs for induced length variation of $0.25mm$ in steps of $1.25\mu m$.

The correlation between the OPDs of the two MIs during the stage induced length variation of $0.25mm$ in steps of $1.25\mu m$ is shown in figure 5.43. The results of a linear fit to the correlation data are given in table 5.13 and the residuals to the fit are shown in figure 5.44.

Parameter	**Value**
Gradient	1.000549 ± 0.000333
Intercept / m	-0.080121 ± 0.002951
RMS of Residuals / μm	0.665

Table 5.13: The results of a linear fit to the $9m$ MI OPD correlation during stage induced length variation of $0.25mm$ in steps of $1.25\mu m$.

	APC-MI	**SPC-MI**
Gradient	1.869997 ± 0.097612	1.940128 ± 0.041363
Intercept / m	$8.834693 \pm 2.82 \times 10^{-7}$	$8.866114 \pm 1.22 \times 10^{-7}$
RMS of Residuals / μm	1.908	0.808
Mean Spectral SNR	2942 ± 52	4629 ± 60

Table 5.14: The results of linear fits to the MI OPDs for induced length variation of $5\mu m$ in steps of $25nm$.

[3]The deviation of the gradient relates to an error on the reference interferometer OPD of around $60mm$ or the motion stage being misaligned by around $15mrad$ from the MI launch axis. Hence motion stage misalignment provides a more reasonable explanation.

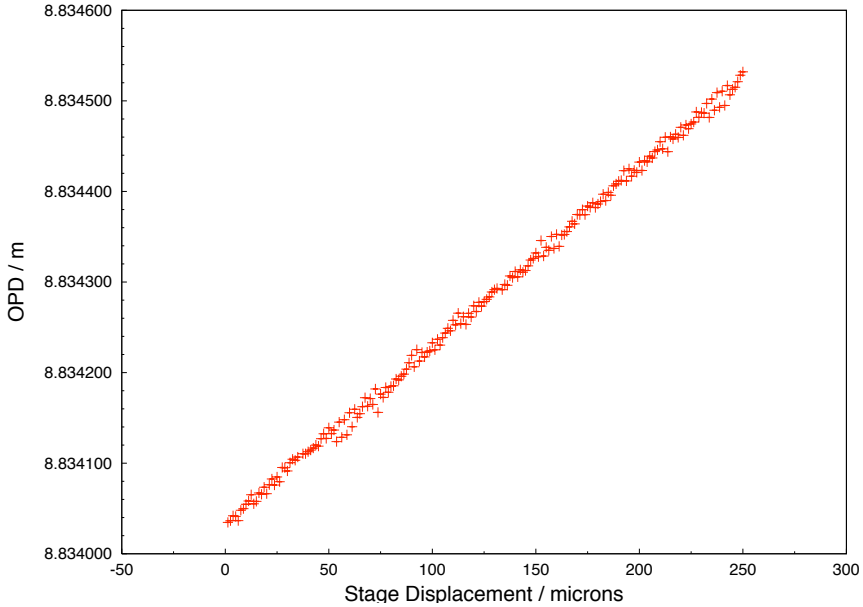

Figure 5.41: APC-MI OPD as a function of stage displacement for length increments of $1.25\mu m$.

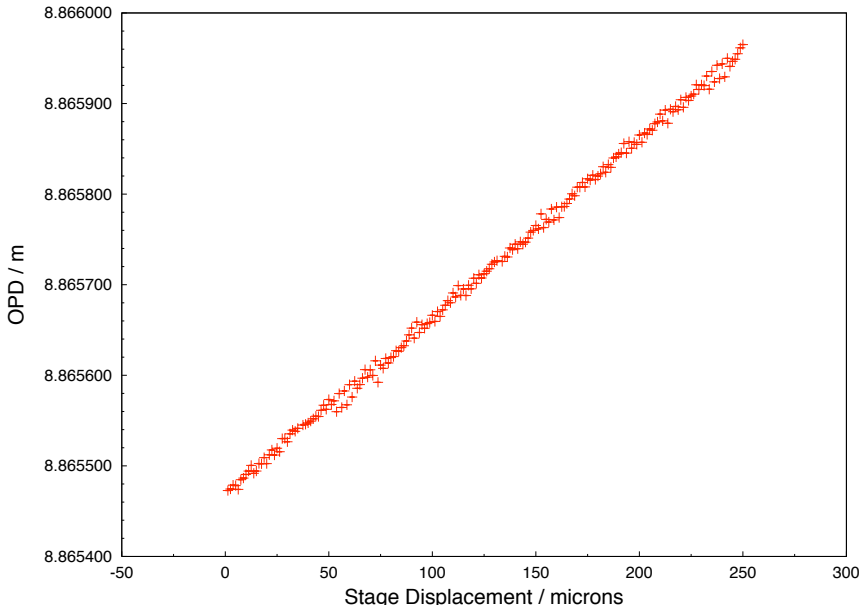

Figure 5.42: SPC-MI OPD as a function of stage displacement for length increments of $1.25\mu m$.

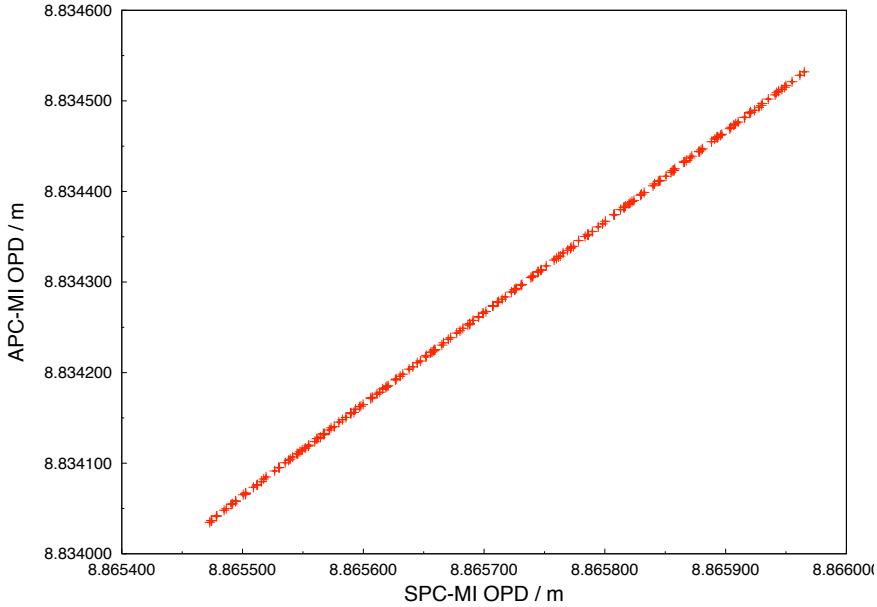

Figure 5.43: $9m$ MI OPD correlation during stage induced length variation of $0.25mm$ in steps of $1.25\mu m$.

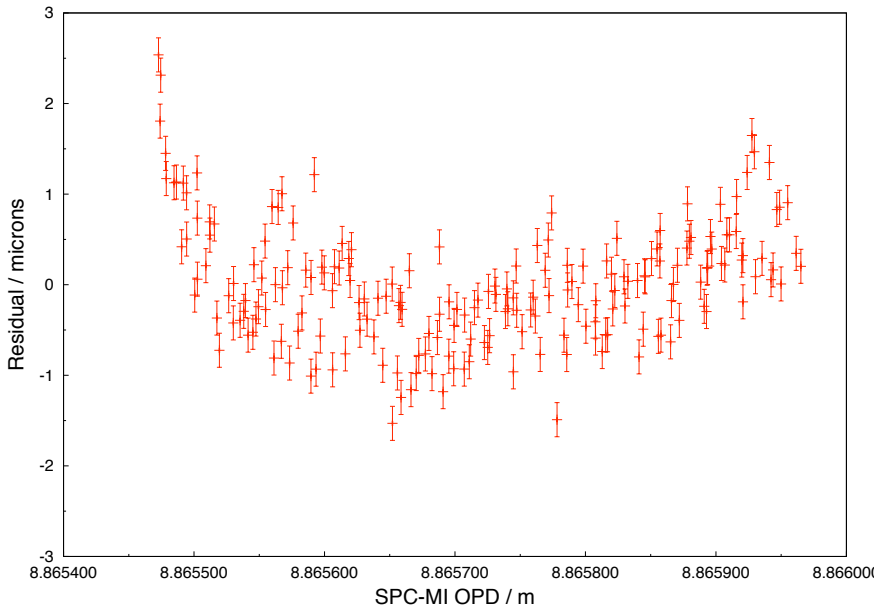

Figure 5.44: Residuals to a linear fit to the $9m$ MI OPD correlation during stage induced length variation of $0.25mm$ in steps of $1.25\mu m$.

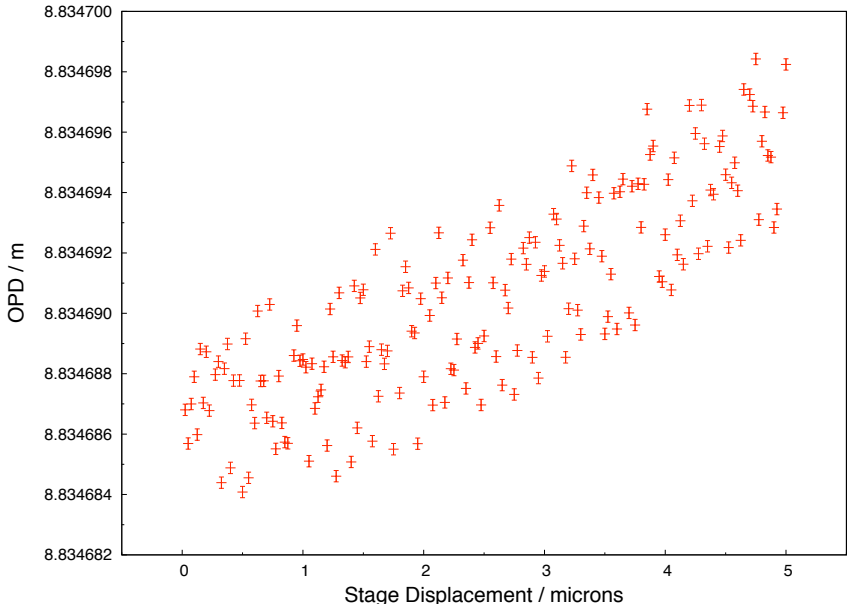

Figure 5.45: APC-MI OPD as a function of stage displacement for lengths increments of $25nm$.

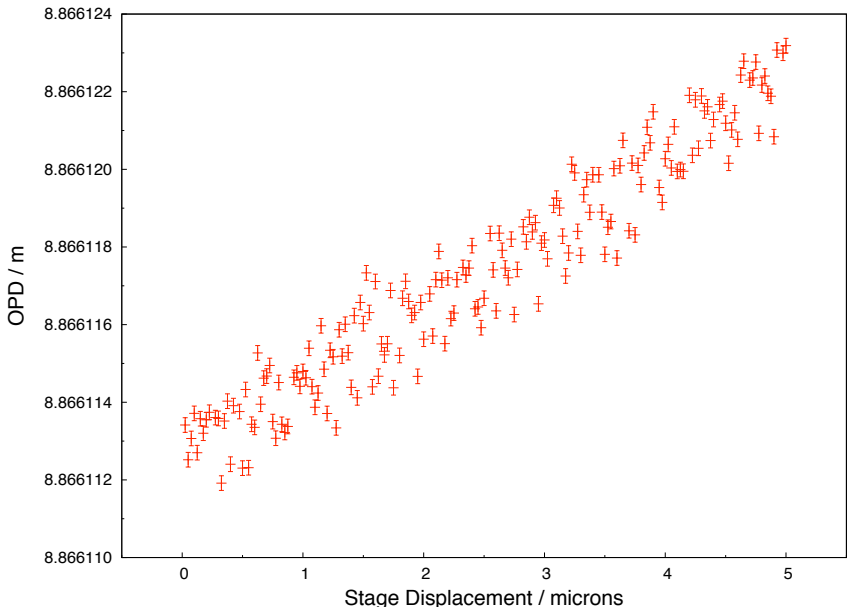

Figure 5.46: SPC-MI OPD as a function of stage displacement for lengths increments of $25nm$.

Figures 5.45 and 5.46 show the OPDs of the parallel APC-MI and SPC-MI as a function of applied stage displacement for increments of $25nm$ respectively. As before a single measurement was taken at each stage position. These results include the corrections for thermal expansion and variations in the refractive index of the air. The results of linear fits to the data shown in figures 5.45 and 5.46 are given in table 5.14. The increase in the RMS of the residuals of the APC-MI data was due to the lower SNR of the APC-MI signal. This was due to a lack of long term position stability of the APC-MI beam splitter, with respect to the collimation unit, which resulted in a reduced short arm interferometric reflection. This effect was not identified until after the data had been acquired and has since been eliminated by using an improved glue curing procedure.

Following the outline of the resolution investigation presented in section 4.3.3 the gradient of OPD variation between points was calculated by modifying equation 4.6 to produce equation 5.3.

$$gradient = \frac{\langle \Delta D \rangle}{\Delta D_{stage}} \tag{5.3}$$

where $\langle \Delta D \rangle$ is the mean observed change in OPD and ΔD_{stage} is the induced change in OPD determined from the stage displacement information. The OPD variation gradients were calculated from the induced OPD variation data for a range of length increments from $25nm$ to $10\mu m$. The standard deviations from the mean calculated gradients are shown in figures 5.47. As expected the errors on the gradients approach zero as the length increments becomes larger.

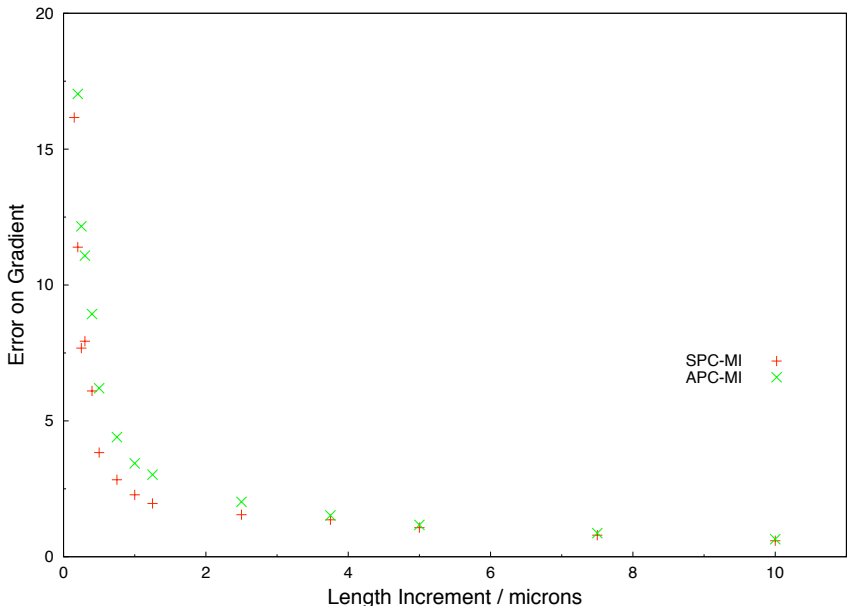

Figure 5.47: The error on the determination of the gradient, defined in equation 5.3, for induced length variations produced with stage displacement increments from $25nm$ to $10\mu m$.

As with the investigation in section 4.3.3 the difference between the calculated OPD variation gradient and the error on the gradient was used as an indicator for the resolution of the system. As an OPD variation becomes fully resolved the gradient will approach 2 and

the error tends to zero[4]. An OPD variation can be considered to have been resolved by the measurement system if the difference between the gradient and the error on the gradient is positive and not consistent with zero. Figure 5.48 shows the difference between the mean calculated gradients and the error on the gradient for groups of 20 combined measurements with length increments from $25nm$ to $10\mu m$.

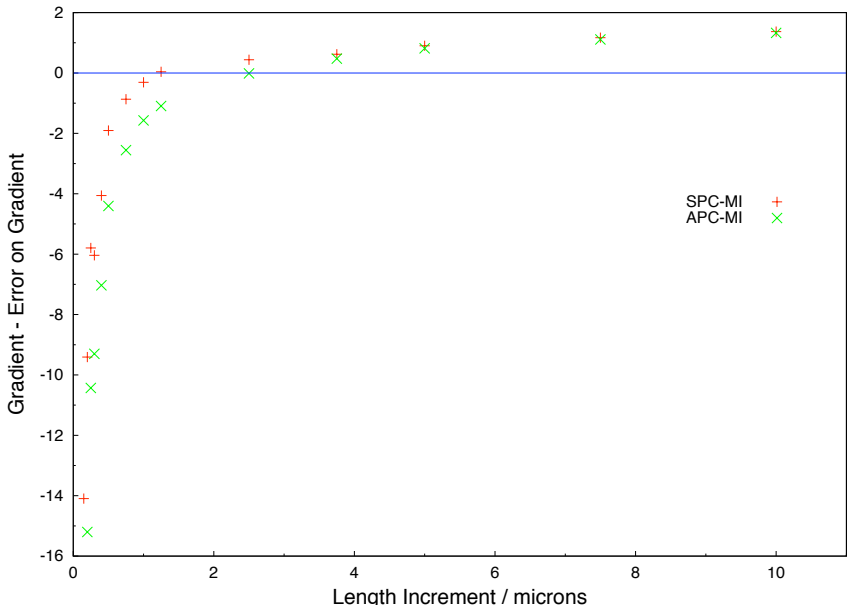

Figure 5.48: The difference between the gradient, defined in equation 5.3, and the error on the gradient for induced length variations produced with stage displacement increments from $25nm$ to $10\mu m$.

The results shown in figure 5.48 indicate that OPD variations of around $2\mu m$ are resolvable from within the laboratory internal FSI measurement system when combining around 20 measurements. This corresponds to a measurement resolution of around $1\mu m$ over a distance of approximately $4.5m$. Since the internal FSI measurement system contains six lines it should therefore mean that only 3 sets of measurements will be required to allow length variations of around $1\mu m$ to be correctly identified.

Figure 5.49 indicates that for the laboratory internal FSI measurement system the systematic limit of the OPD variation resolution was approximately $1.5\mu m$. For both the APC-MI and the SPC-MI the resolution is not improved significantly by large increases in the number of combined measurements. This systematic limit is most likely due to the laboratory measurements being undertaken in open-air. Hence it is expected that placing both the reference and measurement interferometers in a vacuum will produce a significant improvement in the measurement resolution of the RTRS internal FSI system.

[4]In this case the indicator asymptotically approaches 2, rather than 1 as in section 4.3.3, since the gradient uses ΔD_{stage} which is twice the change in OPD.

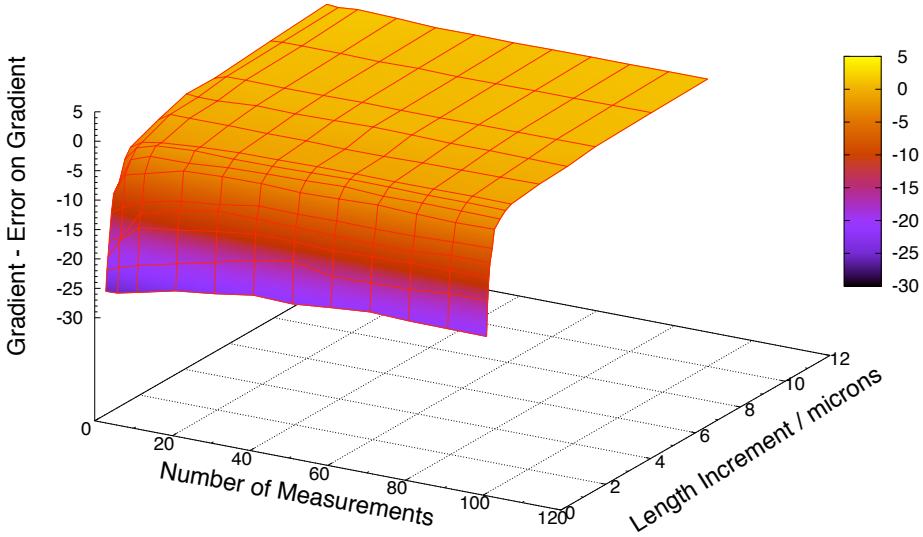

(a) $9m$ APC-MI OPD variation resolution.

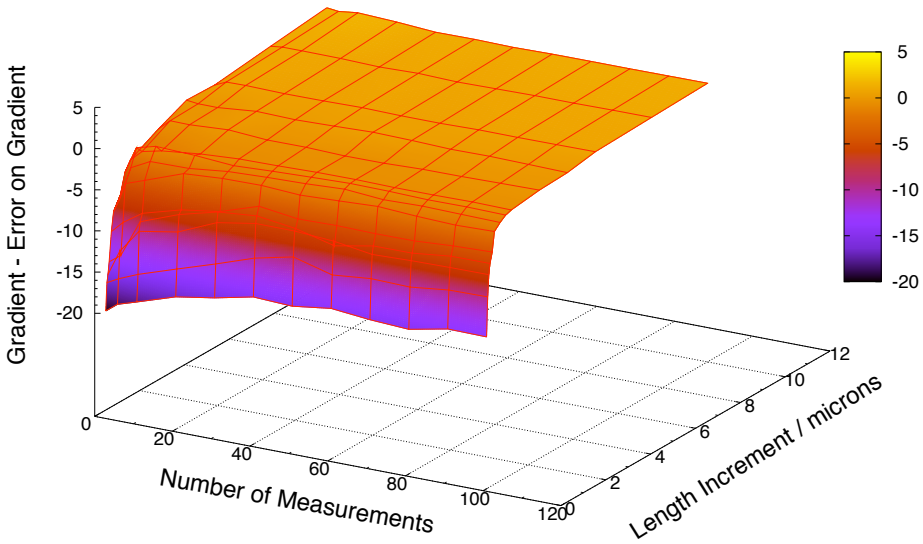

(b) $9m$ SPC-MI OPD variation resolution.

Figure 5.49: The difference between the gradient and the error on the gradient with respect to number of combined measurements and induced length variations.

5.6 Summary

A summary of the stability results for the Michelson Reference Interferometer and the Short Reference Interferometer on time scales of around 20 minutes and 24 hours is given in table 5.15. These results were obtained after the application of vacuum deterioration, thermal expansion and air refractive index variation corrections. The relative stability of the two reference interferometers over these time scales are shown in table 5.16.

	Stability Over 20 Minutes	**Stability Over 24 hours**
Michelson	$0.80\mu m$ ($170ppb$)	$3.1\mu m$ ($660ppb$)
SRI	$0.15\mu m$ ($152ppb$)	$0.59\mu m$ ($600ppb$)

Table 5.15: A summary of the stability of the Michelson Reference Interferometer and Short Reference Interferometer on time scales of around 20 minutes and 24 hours.

	Relative Stability
Over 20 Minutes	$110ppb$
Over 24 Hours	$487ppb$

Table 5.16: A summary of the OPD ratio stability of the Michelson Reference Interferometer and Short Reference Interferometers on time scales of around 20 minutes and 24 hours.

The application of the corrections produced around a 60% improvement in short term stability of the Michelson Reference Interferometer whilst providing little change to the stability of the SRI. The effect of the corrections on longer term stability was much greater. The Michelson Reference Interferometer stability was increased by a factor of 5.9 and the SRI by a factor of 3.6. These much more significant improvements in stability are due to the removal of thermally driven length variations which dominate on larger time scales. The scale of the correction for thermal expansion and refractive index variations on time scales of around 24 hours are shown in table 5.17. The remaining dominant sources of instability in the laboratory reference interferometers after the application of the corrections were air turbulence on short time scales and atmospheric pressure variations on longer time scales.

	Thermal Expansion	**Air Refractive Index Variation**
Michelson / $\mu m/°C$	40	4
SRI / $\mu m/°C$	3.5	0.1

Table 5.17: A summary of the scale of the effects of thermal expansion and air refractivity variations as a result of temperature variations within the laboratory reference interferometers on time scales of approximately 24 hours.

Preliminary investigations indicate that a measurement interferometer implementation consisting of a bare fibre launch can achieve the acceptance requirements of the external RTRS FSI measurement system. Previous investigations also indicate that this style of

interferometer is capable of producing the measurement precision and accuracy required for the RTRS systems [44]. Further dedicated investigations are required to confirm that the implementation of bare fibre MIs within the external FSI measurement system can achieve the required performance.

The calculated mean differences in the OPDs of the APC-MI and the SPC-MI for the $1.6m$ and $9m$ investigations are given in table 5.18. The correlation between the determined OPDs of the $9m$ MIs for the precision studies are given in table 5.19. These results were obtained using fully corrected reference interferometer data. These results correspond to a measurement precision of $0.25\mu m$ over $4.5m$ ($55ppb$) for the internal RTRS FSI system.

	OPD Difference / mm
$1.6m$ OPD MI	45.407311 ± 0.000008
$9m$ OPD MI	44.786310 ± 0.000015

Table 5.18: The mean difference in the OPDs of the APC-MI and SPC-MI for the $1.6m$ and $9m$ MI investigations.

	RMS of MI Correlation
Over 6 Minutes	$0.228\mu m$
Over 24 Hours	$0.487\mu m$

Table 5.19: A summary of the OPD determination precision of the $9m$ MIs on short and long time scales.

The results of the resolution investigation indicate that the measurement resolution of the open-air laboratory FSI system was around $2\mu m$ for an OPD of $9m$ when combining around 20 measurements. This relates to a system measurement resolution of approximately $1\mu m$ over $4.5m$ for sets of 3 measurements from the 6 lines acquired by the internal RTRS FSI system. The resolution should be improved by a factor of $\sqrt{N}$ by combining multiple measurements although within the laboratory a systematic limit of around $1\mu m$ in OPDs of $9m$ was estimated due to the measurements being made in open air. The resolution is expected to be improved in an evacuated system as turbulence is the main contributor to the error.

The measurement precision and length resolution results obtained for the $9m$ MIs exceeded the requirements for the internal FSI measurement system of the RTRS. It is anticipated that the measurement correlation between the internal interferometers within the RTRS will further improve since the FSI system will employ identical interferometers and both the measurement and reference systems will be evacuated.

For both the internal and external FSI measurement systems the absolute length determination accuracy will ultimately depend upon the absolute calibration and stability of the reference interferometer within the RTRS FSI system.

Chapter 6

Conclusions

Simulations and laboratory investigations have been undertaken to evaluate the performance of the FSI measurement systems within the LiCAS RTRS. The basis for the instrument control and signal acquisition systems for a prototype RTRS have been developed. An FSI analysis package based on phase extraction and spectral analysis techniques has been designed, produced and tested.

Investigations into the performance of the analysis technique developed for the FSI measurement system were undertaken using simulated data characteristic of that produced in the laboratory and within the RTRS. The results are summarised in table 6.1.

Investigated Parameter	**Value**
Internal FSI Precision / μm	0.038(syst) + 0.052(stat)
Internal FSI Accuracy / μm	0.023(syst) + 0.012(stat)
Internal FSI Resolution / μm	0.074 @ $N = 1$ ≈ 0.007 @ $N = 50$
External FSI Precision / μm	0.136(syst) + 0.266(stat)
External FSI Accuracy / μm	0.106(syst) + 0.029(stat)
External FSI Resolution / μm	0.376 @ $N = 1$ ≈ 0.068 @ $N = 50$

Table 6.1: A summary of the simulations into the nominal performance of the analysis for the internal and external FSI systems.

The investigation also indicated that $10nm$ variations in OPD could be resolved by the internal RTRS FSI systems by combining 32 measurements while $0.1\mu m$ OPD variations could be resolved in the external RTRS FSI system by combining 20 measurements.

The evaluation of the effects of signal quality degradation indicate that the theoretical precision of the analysis is achievable for SNR exceeding 2. There appear to be no additional systematic effects, introduced by the analysis, as a result of decreased signal quality. Therefore the measurement precision should be regained by combining multiple measurements although further experimental investigations are required to confirm this. The theoretical resolution of the measurement system should also be improved by the inclusion of a reference

interferometer with a greater OPD.

The high laser tuning rate limits the effects of thermally driven interferometric drift significantly. A true expansion of a $1m$ OPD interferometer of around $20nm$ is required to produce a drift error of $1\mu m$. This relates to a rate of change of temperature of around $600\mu K/s$, assuming a CTE of $10ppm/K$. The greatest rate of change of temperature observed during the laboratory investigation was around $150\mu K/s$. Hence drift due to thermal expansion was not a significant source of error within the laboratory FSI systems.

Drift error resulting from refractive index variations in the transmission media as a result of the induced wavelength change during a laser scan are more significant. The absolute drift error is the total drift error introduced due to dispersion within an interferometer. The relative drift error relates to the variation from scan-to-scan as a results of the error in controlling the end point wavelengths of each laser scan. A summary of the scale of the absolute and relative drift errors within the laboratory interferometers is given in table 6.2.

Interferometer	**Absolute Drift Error** / μm	**Relative Drift Error** / nm
Michelson Reference	6.0	2.9
SRI	0.013	0.005
External Bare Fibre	1.1	0.6
Internal APC-MI	11.6	5.6
Internal SPC-MI	11.6 (air) + 74 (lens)	5.6 (air) + 36 (lens)

Table 6.2: A summary of the scale of the absolute and relative drift errors affecting the interferometers used during the laboratory investigations.

Preliminary tests indicate that the acceptance requirements for the RTRS external FSI system are achievable using an APC terminated fibre launch. Previous investigations using similar launch solutions suggest that the required measurement precision can be achieved [44]. Further investigation are required to confirm that the performance requirements can be achieved using this style of interferometer.

Investigations were carried out to assess the precision and resolution of the collimated measurement solution designed for the RTRS internal FSI system. These investigations revealed that over the $4.5m$ car separation distance the measurement precision is around $0.25\mu m$ ($55ppb$) in open air. The resolution of the 6 measurements made by the internal FSI system in open air would be around $1\mu m$ and could be improved by a factor of $\sqrt{N}$ by combining more measurements. Both the measurement precision and resolution are expected to be improved by placing the reference and measurement interferometers inside a vacuum. Thermal stabilisation of the reference interferometer is also expected to provide an improvement in performance. A summary of the errors due to the thermal variations is given in table 6.3.

The relative stability of the reference interferometers was around $490ppb$, on time scales of around 24 hours, after the applications of corrections for thermal expansions and air refractive index variations. This represents a significant source of systematic error upon absolute length determinations. The evaluation of the absolute length determination accuracy

Interferometer	**Thermal Expansion** / $\mu m/°C$	**Thermally Driven Refractive Index Variations** / $\mu m/°C$
Michelson Reference	28.2	1.4
SRI	9	0.005
Internal APC-MI	104	5
Internal SPC-MI	104	5
External Bare Fibre	5.4	0.5

Table 6.3: A summary of the scale of the errors affecting the interferometers used during the laboratory investigations.

will require further investigations using the stabilised, evacuated and calibrated reference interferometer.

The performance measures evaluated during these investigations suggest that the FSI measurement systems within the RTRS should be capable of exceeding the requirements extracted from the preliminary system simulations. Therefore a survey solution incorporating such an FSI measurement system should be capable of achieving the global survey requirements of the ILC.

Bibliography

[1] D. Griffiths. "Introduction to Elementary Particles". Wiley & Sons (1987).

[2] R. D. Heuer, D. Miller, F. Richard & P. Zerwas (editors). "Part III: Physics at an e^+e^- Linear Collider". In "TESLA Techinical Design Report", page 159. The TESLA Colaboration (2001).

[3] F. Mandl & G. Shaw. "Quantum Field Theory". Wiley & Sons, 2nd edition (1996).

[4] R. D. Heuer, D. Miller, F. Richard & P. Zerwas (editors). "Part III: Physics at an e^+e^- Linear Collider". In "TESLA Techinical Design Report", page 14. The TESLA Colaboration (2001).

[5] P. Janot. *CERN 96-01*, **2**, 309.

[6] P. Garcia-Abia, W. Lohmann & A. Raspereza. "Measurement of the Higgs Boson Mass with a Linear e^+e^- Collider" (2005). ArXiv:hep-ex/0505096.

[7] K. Abe et al. "ACFA Linear Collider Working Group: Particle Physics Experiments at JLC" (2001). ArXiv:hep-ph/0106166.

[8] M. Battaglia. "Measuring Higgs Branching Ratios and telling the SM from a MSSM Higgs Boson at the e^+e^- Linear Collider" (1999). ArXiv:hep-ph/9910271.

[9] J. C. Brient. "The direct method to measure the Higgs branching ratios at the future e^+e^- linear collider" (2002). LC-PHSM-2002-003.

[10] T. Kuhl & K. Desch. "Simulation of the measurement of the hadronic branching ratios for a light Higgs boson at the ILC" (2007). LC-PHSM-2007-001.

[11] G. Borisov & F. Richard. "Precise measurement of Higgs decay rate into WW* at future e^+e^- Linear Colliders" (1999). ArXiv:hep-ph/9905413.

[12] E. Boos, J. C. Brient, D.W. Reid, H.J. Schreiber & R.Shanidze. "Measuring the Higgs Branching Fraction into two Photons at Future Linear e^+e^- Colliders" (2000). ArXiv:hep-ph/0011366.

[13] S.Jadach, W. Płaczek, M. Skrzypek, B.F.L. Ward & Z. Wąs. *Phys. Rev*, **61**, 113010. ArXiv:hep-ph/9907436.

[14] F. Jegerlehner. "The Effective Fine Structure Constant at TESLA Energies" (2001). LC-TH-2001-035.

[15] S. Kuhlman et al. "Physics and Technology of the Next Linear Collider". In "Snowmass '96", (1996). Arxiv:hep-ex/9605011.

[16] F. Richard, J. R. Schneider, D. Trines & A. Wagner (editors). *The TESLA Colaboration*. `http://tesla.desy.de/new pages/TDR CD/PartI/exec.html`

[17] W. Öller, H. Eberl & W. Majerotto. "Precise Predictions for Chargino and neutralino Pair Production in e^+e^- annihilation" (2005). ArXiv:hep-ph/0504109.

[18] Abdelhak Djouadi, Joseph Lykken, Klaus Mönigand Yasuhiro Okada, Mark Oreglia & Satoru Yamashita (editors). "ILC Reference Design Report: Physics at the ILC" (2007). The ILC Colaboration. `http://ilc.kek.jp/RDR/Executive_Physics.pdf`

[19] R. D. Heuer, D. Miller, F. Richard & P. Zerwas (editors). "Part III: Physics at an e^+e^- Linear Collider". In "TESLA Techinical Design Report", page 64. The TESLA Colaboration (2001).

[20] M. A. Furman & M. S. Zisman. "Luminosity". In "Handbook of Accelerator Physics and Engineering", pages 247 – 250. World Scientific (1999).

[21] S. Baird. "Accelerators for Pedestrians" (1998). Lecture course given for CERN PS Division. `http://ps.web.cern.ch/ps/training/pedestrians`

[22] J. Roßbach & P. Schmüser. "Basic Course on Accelerator Optics". In "Fifth General Accelerator Physics Course Vol. I", pages 17 – 88. CERN Accelerator School (1994).

[23] The American Linear Collider Working Group. "Linear Collider Physics Resource Book for Snowmass 2001". In "SLAC-R-0570", (2001). `http://www.slac.stanford.edu/pubs/slacreports/slac-r-570.html`

[24] J. Rees. "Colliders". In "Handbook of Accelerator Physics and Engineering", pages 11 – 13. World Scientific (1999).

[25] R. D. Heuer, D. Miller, F. Richard & P. Zerwas (editors). "Part III: Physics at an e^+e^- Linear Collider". In "TESLA Techinical Design Report", The TESLA Colaboration (2001). `http://tesla.desy.de/new pages/TDR CD/PartIII/physic.html`

[26] R. P. Walker. "Synchrotron Radiation". In "Fifth General Accelerator Physics Course Vol. I", pages 437 – 459. CERN Accelerator School (1994). CERN-94-01. `http://preprints.cern.ch/yellowrep/1994/94-01/p437.pdf`

[27] E. J. N. Wiedemann. "Radiation of a Point Charge". In "Handbook of Accelerator Physics and Engineering", pages 181 – 182. World Scientific (1999).

[28] K. Yokoya & P. Chen. "Beam-Beam Phenomena in Linear Colliders". In "US-CERN School on Particle Accelerators - Frontiers of Particle Beams: energy Limitations", pages 415–445 (1990).

[29] F. Zimmermann. "Accelerator Physics and Technologies for Linear Colliders: Beam Delivery". February 2002.

[30] T. Raubenheimer. "Accelerator Physics Issues in linear Colliders". March 2002.

[31] James Brau, Yasuhiro Okada & Nicholas Walker (editors). "ILC Reference Design Report: Executive Summary" (2007). The ILC Colaboration. `http://ilc.kek.jp/RDR/Executive_Summary.pdf`

[32] Barry Barish (Director GDE). "The International Linear Collider Global Design Effort Baseline Configuration Document". Revision May 8 2006.

[33] Nan Phinney, Nobukasu Toge & Nicholas Walker (editors). "ILC Reference Design Report: Accelerator" (2007). The ILC Colaboration. `http://ilc.kek.jp/RDR/Executive_Accelerator.pdf`

[34] Barry Barish (Director GDE). "The International Linear Collider Global Design Effort Baseline Configuration Document". Revision March 4 2007.

[35] TESLA Collaboration. "TESLA TDR" (2001). `http://tesla.desy.de/tdr/`

[36] KEK. "First prototype model of KEK L-band 9-cell cavity (ICHIRO cavity)" (2005). KEK image number KE0057. `http://www.interactions.org/imagebank/images/KE0057H.jpg`

[37] R. Amirikas, A. Bertolini, W. Bialowons & H. Ehrlichmann. "Ground Motion & Comparison of Various Sites". In "Nanobeam 2005", (2005). `http://atfweb.kek.jp/nanobeam/files/proc/proc-WG2b-01.pdf`

[38] K. Kubo. "Alignment tolerances in the main linac." Private communication, October 2006.

[39] G. Grzelak. "Simulations of the LiCAS Survey System for the ILC". In "9th International Workshop on Accelerator Alignment", (2006).

[40] A. Reichold, M. Dawson, J. Green, M. Jones Y. Han, G. Moss, B. Ottewell, R. Wastie, D. Kämtner, J. Prenting, M. Schlösser & G. Grzelak. "The LiCAS-RTRS A Rapid and Cost Efficient Survey System for the ILC". In "9th International Workshop on Accelerator Alignment", (2006).

[41] L. Brunel. "SIMULGEO: Simulation and Reconstruction Software for Optogeometrical Systems" (1998). CERN CMS Note 1998/079.

[42] E. Hecht. "Optics". Addison Wesley Longman, 3rd edition (1998).

[43] R. Loudon. "The Quantum Theory of Light". Oxford University Press, 2nd edition (1995).

[44] P. A. Coe. "An Investigation of Frequency Scanning Interferometry for the Alignment of the ATLAS Semiconductor Tracker". Ph.D. thesis, University of Oxford (2002).

[45] Optima Research Ltd. "Zemax Optical Design Software". `http://www.optima-research.com/Software/Optical/Zemax/index.htm`

[46] R. Bingham. "Optimum Gaussian Beams for off-axis retroreflectors". Private communication, November 2004.

[47] R. Bingham. "Relative Power Returned to a Bare Fibre". Private communication, March 2005.

[48] PLX Inc. "1.0" Clear Aperture Hollow Retroreflector & Ball Mount" (2001). `www.plxinc.com/pdf/1.5bmrP-no_pic.pdf`

[49] R. Bingham. "Gaps in Retroreflectors and their effect on LiCAS". Private communication, March 2005.

[50] PLX Inc. "0.31" Clear Aperture Hollow Retroreflector & Ball Mount" (2004). `www.plxinc.com/pdf/0.5bmrP-no_pic.pdf`

[51] Agilent. "Agilent 81642A Tunable Lase Technical Specifications" (2002).

[52] C. Randy Giles. *Journal of Lightwave Technology*, **9**, 2.

[53] D. M Baney, P. Gallion & R. S. Tucker. *Optical Fiber Technology*, **6** (2000) 122–154.

[54] Keopsys. "Test and Measurement Fiber Product Technical Specification" (2003). `www.keopsys.com`

[55] Corning. "Corning SMF-28 Optical Fiber Product Information" (2002). `www.corning.com/opticalfiber`

[56] Albert A. Michelson & Edward W. Morley. *The American Journal Of Science*, **CXXXIV**, 203 (1887) 333–345.

[57] H-J Yang, J. Deibel, S. Nyberg & K. Riles. "High-precision Absolute Distance and Vibration Measurement using Frequency Scanned Interferometry" (2004). ArXiv:physics/0409110.

[58] Thorlabs. "350560, LightPath Aspheric Lenses" (2004). `http://www.thorlabs.com/Thorcat/8900/8914-S01.pdf`

[59] G. Kaye & T. Laby. "Kaye & Laby Online: Tables of Physical & Chemical Constants" (2006). `http://www.kayelaby.npl.co.uk/general_physics/2_3/2_3_3.html`

[60] IOTECH Inc. "IOTECH ADC488 User Manual" (1997). ADC488-901, Rev. 4.0.

[61] MICOS. "Ultra Precision Linear Stage UPM-160" (2004). `www.micos.ws/UPM_160.html`

[62] National Instruments. "National Instruments PCI-6115 ADC card Specifications" (2005).

[63] P. Carré. *Metrologia*, **2**, 1 (1966) 13–23.

[64] N.R. Lomb. *Astrophysics and Space Science*, **39** (1982) 447–462.

[65] W.H. Press & G.B Rybicki. *Astrophysical Journal*, **338** (1989) 277–280.

[66] D. W. Jordan & P. Smith. "Mathematical Techniques". Oxford University Press, 2nd edition (1997).

[67] D. W. Marquardt. *Journal of the Society of Industrial and Applied Mathematics*, **11**, 2 (1963) 431–441.

[68] B. Edlén. *Metrologia*, **2** (1966) 71–80.

[69] K. P. Birch & M. J. Downs. *Metrologia*, **30** (1993) 155–162.

[70] K. P. Birch & M. J. Downs. *Metrologia*, **31** (1994) 315–316.

[71] P. E Ciddor. *Applied Optics*, **35**, 9 (1996) 1566–1573.

[72] Y. Han. "Data for preliminary collimated external FSI studies." Private communication, February 2005.

[73] Y. Han. "Data for preliminary bare fibre external FSI studies." Private communication, May 2005.

[74] G. Kaye & T. Laby. "Kaye & Laby Online: Tables of Physical & Chemical Constants" (2006). `http://www.kayelaby.npl.co.uk/general_physics/2_3/2_3_5.html`

Appendix A

Abbreviations

Abbreviations used in this thesis:
AC Alternating Current.
ADC Analogue Digital Converter.
AMSB Anomoly Mediated Symmetry Breaking.
APC Angle Polished Connector.
ASCII American Standard Code for Information Interchange.
ASE Amplified Stimulated Emission.
BDS Beam Delivery System.
BNC Bayonet Neill-Concelman Connector.
BPM Beam Position Monitor.
CERN Conseil Européen pour la Recherche Nucléaire or European Organisation for Nuclear Research.
CPU Central Processing Unit.
CTE Coefficient of Thermal Expansion.
DAQ Data Acquisition.
DC Direct Current.
DESY Deutsches Elektronen Synchroton.
DFT Discrete Fourier Transform.
EDFA Erbium-Doped Fibre Amplifier.
FFT Fast Fourier Transform.
FNAL Fermi National Accelerator Laboratory (Fermilab).
FSI Frequency Scanning Interferometry.
GLC Global Linear Collider.
GMSB Gauge Mediated Symmetry Breaking.
GPIB General Purpose Interface Bus.
GPS Global Positioning System.
GRP Gas Return Pipe.
GUT Grand Unified Theory.
HERA Hadron Electron Ring Accelerator.
HGRP Helium Gas Return Pipe.
ILC International Linear Collider.

IO Input/Output.
IP Interaction Point.
LED Light Emitting Diode.
LEP Large Electron Positron Collider.
LHC Large Hadron Collider.
LiCAS Linear Collider Alignment and Survey.
LSM Laser Straightness Monitor.
MI Measurement Interferometer.
mSUGRA Minimal Supergravity.
MSSM Minimally Supersymmetric Standard Model
NA Numerical Aperture.
NaN Not a Number.
NF Noise Figure.
NLC Next Linear Collider.
OPD Optical Path Difference.
PCI Peripheral Component Interconnect.
PD Photodetector.
PSD Power Spectral Density.
RF Radio Frequency.
RMS Root-Mean-Square.
RTML Ring-to-Main-Linac.
RTRS Rapid Tunnel Reference Surveyor.
SLD Standford Linear Detector.
SM Standard Model.
SNR Signal-to-Noise Ratio.
SPC Straight Polished Connector.
SPS Super Proton Synchrotron.
SRI Short Reference Interferometer.
SUSY Supersymmetry.
TESLA Tera-Electron Volt Linear Accelerator.
TTL TransistorTransistor Logic.
UV Ultra Violet.

Appendix B

List of Algebraic Symbols

Accelerator Related

$\mathcal{L}$ - Luminosity.

σ - Cross-section.

ε - Emittance.

Υ - Beamstrahlung Parameter.

$\mathcal{D}$ - Disruption Parameter.

$\mathcal{H}_{\mathcal{D}}$ - Pinch Enhancement Factor.

A - Divergence Parameter.

γ - Lorentz factor.

β - Amplitude function.

General

c - Speed of light.

ν - Optical frequency.

q - Phase ratio.

Ω - Drift error magnification factor.

ϵ - Relative interferometer drift error.

Interferometric Phases

Φ - Reference Interferometer phase.

Θ - Measurement Interferometer phase advance.

Interferometric Optical Path Differences

L - Reference Interferometer optical path difference.

D - Measurement Interferometer optical path difference.

EDFA Noise Analysis

ρ_{ASE} - Amplifies spontaneous emission spectral density.

Phase Analysis

α_s - 4-point Carré phase step size.

Spectral Analysis

ω - Spectral angular phase ratio.

Appendix C

Derivation of The Lomb Periodogram

The Discrete Fourier Transform (DFT) of a sequence of a series of intensities I sampled at equally spaced times t_j is given by

$$DFT(\omega) = \sum_{j=0}^{N-1} I(t_j) e^{-i\omega t_j} \tag{C.1}$$

where $\omega = 2\pi f$ and $j = 1, 2, 3, \ldots N$. The power spectral density is then given by the standard method

$$P(\omega) = \frac{1}{N} \sum_{j=0}^{N-1} \left| I(t_j) e^{-i\omega t_j} \right|^2 . \tag{C.2}$$

When the intensities are transformed into a function of reference interferometer phase, $t_i \rightarrow \Phi_n$, the sampling becomes uneven producing equation 3.10 which can be re-expressed as

$$DFT(\omega) = \left(\frac{N}{2}\right)^{\frac{1}{2}} \sum_{n=0}^{N-1} I(\Phi_n) \left(A \cos(\omega \Phi_n) - iB \sin(\omega \Phi_n)\right) \tag{C.3}$$

where A and B are unspecified functions of ω. The corresponding normalised periodogram is then

$$P(\omega) = \frac{1}{N} \left|DFT(\omega)\right|^2 = \frac{A^2}{2} \left(\sum_n I(\Phi_n) \cos(\omega \Phi_n) \right)^2 + \frac{B^2}{2} \left(\sum_n I(\Phi_n) \sin(\omega \Phi_n) \right)^2 . \tag{C.4}$$

If $A = B = (\frac{2}{N})^{\frac{1}{2}}$ then equations C.3 and C.4 reduce to the forms given in equations C.1 and C.2. However A and B are not unique and other choices exist which also reduce to the evenly sampled case. Therefore A and B must be determined uniquely. If we require the Lomb Periodogram to have an exponential distribution, as with the evenly sampled case, it is possible to make simple choices for A and B.

If we consider the case where $I(\Phi)$ is normally distributed noise with zero mean and constant unit variance. Then

$$G(\omega) = A \sum_n I(\Phi_n) \cos(\omega \Phi_n) \tag{C.5}$$

is a linear combination of independent normal random variables. Since a linear combination of normally distributed random variables is also normal the mean of G, $\langle G \rangle = 0$ and the variance of G is

$$\sigma_g^2 = \langle G^2 \rangle = A^2 \sum_{n=1}^{N} \sum_{m=1}^{N} \langle I(\Phi_n) I(\Phi_m) \rangle \cos(\omega \Phi_n) \cos(\omega \Phi_m) \tag{C.6}$$

where $\langle\rangle$ denotes the evaluation of the expectation. Since the terms where $n \neq m$ vanish this reduces to

$$\sigma_g^2 = A^2 N \sigma_0^2 \sum_n \cos^2(\omega \Phi_n). \tag{C.7}$$

Similarly defining

$$H(\omega) = B \sum_n I(\Phi_n) \sin(\omega \Phi_n) \tag{C.8}$$

which is also a linear combination of independent normal random variables with zero mean and variance given by

$$\sigma_h^2 = B^2 N \sigma_0^2 \sum_n \sin^2(\omega \Phi_n). \tag{C.9}$$

Equation C.3 can then be rewritten so that $P(\omega)$ is expressed as the sum of squares of two normally distributed, zero-mean random variables

$$P(\omega) = \frac{1}{2} \left[G(\omega)^2 + H(\omega)^2 \right]. \tag{C.10}$$

To force such a sum to have an exponential probability distribution the variance of both normal variables must be equal. Let U and V be two zero-mean random variables with variance σ_u and σ_v respectively and let $Z^2 = U^2 + V^2$. Z is then distributed according to

$$P(z) = \frac{e^{-\frac{z}{2\sigma_u \sigma_v}}}{2\sigma_u \sigma_v} S \left[\frac{z}{4} \left(\frac{1}{\sigma_u^2} - \frac{1}{\sigma_v^2} \right) \right]. \tag{C.11}$$

Where $\sigma_u \neq \sigma_v$ and

$$S(y) = e^{-y} I_0(y) \tag{C.12}$$

where I_0 is the modified Bessel function of the first kind:

$$I_0(y) = 1 - \frac{y^2}{2^2} + \frac{y^4}{2^2 4^2} - \frac{y^6}{2^2 4^2 6^2} + \ldots \tag{C.13}$$

with $y = \frac{z}{4} \left(\frac{1}{\sigma_u^2} - \frac{1}{\sigma_v^2} \right)$. If $\sigma_u = \sigma_v = \sigma$ equation C.11 reduces to

$$P(z) = \left(\frac{1}{2\sigma^2} \right) e^{-\frac{z}{2\sigma^2}} \tag{C.14}$$

which is the usual exponential result for the sum of the squares of two normal variables of equal variance and mean. Therefore setting $\sigma_g = \sigma_h = \sigma_0$ makes the distribution of the generalised periodogram exponential.

It follows from equations C.7 and C.9 that the choices

$$A(\omega) = \frac{Q(\omega)}{\sqrt{N}} \left(\sum_n \cos^2(\omega\Phi_n) \right)^{-\frac{1}{2}} \tag{C.15}$$

and

$$B(\omega) = \frac{Q(\omega)}{\sqrt{N}} \left(\sum_n \sin^2(\omega\Phi_n) \right)^{-\frac{1}{2}} \tag{C.16}$$

give the necessary equality of variance since the $N \sum_n \cos^2(\omega\Phi_n)$ and $N \sum_n \sin^2(\omega\Phi_n)$ terms cancel. Here $Q(\omega)$ is a function of ω the value of which is determined by the condition that $P(\omega)$ for the unevenly sampled case has the same mean value as in the evenly sampled case. Hence the periodogram in equations C.4 becomes

$$P(\omega) = \frac{1}{2N} \left(\frac{[\sum_n I_n \cos(\omega\Phi_n)]^2}{\sum_n \cos^2(\omega\Phi_n)} + \frac{[\sum_n I_n \sin(\omega\Phi_n)]^2}{\sum_n \sin^2(\omega\Phi_n)} \right) \tag{C.17}$$

where $I_n \equiv I(\Phi_n)$. Note that for evenly spaced Φ_ns $A(\omega) = B(\omega) = \sqrt{(\frac{2}{N})}$ whenever $\omega = \omega_n = \frac{2\pi n}{T}$ where n ranges over a set of well known natural frequencies $n = -\frac{N_0}{2}, \ldots, +\frac{N_0}{2}$. This can be seen by equating equations C.15 and C.16 and using the identity $\sin^2 x = 1 - \cos^2 x$ to give $\cos x = \frac{1}{\sqrt{2}}$, which is true for multiples of $\frac{2\pi}{N}$. Equations C.3 and C.4 then reduce to the evenly spaced definitions given in equations C.1 and C.2.

Further generalisation is required if the data is not zero mean with unit variance. The mean and variance are given by the usual formulas

$$\bar{I} \equiv \frac{1}{N} \sum_{n=0}^{N-1} I_n \qquad \sigma^2 \equiv \frac{1}{N-1} \sum_{n=0}^{N-1} (I_n - \bar{I})^2. \tag{C.18}$$

Hence $[\sum_n I_n]^2 / N$ is replaced by $\left[\sum_n (I_n - \bar{I})\right]^2 / \sigma^2$ and the periodogram becomes

$$P(\omega) = \frac{1}{2N} \left(\frac{[\sum_n (I_n - \bar{I}) \cos(\omega\Phi_n)]^2}{\sum_n \cos^2(\omega\Phi_n)} + \frac{[\sum_n (I_n - \bar{(I)}) \sin(\omega\Phi_n)]^2}{\sum_n \sin^2(\omega\Phi_n)} \right) \tag{C.19}$$

The periodogram in equation C.19 is not invariant to translation in phase. This restriction can be removed by subtracting a phase delay φ from all of the phase arguments in equation C.19 producing

$$P(\omega) = \frac{1}{2\sigma^2} \left(\frac{\left[\sum_n (I_n - \bar{I}) \cos \omega(\Phi_n - \varphi)\right]^2}{\sum_n \cos^2 \omega(\Phi_n - \varphi)} + \frac{\left[\sum_n (I_n - \bar{I}) \sin \omega(\Phi_n - \varphi)\right]^2}{\sum_n \sin^2 \omega(\Phi_n - \varphi)} \right) \tag{C.20}$$

where

$$\tan(2\omega\varphi) \equiv \frac{\sum_n \sin(2\omega\Phi_n)}{\sum_n \cos(2\omega\Phi_n)}. \tag{C.21}$$

The offset φ make $P(\omega)$ completely independent of shifting all the Φ_ns by any constant. Equation C.20 is the Normalised Lomb Periodogram.